RÉPUBLIQUE FRANÇAISE
Liberté Égalité Fraternité

Université de Toulouse

Doctorat de l'Université de Toulouse

préparé à l'Université Toulouse III - Paul Sabatier

Effets des tourbillons de la zone de déferlement et du cisaillement vertical du courant de retour sur la dispersion des traceurs : approche de modélisation 3D à vagues résolues

---

Thèse présentée et soutenue, le 27 novembre 2024 par

Simon TREILLOU

École doctorale
SDU2E - Sciences de l'Univers, de l'Environnement et de l'Espace

Spécialité
Océan, Atmosphère, Climat

Unité de recherche
LEGOS - Laboratoire d'Etudes en Géophysique et Océanographie Spatiale

Thèse dirigée par
Patrick MARCHESIELLO

Composition du jury
M. Rafael ALMAR, Président, IRD Occitanie
M. Damien SOUS, Rapporteur, Université de Pau et des Pays de l'Adour
M. Volker ROEBER, Rapporteur, Université de Pau et des Pays de l'Adour
Mme France FLOC'H, Examinatrice, Université de Bretagne Occidentale
M. Laurent LACAZE, Examinateur, CNRS Occitanie Ouest
M. Patrick MARCHESIELLO, Directeur de thèse, IRD Occitanie

Membres invités
M. Pascal NOBLE, INSA Toulouse
M. Franck DUMAS, SHOM

À mes grands-parents


Recette pour une thèse agréable


300G DE SUJET PASSIONNANT


UN DIRECTEUR DE THESE QUI EN VEUT
MINI-RIPS
MMM OUI..


UN BON LABO, DE BONS CO-BUREAUX ET DES POST-ITS
RO LA LA


UNE VILLE, ROSE DE PREFERENCE (MAIS AUSSI VIOLETTE)


UNE BONNE LOUCHE DE PAUSES CAFE
OULA, DEJA 15H !


UN ZESTE DE DEBAT (UTILE)
MAIS ELLE EST TRES BIEN CETTE COLORMAP !


UNE LEGERE DOSE DE STRESS
IL VIENT DE RM -R * SON TMPDIR
NOOOOOOOOOOO

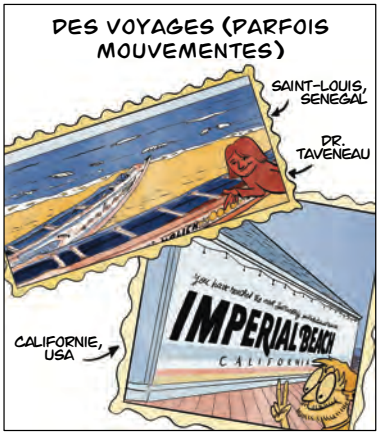
DES VOYAGES (PARFOIS MOUVEMENTES)
SAINT-LOUIS, SENEGAL
DR. TAVENEAU
CALIFORNIE, USA
IMPERIAL BEACH
CALIFORNIE

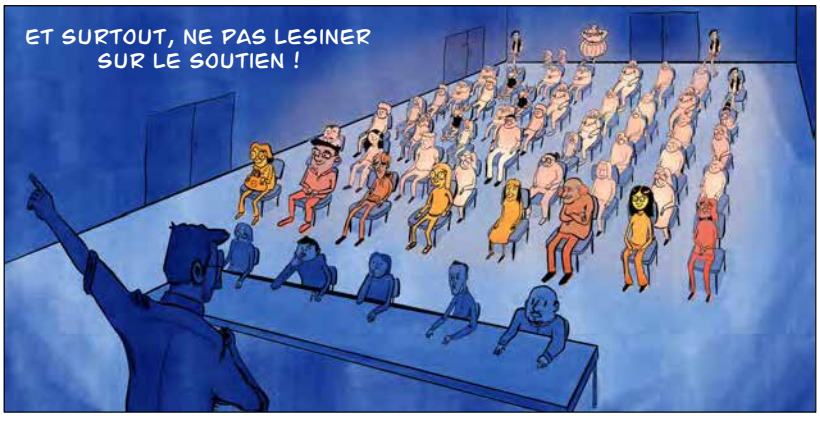
ET SURTOUT, NE PAS LESINER SUR LE SOUTIEN !


Bon appétit !

Remerciements

"Dis Chat, comment écrit-on des remerciements de thèse ?". Peu satisfait des résultats de cette incontournable IA, je me vois donc livré à moi-même. Difficile de résumer trois riches années et de remercier correctement, car si seul mon nom apparaît ici, cette thèse est l'oeuvre d'un grand nombre de personnes. Je vais m'efforcer de les remercier comme il se doit, et qu'on me pardonne les oublis.

Je peux déjà donner mon plus grand merci à Patrick, sans qui cette thèse ne serait pas. J'ai rencontré Patrick pour la première fois lors d'un stage de M1 marqué par le COVID. Il m'a ensuite proposé de continuer en thèse avec lui, sur un étrange sujet à base de vagues et de crocodiles. Porté par la curiosité, j'ai accepté et je m'en félicite. Si les connaissances et l'expertise de Patrick ne sont plus à démontrer, j'aimerais souligner sa pédagogie, sa disponibilité et sa passion (il faut le voir parler de mini-rips, c'est quelque chose). J'estime avoir appris énormément à ses côtés, que ce soit sur l'océan, mais aussi sur le monde de la recherche et sur cette flamme qu'ont les chercheurs. Je souhaite à tout doctorant de trouver un Patrick sur son chemin !

Merci aux membres de mon jury, rapporteurs, examinateurs et invités, de m'avoir fait l'honneur d'examiner ma thèse. Merci particulièrement à Rafael, Laurent et Franck, qui auront aussi suivi cette thèse depuis le début à travers mon CSI. Au plaisir de se recroiser !

Merci à tous ceux qui font marcher le LEGOS, l'OMP ou encore l'école doctorale, qu'ils soient permanents, doctorants ou dans l'administration ! Brigitte, SUPAERO a bien de la chance de t'avoir maintenant. Frédéric, merci pour ton enthousiasme dès qu'il s'agissait d'écouter ou de soutenir les doctorants (et allez violets) !

Un merci particulier à l'équipe Littoral du LEGOS, qui a connu une superbe dynamique ! Je pense en particulier aux cafés plage et à ce séminaire au Pic du Midi (seulement 2876 mètres au-dessus des plages mais il faut, paraît-il, prendre de la hauteur).

Je tiens également à remercier tous les chercheurs et chercheuses avec qui j'ai pu échanger ou collaborer, de près ou de loin, en dehors du LEGOS. *I would particularly like to thank James McWilliams and his team (Delphine Hypolite and Daniel Dauhajre), who did me the honor of welcoming me for a visit to UCLA, as well as Falk Feddersen and Drew Davey, who welcomed me to Scripps for a seminar and insightful discussions. I would like to extend a special thank you to Christine Baker for her collaboration throughout my PhD. I was delighted to discover that she had the brilliant idea of releasing dye into her laboratory experiment! Thank you very much, I am extremely happy to continue this collaboration as a postdoc in California.* Et merci plus généralement à toutes les personnes avec qui j'ai pu échanger scientifiquement au cours de ces trois années.

Je tiens à remercier les professeurs et instituteurs (merci maman) qui ont jalonné mon parcours, du CP à l'école d'ingénieur. Je pense en particulier à mes derniers professeurs à l'INSA, notamment Charles Dossal et Pascal Noble, qui lors de mes premières interrogations sur la thèse, ont su trouver les mots et m'ont donné cette envie d'y aller. Je voudrais aussi

remercier Rémi Vezy et Emilie Peynaud, mes deux encadrants de stage de M2. Mon passage dans le monde des plantes aura été court, mais très instructif sur le monde de la recherche !

Merci à tous ceux qui font des pauses cafés et déjeuner du LEGOS un haut lieu de la scène toulousaine ! Adé pour avoir légué son joint de machine à laver, Adrien et sa fine connaissance de la BD, de la darksynth et du spurious mixing (c'est très important), Arne et sa joie de vivre contagieuse (surtout quand il rédige), Amélie et son sens aiguisé du potin pas discret, Camille qui arrive un peu trop tôt au labo (quelqu'un a déjà vu des ondes internes ?), Elisa pour son tour de Beverly Hills, Hugo et ses conversations sur tout et n'importe quoi (surtout n'importe quoi), Julia et ses canards en folie, Juliette et son enthousiasme tout-terrain (même pour les bouchons vaseux !), Marie et son modèle trop cool, Quentin et ses ressources infinies (quel template mes aïeux, quel template !). Dédicace spéciale à la team plage : Adrien, Salomé, Marcan, Harold, Grégoire, Wagner, Yohan et Dimitri, enfin des gens qui osent s'attaquer aux sujets brûlants ! Merci aux "anciens" d'avoir montré la voie, Adé, Manon, Lisa M, Lisa W, Pierre, Simon, Morgane, Marion, Antonin, Benjamin, vos conseils sont de l'or. Adé tout particulièrement, qui m'aura fait découvrir le Sénégal et m'aura soutenu dans les moments les plus sombres. Pensée aussi pour le latin-LEGOS, Gabriela, Julia, Sly, Marco, Marcela, Roberto, *fue un placer conocerles* ! Et pour ceux avec qui nous avons avancé au même rythme, Margot, Alexandra, Jules, Arame. Merci à tous mes co-bureaux depuis le début, en particulier Lucrèce au tout début, Julia et Hanh pour une courte période, puis Louis et Hugo (des gens sérieux oui, mais facilement distraits par une session de Pédantix). Et bonne continuation pour tous les "nouveaux" (qui ne le sont plus depuis un bon moment) !

Merci à tous mes amis de collège, lycée et INSA, je suis fier de grandir à vos côtés. Toz (je n'aurais pas pensé avoir ce mot dans ma thèse honnêtement), vous êtes toujours là pour donner de la force quand il le faut, merci du soutien constant, j'espère que vous allez garder la même pêche tout le temps. Petite mention pour les budinos di cacca également (encore une fois, ces mots n'étaient pas censés apparaître ici). Mathis, Jérôme, Nathan, la Garonne est viola. Les étoiles de mon coeur, je vous aime, ne changez pas. Spécial big up à Anaïs, Landry, Mathis, Paul D, Paul L et Roman pour vos thèses et pour m'apprendre plein de choses sur la recherche. Guillaume, faut qu'on se capte tiens !

Un énorme merci à toi, Moni, d'avoir toujours été là pour me soutenir, pour m'avoir souvent remis dans le droit chemin du travail et d'avoir cru en moi. J'espère que tu es fière de moi comme je suis fier de toi, je suis impatient de voir ta thèse et tu sais que je serais toujours là pour toi.

Merci à toute ma famille, de faire qui je suis. Merci papa et maman, de m'avoir toujours soutenu, merci Léo et Lucie (et Raïna, aussi) parce que vous êtes sympas quand même (plus que sympas en fait). Merci à tous mes grands-parents, cette thèse est aussi la vôtre. Merci Papi Yvou et Mamie Simone pour m'avoir transmis cet amour des mots et de la culture, merci Papi Robert pour avoir su lier ski et mathématiques avec brio (ce n'était pas tâche aisée), et merci Mamie Bernadette pour ton énergie sans limites pour être là pour tes petits-enfants.

Merci et bonne lecture !

Plain language summary

The nearshore zone is a dynamic environment subject to both natural and human pressures. Many environmental tracers (larvae, plankton, pollutants, sediments) transit through it. Understanding the mechanisms that control the transport and mixing of these tracers is essential. Most current studies use 2D models, which overlook the effects of vertical shear caused by wave breaking at the surface and its return flow, the undertow, near the seabed. This thesis studies this effect using a 3D model (CROCO). The results show that tracers disperse less efficiently offshore in 3D models than in 2D models, while they reveal a new mixing mechanism in the surf zone, involving mini-rips, a type of intermediate-scale transient current recently discovered. This work, which describes coastal mixing processes in greater detail, will help improve the simplified models used for coastal zone management.

* * *

Résumé grand public

Le littoral est un environnement dynamique, soumis à des pressions naturelles et humaines. De nombreux types de traceurs environnementaux (larves, plancton, polluants, sédiments), transitent par cette zone. Comprendre les mécanismes de transport et de mélange de ces traceurs est essentiel. La plupart des études actuelles utilisent des modèles 2D, ignorant l'impact du cisaillement vertical causé par le déferlement des vagues en surface et le courant de retour au fond. Grâce à l'utilisation de nouveaux modèles 3D (CROCO), cette thèse explore cet impact. Les résultats montrent qu'en 3D, les traceurs se dispersent moins loin au large qu'en 2D, et révèlent un nouveau mécanisme de mélange dans la zone de déferlement, impliquant les mini-rips, des courants transitoires d'échelle intermédiaire récemment découverts. Ce travail, qui décrit plus précisément les processus de mélange littoraux, permettra d'améliorer les modèles simplifiés utilisés pour la gestion de la zone côtière.

Abstract

The nearshore zone, encompassing the surf zone and the inner shelf, is a highly dynamic region where surfzone eddies and rip currents of varying scales coexist and interact. This critical interface between land and sea determines the transport of various elements, including sediments, contaminants (such as heavy metals, microplastics, and pathogens), as well as biological tracers like plankton and larvae. These tracers are central to addressing key coastal challenges, such as beach erosion, coastal pollution, and ecosystemic services. On longshore-uniform sandy beaches, one of the primary transport mechanisms is transient rip currents, driven by wave directional spread. While numerous studies have investigated passive tracer transport under these conditions, most have relied on depth-averaged wave-resolving models (Boussinesq models). Although these models offer valuable insights, they fail to capture the effect of vertical shear resulting from shoreward surface flow induced by breaking waves and seaward undertow. They typically underestimate mixing within the surf zone and overestimate offshore dispersion. Recently, 3D wave-resolving models such as CROCO have provided researchers with the tools to conduct more comprehensive studies. The objective of this thesis is to contribute to the ongoing improvement of these models and to assess the impact of undertow vertical shear on tracer dispersion. The first step was to correct a coherent interference problem in the CROCO wavemaker, then to validate its ability to resolve transient nearshore dynamics using a recent wave basin experiment. After confirming the robustness of the model, the influence of vertical shear was examined through two dye release experiments, one in a wave basin and the other during a large-scale field experiment at Imperial Beach, California. Comparisons of simulations with and without undertow vertical shear revealed two key findings: a reduction in offshore dispersion due to a weakening in the 2D inverse kinetic energy cascade, and enhanced mixing within the surf zone through a newly identified 3D process associated with "mini-rips", a type of intermediate-scale transient current recently discovered. This research, which provides a more accurate representation of transport mechanisms in the nearshore zone, offers valuable feedback for improving parameterizations in coarser models.

Keywords: Surf zone, inner shelf, tracer dispersion, wave-resolving model, undertow vertical shear

Résumé

La zone côtière, englobant à la fois la zone de déferlement et le plateau interne, est une région extrêmement dynamique, où coexistent et interagissent des tourbillons et des courants d'arrachement à différentes échelles. Cette interface critique entre la terre et la mer joue un rôle essentiel dans le transport de divers éléments, tels que sédiments, contaminants (métaux lourds, microplastiques, pathogènes), et traceurs biologiques comme le plancton et les larves. Ces traceurs sont liés à des enjeux côtiers majeurs, comme l'érosion des plages, la pollution littorale et la préservation des écosystèmes. Sur des plages sableuses quasi uniformes le long du littoral, les principaux mécanismes de transport sont les courants d'arrachement transitoires, induits par des vagues multidirectionnelles. Bien que de nombreuses études aient exploré le transport de traceurs passifs dans ces conditions, la plupart reposent sur des modèles à vagues résolues bidimensionnels (Boussinesq), qui ne prennent pas en compte le cisaillement vertical, causé par les courants de surface dirigés vers la côte (dus au déferlement) et le courant de retour vers le large près du fond. Cette lacune conduit à sous-estimer le mélange dans la zone de déferlement et à le surestimer sur le plateau interne. Récemment, des modèles 3D à vagues résolues comme CROCO ont permis des études plus approfondies. L'objectif de cette thèse est d'améliorer ces modèles et d'évaluer l'impact du cisaillement vertical du courant d'arrachement sur la dispersion des traceurs. La première étape a consisté à corriger un problème d'interférence cohérente dans le générateur de vagues de CROCO, suivi de la validation de sa capacité à reproduire les dynamiques transitoires côtières à l'aide d'expériences en bassin à vagues. Une fois le modèle validé, l'influence du cisaillement vertical a été examinée à travers deux expériences de rejet de traceurs, l'une en bassin à vagues et l'autre lors d'une grande campagne de terrain à Imperial Beach, Californie. Les comparaisons des simulations avec et sans cisaillement vertical ont révélé deux résultats majeurs : une réduction de la dispersion vers le large due à l'affaiblissement de la cascade inverse de l'énergie cinétique 2D, et une augmentation du mélange dans la zone de déferlement via un nouveau processus 3D, impliquant les "mini-rips", des courants transitoires d'échelle intermédiaire récemment découverts. Ce travail, qui permet de mieux comprendre les mécanismes de transport dans les zones côtières, offre des perspectives pour améliorer la paramétrisation de modèles simplifiés.

Mots clés : Zone de déferlement, plateau intérieur, dispersion de traceur, modèle à vagues résolues, cisaillement vertical

Scientific activity and collaborations

Field work

December 2021	**Topography measurements of the sandy tongue of Saint-Louis with Adélaide Taveneau**

International collaborations

June-August 2023	**Visiting scholar at the University of California, Los Angeles, USA (UCLA) within the James McWilliams research team**

Conferences, seminars and workshops

June 2024	**Journées Nationales Génie Civil Génie Côtier, Anglet, France** Effects of vertical shear on nearshore transport using a 3D wave-resolving model (talk and proceedings; Treillou & Marchesiello, 2024)
September 2023	**CROCO Users meeting, Marseille, France** How do 3D non-hydrostatic dynamics affect transport in the nearshore region ? (talk)
July 2023	**Scripps Institution of Oceanography, San Diego, USA** How do 3D non-hydrostatic dynamics affect transport in the nearshore region ? (seminar)
June 2023	**University of California, Los Angeles, USA** How do 3D non-hydrostatic dynamics affect transport in the nearshore region ? (seminar)
April 2023	**European Geosciences Union (EGU), Vienna, Austria (online)** Impact of 3D non-hydrostatic dynamics on tracer transport in the nearshore region (poster)
October 2022	**Journées Nationales Génie Civil Génie Côtier, Chatou, France** Impact of 3D non-hydrostatic dynamics on tracer transport in the nearshore region (talk and proceedings; Treillou & Marchesiello, 2022)

Scholarships

2023	**Toulouse Graduate School of Earth and Space Science (TESS) BOOSTER award in the amount of 4.000 euros**

Contents

List of Figures

List of Tables

List of Boxes

General introduction

The coastline is a unique space, rich in contrasts and meanings. It embodies both the ultimate boundary before the vastness of the ocean and the starting point toward distant horizons. This area is a crossroads where elements meet, a place filled with symbolism, oscillating between hope and exile, the beginning and end of a journey. In perpetual motion, it is governed by powerful and complex dynamics that have, for millennia, fueled the imagination of artists—from Neruda's evocative poems to Hokusai's prints. Beyond this abundant imagery linked to the sea, waves, and coasts, the physics of the coastline reveals an equally fascinating world. The coastline serves as the first line of defense against the ocean's energy, enduring both intense natural pressures and increasing human impacts. It is also an important living space, with more than 40% of the world's population living within 100 km of the coast (CIESIN, 2012). The coastline features a diversity of landscapes, ranging from sandy beaches to steep cliffs and coral reefs, stretching over hundreds of thousands of kilometers. The challenges are numerous: preserving biodiversity, managing coastal retreat in the face of rising sea levels, and combating pollution with disastrous consequences.

The coastline, a veritable interface between the continent and the ocean, is a place of permanent exchange where many materials are transported, either to be dispersed offshore or to accumulate on the coasts. During storms, contaminated continental waters are drained by rivers (see Fig. 1a) or discharged directly into the sea via outfalls, then dispersed along the coast by coastal currents. These conditions favor the concentration of **pathogens**, including the fecal bacterium *E. Coli*, frequently used as an indicator of water quality. When levels exceed a certain threshold, the beaches concerned are deemed unfit for bathing and closed by the authorities (see Fig. 1b). But pathogens are only part of the problem. Among the main coastal pollutants are **microplastics**, derived from the fragmentation of macroplastics or synthetic textile fibers, **heavy metals** from factories close to the coast, **hydrocarbons** and various **nutrients**. Each of these pollutants poses risks to human health, ranging from simple infections to severe carcinogenic hazards. The extent of these risks varies considerably around the world, with developing countries often more exposed to particularly dangerous heavy metal pollution. In France, although coastal pollution has diminished over the last fifty years, it remains a topical issue, particularly around major cities, river mouths and sewage treatment

plants. For example, beaches along the Aquitaine coast are frequently closed following storms due to poor water quality[1], with induced consequences on tourism. In-depth knowledge of the transport and mixing of these pollutants therefore serves *in fine* better public management of such events. The presence of pollutants can also have an indirect impact on human populations, notably through local flora and fauna. Fish intended for consumption can be contaminated with heavy metals or micro-plastics. Altered water quality can cause excess mortality in marine populations, and severely impact local economies based on fishing (Middlebrooks et al., 1981).

Figure 1: (a) Plume of wastewater from the Tijuana River flowing along the Californian coast (photo by Serge Dedina[a]). (b) Biarritz's main beach is closed to swimming (purple flag) (photo by Véronique Fourcade[b])

[a] See sergededina.com/tag/tijuana-river-plume/, consulted on August 30, 2024.
[b] See sudouest.fr/pyrenees-atlantiques/anglet/biarritz-mais-pourquoi-les-plages-ferment-elles-3336707.php, consulted on August 30, 2024.

Other elements are also transported, such as **plankton** and **fish larvae**. These organisms often depend on cross-shore transport to migrate offshore or reach the coast. On the other hand, their development may depend on the retention capacity of the littoral zone. **Temperature**, dependent on transport processes, is another important factor for nearshore ecosystems. For example, it can reduce pathogen mortality or disrupt larval production, thus impacting biodiversity. Another application is coastal currents, in particular **rip currents**, which are powerful enough to carry swimmers out to sea, posing a significant safety risk on beaches. These currents are considered to be the **deadliest phenomenon on beaches**, accounting for over 80% of drownings in south-west France (Castelle et al., 2018). Finally, currents and waves transport **sediment** and contribute to the erosion or accretion of sandy beaches, which account for more

[1] francebleu.fr/infos/environment/la-baignade-interdite-sur-16-plages-du-pays-basque-a-cause-dune-mauvaise-qualite-de-l'-eau-8290875, consulted August 30, 2024.

than 30% of the world's coastline (Luijendijk et al., 2018). Erosion is one of the major coastal problems, with some regions of the world seeing their coastlines retreat significantly every year. This retreat puts populations and homes at risk, particularly in developing countries where rapidly growing coastal populations are more exposed to erosion (Dada et al., 2023). In West Africa, for example, Benin's coastline retreats by an average of 4 meters per year along 65% of its coastline, costing the equivalent of 2.5% of the country's GDP (Croitoru et al., 2019).

A better understanding of the various transport and mixing mechanisms is therefore necessary to better apprehend these different phenomena, and arrive at public policies in line with the reality on the ground. In this thesis, we focus on tracer dispersion by currents and waves on sandy beaches only. We consider Eulerian passive tracers (typically chemical compounds or pathogens) and their evolution in the surf zone and inner shelf. The surf zone represents the area of high seabed in which waves break, while the inner shelf extends from the edge of the surf zone to a depth of around ten meters. Numerous advances have been made in recent decades, highlighting the vital role played by rip currents in the exchange between the coast and the shelf. They are characterized by a strong offshore current, relatively fine (of the order of ten meters) and stretching over several hundred meters (generally 2 to 3 times the width of the surf zone; Kumar & Feddersen, 2017c). They are generally caused either by bathymetric irregularities, or by short-crested waves resulting from crossed swells (multidirectional wave field). In the latter case, they are transient and are considered an essential process for tracer transport offshore (Tang & Dalrymple, 1989), as illustrated in Figure 2. This is why, in this thesis, we will focus on these transient rip currents, commonly referred to as *flash rips* in the jargon of coastal oceanographers. To model short-crested waves, an explicitly wave-resolving model is required, and tracer dispersion has therefore often been studied using depth-averaged (and therefore 2D) resolved wave models, neglecting until now the potential impact of vertical shear present in the breaking zone. This vertical shear results from the combined action of the shoreward breaking current at the surface (added to the Stokes drift due to the net transport of material by the waves), and the seaward return current (*undertow*), to ensure continuity of flow (conservation of water mass).

Thanks to ongoing improvements in numerical methods and computing capacity, new wave-resolving 3D models have emerged over the last decade. CROCO is one of them (alongside SWASH and NHWAVE), and is applied here to tracer dispersion in coastal areas. **The overall**

Figure 2: Rip currents are strong, narrow seaward currents that carry all types of material, in this case sediment (photo taken from photopilot.com/blog/rip-currents-rip-tides-understanding-the-dangers-staying-safe-at-the-beach/). The breaker zone is visible thanks to the foam produced by the breaker, and the inner shelf extends off this zone.

aim of this thesis is therefore to propose a new, completely three-dimensional vision of wave-induced nearshore transport, thus shedding light on hitherto unexplored phenomena and processes. An intermediate objective of this research is also to contribute to the continuous improvement of existing models. The two main issues of this thesis can therefore be summarized by the following questions:

Challenges

1) **How can we improve the realism of wave-resolving models?**

2) **What is the impact of vertical shear on tracer dispersion in the nearshore zone?**

In the First Chapter, an overview of current knowledge of coastal dynamics and tracer dispersion in the coastal zone is presented. I begin with an overview of the impacts of dispersion on ecosystems and populations, before going into more detail on the processes at work. The first focus is on waves, with an overview (from linear theory to wave spectra). I then focus on

nearshore circulation (averaged over the wave period), looking in particular at cross-shore and longshore currents, rip currents and larger-scale processes such as wind. The state of the art in tracer dispersion on the coast is then presented, followed by a brief history of the models used.

The Second Chapter describes in detail CROCO, the non-hydrostatic free-surface wave-resolving model used throughout my thesis. A section of this chapter is also devoted to presenting the FUNWAVE-TVD wave-resolving Boussinesq model. As this model has only been used occasionally and for comparison purposes, its description is kept brief. The final section explains the methods and diagnostics used throughout the thesis.

The Third Chapter is taken from the article *Correction of coherent interference in wave-resolving nearshore models and validation with experimental data* (Treillou et al., 2024), published as first author in 2023 in *Ocean Modelling*. A wave maker-related coherent wave problem, inducing stationary rip currents, is described. The solution proposed by Salatin et al. (2021) is then implemented in CROCO before being validated using data from a basin experiment.

In the Fourth Chapter, the impact of vertical shear on mixing and transport in the nearshore zone is studied using two complementary experiments, one in a wave basin and the other on a Californian beach. These two experiments once again validate CROCO, but also highlight the differences induced by vertical shear. In this work, submitted to *Journal of Physical Oceanography*, I highlight the ability of vertical shear to reduce the inverse cascade, sufficiently to have a strong impact on cross-shore dispersion. I also test for the first time the impact of mini-rips, which play an extremely active role in mixing the surf zone. Mini-rips are also the dominant mixing process on a beach free of rip currents.

Finally, the last section of Conclusion and Perspectives takes stock of this thesis and places all the results obtained in a more global context, at the level of the scientific community and beyond. The limitations of this thesis are also discussed, along with ideas for improving the results obtained, before looking ahead to the prospects opened up by this work.

Introduction générale

Le littoral est un espace unique, riche en contrastes et en significations. Il incarne à la fois la frontière ultime avant l'immensité de l'océan et le point de départ vers des horizons lointains. Cet espace est un carrefour où se rencontrent les éléments, un lieu chargé de symbolisme, oscillant entre espoir et exil, début et fin de parcours. En perpétuel mouvement, il est régi par des dynamiques puissantes et complexes qui, depuis des millénaires, nourrissent l'imagination des artistes, des poèmes évocateurs de Neruda aux estampes d'Hokusai. Au-delà de cet imaginaire foisonnant lié à la mer, aux vagues et aux côtes, la physique du littoral révèle un univers tout aussi fascinant. Le littoral constitue la première ligne de défense face à l'énergie de l'océan, subissant à la fois des pressions naturelles intenses et des impacts anthropiques croissants. Le littoral est également un lieu de vie important, avec plus de 40% de la population mondiale vivant à moins de 100 km des côtes (CIESIN, 2012). Il présente une grande diversité de paysages, allant des plages de sable aux falaises escarpées, en passant par les récifs coralliens, s'étendant sur des centaines de milliers de kilomètres. Les défis y sont multiples : préserver la biodiversité, gérer le recul des côtes face à l'élévation du niveau de la mer, et lutter contre une pollution aux conséquences désastreuses.

Le littoral, véritable interface entre le continent et l'océan, est un lieu d'échanges permanents où transitent de nombreux matériaux, que ce soit pour se disperser au large ou pour s'accumuler sur les côtes. Lors d'épisodes de tempête, les eaux continentales contaminées sont drainées par les fleuves et rivières (voir Fig. 3a) ou déversées directement en mer via des exutoires, puis dispersées le long du littoral par les courants côtiers. Ces conditions favorisent la concentration de **pathogènes**, dont la bactérie fécale *E. Coli*, fréquemment utilisée comme indicateur de la qualité de l'eau. Lorsque les niveaux dépassent un certain seuil, les plages concernées sont jugées impropres à la baignade et fermées par les autorités (voir Fig. 3b). Les pathogènes ne sont cependant qu'une partie du problème. Parmi les principaux polluants littoraux, on trouve les **micro-plastiques**, issus de la fragmentation de macro-plastiques ou de fibres textiles synthétiques, les **métaux lourds**, provenant d'usines proches de la côte, les **hydrocarbures** ainsi que divers **nutriments**. Chacun de ces polluants présente des risques pour la santé humaine, allant de simples infections à des dangers cancérigènes sévères. L'ampleur de ces risques varie considérablement à travers le monde, les pays en développement étant souvent

plus exposés à une pollution aux métaux lourds particulièrement dangereuse. En France, bien que la pollution côtière ait diminué au cours des cinquante dernières années, elle demeure un enjeu d'actualité, notamment autour des grandes métropoles, des embouchures et des stations d'épuration. Par exemple, les plages du littoral aquitain sont fréquemment fermées à la suite d'orages en raison de la mauvaise qualité de l'eau[2], avec des conséquences induites sur le tourisme. Une connaissance approfondie du transport et du mélange de ces polluants sert donc *in fine* une meilleure gestion publique de ces événements. La présence de polluants peut également avoir un impact indirect sur les populations humaines, notamment par le biais de la flore et de la faune locales. Les poissons destinés à la consommation peuvent être contaminés aux métaux lourds ou micro-plastiques. L'altération de la qualité de l'eau peut d'ailleurs engendrer une surmortalité dans les populations marines, et sévèrement impacter des économies locales basées sur la pêche (Middlebrooks et al., 1981).

Figure 3: (a) Panache d'eaux usées issues de la rivière Tijuana se déversant le long des côtes californiennes (photographie par Serge Dedina[a]). (b) Grande plage de Biarritz interdite à la baignade symbolisée par un drapeau violet (photographie par Véronique Fourcade[b])

[a] Voir sergededina.com/tag/tijuana-river-plume/, consulté le 30 août 2024.
[b] Voir sudouest.fr/pyrenees-atlantiques/anglet/biarritz-mais-pourquoi-les-plages-ferment-elles-3336707.php, consulté le 30 août 2024.

D'autres éléments sont également transportés, tels que le **plancton** ou les **larves** de poissons. Ces organismes dépendent souvent du transport *cross-shore* (perpendiculaire à la côte) pour migrer vers le large ou atteindre la côte. Leur développement peut au contraire dépendre de la capacité de retention de la zone littorale. La **température**, dépendant des processus de transport, est un autre facteur important pour les écosystèmes littoraux. Par exemple, elle peut

[2] Voir par exemple : francebleu.fr/infos/environnement/la-baignade-interdite-sur-16-plages-du-pays-basque-a-cause-d-une-mauvaise-qualite-de-l-eau-8290875, consulté le 30 août 2024.

réduire la mortalité des pathogènes ou perturber la production de larves, impactant ainsi la biodiversité. Autre application, les courants côtiers, en particulier les **courants d'arrachements** (*rip current* en anglais), sont suffisamment puissants pour entraîner des nageurs vers le large, posant un risque significatif pour la sécurité sur les plages. Ces courants sont considérés comme le **phénomène le plus mortel sur les plages**, représentant la cause de plus de 80% des noyades recensées dans le sud-ouest de la France (Castelle et al., 2018). Enfin, les courants et les vagues transportent du **sédiment** et contribuent à l'érosion ou à l'accrétion des plages sableuses, qui représentent plus de 30% des côtes mondiales (Luijendijk et al., 2018). L'érosion est l'un des grands problèmes du littoral, certaines régions du monde voyant leur trait de côte reculer significativement chaque année. Ce recul met en danger les populations et habitations, notamment dans les pays en voie de développement où les populations côtières en forte augmentation sont plus exposées (Dada et al., 2023). En Afrique de l'Ouest par exemple, le Bénin voit ses côtes reculer de 4 mètres en moyenne par année sur 65% de ses côtes, coûtant l'équivalent de 2,5% du PIB du pays (Croitoru et al., 2019).

Une meilleure compréhension des différents mécanismes de transport et de mélange est donc nécessaire pour mieux appréhender ces différents phénomènes, et arriver à des politiques publiques en adéquation avec la réalité du terrain. Dans le cadre de cette thèse, on s'intéresse donc à la dispersion de traceur par les courants et les vagues sur les plages sableuses uniquement. On considère ici des traceurs passifs eulériens (typiquement des composés chimiques ou des pathogènes) et leur évolution dans la zone de déferlement et le plateau interne. La zone de déferlement (*surf zone* en anglais) représente la zone de haut fond dans laquelle les vagues déferlent, tandis que le plateau interne (*inner shelf*) s'étend de la limite de la zone de déferlement jusqu'à une profondeur de l'ordre d'une dizaine de mètres. Au cours des dernières décennies, de nombreuses avancées ont pu être faites, et ont notamment mis en avant le rôle primordial des courants d'arrachements dans l'échange entre la côte et le plateau. Ils sont caractérisés par un fort courant dirigé vers le large, relativement fin (de l'ordre de la dizaine de mètres) et s'étirant sur plusieurs centaines de mètres (généralement 2 à 3 fois la largeur de la zone de déferlement; Kumar & Feddersen, 2017c). Ils sont généralement causés soit par des irrégularités de la bathymétrie, soit par des vagues à crête courte résultant de houles croisées (champ de vague multidirectionnel). Dans le dernier cas, ils sont transitoires et sont considérés comme un processus essentiel pour le transport de traceur vers le large (Tang & Dalrymple, 1989), comme

illustré sur la Figure 4. C'est la raison pour laquelle nous nous intéresserons dans cette thèse à ces courants d'arrachement transitoires, dénommés couramment *flash rips* dans le jargon des océanographes littoraux. Pour la modélisation des vagues à crête courte, un modèle résolvant explicitement les vagues est requis, et la dispersion de traceur a souvent donc été étudiée à l'aide de modèles à vagues résolues, moyennés sur la profondeur (et donc 2D), négligeant jusqu'à présent l'impact potentiel du cisaillement vertical présent en zone de déferlement. Ce cisaillement vertical résulte de l'action conjointe du courant de déferlement dirigé vers la côte en surface (ajouté à la dérive de Stokes due au transport net de matière par les vagues), et du courant de retour au fond (*undertow* en anglais) dirigé vers le large, pour assurer la continuité de l'écoulement (conservation de la masse d'eau).

Figure 4: Les courants d'arrachements sont de forts et étroits courants dirigés vers le large, transportant tout type de matériel, ici du sédiment (photographie reprise de photopilot.com/blog/rip-currents-rip-tides-understanding-the-dangers-staying-safe-at-the-beach/). La zone de déferlement est visible grâce à la mousse produite par le déferlement, et le plateau interne s'étend au large de cette zone.

Grâce à l'amélioration permanente des méthodes numériques et de notre capacité de calcul, de nouveaux modèles 3D à vagues résolues ont émergé lors de la dernière décennie. CROCO est l'un d'entre eux (à coté de SWASH et NHWAVE), et est ici appliqué à la dispersion de traceur en zone littorale. **L'objectif général de cette thèse est donc de proposer une**

nouvelle vision complètement tri-dimensionnelle du transport littoral induit par les vagues, mettant ainsi en lumière des phénomènes et processus jusqu'alors inexplorés. Un objectif intermédiaire de cette recherche est également de contribuer à l'amélioration continue des modèles existants. Les deux grandes problématiques de cette thèse peuvent donc être résumées par les questions suivantes :

Problématiques

1) **Comment améliorer le réalisme des modèles à vagues résolues ?**

2) **Quel est l'impact du cisaillement vertical sur la dispersion de traceur en zone littorale ?**

Dans le Premier Chapitre, une vision globale des connaissances actuelles sur la dynamique littorale et la dispersion de traceur en zone côtière est présentée. Je fais d'abord un tour d'horizon des impacts liés à la dispersion sur les écosystèmes et les populations, avant d'expliciter plus en détails les processus à l'oeuvre. Un premier focus est donc fait sur les vagues, en proposant une vision d'ensemble (de la théorie linéaire aux spectres de vagues). Je m'attarde ensuite sur la circulation littorale (moyennée sur la période des vagues), en m'intéressant notamment aux courants *cross-shore* et *longshore*, aux courants d'arrachements et aux processus plus grande échelle tels que le vent ou la stratification. Un état de l'art de la connaissance sur la dispersion de traceur sur le littoral est ensuite donné, avant de proposer un rapide tour d'horizon des modèles traditionnelement utilisés.

Le Deuxième Chapitre décrit en détail CROCO, le modèle non-hydrostatique à vagues résolues et à surface libre utilisé tout au long de ma thèse. Une section de ce chapitre est consacrée à présenter le modèle Boussinesq à vagues résolues FUNWAVE-TVD. Comme ce modèle n'a été utilisé ici que ponctuellement et à des fins de comparaison, sa description reste brève. Les expériences de terrain et de bassin à vagues utilisées pour cette thèse sont également décrites. Une dernière partie s'attache à expliciter les méthodes et diagnostics utilisés tout au long de la thèse.

Le Troisième Chapitre tente de répondre à la première problématique de ma thèse, en corrigeant un défaut inhérent aux générateurs de vagues à double sommation. Ce chapitre est issu de l'article *Correction of coherent interference in wave-resolving nearshore models and*

validation with experimental data (Treillou et al., 2024), publié en tant que premier auteur en 2023 dans *Ocean Modelling*. Le problème d'ondes cohérentes lié au générateur de vagues, induisant des courants d'arrachements stationnaires, est décrit. Une solution est ensuite implémentée dans CROCO avant d'être validée à l'aide de données issues d'une expérience en bassin.

Dans le Quatrième Chapitre, l'impact du cisaillement vertical sur le mélange et le transport en zone littorale est étudié à l'aide de deux expériences complémentaires, l'une en bassin à vagues et l'autre sur une plage californienne. Ces deux expériences permettent une fois de plus de valider CROCO, mais également de mettre en évidence les différences induites par le cisaillement vertical, et donc de répondre à la seconde problématique de ma thèse. Dans ce travail, soumis à *Journal of Physical Oceanography*, je montre la capacité du cisaillement vertical à réduire la cascade inverse, suffisamment pour avoir un fort impact sur la dispersion cross-shore. Je teste également pour la première fois l'impact des mini-rips, qui jouent un rôle extrêmement actif dans le mélange de la zone de déferlement. Les mini-rips, mis en évidence dans une étude récente utilisant CROCO (Marchesiello et al., 2021), apparaissent ici comme le processus de mélange dominant sur une plage exempte de courants d'arrachements.

Enfin, la dernière partie de Conclusion et Perspectives permet de dresser le bilan de cette thèse et de replacer tous les résultats obtenus dans un contexte plus global, au niveau de la communauté scientifique et au-delà. Les limitations de la thèse sont également discutées, ainsi que des idées pouvant améliorer les résultats obtenus, avant d'essayer de se projeter vers les perspectives ouvertes par ce travail.

Chapter I

Scientific background

C'est le commencement du monde
Les vagues vont bercer le ciel

Marine, Paul Eluard

Contents

I.1 Preamble

I.1.1 Area of interest: inner shelf, surf zone and swash zone

In this thesis, we focus exclusively on sandy beach types, thereby excluding cliffs, gravel beaches, and coral reefs. Sandy beaches account for more than 30% of the world's coastlines (Luijendijk et al., 2018). These beaches can be divided into several distinct regions, with the most onshore area being the **swash zone**. The swash zone is the section of the beach where waves run up and down the shore, located between the high water mark and the low water mark, where waves actively wash over the sand. This zone is characterized by alternating periods of water coverage and exposure as the waves advance (*swash*) and retreat (*backwash*). The swash zone plays a critical role in sediment transport and beach morphology, as the movement of water in this area transports sand and other materials up and down the beach face, shaping the overall structure of the shoreline.

The **surf zone** extends seaward from the swash zone to the area where waves begin to break due to depth limitations. It is the region of the nearshore environment where incoming waves break, generating turbulent motions and strong currents. The surf zone is a highly dynamic area where breaking waves transfer momentum and energy from periodic wave motions to persistent currents, transient low-frequency surf eddies, and smaller-scale turbulence. These motions are crucial for coastal processes, as they transport materials and stir up sediments, playing a significant role in shaping the coastal environment.

The most offshore area in our zone of interest is the **inner shelf**. It lies beyond the surf zone and extends to the middle of the continental shelf, typically at depths ranging from a few meters to tens of meters. The offshore boundary of the inner shelf can vary depending on the specific application and processes being considered, leading to multiple definitions. In coastal oceanography, the inner shelf is generally defined as the region where turbulent surface and

bottom boundary layers merge, occupying the entire water column (Estrade et al., 2008; Lentz & Fewings, 2012; Moulton et al., 2023). This region is crucial for tracer transport and acts as a transition zone between the highly dynamic surf zone, dominated by breaking waves, and the predominantly wind-driven shelf waters.

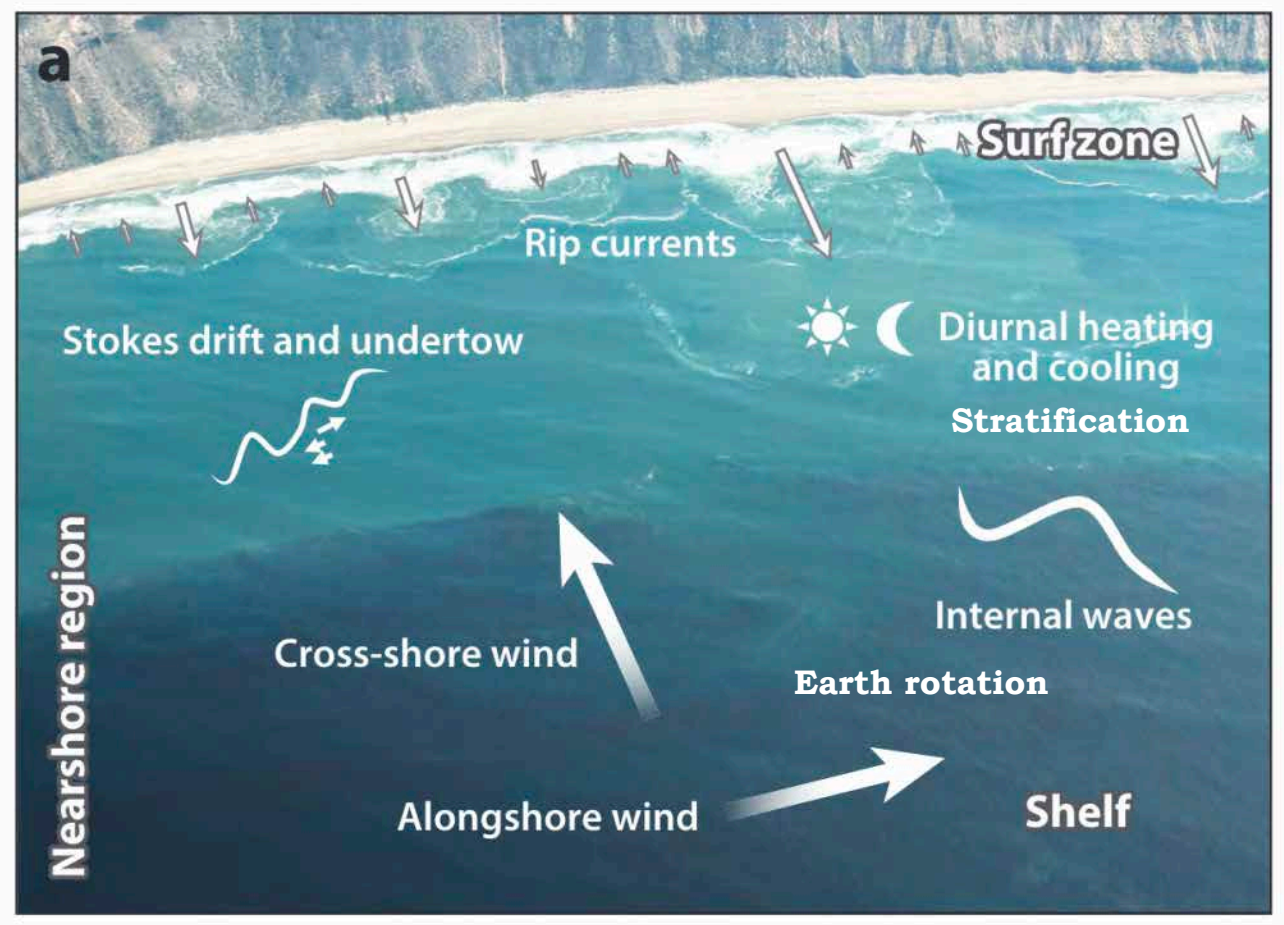

Figure I.1 Descriptive picture of the nearshore region in the central coast of California with main acting processes. The surf zone encompasses the foam area in the northern part of the picture while the inner shelf extends offshore. Aerial photography by M. Moulton and C. Chickadel, modified and reprinted from Moulton et al. (2023).

It is important to acknowledge that the surf-shelf interface is dynamic and varies over time, influenced by factors such as incoming wave conditions. For example, a mild wave climate will result in a narrower surf zone closer to the shore, while during storms, the surf zone can extend hundreds of meters offshore. Bathymetry also plays a crucial role in this variability. A reflective beach, characterized by steep bathymetry, will generally have a narrower surf zone (or almost none) compared to a more dissipative beach. Additionally, wind forcing can modify conditions within the inner shelf; for instance, wind relaxation can reduce wind-induced

turbulence, allowing stratification to occur. Winds, stratification, and the Coriolis force can then influence the dynamics of currents that originate in the surf zone.

I.1.2 Why do we need to better understand nearshore dynamics ?

Now that we have described the place of interest, we can turn our attention to the question of *why*. Why is it important to study and better understand nearshore dynamics? Besides a fundamental scientific interest in studying rip currents and other surfzone eddies, a better understanding of these dynamics is also highly relevant to a number of issues affecting human populations and ecosystems. I have tried to list them (non-exhaustively) and provide key points of interest in each case below.

I.1.2.1 Predicting beach morphodynamics and shoreline evolution

Erosion (and **accretion**) is perhaps one of the best-known beach phenomena, and a major source of vulnerability for human populations worldwide. A large proportion of the population lives close to the coast (40% of the population is concentrated within 100 km of the coast; CIESIN, 2012), and the growing coastal population, particularly in Africa, is seen as the main factor increasing vulnerability (Dada et al., 2023). In Benin, for example, beaches are eroded by more than 4 meters per year on 65% of their coasts, representing a total loss of approximately 2.5 % of their GDP (Croitoru et al., 2019).

Erosion can arise from natural causes associated with variations in waves, tides, winds and precipitation at synoptic, seasonal or interannual scales, including global interannual climate fluctuations such as ENSO[1] (Almar et al., 2023). Erosion can also be due to various human activities that include reduction of river fluxes due to damming and sand mining, perturbation of sediment transport by coastal development and inappropriate protection measures, land subsidence due to groundwater extraction, etc. (Marchesiello et al., 2019). However, sandy shores can also be resilient, as they are extremely dynamic and constantly changing (Wright & Short, 1984). Depending on the season, for example, they can erode during winter storms and accrete when the wave climate is milder. It is therefore of high importance to propose adequate solutions for the populations living near the coast: hard structures (long life expectancy but costly, including for dismantling), nature-based solutions, beach nourishment or even relocation

[1] El Niño Southern Oscillation

and population retreat. That is why a good understanding of nearshore processes is important, through *in situ* and satellite observations (e.g. Taveneau et al., 2021; Graffin et al., 2023; Klotz et al., 2024), modeling (e.g. Marchesiello et al., 2022; Shafiei et al., 2023) or social sciences (e.g. Dada et al., 2021). It is even possible to help understand the historical fate of beaches using art representations (Motte, 2017).

I.1.2.2 Beach users safety

Sandy beaches are an attractive place for recreational activities and tourism, and concentrate the visit of millions of persons worldwide each year. These beaches remain dangerous places, with different hazards such as rip currents, shore-break waves or wave-related activities such as surfing (Castelle et al., 2018). Rip currents are particularly dangerous, as they are capable of dragging bathers out to sea. The real danger comes when people want to swim against the current, which is like swimming against the current of a river, leading to fatigue and the risk of drowning. Several studies have shown that this phenomenon is the main cause of injury or death on beaches in various countries, as rip currents are ubiquitous (e.g. Woodward et al., 2013; Liu & Wu, 2022; Cornell et al., 2023). On the southwest coast of France, where rip currents are known as *baïnes*, most accidents involve young people living far from the sea (Castelle et al., 2018), emphasizing that the lack of information is crucial.

In that sense, signaling is one way to reduce the number of accidents (see e.g. in Brazil Silva-Cavalcanti et al., 2018), especially in the case of bathymetric rip currents, which remain fixed in space for at least a few hours (see next section about rip currents). When considering transient rip currents that can occur randomly on the beach, signaling may be more complicated. That is why education is important, so that beachgoers know how to react when caught in a rip current. The main advice is to stay calm and avoid swimming against the current. If there are lifeguards, it is advisable to let yourself be carried away by the current (which will not take you more than a few hundred meters from the shore), while signaling your presence. If there are no lifeguards, it is possible to wait until the current takes you back to the shore, in the case of a recirculation cell, or to swim parallel to the coast in order to escape the rip current (their typical width is only $\mathcal{O}(10\text{ m})$).

I.1.2.3 Biodiversity: plankton, larvae and temperature

Nearshore dynamics play a crucial role in shaping the ecological characteristics of coastal environments, particularly regarding the distribution and abundance of **plankton**, **larvae**, and other key biological components (Morgan et al., 2018). The transport of plankton and larvae from offshore waters into the nearshore zone is a critical subsidy that sustains various coastal ecosystems. For instance, planktonic subsidies, including zooplankton and phytoplankton, are essential food sources for filter-feeding benthic organisms in the surf zone, such as mole crabs or barnacles (Leslie et al., 2005). This transport process generally occurs in two stages (Morgan et al., 2018). First, plankton and larvae are carried into the inner shelf through mechanisms like upwelling relaxation events (Adams et al., 2006), onshore winds (Shanks, 1995), internal waves and bores (Pineda, 1999), or large waves. Subsequently, their entry into the surf zone is largely determined by surfzone hydrodynamics, which are primarily influenced by coastal morphology and wave climate.

The slope of the beach plays a crucial role in nearshore dynamics. More dissipative surf zones tend to have higher plankton concentrations due to increased connectivity with the shelf, facilitated by bathymetric rip currents. These rip current recirculation cells can trap and retain plankton within the surf zone, leading to higher phytoplankton concentrations as growth rates are elevated in this area (Shanks et al., 2018). This is why estimating surfzone residence time is often very useful. The width of the surf zone can account for 60-90% of the variation in phytoplankton concentration (Shanks et al., 2018). Consequently, reflective surf zones generally exhibit lower overall biodiversity compared to intermediate or dissipative zones. Bathymetric rip currents can also be particularly beneficial for filter-feeding organisms. For example, species like the mole crab *Emerita analoga*, which reside near rip currents, benefit from higher concentrations of phytoplankton food (Shanks et al., 2016). However, while these crabs may grow faster due to the abundance of food, they are also at greater risk of exposure to harmful algal species. The slope of the surf zone is also significant for human populations, as more dissipative zones tend to harbor more larvae and fish, owing to the high concentrations of zooplankton (McLachlan & Hesp, 1984). Indeed, Morgan et al. (2018) even refers to dissipative surf zones as "*nursery habitats for larval and juvenile fishes*".

Temperature variability, as an active tracer, can significantly influence nearshore biodiversity. Temperature serves as an indicator for nutrient delivery to coastal waters and can also affect

growth rates, egg mass production, and coral health. For example, temperature changes can alter the egg mass production rates in species such as the crab *Cancer setosus* (Fischer & Thatje, 2008), and it can impact coral health (Schramek et al., 2018). Therefore, a deeper understanding of nearshore dynamics is crucial to support the work of marine biologists and to better predict the evolution of coastal ecosystems.

I.1.2.4 Dispersion of pollutants and bacteria

Pollutants in the nearshore area are diverse and can enter coastal waters from both the open sea and land-based sources. These contaminants pose significant threats to both human health and ecosystem integrity.

Pathogens, such as the fecal bacteria *E. Coli*, can be introduced into the ocean through various pathways: they may be carried by rivers during storm events, directly discharged through outfall pipes, or even introduced during beach nourishment activities (Rippy et al., 2013b). Fecal bacteria can cause severe illnesses in swimmers, often leading to beach closures that impact seaside tourism and local economies. A deeper understanding of the physical and biological processes (such as inactivation and mortality rates; Boehm et al., 2005) governing pathogen transport could enable more effective coastal management. This is particularly important given the frequent mismatches between actual health risks and beach closures, leading to unnecessary closures or, conversely, leaving beaches open when they should be closed (Saleem et al., 2023).

Microplastics are also prevalent on beaches in significant quantities, with severe consequences for biodiversity. These microplastics originate from the fragmentation of larger plastic debris or from synthetic textile fibers (e.g. in the sandy beaches of Peru De-la-Torre et al., 2020). Given that plastic input from land to sea is expected to continue increasing (Jambeck et al., 2015), understanding how microplastics are transported by nearshore currents is crucial. A more detailed understanding of plastic transport along the coast can enhance larger-scale regional models, typically with resolutions of $\mathcal{O}(1\text{ km})$. In these models, coastal boundaries are often treated with probabilistic conditions to determine whether particles will reach the shore or settle at a specific nearshore water depth (Weiss, 2021; Moulton et al., 2023).

Other contaminants can include **heavy metals**, **excess nutrients** or **oil**. Heavy metals can be issued from near-coast industries and significantly damage human and ecosystem health (Middlebrooks et al., 1981). For example, mercury is known to significantly affect fish population

dynamics. Recent studies have demonstrated that mercury exposure reduces the reproductive rates of Atlantic cods (Ono et al., 2019), which could have severe negative impacts on fishing-dependent communities, particularly in developing regions more exposed to such pollutants (e.g. in Senegal and West Africa; Middlebrooks et al., 1981; Dione et al., 2018). Additionally, excessive nutrient runoff from terrestrial sources, such as agriculture and sewage, can trigger harmful algal blooms (Elko et al., 2015).

To equip public authorities with reliable information, simplified models are frequently employed. These models heavily rely on the latest advancements in understanding nearshore transport (e.g., Ki et al., 2009; Rippy et al., 2013a), necessitating a thorough comprehension of the physical processes that govern nearshore dynamics. With an overview of the key coastal challenges established, we can now explore the historical progression of scientific research in the field of nearshore dynamics.

I.1.3 A brief scientific historical overview

Although oceanic processes have been the subject of study for centuries, the field of coastal hydrodynamics is relatively young. The pioneering work of the Irish scientist Sir George G. Stokes is often considered the foundation of this field. In 1847, Stokes published the first theory of linear and non-linear waves, now known as Stokes waves (Stokes, 1847), shortly after the development of Airy's theory of small-amplitude linear waves. Over the second half of the century, significant mathematical advances were made in wave theory. Among the most notable contributions was that of French mathematician Joseph Boussinesq, who developed the first successful approximation for non-linear waves in shallow water, along with many other important findings. Observational discoveries also played a crucial role in advancing the field. For example, British engineer John Russell unveiled the concept of the solitary wave while studying ship waves in canals. The 20$^{\text{th}}$ century brought further breakthroughs that were of great interest to the coastal hydrodynamics community. Key developments included advances in wave spectrum theory, such as the Pierson-Moskowitz spectrum in 1964 (Pierson & Moskowitz, 1964) and the JONSWAP[2] spectrum in 1973 (Hasselmann et al., 1973), both of which remain widely used today. The contributions of British researcher Michael Longuet-Higgins during the mid-20th century were also significant, particularly in the understanding of wave statistics,

[2] JOint North Sea WAve Project

breaking waves, and energy transfer within wave systems, notably through the concept of wave radiation stress (e.g. Longuet-Higgins & Stoneley, 1953). The vortex force formalism has extended to 3D equations the description of wave-current interactions (McWilliams et al., 2004). Recently, the advent of computer technology has revolutionized the field, enabling the development of high-resolution numerical models like FUNWAVE, X-Beach and CROCO, which simulate complex interactions between waves and currents. The combination of high-resolution modeling and *in situ* measurements allows for refining parameterization of processes that are still poorly known. Moreover, the introduction of satellites, particularly in coastal studies, has made global or regional analyses of shoreline evolution possible on a scale that was unimaginable just a few decades ago (e.g. Taveneau et al., 2021; Graffin et al., 2023). A non-exhaustive overview of the current state of the art is provided below.

I.2 Surface gravity waves

Our focus in this thesis work is on wave-driven nearshore currents, rather than wave dynamics, but a brief summary of the latter is useful to understand the patterns and mechanisms of momentum and energy transfer in the surf zone.

I.2.1 Generation of wind waves

Before looking at wave dynamics in more detail, here is a brief summary of wave generation by winds, based on Stewart (2008).

When a realistic wind starts to blow over the sea surface, wind turbulence will produce random pressure fluctuations, that will lead to the creation of small waves with wavelengths of a few centimeters (Phillips, 1957). The wind then interacts with the small waves. As the wind blows over the wave, it creates pressure variations, causing the wave to grow. As the wave grows, so do the pressure differences, accelerating the process. This instability (the Miles mechanism) results in exponential wave growth (Miles, 1957).

Eventually, the waves begin to interact with each other, resulting in the formation of longer waves (Hasselmann et al., 1973). This interaction transfers energy from short waves produced by the Miles mechanism to waves whose frequency is slightly lower than that of the waves at the top of the spectrum. Ultimately, this process results in waves moving faster than the wind,

as observed by Pierson and Moskowitz.

I.2.2 Linear wave theory basics

The simplest way to describe wave motion is **linear wave theory**, also known as Airy wave theory, which is based on potential flow. Although limited for realistic cases, this theory contains the main features of wave motion and is of great interest to understand and explore the different mechanisms at stake. We consider the following assumptions:

- plane waves of period T on a constant depth h on a vertical plane (x, z), propagating in the x-direction (Figure I.2);
- effects of boundary layers are neglected;
- the flow is potential (irrotational), i.e., the vorticity vector $\nabla \times \mathbf{u} = 0$, where $\mathbf{u}$ is the velocity vector with horizontal and vertical components (u, w).

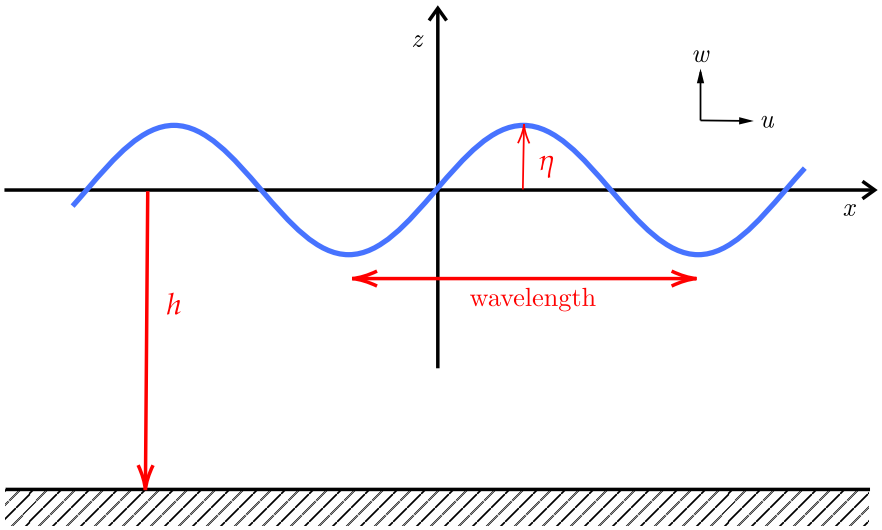

Figure I.2 Descriptive sketch of a linear wave propagating over constant horizontal bottom of depth h.

As the flow is irrotational, the continuity equation $\nabla \cdot \mathbf{u} = 0$ can be written as:

$$\nabla^2 \phi = 0 \tag{I.1}$$

with ϕ the velocity potential defined as $\mathbf{u} = \nabla\phi$. In order to solve Equation I.1, we consider simplified boundary conditions, where all quadratic terms are neglected. The surface kinematic

boundary condition reads:

$$\frac{\partial \eta}{\partial t} = \left.\frac{\partial \phi}{\partial z}\right|_{z=0} \tag{I.2}$$

while the surface dynamic boundary condition is reduced to:

$$\left.\frac{\partial \phi}{\partial t}\right|_{z=0} = -g\eta \tag{I.3}$$

There is a no-flux condition at the bottom:

$$\left.\frac{\partial \phi}{\partial z}\right|_{z=-h} = 0 \tag{I.4}$$

A sinusoidal solution for the free surface elevation η can then be find:

$$\eta(x,t) = a\cos(kx - \omega t + \phi) \tag{I.5}$$

where a is the wave amplitude (from mean water level to crest), k the wavenumber related to the wavelength λ (depicted in Figure I.2) by $k = \frac{2\pi}{\lambda}$, ω is the angular frequency related to the period T by $\omega = \frac{2\pi}{T}$ and ϕ is a phase shift. Using the boundary conditions and mathematical tricks, a full solution for the velocity field is:

$$u(x,z,t) = a\omega\frac{\cosh k(z+h)}{\sinh kh}\cos kx - \omega t \tag{I.6}$$

$$w(x,z,t) = a\omega\frac{\sinh k(z+h)}{\sinh kh}\sin kx - \omega t \tag{I.7}$$

with the dispersion relationship:

$$\omega^2 = gk\tanh kh \tag{I.8}$$

A detailed derivation can be found in a large number of books[3] (e.g., Svendsen, 2005). Note that all this derivation is only valid if $ak \ll 1$, i.e. the non-dimensional wave slope is small.

It is useful to distinguish between deep and shallow water. Deep water is defined as waters where the depth h is much larger than the wavelength λ such that $\lambda/h \ll 1$ or relative depth $kh \gg 1$, i.e., $\tanh kh \approx 1$. On the contrary, shallow water is defined by $kh \ll 1$, i.e. $\tanh kh \approx kh$. It is then easy to derive simpler phase velocity and dispersion relationship. But

[3] Interested reader can also take a look at Falk Feddersen's notes, available at falk.ucsd.edu.

in reality, waves are not monochromatic and many wave frequencies can coexist at the same time. The presence of various frequencies gives birth to wave groups, the envelope of wave amplitudes, due to the dispersive nature of waves. It can be described with group velocity c_g. Group velocity, phase velocity and dispersion relationships are summarized in Table I.1.

Table I.1 Main properties for deep and shallow water waves.

	Phase velocity	Group velocity	Dispersion relationship
Shallow water	$c_p = \sqrt{gh}$	$c_g = \sqrt{gh}$	$\omega^2 = gk^2h$
Deep water	$c_p = \sqrt{\frac{g}{k}}$	$c_g = \sqrt{gh}$	$\omega^2 = gk$

We now focus on depth-averaged wave energy. Thinking of waves in term of energy is useful, especially in models that cannot resolve directly each individual wave. We decompose the total wave energy E into their potential (PE) and kinetic (KE) energy parts. The wave potential energy is defined as the excess potential energy due to the wave field:

$$\rho g \left[\int_{-h}^{\eta} z dz - \int_{-h}^{0} z dz \right] = \frac{1}{2}\rho g \eta^2 = \frac{1}{2}\rho g a^2 \cos \omega t^2 \tag{I.9}$$

Note that the last part of the equation is valid for linear waves only. When this term is time-averaged, the wave-averaged potential energy is:

$$PE = \frac{1}{4}\rho g a^2 \tag{I.10}$$

The wave kinetic energy is:

$$\rho \int_{-h}^{\eta} (u^2 + w^2) dz \tag{I.11}$$

and when time-averaged:

$$KE = \frac{1}{4}\rho g a^2 \tag{I.12}$$

The equality between PE and KE reflects the balanced partitioning of kinetic and potential energy in irrotational flows. It can be used to estimate the contributions of irrotational and vortical flows from current measurements (Lippmann et al., 1999). The total mean wave energy is:

$$E = \frac{1}{2}\rho g a^2 = \frac{1}{2}\rho g \overline{\eta^2} \tag{I.13}$$

The second part of Equation I.13 is here to offer a generalized view, valid without linear wave theory and thus useful when looking at irregular wave states.

The equation of wave energy conservation, without sources (wind), sinks (breaking, bottom friction) or nonlinear advection reads:

$$\frac{\partial E}{\partial t} + \nabla \cdot (E c_g) = 0 \tag{I.14}$$

This equation, although expressed here in its simplest form, can be used in many wave-related problems. Lastly, it is important to remember that linear waves are a good approximation only in special cases. In the surf zone where waves are breaking, other approaches are more in line with the reality, such as Stokes, cnoidal or solitary wave theories. For more details, the reader is referred to one of the many books existing on the topic (e.g., Svendsen, 2005; Stewart, 2008).

I.2.3 Wave statistics for irregular sea state

Unfortunately, realistic waves in the ocean are far from linear and monochromatic. Waves can be considered as wind waves or swell, depending on the distance from generation. The wave fields created locally by winds are heterogeneous and present a wide distribution of different frequencies and directions. The swell, with narrower frequency and direction distribution, is found at a distance from a generating storm, as these long-period waves move faster due to wave dispersion (Munk et al., 1963).

Statistical tools are needed to represent more realistic wave fields. We can define a wave spectrum in frequency and direction as $S(f;\theta)$, where f is the frequency and θ the wave direction. Energy spectra represent all the frequencies of motions that coexist in the ocean, not only waves but also currents (illustrated in Figure I.3). The timescale ranges from periods smaller than the second for capillary waves to tides having period of $\mathcal{O}(1)$ day. In the framework of this thesis, we are essentially interested in frequencies between 1 and 10^{-4} Hz, including, in order of increasing periods, swell, IG[4] waves and VLF[5] motions, typically surf eddies and rip currents.

The representation of waves in spectral space is useful for comparing with observations, typically a time series of velocities or surface elevation. One of the best known indicators of

[4] Infra-Gravity
[5] Very Low Frequency

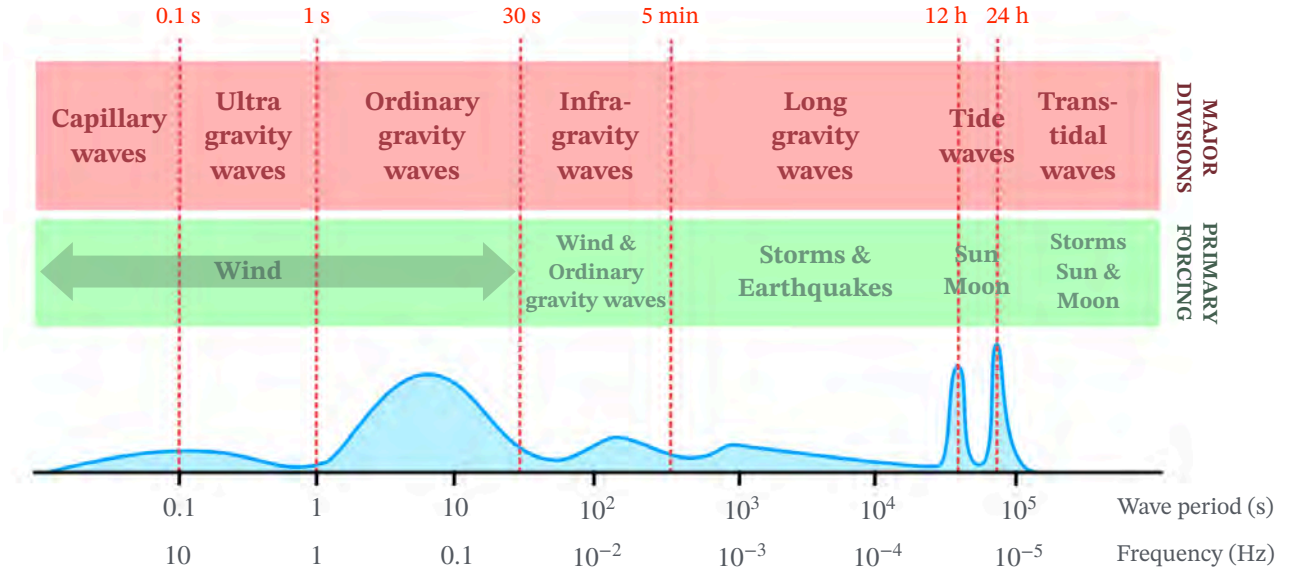

Figure I.3 Schematic spectrum of ocean waves, showing major divisions (red) and their main forcing mechanisms (green). Re-adapted after Munk (1950).

wave fields is the significant wave height H_s. This indicator was originally proposed by Munk (1944), defined as the mean of the highest one-third of all individual waves in a record, and intended to mathematically describe what a well-informed eye could have measured. When we assume a Rayleigh distribution in frequencies, it can be expressed as four times the square root of the zeroth-order moment (or four times the standard deviation of free surface elevation):

$$H_s = 4\sqrt{\int Sdf} = 4\sigma_\eta \tag{I.15}$$

with σ_η the standard deviation of the surface elevation. In parallel, the peak period can be defined as the highest peak of energy in the frequency spectrum, if considering uni-modal spectrum (i.e. spectrum with a unique peak). Similarly to Equation I.13, wave energy can then be formulated as:

$$E = \frac{1}{8}\rho g H_s^2 \tag{I.16}$$

A particularly important objective for oceanographers was to find a generalized parametric formulation for the wave spectrum. Pierson and Moskowitz (1964) proposed in 1964 a parameterization of the wave spectrum in a fully developed sea (i.e. waves and winds are at equilibrium)

from measurements taken in the North Atlantic. Their spectrum reads as:

$$S(f) = \alpha \frac{g^2}{(2\pi)^5 f^5} \exp\left(-\frac{5}{4}\left(\frac{f_p}{f}\right)^4\right) \tag{I.17}$$

with $\alpha = 8.1 \times 10^{-3}$ a constant and $f_p = \frac{1}{T_p}$.

An amelioration of this spectrum was done a decade later by Hasselmann et al. (1973) during the JONSWAP project, who found that the wave spectrum is never fully developed as nonlinear wave-wave interactions happen even after a long period. They built on the Pierson-Moskowitz spectrum by modifying it with a peak enhancement factor γ^r. A typical JONSWAP spectrum formulation is (Goda, 2000):

$$S(f) = H_s^2 \beta_J \frac{f_p^4}{2\pi f^5} \exp -\frac{5}{4}\left(\frac{f_p}{f}\right)^4 \gamma^r \tag{I.18}$$

with

$$r = \exp\left[-\frac{1}{2}\left(\frac{f - f_p}{\sigma_\omega f_p}\right)^2\right] \tag{I.19}$$

$$\sigma_\omega = \begin{cases} 0.07, & \text{if } f \leq f_p \\ 0.09, & \text{if } f > f_p \end{cases} \tag{I.20}$$

$$\beta_J = \frac{0.06238(1.094 - 0.01915 \log \gamma)}{0.23 + 0.0336\gamma - 0.185(1.9 + \gamma)^{-1}} \tag{I.21}$$

γ is typically set to 3.3 (at least in the North Sea). The difference between Pierson-Moskowitz and JONSWAP spectra (with $\gamma = 3.3$) is illustrated in Figure I.4.

The other aspect of a spectral representation of waves is their direction. When a wave field is multidirectionnal, it can be expressed as $S(f;\theta) = S(f)D(\theta)$ with D the directional spread. There are various way to parameterize directional spread, such as squared cosine functions for example, but in this thesis, we use a Gaussian-type distribution (such as Feddersen et al., 2011):

$$D(\theta) = \exp\left[-\left(\frac{\theta - \theta_m}{1.5\sigma_\theta}\right)^2\right] \tag{I.22}$$

with $\int_{-\pi/2}^{\pi/2} D(\theta) d\theta = 1$ to ensure that the directional spread (σ_θ) around the mean wave angle does not affect wave energy. Directional spread determines the distinction between long- and

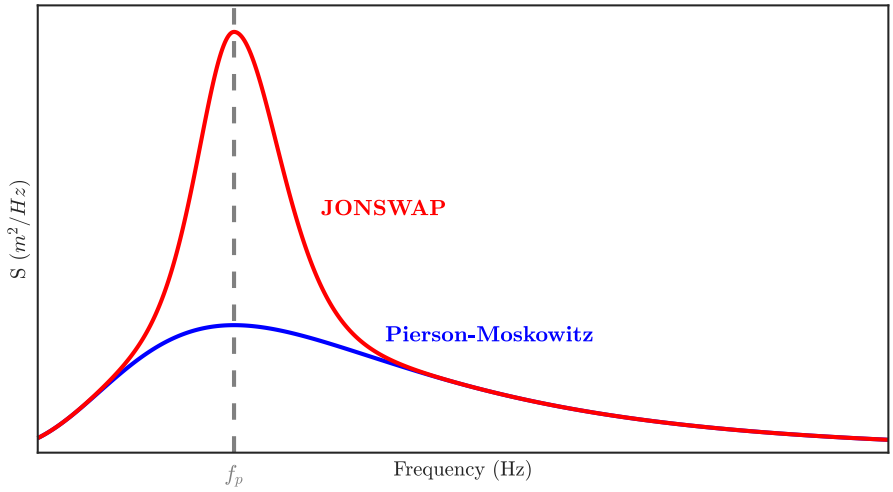

Figure I.4 Descriptive graphic of differences between JONSWAP (red line) and Pierson-Moskowitz (blue line) spectra.

short-crested waves. Long-crested waves (i.e. those without a crest end) have almost zero spread, while short-crested waves have $\sigma_\theta \gg 0$. For illustration purposes, both types of waves are shown in Figure I.5.

All wave statistics can be inferred from measurements in different manners. Some of them are presented in Chapter II.

I.2.4 Depth-induced breaking

The study of waves in coastal areas is enriched by aspects other than those of deep-water waves. As waves move from deep to shallow water, they undergo several transformations. Wave refraction occurs when waves bend due to changes in water depth, causing wave crests to become more parallel to the shoreline. Diffraction involves the bending of waves around obstacles such as ports, while reflection occurs when waves bounce back from barriers. But among all these processes, the most dramatic, and maybe the most important, is **wave breaking**.

Waves break in shallow water due to nonlinear acceleration of wave crests as the base of the wave is slowed down by friction against the sea bottom, a process called depth-induced wave breaking — or in deep water when wave steepness reaches a limit under wind forcing, a process known as white-capping. In the nearshore zone, wave breaking is preceded by wave shoaling.

Wave shoaling occurs when waves approaching shallow water begin to interact strongly with the bottom, which is at a depth of about half their wavelength. The dispersion relation for

Figure I.5 Photographs of long-crested (left) and short-crested waves. Reprinted from lacanausurfinfo.com. Long-crested waves appear to be longshore-uniform, while short-crested waves present strong longshore variability.

shallow waters predict that waves reaching these depth will slow down, thus reducing their wavelength. By conservation of energy, if the wavelength decreases, the wave height must increase and the wave become steeper, with high skewness as wave crests are narrower than wave troughs. The shoaling process is illustrated in Figure I.6.

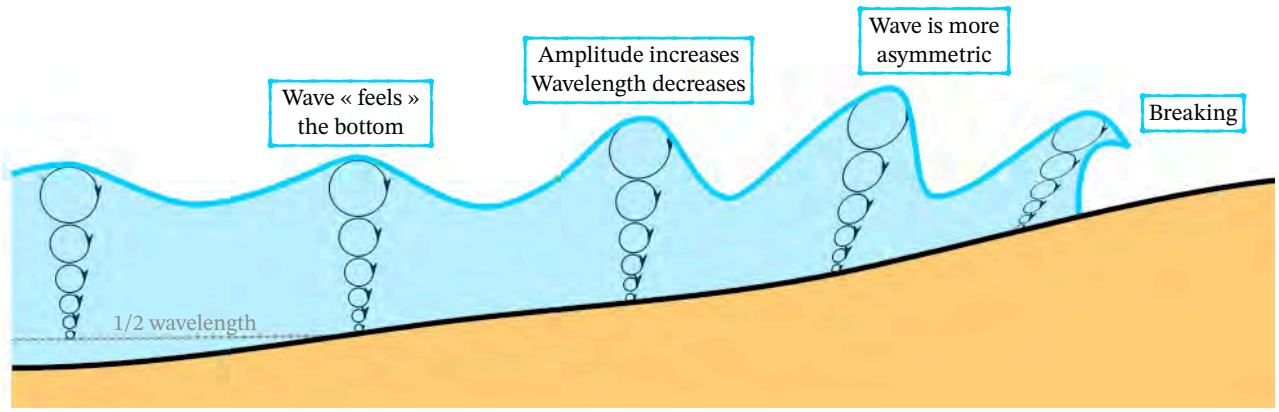

Figure I.6 Descriptive sketch of the shoaling process. Inspired from Earle (2019).

Wave steepening leads at some point to instability, causing the wave crest to accelerate and break. An important question is: at what point exactly will the wave break? Criteria have been defined, for example, Miche (1944) proposed one based on Stokes wave theory:

$$\left(\frac{H}{L}\right)_{\max} = 0.14 \tanh kh \tag{I.23}$$

This criterion reduces to $\sim \frac{1}{7}$ in deep water. Other versions link the depth of breaking h_b with

the breaking wave height H_b through a "constant" coefficient γ_b:

$$\gamma_b = \frac{H_b}{h_b} \tag{I.24}$$

with γ_b estimated with observations to vary between 0.2 and 0.8 depending on beach slope (Raubenheimer et al., 1996). The quest for a generalized breaking criterion is still an open question.

The type of wave breaking differs depending on the bathymetric profile, with three main types standing out: spilling breakers (forming on gently slopes and gradually dissipating wave energy); plunging breakers (on steeper slopes, allowing the wave to grow and *plunge*, creating tubes) and surging breakers (on the steepest slopes, where there is a lot of reflection).

Once the breaking has begun, the energy is no longer conserved due to wave dissipation and Equation I.14 should be replaced by : $\frac{\partial E}{\partial t} + \nabla \cdot (E c_g) = -D$, with D the wave dissipation. In depth-averaged momentum equations, wave dissipation is often introduced as a breaking force F_{br} for the horizontal component u:

$$\frac{\partial u}{\partial t} + u \cdot \nabla u = \frac{1}{\rho} \nabla p + F_{\text{br}} \tag{I.25}$$

neglecting surface and bottom stresses, and viscosity. The term F_{br} will be useful to understand the dynamics of transient rip currents. It introduces the effect of breaking on the mean flow (transfer of momentum from waves to currents) in many models, typically Boussinesq-type models. This part will be discussed in Chapter II.

I.3 Nearshore circulation

Now that the basics of surface gravity waves have been recalled, we can focus on **nearshore circulation** and list the processes involved. We can use the classical concept of radiation stress, even though it is generally valid for depth-averaged processes. It allows to describe different phenomena such as set-up, set-down, undertow or longshore currents, before addressing rip currents in more details. Finally, some information is given about what we will call "innershelf forcing", including the effects of winds, stratification or Coriolis force.

I.3.1 Radiation stress

In nearshore dynamics, currents are often studied using a depth-integrated and wave-averaged framework. When averaging the momentum equation over the wave period, a new term S_{xx} arises, representing the excess momentum flux caused by the presence of waves, similar to what Reynolds stresses are to turbulent flows. The concept of **radiation stress** was developed by Longuet-Higgins and Stewart in the 1960's (Longuet-Higgins & Stewart, 1962, 1964)[6]. To derive the radiation stress term, we first need to establish the depth- and time-averaged momentum equation. Considering shore-normal linear waves over a flat bottom with depth uniform currents and neglecting turbulent and surface stresses, the equation for component u in the x-direction is (Svendsen, 2005):

$$\underbrace{\rho\frac{\partial}{\partial t}\overline{\int_{-h}^{\eta} u dz}}_{\text{Rate}} + \underbrace{\rho\frac{\partial}{\partial x}\overline{\int_{-h}^{\eta} u^2 dz}}_{\text{Advection}} = \underbrace{-\rho g h\frac{\partial \overline{\eta}}{\partial x}}_{\text{Hydrostatic pressure}} \underbrace{-\frac{\partial}{\partial x}\left(\overline{\int_{-h}^{\eta} p dz} - \frac{1}{2}\rho g h^2\right)}_{\text{Wave-induced pressure}} \underbrace{-\overline{\tau_x^b}}_{\text{Bottom stress}} \tag{I.26}$$

If we decompose the total velocity field u into a wave-averaged component $\overline{u}$ and oscillatory flow $\tilde{u}$, such that $u = \overline{u} + \tilde{u}$, we can write the depth- and wave-averaged momentum balance equation:

$$\frac{\partial}{\partial t}\int_{-h}^{\eta} \overline{u} dz + \frac{\partial}{\partial x}\left[\int_{-h}^{\eta} \rho\overline{u}^2 + S_{xx}\right] = -\rho g h\frac{\partial \overline{\eta}}{\partial x} - \tau_x^b \tag{I.27}$$

where $S_{xx} = \overline{\int_{-h}^{\eta}(\rho\tilde{u}^2 + p)dz} - \frac{1}{2}\rho g h^2$. S_{xx} includes the momentum flux due to wave velocity, the wave-induced pressure in the water column, and the contribution of total pressure from crest to trough. In a 2D framework, the additional radiation stress components S_{xy} and S_{yy} are:

$$S_{yy} = \overline{\int_{-h}^{\eta}(\rho\tilde{v}^2 + p)dz} - \frac{1}{2}\rho g h^2 \tag{I.28}$$

$$S_{xy} = \int_{-h}^{\eta} \rho\overline{\tilde{u}\tilde{v}} dz \tag{I.29}$$

where $\overline{\tilde{u}\tilde{v}} = 0$ with shore-normal waves. Using linear wave solutions, the radiation stresses can be related to wave energy, writing them as a 2$^{\text{nd}}$ order tensor:

$$S = \begin{pmatrix} S_{xx} & S_{xy} \\ S_{yx} & S_{yy} \end{pmatrix} = E\begin{pmatrix} 2n - 1/2 & 0 \\ 0 & n - 1/2 \end{pmatrix} \tag{I.30}$$

[6] Note that the same concept was also developed in parallel by H. Lundgren (Svendsen, 2005).

where $n = c_g/c_p$ is the ratio of group and phase celerity. In shallow water, $n = 1$, meaning that the radiation stress gradient is directly related to the energy loss by breaking waves. It therefore represents breaking acceleration of wave-mean currents, i.e., the source of all surfzone vortical currents. When considering oblique incident waves with mean direction θ, the radiation stress tensor becomes:

$$S = E \begin{pmatrix} n(\cos^2\theta + 1) - 1/2 & n\ \cos\theta\sin\theta \\ n\cos\theta\sin\theta & n(\sin^2\theta + 1) - 1/2 \end{pmatrix} \tag{I.31}$$

The radiation stress theory is a powerful tool to explore and explain wave-driven currents in

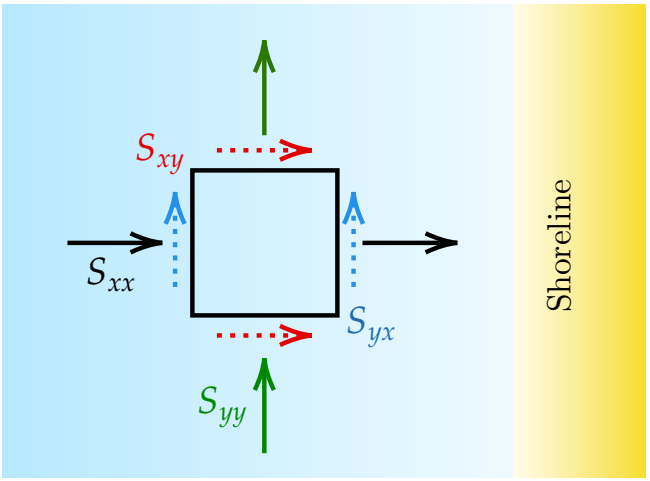

Figure I.7 Descriptive sketch of how radiation stress tensor acts on a depth-averaged water cell.

the nearshore. Nevertheless, the expressions derived with linear wave theory underestimate radiation stresses when the wave shape is not sinusoidal (e.g., when waves steepen and become more skewed in the shoaling zone). In addition, a different approach to radiation stress, called vortex-force formalism, has recently emerged to address wave-current interactions in 3D models such as CROCO (see e.g. Weir et al., 2011; Uchiyama et al., 2009, 2010; Kumar et al., 2012; Lane et al., 2007). In this formalism too, the breaking acceleration is linked to the loss of wave energy during breaking, and must be parameterized in the wave-averaging equation approach. In any case, the radiation stress formalism is still widely used for pedagogic purposes and more details can be found in several books, such as Svendsen (2005).

I.3.2 Set-up and set-down

Waves affect the mean water level in the nearshore zone, which can also be explained by the radiation stress gradient (Bowen, 1969):

$$\frac{\partial \overline{\eta}}{\partial x} = -\frac{1}{\rho g(h+\overline{\eta})}\frac{\partial S_{xx}}{\partial x} \tag{I.32}$$

It shows that the water level η is modified by changes in wave energy, i.e. wave height. In the shoaling zone, where energy increases locally (and $-\partial S_{xx}/\partial x$ is negative), η decreases, a phenomenon called "set-down", while in the surf zone, where wave energy is lost to currents and turbulence, there is a "set-up" on the contrary (Figure I.8).

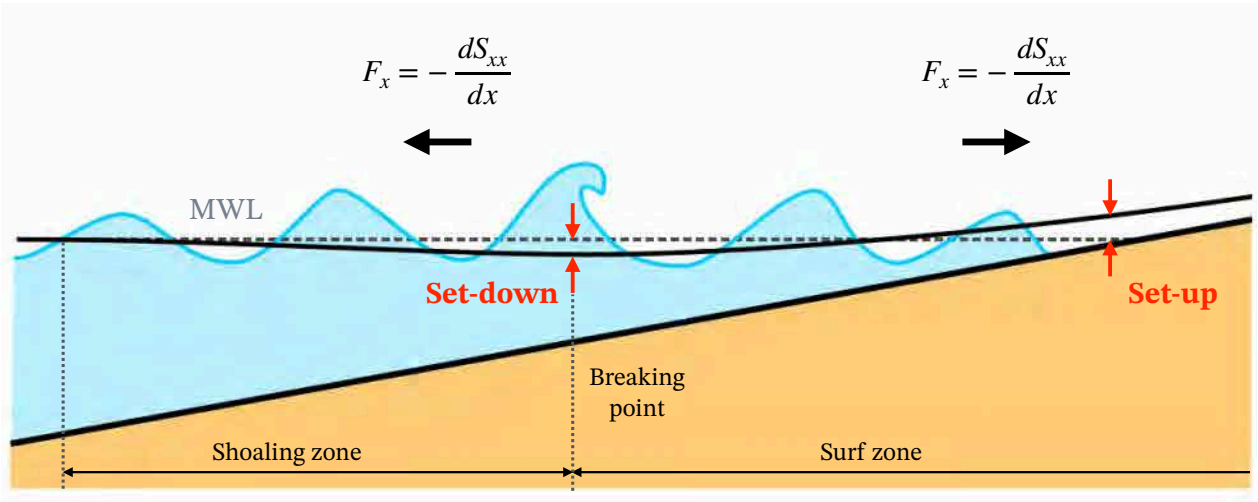

Figure I.8 Descriptive sketch of set-down and set-up caused by waves (re-adapted from geo.libretexts.org)

I.3.3 Cross-shore circulation and undertow

Waves also produce a **cross-shore circulation** in the nearshore zone, i.e., Stokes drift and wave streaming dominating in the shoaling zone, and breaker-induced surface onshore flow and seaward undertow in the surf zone. We propose a quick overview of these different processes illustrated in Figure I.9.

Although a pure wave transports only energy and not matter, a net transport of matter can nevertheless be observed due to the **Stokes drift**. Stokes drift is a nonlinear phenomenon (varying with $(ka)^2$) that can be derived from linear theory. It is often interpreted in the Eulerian framework as water carried between the through and the crest or, in the Lagrangian framework,

as quasi-circular paths of particles that do not close perfectly, allowing motion in the direction of wave propagation.

In depth-averaged models, the **undertow** is linked to the depth-averaged Stokes drift by mass conservation, and is therefore sometimes referred to as the anti-Stokes Eulerian current (or simply anti-Stokes). In this case, the undertow simply fills the need for a net zero Lagrangian mass flux through the water column. In a 3D model, the undertow acts as a return current balancing the onshore flow intensified by surface-breaking waves. It can be much stronger in this case, depending on wave conditions and the associated breaking force. The undertow (besides the associated longshore drift, which occurs when waves propagate at an angle to the shoreline) is one of the main drivers of coastal erosion, leading to the creation and migration of sandbars, for example (Marchesiello et al., 2022).

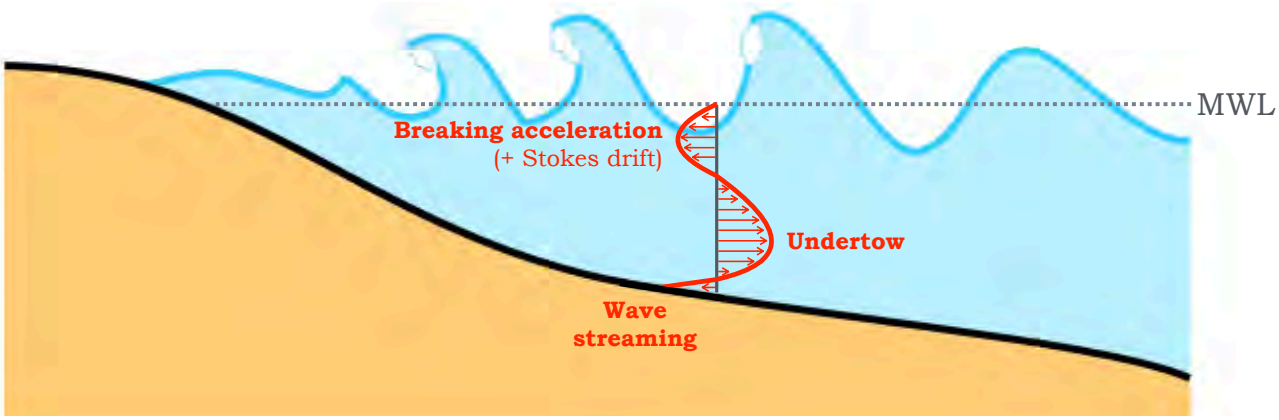

Figure I.9 Descriptive sketch of the cross-shore vertical circulation with surface onshore-directed flow (breaking acceleration, Stokes drift and wave streaming), seaward undertow near the bottom.

The **wave streaming** is a shoreward Eulerian current taking place in the wave boundary layer. It may be forced by two different mechanisms (Kranenburg et al., 2012):

- progressive wave streaming;
- waveshape streaming.

The process of progressive wave streaming consists on the generation of a near-bottom onshore current in the wave boundary layer current (Longuet-Higgins & Stoneley, 1953). It is produced by the bottom drag on waves, the bed affecting the phase of horizontal and vertical orbital velocities, inducing downward transport of the mean horizontal wave momentum, which drives an onshore boundary layer current.

The second process, called waveshape streaming, is due to the skewness and asymmetry of the wave (Trowbridge & Madsen, 1984) and can counter progressive wave streaming, potentially leading to offshore-directed streaming (Kranenburg et al., 2012; Holmedal & Myrhaug, 2009).

In the present study, wave streaming, which is only a few cm/s, is assumed to be of secondary importance to dispersion of surfzone tracers. In addition, this process is not well understood, and the thin bottom boundary layer may be unresolved due to vertical resolution limits.

I.3.4 Longshore drift

Longshore drift is one of the wave-induced processes best known to non-specialists (after rip currents), as its manifestation can be seen from the beach. Longshore drift is critical to sediment transport, reshaping the coastline over long time scales. It requires oblique waves with non zero angle θ_0. As waves are approaching the shore in shallow depth, the wave angle changes due to refraction and can be expressed as a function of x. We can then use the Snell-Descartes law to write:

$$\frac{\sin\theta(x)}{c_p} = \text{const} \tag{I.33}$$

with c_p the phase celerity of the wave. Considering a longshore-uniform beach, the steady inviscid momentum equation in the longshore direction is:

$$\frac{\partial S_{xy}}{\partial x} + \tau_{by} = 0 \tag{I.34}$$

where the second term is the longshore bottom shear stress, expressing a balance between breaking acceleration and friction by the resulting longshore current. For non-breaking waves, we had $S_{xy} = E\,n\,\cos\theta_0 \sin\theta_0$. Using the energy equation with oblique waves $\frac{\partial}{\partial x}(Ec_g\cos\theta_0) = -D_w$ (see Eq. I.14), with D_w the wave breaking energy dissipation, we obtain:

$$-\frac{\partial S_{xy}}{\partial x} = \frac{D_w}{c_p}\sin\theta_0 \tag{I.35}$$

$\frac{\partial S_{xy}}{\partial x}$ is thus non-zero only in the surf zone. Writing $\tau_{by} = \rho C_d v^2$, leads to an expression for the longshore drift :

$$v = \sqrt{\frac{D_w}{\rho C_d c_p}\sin\theta_0} \tag{I.36}$$

The inclusion of turbulent stresses in the equation I.34 would tend to diffuse the cross-shore profile of v. Similarly, the addition of nonlinear advection terms, particularly in the presence of u vertical shear (in a 3D model), would stretch and distort this profile asymmetrically.

I.3.5 Rip currents

Of all nearshore currents, **rip currents** are the ones that attract the most attention. As noted by Castelle (2016) in their review paper, the number of publications on rip currents has increased almost exponentially, particularly since the beginning of the 21st century. Rip currents are characterized by a narrow seaward flow with time scales ranging from $\mathcal{O}$(1 min) to $\mathcal{O}$(1 hr) and a cross-shore spatial scale $\mathcal{O}$(100 m). Although this thesis is focused on transient rip currents, driven by wave directional spread, we try here to provide an overview of these phenomena of high complexity. Note that rip currents, sometimes confused in the public mind with the undertow or with "rip-tides", can be found not only in the ocean but also in lakes large enough (see e.g., Liu & Wu, 2022).

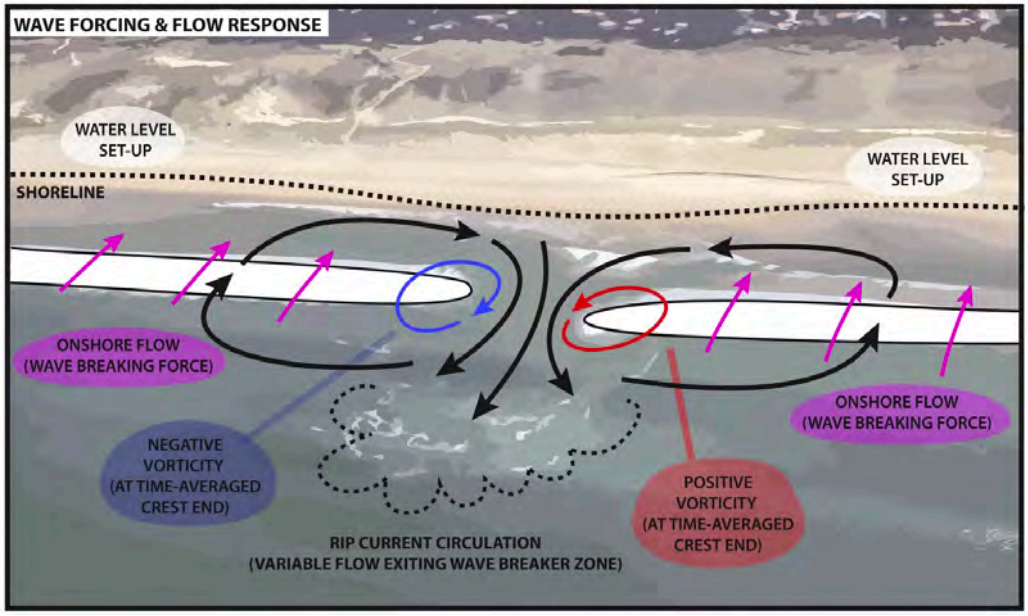

Figure I.10 Conceptualized view of vortical motions driven by longshore variability of wave breaking, leading to the formation of rip currents. Reprinted from Castelle (2016).

Rip currents are generally linked with the longshore variability of wave breaking, that are caused by bathymetric or hydrodynamic features. As depicted in Figure I.10, the longshore variability of wave breaking creates regions of vanishing breaking force that are source of vertical vorticity. This is the key mechanism of rip current generation.

I.3.5.1 Bathymetric rip currents

Bathymetric rip currents are the most extensively studied and documented type of rip currents due to the relative ease of their observation. These currents are notably persistent in both space and time under specific wave and tide conditions, making them easier to measure and analyze. Castelle (2016) classify bathymetric rip currents into two categories: channel rip currents and focused rip currents.

Channel rip currents are among the most straightforward to understand. These currents typically occur in intermediate beach states, where they flow through deep channels located between surfzone sandbars. Sandbars, which are underwater ridges composed of sand, are generally found at depths of less than 10 meters and often exhibit a quasi-regular pattern in their depth and position relative to the shore (Wright & Short, 1984). The rip channels cut through these sandbars, creating deeper channels that lead to variability in wave breaking, and therefore persistent rip currents. This persistence is of particular interest not only to scientists, who find these stable features easier to study, but also to lifeguards, who can identify and warn beachgoers about their presence. While channeled rip currents may migrate over time on sandy beaches, they can persist for much longer periods and remain nearly stationary on fringing reef beaches (in this case referred to as *reef rip currents*).

Focused rip currents, unlike channeled rips, do not necessarily form in areas where wave breaking is less intense due to bathymetric variations. Instead, they are influenced by offshore bathymetric anomalies, such as underwater ridges or canyons. These anomalies cause alongshore variability in breaking wave height and angle, which can lead to the formation of rip currents. Focused rip currents tend to remain fixed in location under stable wave and tide conditions, but they can shift alongshore as the wave incidence and period change[7].

I.3.5.2 Boundary-driven rip currents

Less discussed in the community compared with bathymetric or transient rips, **boundary-driven rip currents** originate from the numerous rigid features that can be found on beaches, whether natural (headlands, rock outcrops) or anthropogenic (jetties, piers). These rips can form through three mechanisms, each slightly different from other types of rip currents. The

[7] The focused rip current mechanism may be linked to the wavemaker problem identified in this study, which is the source of spurious rip currents described in Chapter III.

first mechanism, which gives its name to these rips, is called *deflection rips*. This occurs when a strong longshore current, driven by oblique waves, encounters an obstacle. As a result, the current is deflected, creating an offshore-directed flow on the upstream side of the rigid obstacle.

The other two mechanisms occur downstream of the obstacle, resulting in the formation of *shadow rips*. When waves approach from an oblique direction, a region of lower wave height, known as the shadow zone[8], forms downstream of the obstacle, where the breaking is less intense, resulting in shadow rip currents.

I.3.5.3 Transient rip currents

Transient rip currents are central to this thesis. They depend solely on sea state, i.e. they do not require bathymetric variability and can occur on beaches that are uniform across the coastline, making them transient in both space and time, hence highly unpredictable. Although transient rips have been studied for several decades (Bowen, 1969), there remains ongoing debate regarding their driving mechanisms. Currently, two primary mechanisms are widely accepted by the scientific community: horizontal shear instability and short-crested wave forcing (also known as the Peregrine process). Let us describe both.

Historically, horizontal shear was viewed as the primary driving mechanism. The shear arises on the edges of a strong longshore current, which can become unstable, generating shear waves that develop vortices of $\mathcal{O}(100\text{ m})$ and $\mathcal{O}(100\text{ s})$, with associated strong seaward flow. Using linear stability analysis, Bowen and Holman (1989) expressed the wavelength, frequency and growth rate of the most unstable shear waves as $\lambda_h = 2.5L$, $f_h = 0.07\frac{V}{L}$ and $\sigma_h = 0.15\frac{V}{L}$ respectively, with V the mean longshore current and L the longshore current half-width. However, this mechanism has recently been reconsidered due to the emergence of the Peregrine process.

Feddersen (2014) provided a comparative analysis between longshore current shear instability and the Peregrine process through modeling study, concluding that in most surf zones, the shear instability mechanism is negligible compared to the Peregrine process. Previous modeling studies using three-dimensional wave-averaged equations have also raised questions about the relevance of this process (Newberger & Allen, 2007; Splinter & Slinn, 2003), as they could not reproduce the results of 2D wave-averaged models (Allen et al., 1996). This result was further corroborated

[8] Shadow zones can also appear in numerical models when periodic boundary conditions (for boundaries normal to the shore) are not preserved, leading to spurious shadow rips, as discussed in Chapter III.

by Marchesiello et al. (2021), who used a 3D wave-resolving model to demonstrate that even in the presence of long-crested waves (i.e., without the Peregrine process), the horizontal shear intensity and magnitude of shear waves was significantly reduced by the vertical shear of mean cross-shore currents (the undertow profile). This strong inhibition effect could explain some field observations, for example that of Castelle et al. (2014) showing a decrease in transient rip activity with increasing intensity of longshore currents (see also Spydell, 2016). Thus, one can infer that horizontal shear instability is relatively uncommon, except in rare cases involving very strong longshore currents.

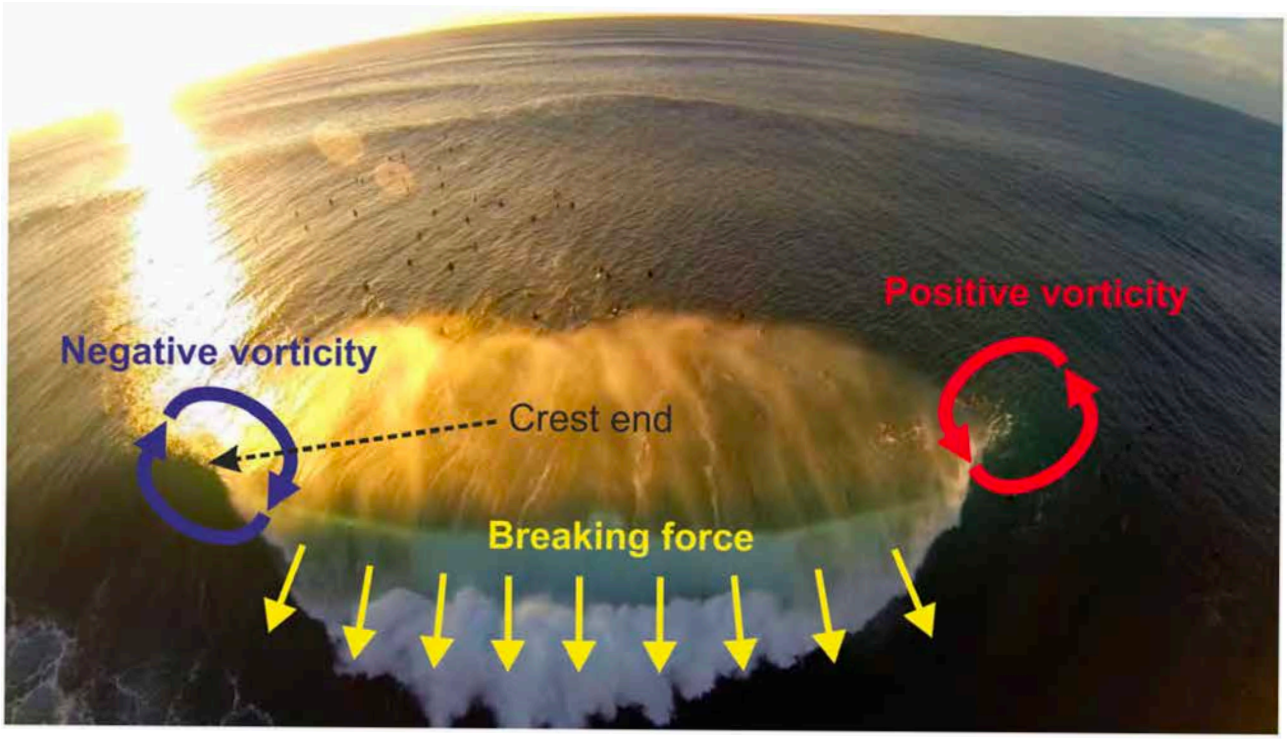

Figure I.11 Example of short-crested wave generating vorticity at the crest ends. Photography by Eric Sterman, reprinted from Castelle (2016).

Flash rips, by contrast, are much more ubiquitous, as they require only a multidirectional sea state (i.e., $\sigma_\theta > 0$, see Sec. I.2.3), producing short-crested breaking waves through interference of wave trains (Peregrine, 1998; Clark et al., 2012; Kirby & Derakhti, 2019). This process was first brought to light by the pioneering work of Peregrine (1998) and is now considered the primary forcing mechanism for transient rip currents by the nearshore research community (Kirby & Derakhti, 2019). When a short-crested wave reaches the shore and breaks, vorticity is injected at scales of $\mathcal{O}(1-10$ m) at the edges of the wave crest due to differential breaking, i.e., the gradients of breaking acceleration (Peregrine, 1998; Clark et al., 2012). An example of

short-crested wave breaking is shown in Figure I.11. Clark et al. (2012) proposed a scaling for vorticity generation by a single wave as $H_s^3 h^{-2.5}$, with maximum values observed in the outer surf zone. One way to mathematically describe this phenomenon is by relating the vertical vorticity to the breaking force as follows:

$$\frac{\partial \omega_z}{\partial t} = -\frac{\partial F_{\text{br}}}{\partial y_c} \tag{I.37}$$

where y_c is the along-crest direction, and F_{br} is the breaking force defined in Equation I.25 (Clark et al., 2012). In the presence of multiple waves, the resulting eddies merge over time into larger surfzone eddies through an inverse cascade mechanism, consistent with 2D turbulence (see Box I.12). Surfzone eddies tend to be driven offshore due to the coastal boundary, leading to the formation transient rip currents, which we will call "flash rips" as they are commonly known. The inverse cascade mechanism has recently been confirmed through both modeling (Spydell & Feddersen, 2009; Feddersen, 2014; Marchesiello et al., 2021) and observational studies (Elgar & Raubenheimer, 2020; Elgar et al., 2023; Baker et al., 2023b), but suggest that flash rip generation occurs more in the inner surf zone than in the outer surf zone. It is important to note that flash rips can be accurately resolved only by wave-resolving models, which are capable of explicitly simulating short-crested waves.

While eddies are generally considered depth-uniform throughout most of the surf zone, vertical dependency starts to appear in the outer surf zone (Lippmann & Bowen, 2016; Henderson et al., 2017; Baker et al., 2021). This vertical dependency is crucial for understanding surfzone eddy dynamics, as it influences the intensity of the inverse cascade (Marchesiello et al., 2021), thus decreasing the coherence and lifespan of nearshore vortices through vortex tilting and stretching (see Figure I.13), and turbulent vertical diffusion (Uchiyama et al., 2017; McWilliams et al., 2018). These processes can be expressed by the vertical vorticity ω_z equation for a 3D velocity field (u, v, w) (Uchiyama et al., 2017; Baker, 2023):

$$\underbrace{\frac{\partial \omega_z}{\partial t}}_{\text{Rate}} + \underbrace{(u \cdot \nabla)\omega_z}_{\text{Advection}} = \underbrace{\omega_x \frac{\partial w}{\partial x} + \omega_y \frac{\partial w}{\partial y}}_{\text{Vortex tilting}} - \underbrace{\omega_z \left(\frac{\partial u}{\partial x} + \frac{\partial v}{\partial y}\right)}_{\text{Vortex stretching}} + \underbrace{\frac{\partial}{\partial z}\left(K_v \frac{\partial \omega_z}{\partial z}\right)}_{\text{Vertical diffusion}} + \underbrace{\nabla \times [F_{\text{br}} - \tau_b - \tau_s]}_{\text{Body forces}} \tag{I.38}$$

where K_v is the vertical turbulent viscosity. In a 2D flow, vortex tilting and stretching, and vertical diffusion are absent, as these processes require a three-dimensional flow structure to

Box I.1

Turbulent cascade

The turbulent cascade is a mechanism that describes how energy is transported across the energy spectrum, due to the non-linearity of the flow. When energy is transferred from larger eddies to smaller ones, this process is referred to as direct (or forward) cascade. Conversely, when energy is transferred from smaller to larger scales, it is known as inverse cascade.

The concept of a **direct cascade** was first qualitatively described by Lewis Richardson (Richardson, 1922), notably through his famous *turbulent* poem. Later, it was statistically formulated by Andrei Kolmogorov (Kolmogorov, 1941), who introduced the famous $-\frac{5}{3}$ slope of kinetic energy spectrum. It characterizes the inertial range of the kinetic energy spectrum, where energy fluxes to smaller scales as $E(k) \propto k^{-5/3}$, with k the wavenumber and E the kinetic energy. Beyond the inertial range at large k, eddies enter the dissipation range. Importantly, the direct cascade, characterized by a positive energy flux $\Pi(k)$, can only occur in 3D flows, where vortex stretching and tilting are possible.

In contrast, in 2D flows, the presence of an **inverse cascade** allows small eddies to merge, forming larger vortices that are more coherent structures than those typically observed in 3D turbulence. The inverse cascade was first predicted through the work of Kraichnan (1967).

Direct and inverse cascades can coexist. In geophysical flows, such as oceanic currents, the water is often considered shallow enough to be approximated by quasi-2D dynamics (Sous et al., 2005), which would favor an inverse cascade. However, the direct cascade can also play a significant role, as 3D processes and vortex stretching becomes important. In this case, the quasi-2D turbulence approximation may not always be accurate (van Heijst, 2014). Despite the shallow waters of the nearshore region, the turbulent cascade of surfzone eddies and rip currents appears to be largely affected by 3D processes (Marchesiello et al., 2021).

For further details on turbulent cascades, readers are encouraged to consult reviews or textbooks on turbulence (e.g., Alexakis & Biferale, 2018; Pope, 2000).

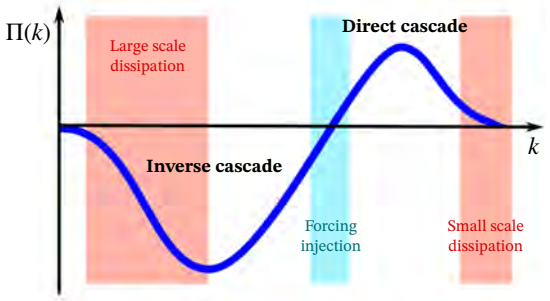

Figure I.12 Schematic view of inverse and direct turbulent cascades, with dissipation scales in red and forcing injection scale in blue.

occur.

Flash rips are commonly illustrated using spectral decomposition, particularly in the Very Low Frequency (VLF; $f < 0.003$ Hz) range. They exhibit velocities of the same order of magnitude as bathymetric rip currents on alongshore-variable beaches (O'Dea et al., 2021; Baker et al., 2021). There exists a weak correlation between wave height and flash rip velocity (MacMahan et al., 2010), but a more robust linear relation seems to exist between flash rip velocities and wave directional spread (Spydell & Feddersen, 2009; Spydell et al., 2009; Suanda & Feddersen, 2015), although recent observations have shown that beyond a certain threshold of σ_θ, flash rip velocity no longer increases (Baker, 2023). The unpredictable nature of flash rips makes them difficult to measure and observe in the field, complicating efforts to understand their behavior under varying forcing conditions (e.g., significant wave height, directional spread, mean wave

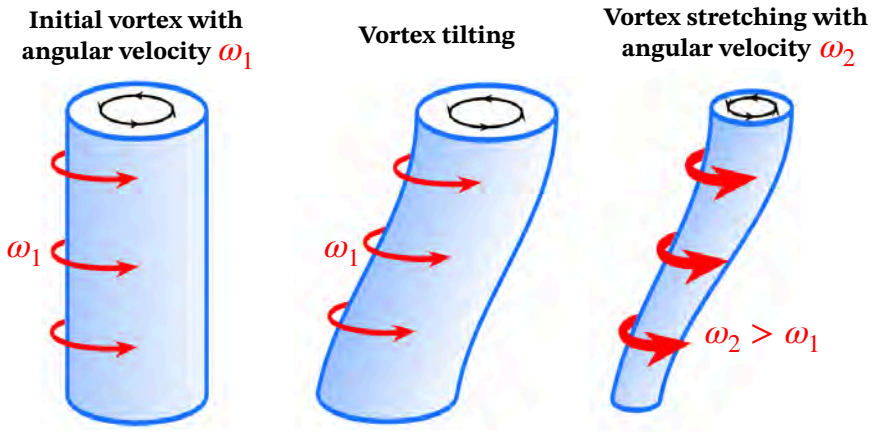

Figure I.13 Schematic view of the vortex stretching and tilting mechanisms.

angle, bathymetry, etc.). This is why numerical and basin experiments are crucial for gaining a better understanding of these phenomena.

I.3.6 Innershelf dynamics

In addition to wave-driven processes, such as those previously described, it is essential to consider *innershelf processes*. These are processes that occur primarily on the shelf and are independent of wave activity. Although tides can be play a very significant role in some continental shelves, we will focus in this thesis work on phenomena occurring over time scales ranging from minutes to a few hours in micro-tidal areas.

Coastal winds are often the source of strong shelf currents. Coastal winds can have both longshore and cross-shore components, with the former being generally dominant due to Earth rotation acting on the difference of pressure between land sea. We begin by recalling how wind surface shear stress, τ_w, is defined:

$$\tau_w = C_d \rho_a W \tag{I.39}$$

with C_d the drag coefficient dependent on wind velocity, ρ_a the air density, and W the wind velocity near the water surface.

Longshore winds, which blow parallel to the coastline, are a primary driver of alongshore shelf currents. Longshore winds contribute to coastal upwelling and downwelling processes, where water is either pushed toward or away from the shore, influencing nutrient distribution and biological productivity (Marchesiello et al., 2003). However, this process may be limited

to the mid-shelf area, while on the innershelf, the merging of the surface and bottom Ekman layers produces a "kinematic barrier" for the Ekman transport, i.e., longshore winds produce only very weak cross-shore currents (Estrade et al., 2008). On the other hand, they have an important role in the longshore transport of material.

Cross-shore winds, e.g., sea/land breezes, blowing perpendicular to the coast, exert a different set of influences. On the inner shelf, the Ekman transport tend to be in the direction of the wind, as mentioned. Therefore, offshore winds can drive coastal water offshore, contributing to upwelling (Estrade et al., 2008). In contrast, onshore winds would push surface waters to the coast, resulting in downwelling or retention of buoyant material. The interaction between wind-driven processes and the nearshore environment is complex and would vary depending on factors such as coastal topography and the presence of stratification in the water column.

The **Coriolis force**, an apparent force arising from the Earth's rotation, may also act on nearshore currents, though its impact is often considered negligible (Kumar & Feddersen, 2017b). Nevertheless, some studies suggest a possible role for Coriolis, considering that the innershelf is a transition between the surf zone and the mid-shelf, where the Earth's rotation becomes a predominant force (Özkan-Haller, 2008).

Although the surf zone is generally considered to be vertically well mixed, strong **stratification** can occur just outside the surf zone, on the inner shelf, during strong summer conditions for example (e.g. Hally-Rosendahl et al., 2014), and can possibly impact the nearshore circulation. Oceanic stratification refers to the layering of water masses with different densities, primarily due to variations in temperature and salinity (in this case, salinity is not considered). The stability of stratification is commonly described by the Brunt-Väisälä frequency (N) :

$$N^2 = \frac{g\alpha}{T_0}\frac{\partial T}{\partial z} \tag{I.40}$$

with g the gravitational acceleration, α the thermal expansion coefficient of seawater, T the temperature, and T_0 a reference temperature.

The heat budget of the surf zone has also been considered, involving solar radiation in a shallow foamy environment and heat produced by the dissipation of breaking waves (Sinnett & Feddersen, 2014). A recent study seems to confirm that breaking waves can contribute to heating the surf zone, but solar heating seems to be reduced by the albedo of the foam, which

could lead to a net cooling depending on the season (Sinnett & Feddersen, 2018). In any case, the temperature of water in the surf zone (regardless of stratification) could play an important role in cross-shore dispersion of tracers. Moulton et al. (2021) showed such an influence on bathymetric rip current plumes: a warm surf zone would result in larger plumes extending within a near-surface layer, whereas a cooler surf zone would lead to shorter plumes that subduct when entering the shelf.

Shelf stratification can affect the nearshore region by various mechanisms, e.g., the propagation of internal waves, which can enhance mixing (Grimes et al., 2021, 2020a; Woodson, 2018). Internal waves can even modulate the temperature of the surf zone by up to 1°C in just 5 minutes (Sinnett et al., 2018). The interaction between transient rip currents and stratification is of significant interest, generating cross-shore circulation cells that would redistribute tracer patches along the vertical direction and modify dispersion pathways (Kumar & Feddersen, 2017b).

I.4 Tracer dispersion in the nearshore

All these processes, particularly rip currents, contribute to tracer mixing and transport in the nearshore area at various scales. Given the challenges facing the coastal zone, tracer dispersion needs to be estimated with greater precision. This thesis focuses on neutrally buoyant material (such as pathogens), and does not address buoyant materials like oil or plastic, nor sinking or swimming particles such as sediment and larvae. Our aim in this section is to provide an overview of the current state of the art in this field. A small section is dedicated to longshore diffusion, followed by a more in-depth exploration of cross-shore exchanges, which is the primary focus of this study.

I.4.1 How to quantify tracer dispersion?

To understand how diffusion works, it is helpful to recall some fundamental properties of mixing and transport processes. At the molecular level, diffusion follows Fick's laws, expressed in the following budget equation for tracer concentration C:

$$\underbrace{\frac{\partial C}{\partial t}}_{\text{Rate}} + \underbrace{\mathbf{u} \cdot \nabla C}_{\text{Advection}} = \underbrace{D \nabla^2 C}_{\text{Diffusion}} \tag{I.41}$$

where D is the molecular diffusion coefficient or diffusivity. This is known as the advection-diffusion equation and has solutions analogous to those of the heat equation. When the concentration distribution is assumed to be Gaussian, diffusivity can be expressed as:

$$D = \frac{1}{2}\frac{d\sigma^2}{dt} \sim \frac{L^2}{T} \tag{I.42}$$

where σ^2 is the variance of the concentration, representing the width of the tracer patch. Molecular diffusion operates only at very small scales and is negligible at the scales we consider. To illustrate this, we can use the example of sugar deposited in a small cup of coffee. Without advection and relying solely on molecular diffusion, the sugar would take approximately one month to mix uniformly. However, by stirring the coffee, we introduce advection and turbulence, reducing the mixing time to just a few seconds[9].

In turbulence fields, large eddies tend to stir and stretch the tracer patch, causing the generation of filaments. Stirring has the effect of increasing gradients in the tracer concentration, which accelerate the onset of mixing by molecular diffusion or smaller eddies generated along the sharp filaments. At this point, the rate of mixing is no longer characterized by D, but by the rate of filamentation by eddies. However, if smaller eddies are weak (e.g., in 2D turbulence), the transition from stirring to mixing will be slower, as will be seen for the nearshore zone. Similarly to molecular diffusion, one can derive an eddy diffusivity, which is much larger than molecular diffusivity. More details about stirring and mixing may be found in the review of Villermaux (2019) or in the pioneering work of Eckart (1948).

Building on the idea of molecular diffusion, Einstein (1905) established the equivalence between random molecular motion and bulk molecular diffusion, before Taylor (1921) derived the relationship between eddy diffusivity and particle displacement variance. This theory is of great interest to the nearshore community, as many studies employ Lagrangian drifters (e.g. Spydell & Feddersen, 2009; Spydell et al., 2019). The particle displacement variance is given by:

$$\overline{X^2(t)} = 2\overline{u'_L(t)u'_L(t)}\int_0^t\int_0^{t'} R_L d\tau dt' \tag{I.43}$$

where u_L is the Lagrangian velocity of the particle, u'_L represents its velocity fluctuation,

[9] Note that coffee seems to have been a prime example of turbulence for many years (e.g. Eckart, 1948; Roberts & Webster, 2002).

and $R_L(\tau) = \frac{\overline{u_L(t)u_L(t+\tau)}}{\overline{u'_L(t)u'_L(t)}}$ is the velocity autocorrelation function. Using Lagrangian theory is beneficial for field studies and allows for the separation of two distinct time scales. To achieve this, we define the Lagrangian time scale as:

$$T_L = \int_0^\infty R_L d\tau \tag{I.44}$$

For short time scales ($t \ll T_L$), Equation I.43 simplifies to $\overline{X^2(t)} = \overline{u'_L(t)u'_L(t)}t^2$, meaning the tracer variance increases proportionally to t^2, and the diffusivity scales with t. This regime is known as the **ballistic regime**. For long time scales ($t \gg T_L$), Equation I.43 becomes $\overline{X^2(t)} = 2\overline{u'_L(t)u'_L(t)}T_L t + C_L$, where C_L is a constant, and the Lagrangian diffusivity is expressed as:

$$\kappa_L = \frac{1}{2}\frac{d\overline{X^2(t)}}{dt} = \overline{u'_L(t)u'_L(t)}T_L \tag{I.45}$$

This implies that diffusivity is no longer correlated with time, similar to molecular diffusion, also known as the **Brownian diffusion regime**. It is important to note that we have only discussed one-particle diffusivity here, but two-particle dispersion can also be estimated (e.g. Spydell et al., 2007), which allows for the assessment of relative dispersion (i.e., dispersion around a time-dependent center of mass). Another way to estimate diffusivity is through the injection of dye into the area of interest (e.g. Clarke et al., 2007; Inman et al., 1971). In this case, we refer to **Eulerian diffusivity**. To estimate bulk diffusivity, we assume that the dye patch is mixed following a Fickian pattern. Applying Equation I.41 at a larger scale, with or without mean currents, becomes straightforward. In the case of a surf-zone plume advected by a longshore drift V (as in Clark et al., 2010), the advection term becomes extremely useful. However, it is important to ensure that the domain length scale is larger than the mixing length and exhibits sufficient statistical significance (i.e., we cannot consider a single flash rip, but an ensemble of rips can be treated as a Fickian process).

In the nearshore area, diffusivity is typically divided into cross-shore and longshore components, κ_{xx} and κ_{yy}, respectively. More details on diffusivity estimation can be found in books such as Roberts and Webster (2002).

Another approach is to use estimated **exchange velocities**, such as:

$$U_{\text{ex}}(x) = \frac{1}{L_y}\overline{\int_0^{L_y} u_{\text{rot}}(x,y,t)dy} \tag{I.46}$$

where $\bar{\cdot}$ denotes a time average, u^-_{rot} represents the seaward rotational (vortical) velocity, and L_y is the longshore domain length used to perform a longshore average (see e.g. Suanda & Feddersen, 2015; Moulton et al., 2023). This estimation is particularly useful for assessing cross-shore dispersion driven by flash rips (hence the use of rotational velocities).

I.4.2 Alongshore dispersion

Alongshore dispersion in the surf zone is primarily driven by longshore drift and is generally greater than cross-shore diffusion (Spydell et al., 2007, 2019), except over very short time scales ($t < 50$ s), where cross-shore transport may dominate. Lagrangian studies on longshore-uniform dissipative beaches have found that $\kappa_{yy} = 2.0 - 18.0$ m^{2}s^{-1} (Spydell et al., 2007; Spydell & Feddersen, 2009) for $t \gg T_L$ (asymptotic values), and $\kappa_{yy} = 2.8 - 3.9$ m^{2}s^{-1} for rip-channeled beaches (Brown et al., 2009). Results indicate that, for longshore-uniform bathymetry, asymptotic diffusivities are similar both inside and outside the surf zone, although the asymptotic value is reached earlier within the surf zone (Spydell et al., 2007).

For rip-channeled bathymetry, the estimated diffusivities are smaller ($\kappa_{yy} = 0.4 - 5$ m^{2}s^{-1}; Brown et al., 2015). On steeper, more reflective beaches, surf-zone diffusivity is reduced, with $\kappa_{yy} = 0.5$ m^{2}s^{-1} (Brown et al., 2019). Longshore diffusivity is expected to increase with a stronger longshore current, primarily due to horizontal shear dispersion (Spydell & Feddersen, 2012a,b).

I.4.3 Cross-shore diffusion

Cross-shore diffusion is crucial for understanding the exchange between the surf zone and the inner shelf. Various studies using Lagrangian drifters (e.g. Spydell & Feddersen, 2009; Brown et al., 2009; Spydell et al., 2019) or fluorescent dye (e.g. Harris et al., 1963; Inman et al., 1971; Clarke et al., 2007; Hally-Rosendahl et al., 2014; Clark et al., 2010) have attempted to address this issue and determine the primary mechanisms driving cross-shore exchange.

Cross-shore diffusivity estimations vary considerably depending on field conditions. Using observed dye dilution, Inman et al. (1971) estimated $\kappa_{xx} = 0.08 - 5.9$ m^{2}s^{-1}. On alongshore-uniform beaches, recent studies using drifters reported values of $\kappa_{xx} = 0.5 - 1.5$ m^{2}s^{-1}, while on rip-channeled beaches, $\kappa_{xx} = 0.9 - 2.2$ m^{2}s^{-1} (Brown et al., 2009).

Box I.2

What is shear dispersion ?

Shear dispersion refers to the process by which a tracer patch (such as pollutants, nutrients, or biological organisms) is spread out over time due to the combined effects of advection by cross-shore flows with a vertical shear and molecular or turbulent vertical diffusion. Shear occurs in the surf zone due to shoreward breaking acceleration (and Stokes drift) near the surface and seaward undertow near the bottom. This velocity gradient stretches and elongates the initial tracer patch, while vertical mixing turns this into horizontal dispersion.

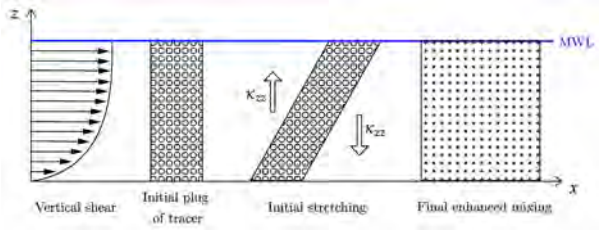

Figure I.14 Schematic view of shear dispersion, after Benoit Cushman-Roisin[10].

Building on the work of Harris et al. (1963) and Inman et al. (1971), Feddersen (2007) proposed a scaling to account for the turbulent mixing produced by breaking waves, with $\kappa_{xx} \propto H_s^2/T_p$. This scaling can also be expressed as $H_s L_{SZ}/T_p$, where L_{SZ} is the surf zone width. Both approaches are equivalent on self-similar bathymetry (i.e., where $\gamma = H/h$ is constant). Although this scaling efficiently models breaking-induced turbulent diffusion, a study by Clark et al. (2010) showed low correlation with observed diffusivities ($r^2 = 0.32$) on beaches with rip currents. This result was later confirmed through a modeling study (Clark et al., 2011).

Using a laboratory basin experiment with longshore current and monochromatic waves, Pearson et al. (2009) highlighted the role of shear dispersion (see Box I.14) – a classic mechanism in ocean dynamics – in surfzone mixing. They proposed a parameterization based on undertow-induced vertical shear:

$$\kappa_{xx} = \frac{(U^+ - U^-)^2 h^2}{48 \kappa_{zz}} \tag{I.47}$$

with U^+ and U^- representing the onshore and offshore directed velocities, h the water depth, and κ_{zz} the vertical diffusivity. Although this parameterization showed a strong correlation with diffusivities from field experiments ($r^2 = 0.94$), it seems to explain only a small part of its magnitude, as shown by Clark et al. (2010). This may suggest that factors of shear dispersion (the vertical shear itself) is important, but the process of shear dispersion is not.

Setting aside these two processes (breaker-induced mixing and shear dispersion), Clark et al. (2010) suggested that the primary mechanism driving surfzone mixing is due to surfzone eddies and transient rip currents. This finding was consistent with both earlier and later studies (Spydell

[10] See cushman.host.dartmouth.edu/courses/engs151/EFM-Rivers-ShearDispersion.pdf, consulted on September 5, 2024

& Feddersen, 2009; Hally-Rosendahl & Feddersen, 2016; Suanda & Feddersen, 2015), and to what is known about bathymetric rip currents (Brown et al., 2015). Clark et al. (2010) also used a mixing-length scaling as $\kappa_{xx} = \alpha\overline{\mathcal{V}_{\text{rot}}}L_{SZ}$, where $\overline{\mathcal{V}_{\text{rot}}}$ is the surfzone-averaged horizontal rotational velocity scale, and α is a constant expected to be < 1, analogous to Von Karman's constant for wall-bounded shear flows. They found that surfzone diffusivity was well explain by this scaling (correlation of $r^2 = 0.59$ and intensity ratio between model and data < 1), and concluded that eddies were the primary mixing mechanism in this configuration.

Nevertheless, while they expected these eddies to be in the VLF range ($\overline{\mathcal{V}_{\text{rot}}^{\text{VLF}}}$), the highest correlation was actually found within the IG range ($\overline{\mathcal{V}_{\text{rot}}^{\text{IG}}}$). This eddy intensity at IG frequencies could not be found in Boussinesq model simulations of observed field experiments. These results thus suggest that surfzone mixing is mainly driven by eddies at a relatively high frequency (in the IG range), which are not represented in Boussinesq models.

Using numerical solutions, Spydell (2016) found that cross-shore diffusivity may also be reduced by longshore drift, with maximum diffusivity κ being parameterized as:

$$\kappa = \frac{\kappa_0}{1 + \alpha^2(V - C)^2} \tag{I.48}$$

where κ_0 is the maximum diffusivity for shore-normal waves, α is approximately 3.1 $\text{s} \cdot \text{m}^{-1}$, V is the mean longshore current, and C is the eddy propagation velocity.

Using the idea of a rotational exchange velocity U_{ex}, similar to the rotational velocity scale $\overline{\mathcal{V}_{\text{rot}}}$, Suanda and Feddersen (2015) derived a self-similar relationship scaling for flash rip-driven cross-shore exchange:

$$\frac{U_{ex}}{\sqrt{gh_b}} = 0.029\sigma_{\theta b}(1 + 70S_b) \tag{I.49}$$

with h_b the water depth, $\sigma_{\theta b}$ the directional spread, and S_b the wave steepness at the breaking point b.

All the results provided earlier were assessed using relatively small space-time domains. For instance, dye releases studied by Clark et al. (2010) were confined to the surf zone and limited in duration to less than 2 hours. More recent studies have enabled visualization of tracer dispersion on a larger scale, such as the IB09 campaign (Hally-Rosendahl et al., 2014, 2015; Hally-Rosendahl & Feddersen, 2016), which combined aerial and *in situ* observations to track dye plumes over distances of several kilometers. Hally-Rosendahl et al. (2015) highlighted the

complexity of surf-shelf exchanges, while estimating an exchange velocity of 0.012 $\mathrm{m} \cdot \mathrm{s}^{-1}$.

I.5 Evolution of modeling tools

Several approaches are used to model the processes under examination. Two main distinctions can be made. One concerns wave-averaged and wave-resolving models, and the other concerns depth-averaged (2D) and three-dimensional (3D) models. An overview of existing models is given below.

I.5.1 Wave-averaged models

As explained earlier, this type of model operates similarly to Reynolds decomposition by separating the flow into a slow, wave-averaged component and a fast component: $u = \overline{u} + \tilde{u}$. The origins of wave-averaged models can be traced back to the initial derivation of radiation stress (see I.3.1 and Longuet-Higgins & Stewart, 1962, 1964). This method enabled the first assessment of nearshore dynamics, i.e., wave set-up, bathymetric rip currents, and longshore drift. However, the radiation stress approach is only strictly valid for 2D equations and attempts to extend it to 3D equations have not been very successful.

A more successful approach was given by the Craik-Leibovich VF[11] formalism, based on an Helmholtz decomposition of the advection terms in the equations of motion. Following this approach, McWilliams et al. (2004) proposed an asymptotic theory to derive Eulerian wave-averaged equations for mass, momentum, and tracers. These equations contain terms for wave-current interactions, which are separated into conservative terms (vortex force and Bernoulli head) and non-conservative terms (wave breaking acceleration, wave-enhanced turbulent mixing, bottom drag, bottom streaming). The successful implementation of the VF formalism in various models (Uchiyama et al., 2009; Kumar et al., 2012; Zheng et al., 2017) has made it a favored approach in the 3D coastal modeling community.

In both approaches, there is a two way coupling, where the mean flow is first modified by wave forcing – known as WEC[12] –, and then feeds back to the wave field – CEW[13]. For some time, CEW was considered negligible because current velocity is much lower than wave phase

[11] Vortex Force
[12] Wave Effect on Currents
[13] Current Effect on Waves

speed, so many studies assumed one-way coupling (e.g. Özkan-Haller & Kirby, 1999). However, recent studies have highlighted the importance of current feedback on waves (e.g. Weir et al., 2011; Özkan-Haller & Li, 2003; Marchesiello et al., 2015).

Several 3D wave-averaged models exists, including:

- COAWST[14], coupling the ocean circulation model ROMS with SWAN wave model (e.g. Kumar et al., 2012);
- Delft3D, coupled with SWAN[15] (Roelvink & Banning, 1995);
- The wave-averaged version of CROCO, coupled with the spectral wave model WW3[16] or a simpler monochromatic model called WKB (e.g. Marchesiello et al., 2015)

Wave-averaged models have the advantage of a relatively low computational cost and can provide insightful information for nearshore processes, but are inadequate when studying transient rips as they do not explicitly resolve individual wave crests.

I.5.2 Boussinesq-type wave-resolving models

Wave-resolving models, on the contrary, resolve explicitly each individual wave, allowing for the generation of vorticity in the surf zone. Boussinesq models, assuming weakly dispersive waves, belong to this class. Although the ability of these models, derived from potential flow theory, to represent vorticity has been questioned (Gobbi et al., 2001), they have demonstrated their ability to generate transient rip currents. Numerical applications were too expensive until the recent explosion in computing power, when the scientific community was able to exploit their capabilities to the full.

The assumptions of initial Boussinesq models were the following:

$$\delta = \frac{a_0}{h_0} \ll 1 \qquad \text{for weak non-linearity} \tag{I.50}$$

$$\mu = \frac{h_0}{\lambda_0} \ll 1 \qquad \text{for weak dispersion} \tag{I.51}$$

[14] Coupled Ocean-Atmosphere-Wave-Sediment Transport
[15] Simulating WAves Nearshore
[16] Wave Watch III

where a_0, λ_0 and h_0 are respectively the wave amplitude, the wavelength and the water depth in deep water. Initially, Boussinesq models were valid only at orders smaller than the leading order effects of non-linearity $\mathcal{O}(\delta)$ and dispersion $\mathcal{O}(\mu^2)$. The weak non-linearity assumption was gradually reduced, until the apparition of fully non-linear Boussinesq-type models (e.g. Nwogu, 1993; Wei et al., 1995; Bonneton et al., 2011)[17].

Similarly, more dispersive Boussinesq-type models can be derived. Noting that $\mu = kh$, by performing a Taylor expansion of the linear wave dispersion relation at the shallow water limit $kh \to 0$, we obtain:

$$\omega^2 h = gkh \tanh kh = gkh \left(kh - \frac{1}{3}(kh)^3 + \frac{2}{15}(kh)^5 + \cdots \right) \tag{I.52}$$

Various sets of equations can then be derived depending on the desired degree of dispersion, e.g.:

- The non-linear shallow water equations with $\omega^2 = ghk^2$;
- The weakly dispersive Boussinesq equations with $\omega^2 = ghk^2 \left(1 - \frac{1}{3}(kh)^2\right)$.

A typical Boussinesq-type model for u taken here as the depth-averaged cross-shore velocity[18] is:

$$\frac{\partial \eta}{\partial t} + \nabla \cdot (h + \eta) u = 0 \tag{I.53}$$

$$\frac{\partial u}{\partial t} + u \cdot \nabla u + \nabla \eta + \mu^2 (V_1 + V_2 + V_3) = \mathcal{O}(\mu^4) \tag{I.54}$$

with (V_1, V_2, V_3) the dispersive effects accounting for the vertical structure of the velocity field and the non-hydrostatic correction to the wave-induced pressure field.

Typical Boussinesq models applied to nearshore modeling are :

- FUNWAVE-TVD, high order and fully nonlinear (Shi et al., 2012), an improved version of the original FUNWAVE model developed in Delaware (Wei & Kirby, 1995). It is briefly described in Chapter II;
- funwaveC, similar to FUNWAVE-TVD, with developments from Scripps, particularly in tracer modeling (Feddersen, 2007; Feddersen et al., 2011);

[17] We therefore refer to these models as "Boussinesq-type", as they do not formally correspond to the equations originally derived by Joseph Boussinesq.
[18] Note that the cross-shore velocity u may either represent a depth-averaged field (Peregrine, 1967) or a value at a reference depth (Nwogu, 1993).

- BOSZ[19], developed initially in Hawaii (Roeber et al., 2010), and expressed in conservative form, with a growing interest on optimization to reduce computational cost.

These models are widely used, especially for the study of flash rips and tracer dispersion (e.g. Hally-Rosendahl & Feddersen, 2016; Clark et al., 2011; Feddersen et al., 2011). They are often used beyond their natural limits (Gobbi et al., 2001), while improvements can drastically increase their complexity and cost (Gobbi et al., 2000). A review of these models can be found in Brocchini (2013); Kirby (2016, 2017). More recently, Marchesiello et al. (2021) has also suggested that all Boussinesq-type models, due to their 2D nature, may overestimate the kinetic energy of surfzone eddies emerging through the 2D inverse cascade. This would explain the evidence of strong overestimation of VLF energy found in previous studies (Feddersen et al., 2011; Clark et al., 2011; Kirby & Derakhti, 2019).

I.5.3 3D wave-resolving RANS models

Thanks to the steady increase in computing power, a new class of models has been introduced over the last two decades, with the aim of offering a solution to the drawbacks of Boussinesq-type models, linked to assumptions on the absence of vertical variation. 3D non-hydrostatic, free-surface, wave-resolving models are designed to solve the full RANS[20] equations, while relying on closure models for breaker-induced turbulence. Early developments started at the beginning of the 21th century (e.g. Lynett & Liu, 2004) and operational models, such as NHWAVE[21] (Ma et al., 2012; Derakhti et al., 2016) or SWASH[22] (Zijlema et al., 2011), were made available during the last decade. CROCO, in its non-hydrostatic version, is another member of this class (Marchesiello et al., 2021).

RANS models deal with frequency dispersion through the resolution of multiple vertical layers (three or four layers appear to provide satisfactory results), while Boussinesq-type models rely on high-order derivatives (Zijlema & Stelling, 2008). The absence of high-order derivatives in RANS models is an advantage for the simplicity of numerical discretization. However, RANS models generally rely on a global Poisson solver for non-hydrostatic pressure correction, that is particularly difficult to optimize on multiprocessors (with parallelization requiring

[19] Boussinesq Ocean and Surf Zone
[20] Reynolds-Averaged Navier-Stokes
[21] Non-Hydrostatic WAVE
[22] Simulating WAves till Shore

subdomain decomposition). CROCO's use of a pseudo-compressible approach (Auclair et al., 2018; Marchesiello et al., 2021) gets around this problem, as all calculations are local in this case. Another advantage of the pseudo-compressible approach is that the surface non-hydrostatic pressure condition is straightforward in this case. Details of CROCO are given later (see Chapter II). Note that the advantage given by local computation in the pseudo-compressibility approach of Auclair et al. (2018) has inspired some equivalent attempts for Boussinesq-type models (Richard, 2021; Bonnet-Ben Dhia et al., 2021).

The ability to resolve vertical variations in the RANS approach has another direct effect on currents in the surf zone, as a surface break can generate strong vertical shear in the undertow. This has been shown to have fundamental effects on surfzone eddies in Marchesiello et al. (2021), and will be the focus of the present study, with regard to tracer dispersion.

Wave breaking is also handled differently in RANS model. The onset of wave breaking is naturally addressed via numerical advection schemes (Smit et al., 2013, 2014), and does not need a criterion-based breaking formulation as in 2D models. More details on RANS models for the nearshore zone, especially CROCO, are provided in Chapter II.

I.5.4 Turbulence-resolving LES models

The most comprehensive class of models available to study nearshore dynamics is turbulence-resolving models, typically relying on eulerian LES[23] implementations, or even gridless Lagrangian schemes such as SPH[24] models. These models are able to resolve the overturning of a plunging wave and provide insightful information about the breaking of single waves (see e.g. Watanabe et al., 2005; Lubin & Chanson, 2017; Lubin & Glockner, 2015). However, LES models are extremely computationally expensive and are currently limited to single waves. In addition, they lose an advantage over free-surface models, where the water surface is always well identified and its boundary condition easier to define.

For more insight on the progress of models for nearshore dynamics, the reader is referred to Contardo et al. (2020); Kirby (2017); Brocchini (2013).

[23] Large-Eddy Simulation
[24] Smooth-Particle Hydrodynamics

Chapter II

Material & Methods

All models are wrong, but some are useful.

George E.P. Box

Contents

II.1 CROCO: a 3D free-surface, non-hydrostatic, wave-resolving model

CROCO[1] is a circulation model developed from the ROMS[2] family (Shchepetkin & McWilliams, 2005) by a consortium of French agencies (IRD, CNRS, SHOM, IFREMER, and INRIA) working in environmental sciences and applied mathematics. CROCO is designed for regional and coastal applications, with a specific focus on linking fine and larger scales. It offers a wide range of capabilities, including ocean-wave-atmosphere coupling, grid refinement (with AGRIF library), marine sediment and biogeochemistry models, turbulence closure models, and a dedicated I/O server (XIOS). In addition, CROCO benefits from high-performance computing and high-order discretization inherited from ROMS and continuously developed.

Recently, an extension of CROCO to a non-hydrostatic, non-Boussinesq version has been proposed on the basis of a pseudo-compressible solver (Auclair et al., 2018), and applied to nearshore wave resolution. (Marchesiello et al., 2021). As a free surface model, CROCO belongs to the same class as other 3D wave resolution models, such as NHWAVE (Derakhti et al., 2016) and SWASH (Zijlema et al., 2011). These models, as described in Chapter I, treat free surface elevation as a scalar (only one free-surface value is allowed at each horizontal location), meaning that explicit wave overturning is excluded during wave breaking, which is instead parameterized using turbulence closure models. Here, we provide a detailed description of the non-hydrostatic version of CROCO. Other versions, such as the wave-averaged equations or the hydrostatic (primitive) equations, are not covered in this section. For further information, readers can refer to the comprehensive CROCO documentation[3].

II.1.1 Navier-Stokes compressible equations

The complete Navier–Stokes equations for a free-surface ocean are explicitly integrated in CROCO's nonhydrostatic, non-Boussinesq (compressible) version, which is built upon ROMS primitive equations. In this compressible approach (Auclair et al., 2018; Hilt et al., 2020; Marchesiello et al., 2021), acoustic waves are solved explicitly to prevent the Boussinesq

[1] Coastal and Regional Ocean COmmunity
[2] Regional Ocean Modeling System
[3] Available online at croco-ocean.gitlabpages.inria.fr/croco_doc/index.html

degeneracy, which would otherwise lead to a 3D Poisson system for nonhydrostatic incompressible equations — a drawback in terms of computational cost, particularly related to parallelization efficiency, and numerical accuracy in the implementation of a free-surface and terrain-following model. The non-Boussinesq equations include the momentum and continuity equations, the surface kinematic condition (for the free surface), the conservation equations for heat, salt, or other tracers, and the equation of state, expressed in Cartesian coordinates as follows:

$$\frac{\partial \rho u}{\partial t} = -\overrightarrow{\nabla} \cdot (\rho \mathbf{u} u) + \rho f v - \rho \tilde{f} w - \frac{\partial P}{\partial x} + \mathcal{F}_u + \mathcal{D}_u + \lambda \frac{\partial \overrightarrow{\nabla} \cdot \mathbf{u}}{\partial x} \tag{II.1}$$

$$\frac{\partial \rho v}{\partial t} = -\overrightarrow{\nabla} \cdot (\rho \mathbf{u} v) - \rho f u - \frac{\partial P}{\partial y} + \mathcal{F}_v + \mathcal{D}_v + \lambda \frac{\partial \overrightarrow{\nabla} \cdot \mathbf{u}}{\partial y} \tag{II.2}$$

$$\frac{\partial \rho w}{\partial t} = -\overrightarrow{\nabla} \cdot (\rho \mathbf{u} w) + \rho \tilde{f} u - \frac{\partial P}{\partial z} - \rho g + \mathcal{F}_w + \mathcal{D}_w + \lambda \frac{\partial \overrightarrow{\nabla} \cdot \mathbf{u}}{\partial z} \tag{II.3}$$

$$\frac{\partial \rho}{\partial t} = -\overrightarrow{\nabla} \cdot (\rho \mathbf{u}) \tag{II.4}$$

$$\frac{\partial \eta}{\partial t} = \ w_f|_{z=\eta} - \mathbf{u}|_{z=\eta} . \overrightarrow{\nabla} \eta \tag{II.5}$$

$$\frac{\partial \rho C}{\partial t} = -\overrightarrow{\nabla} \cdot (\rho \mathbf{u} C) + \mathcal{F}_C + \mathcal{D}_C \tag{II.6}$$

$\mathbf{u} = (u, v, w)$ is the vector velocity with (x, y, z) components; η is the free surface; P the total pressure; ρ the density; $f(x, y)$ and $\tilde{f}(x, y)$ are the traditional and non-traditional Coriolis parameters, function of latitude; g is acceleration of gravity; $\mathcal{D}_u, \mathcal{D}_v, \mathcal{D}_C$ are eddy-diffusion terms requiring second-moment turbulence closure models; $\mathcal{F}_u, \mathcal{F}_v, \mathcal{F}_C$ are forcing terms; λ is the second (bulk) viscosity, associated with compressibility (used to damp acoustic waves).

II.1.2 Time-splitting principle

As we consider non-hydrostatic equations, a relationship between ρ (density) and P (pressure) must be established. The dynamics are separated into fast and slow modes through a first-order linear decomposition of the total pressure. Subscripts s and f refer to the slow and fast modes,

Box II.1
Model approximations

• **Hydrostatic approximation:** Vertical accelerations are small compared to gravitational forces. Therefore the vertical momentum equation is $\partial p/\partial z = -\rho g$.

• **Boussinesq approximation:** Under the Boussinesq approximation, the variations in density are considered negligible except for the buoyancy term: density variations only affect the gravitational force term and the continuity equation is $\overrightarrow{\nabla} \cdot \mathbf{u} = 0$.

• **Non-Boussinesq approach:** When relaxing both hydrostatic and Boussinesq approximations, the fluid is considered compressible as density variations impact all equations, momentum and continuity. The continuity equation then reads $\partial\rho/\partial t + \overrightarrow{\nabla} \cdot \rho\mathbf{u} = 0$.

respectively. The decomposition is expressed as follows:

$$\rho = \rho_s(T, S, P_s) + \underbrace{\left.\frac{\partial \rho}{\partial P}\right|_{T,S} \delta P}_{\rho_f = c_s^{-2} P_f} + \mathcal{O}(\delta P^2) \tag{II.7}$$

$$P = \underbrace{P_{atm} + \int_z^\eta (\rho_s - \rho_0) g dz'}_{\text{Slow}} + \underbrace{\rho_0 g(\eta z) + \overbrace{\delta P}^{P_f}}_{\text{Fast}} \tag{II.8}$$

with c_s representing the speed of sound and $\delta_P = P_f$, the non-hydrostatic pressure.

As in ROMS primitive equations (PE), the Navier-Stokes equations are integrated using two different time steps. The slow-mode integration is similar to ROMS, with the inclusion of the slow part of the vertical momentum equation. The fast-mode integration handles the compressible terms, in addition to the barotropic (depth-averaged or external) mode inherited from ROMS. In vector form, the governing equations can be expressed as:

$$\begin{aligned} \frac{\partial \rho \mathbf{u}}{\partial t} = & \underbrace{-\overrightarrow{\nabla} \cdot (\rho \mathbf{u} \otimes \mathbf{u}) - 2\rho \overrightarrow{\Omega} \times \mathbf{u} - \overrightarrow{\nabla} \left[\int_z^{\eta_f} (\rho_s - \rho_0) g dz' \right] + \overrightarrow{\mathcal{F}_\mathbf{u}} + \overrightarrow{\mathcal{D}_\mathbf{u}}}_{\text{Slow}} \\ & \underbrace{- \rho_0 g \overrightarrow{\nabla} \eta_f - \overrightarrow{\nabla} P_f + \rho_f \overrightarrow{g} + \lambda \overrightarrow{\nabla} (\overrightarrow{\nabla} \cdot \mathbf{u})}_{\text{Fast}} \end{aligned} \tag{II.9}$$

$$\frac{\partial \rho_f}{\partial t} = -\frac{\partial \rho_s}{\partial t} - \overrightarrow{\nabla} \cdot (\rho \mathbf{u}) \tag{II.10}$$

$$P_f = c_s^2 \rho_f \tag{II.11}$$

$$\frac{\partial \eta_f}{\partial t} = w_f|_{z=\eta} - \mathbf{u}_f|_{z=\eta} \cdot \overrightarrow{\nabla} \eta_f \tag{II.12}$$

$$\frac{\partial \rho C_s}{\partial t} = -\overrightarrow{\nabla} \cdot (\rho \mathbf{u} C_s) + \mathcal{F}_C + \mathcal{D}_C \tag{II.13}$$

$$\rho_s = \rho(T_s, S_s, \eta_f) \tag{II.14}$$

$$\rho = \rho_s + \rho_f \tag{II.15}$$

The slow part of the equation includes advection, Coriolis force, baroclinic pressure force, and viscous dissipation, while the fast part comprises the terms of barotropic and acoustic modes, i.e., surface-induced and compressible pressure forces, weight, and dissipation related to bulk viscosity. During integration, the slow part is held constant while the fast part is computed, then feedbacks to the slow part, which is integrated with larger time step. This approach helps reduce the computational cost of the compressible version. More details can be found in Auclair et al. (2018). However, Auclair et al. (2018) originally used three separate time steps for internal (baroclinic), external (barotropic) and acoustic modes. This has been simplified in CROCO, by solving the acoustic and external modes together, since the speed of sound can be artificially modified in practice.

The speed of sound, c_s, can be reduced to relax the CFL[4] constraint for the resolution of fast acoustic waves. Although this may introduce bias in high-frequency processes, it does not affect the lower-frequency non-hydrostatic dynamics of interest. This pseudo-compressibility technique significantly reduces computational time: Marchesiello et al. (2021) found that decreasing c_s from $c_s = 1500$ m.s^{-1} to $c_s = 200$ m.s^{-1} halved the computational time while maintaining the physical accuracy of the solution. We found that the same result is achieved with c_s as low as 100 or even 50 m.s^{-1}.

II.1.3 Numerics and boundaries

CROCO is discretized on an Arakawa C-grid using finite-difference methods (Shchepetkin & McWilliams, 2005; Soufflet et al., 2016). The slow-mode time-stepping is handled by a Leapfrog Adams-Moulton predictor-corrector scheme, while the fast-mode time-stepping uses a generalized third-order accurate forward-backward scheme. Horizontal and vertical advection are solved

[4] Courant-Friedrich-Levy

Box II.2
WENO schemes

The WENO5 scheme is a 5th-order numerical scheme used to solve hyperbolic partial differential equations. It is specially designed to deal with shocks and discontinuities, while maintaining high accuracy in smooth regions. WENO5 achieves this by combining multiple stencils and assigning weights based on the local smoothness of the solution. Stencils that exhibit high smoothness receive greater weights, whereas those that encompass discontinuities are assigned lower weights. As a result, the scheme adaptively reduces its order near shocks to prevent oscillations, while preserving high-order accuracy in regions where the solution is smooth.

using a WENO5[5] scheme (Borges et al., 2008), which is well-suited for handling shocks like breaking waves. CROCO is parallelized using MPI (and OPENMP for the PE version).

Different types of boundaries are implemented. For a beach configuration, periodic boundaries are generally adequate to handle the lateral boundaries normal to shore. For the offshore boundary, open boundary conditions are available (Marchesiello et al., 2001). For the waterline, CROCO uses the robust wetting and drying scheme of Warner et al. (2013) to simulate the shoreline evolution in coastal and estuarine environments, especially for realistic modeling of tidal flats, intertidal zones, and coastal floodplains. This scheme is essential to us for accurately capturing the transition between submerged and exposed states in the swash zone. The scheme is based on a critical water depth (D_{crit}), below which a cell is considered dry. At each time step, the total water depth (D) is calculated as the sum of the bathymetry (h) and the free surface elevation (η): $D = h + \eta$. Cells where $D < D_{\text{crit}}$ are marked as dry, and outward (not inward) horizontal velocities are set to zero to prevent negative water depths, thus ensuring numerical stability.

II.1.4 Turbulence closure

Vertical mixing can be parameterized in various ways in CROCO, ranging from simple fixed values to KPP[6] method, the Smagorinsky model, or the two-equation turbulence closure family of the GLS[7] method . In our case, turbulence is modeled by a $k-\omega$ model (Wilcox, 2008) within the GLS framework. This scheme solves the closure equations for turbulent kinetic energy (k) and dissipation rate (ω), with $\omega \propto \epsilon k^{-1}$ (Warner et al., 2005; Marchesiello & Treillou, 2023). In

[5] Weighted Essentially Non-Oscillatory scheme at 5th order
[6] K-Profile Parametrization
[7] Generic Length Scale

the absence of buoyancy forcing, the turbulence equations are balanced by terms representing shear production, dissipation, transport, and diffusion:

$$\frac{\partial \rho k}{\partial t} = -\overrightarrow{\nabla} \cdot (\rho \mathbf{u} k) + D_k + \rho(P - \epsilon) \tag{II.16}$$

$$\frac{\partial \rho \omega}{\partial t} = -\overrightarrow{\nabla} \cdot (\rho \mathbf{u} \omega) + D_\omega + \rho \frac{\omega}{k}(c_{\omega 1} P - c_{\omega 2} \epsilon) \tag{II.17}$$

where D_k and D_ω are diffusion terms, ϵ represents the turbulent kinetic dissipation, and $c_{\omega 1}$ and $c_{\omega 2}$ are stability functions. The eddy viscosity $\nu_t = c_\mu l k^{1/2}$ is derived from these equations, with the coefficient c_μ depending on stability functions, and the mixing length $l \propto k^{3/2}\epsilon^{-1}$. A recent correction to the turbulent closure in CROCO was introduced to resolve an overmixing issue in potential flow regions (e.g., non-breaking waves on the continental shelf) caused by a linear instability in two-equation closure systems (Marchesiello & Treillou, 2023). This correction, needed to maintain stratification on the shelf, is presented in detail in Appendix 2.

II.1.5 Wavemaker corrections

The wavemaker is the main topic of Chapter III, where a coherent interference problem is addressed (Treillou et al., 2024). The reader is thus referred to Chapter III for more details on the corrections made to the wavemaker during the present study.

II.1.6 List of corrections to CROCO for nearshore applications

Here is a list of all corrections made to CROCO during my PhD, including those on the turbulence scheme and wavemaker, mentioned above.

- **Turbulence closure**

This problem, responsible for overmixing by non-breaking waves, was addressed in a publication with my advisor Patrick Marchesiello as first author (Marchesiello & Treillou, 2023), which is available in Appendix I.

- **Wavemaker**

The wavemaker, corrected for coherent interference and associated spurious rip currents, is the main subject of Chapter III.

• **Choice of time step**

Although not strictly speaking a correction, this issue is highlighted here to raise awareness. Choosing too large a time step can lead to unacceptable numerical errors in the Euler Backward implicit scheme used to resolve the acoustic mode in the vertical direction (this implicit scheme is used to avoid the stability constraint on the vertical Courant number $c_s \Delta t / \Delta z$ of an explicit scheme). With an implicit scheme, a Courant number larger than the CFL condition may not cause the simulation to blow up but can significantly degrade its accuracy. In my case, running the nearshore simulations at coarse resolution for tests (with a mesh size of 2-5 m) allowed me a greater time step with respect to CFL constraint on the explicit schemes of the model, but the implicit scheme produced an unrealistic longshore current opposed to longshore drift. Reducing the time step solved the issue, but model users should be cautious. The same problem was identified, during my study, by another PhD student using CROCO at the University of Grenoble in the case of idealized internal waves (Emilie Duval's thesis in Applied Maths, supervised by Laurent Debreu and Eric Blayo; Duval, 2022). CROCO developers are now investigating alternatives to the Euler Backward implicit scheme. Nevertheless, it should be noted that for the higher resolution simulations (< 2 m) used in this study, the implicit scheme posed no obvious problems, since the explicit schemes for horizontal motions also required a smaller time step in this case.

• **Interpolation of vertical advection velocity in WENO**

A recent improvement in CROCO involved upgrading the interpolation scheme for vertical advection velocities used in vertical advection of horizontal currents with the WENO scheme. This upgrade applied a 6^{th}-order horizontal interpolation of w to advect u and v (w is not located at the same location as u or v in a C-grid). However, numerical simulations of tank experiments revealed that using such a high-order interpolation was not necessarily the best approach for handling the wave front of breaking waves. In fact, the simpler central difference interpolation yielded significantly better results, because, as we understand it, it avoids interpolation across discontinuities, which is the very principle of the WENO method (Borges et al., 2008). These results were taken into account by the CROCO development team.

• **Open boundaries for tracers**

A code correction has been implemented to differentiate the lateral boundary conditions for tracers and momentum. Previously, when periodic boundary conditions were applied, tracers

also adhered to the periodic condition. With this correction, it is now possible to apply periodic boundary conditions for momentum – essential for the development of longshore drift – while using open boundary conditions for tracers. This allows tracers to be freely advected out of the domain at the downstream boundary, without re-injection at the upstream boundary.

- **Correction of point source implementation**

The `PSOURCE` option allows us to inject tracers and temperature as a point source. An error occurred when the flux associated with the source was negative (opposite to x direction), leading to unrealistic temperature values that often caused the simulation to blow up. This issue has been corrected in the `step3d_fast.F` routine of CROCO.

II.2 2D wave-resolving Boussinesq model: FUNWAVE-TVD

Although the main model used in this thesis is CROCO, the Boussinesq FUNWAVE-TVD model has been used on some occasions, in particular to validate CROCO's pseudo-2D approach and to assess its computational cost compared with widely used nearshore models (see Chapter IV). I will briefly describe FUNWAVE-TVD here.

FUNWAVE[8] is a Boussinesq wave model that solves the weakly dispersive and fully nonlinear depth-integrated Boussinesq equations discussed in Chapter I. FUNWAVE-TVD solves the following conservative form of the fully nonlinear Boussinesq equations (Yuan et al., 2020):

$$\frac{\partial \eta}{\partial t} + \nabla \cdot \mathbf{M} = 0 \tag{II.18}$$

$$\frac{\partial \mathbf{M}}{\partial t} + \nabla \cdot \left(\frac{\mathbf{M}\mathbf{M}}{H}\right) + gH\nabla\eta = H\left[\frac{\partial \overline{\mathbf{u}}_2}{\partial t} + \mathbf{u}_\alpha \cdot \nabla \overline{\mathbf{u}}_2 + \overline{\mathbf{u}}_2 \cdot \nabla \mathbf{u}_\alpha - \mathbf{V}_1 - \mathbf{V}_2 - \mathbf{V}_3 - \mathbf{R}\right] \tag{II.19}$$

where $H = \eta + h$ represents the total water depth, and $\mathbf{M} = H\left[\mathbf{u}_\alpha + \overline{\mathbf{u}}_2\right]$ is the horizontal volume flux. Here, $\mathbf{u}_\alpha$ is the horizontal velocity vector at the reference depth $z_\alpha = \zeta h + (1-\zeta)\eta$, with ζ a constant taken as -0.53, placing the reference water elevation at 53% of the total local depth (Kennedy et al., 2001). $\overline{\mathbf{u}}_2$ represents the depth-averaged correction of $\mathcal{O}(\mu^2)$ (see Chapter I). The vector $\mathbf{R}$ accounts for diffusive and dissipative terms (such as bottom friction or subgrid

[8] FUlly Nonlinear Boussinesq WAVE

Box II.3
TVD schemes

TVD schemes are a class of numerical methods designed to solve hyperbolic partial differential equations while preventing the introduction of non-physical oscillations in the numerical solutions, particularly near discontinuities such as shock waves or sharp gradients.

The total variation of a function represents the cumulative magnitude of its gradients across a domain. For a scalar function $u(x)$, the total variation is defined as:

$$TV(u) = \int_{-\infty}^{\infty} \left| \frac{\partial u}{\partial x} \right| dx \tag{II.20}$$

TVD schemes ensure that the total variation does not increase over time, thus avoiding the creation of spurious extrema or oscillations. A numerical scheme is considered TVD if it satisfies the condition:

$$TV(u^{n+1}) \leq TV(u^n) \tag{II.21}$$

This guarantees stability and the physical accuracy of the solution by controlling oscillations during the numerical integration process.

lateral mixing). V_1 and V_2 correspond to the dispersive Boussinesq terms as described in Shi et al. (2012), while V_3 represents the second-order effect of vertical vorticity.

FUNWAVE-TVD is implemented using a high-order MUSCL-TVD spatial scheme. TVD[9] schemes are specifically designed to prevent non-physical oscillations near shocks, making them particularly well-suited for modeling wave breaking (see Box II.3) — in comparison, WENO5 is quasi-monotonic and does not guarantee complete absence of oscillations, but it is much more accurate and in practice the WENO5-Z version of (Borges et al., 2008) generates very few oscillations. For time discretization, a third-order Strong Stability-Preserving Runge-Kutta scheme is employed. It is important to note that the time step in FUNWAVE-TVD is adaptive, adjusting based on the desired resolution and maximum velocities rather than being fixed. More details can be found in Shi et al. (2012). The model is written in Fortran 90, is open-source, and includes parallel implementation using MPI.

Breaking may be handled in two different manners. The first one follows the approach of Tonelli and Petti (2009): when the wave reaches a breaking criterion, the Boussinesq equations are degenerated into NSWE[10] i.e. the dispersive terms are set to zero. Thanks to the TVD scheme and the ability of NSWE to simulate bores and hydraulic jumps, the breaking wave is then treated as a bore. Breaking criterion is, for example, set to $\frac{\eta}{h} > 0.8$ in Yuan et al. (2020); Tonelli and Petti (2009). The second approach is Newtonian damping (Kennedy et al., 2001),

[9] Total Variation Diminishing
[10] Nonlinear Shallow Water equations

where the breaking acceleration is written as:

$$\mathbf{F}_{\mathrm{br}} = (h+\eta)^{-1}\overrightarrow{\nabla}\cdot\left[\nu_{\mathrm{br}}(h+\eta)\overrightarrow{\nabla}\mathbf{u}\right] \tag{II.22}$$

with ν_{br} the viscosity associated with breaking waves:

$$\nu_{\mathrm{br}} = B\delta^2(h+\eta)\frac{\partial\eta}{\partial t} \tag{II.23}$$

In that case, δ is a constant and B is nonzero when a certain condition is fulfilled (for instance $\partial\eta/\partial t > C_1\sqrt{gh}$). All simulations with FUNWAVE-TVD in this work use the approach of Kennedy et al. (2001), with $C_1 = 0.45$ and $C_2 = 0.35$. Note that both methods need specific criteria, tuned from laboratory experiments, at unlike full 3D models, which are valid across the entire dynamic range.

The wavemaker differs slightly from the one in CROCO, as it is implemented as a source within the domain (Wei et al., 1999). This configuration requires an additional sponge layer at the offshore boundary and therefore additional computing resources. The wavemaker was recently corrected for coherent interference by Salatin et al. (2021).

II.3 Data

Two experiments are used in this thesis: a lab experiment by Baker et al. (2023c) and a field campaign by Hally-Rosendahl and Feddersen (2016). Both experiments are specifically described in Chapter III and Chapter IV. Illustration of both experiments is provided in Figure II.1.

II.4 Diagnostics

II.4.1 Q-criterion

The Q-criterion is a widely used diagnostic in turbulence studies, facilitating the detection and identification of coherent vortical structures within a flow (Hunt et al., 1988). It is defined as:

$$Q = \frac{1}{2}\left(|\mathbf{\Omega}|^2 - |\mathbf{S}|^2\right) \tag{II.24}$$

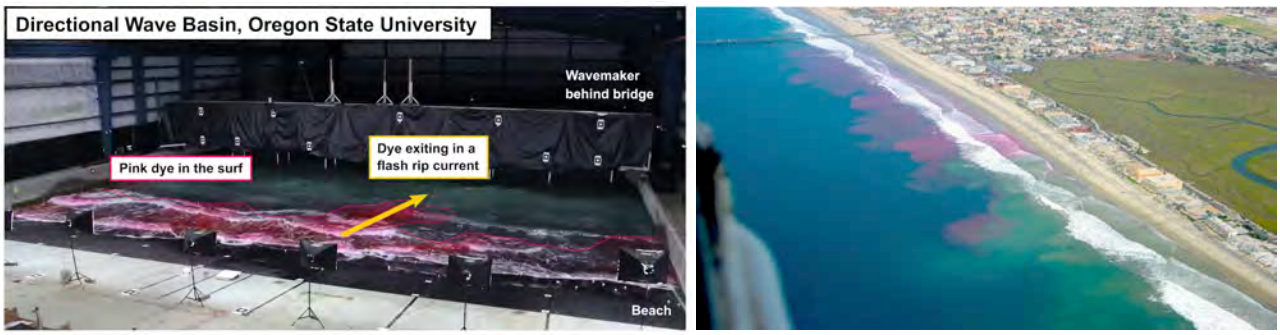

Figure II.1 Photograph of used experiments: (left) wave basin experiment, reprinted from an online outreach article of Christine Baker[a] and (right) IB09 field scale experiment, reprinted from Guza and Feddersen (2011).

[a] See https://theconversation.com/rip-currents-are-dangerous-for-swimmers-but-also-ecologically-important-heres-how-scientists-are-working-to-understand-these-rivers-of-the-sea-208922

where $\mathbf{S}$ and $\mathbf{\Omega}$ are the strain rate tensor (the symmetric part of the velocity gradient tensor) and the vorticity tensor (the antisymmetric part), respectively. These tensors are expressed as:

$$\mathbf{S} = \frac{1}{2}\left(\frac{\partial u_i}{\partial x_j} + \frac{\partial u_j}{\partial x_i}\right) \tag{II.25}$$

$$\mathbf{\Omega} = \frac{1}{2}\left(\frac{\partial u_i}{\partial x_j} - \frac{\partial u_j}{\partial x_i}\right) \tag{II.26}$$

using Einstein summation notation. When $Q > 0$, the flow is predominantly characterized by vorticity, while $Q < 0$ indicates that the strain is dominant. By visualizing Q-isosurfaces, coherent structures within the flow can be identified. This diagnostic will be employed in Chapter IV.

II.4.2 Estimation of directional spread

Using a collocated pressure sensor and bidirectional velocimeter, it is possible to derive bulk directional informations about a wave field (Herbers et al., 1999; Feddersen et al., 2011; Nuss et al., 2025). By computing the power and cross spectra of pressure (here free surface elevation η) and horizontal velocities (u and v), we obtain the lowest four Fourier moments of the directional distribution of wave energy. It yields:

$$a_1(f) = \int_{-\pi}^{\pi} \cos(\theta) S(\theta; f) d\theta = \frac{S_{\eta u}(f)}{\sqrt{S_{\eta\eta}(f)[S_{uu}(f) + S_{vv}(f)]}}$$

$$b_1(f) = \int_{-\pi}^{\pi} \sin(\theta) S(\theta; f) d\theta = \frac{S_{\eta v}(f)}{\sqrt{S_{\eta\eta}(f)[S_{uu}(f) + S_{vv}(f)]}}$$

$$a_2(f) = \int_{-\pi}^{\pi} \cos(2\theta) S(\theta; f) d\theta = \frac{S_{uu}(f) - S_{vv}(f)}{S_{uu}(f) + S_{vv}(f)} \qquad b_2(f) = \int_{-\pi}^{\pi} \sin(2\theta) S(\theta; f) d\theta = \frac{2S_{uv}(f)}{S_{uu}(f) + S_{vv}(f)}$$

with θ the wave direction; $S(\theta; f)$ the distribution of wave energy along frequency f and wave direction θ; $S_{\eta\eta}$, S_{uu} and S_{vv} the power spectra of free surface elevation, cross-shore and longshore velocities, respectively, and $S_{\eta u}$, $S_{\eta v}$ and S_{uv} the cross spectra. Energy-weighted Fourier moments $\overline{a_1}$ (Feddersen et al., 2011) are defined as:

$$\overline{a_1} = \frac{\int_{\text{swell}} a_1(f) S(f) df}{\int_{\text{swell}} S(f) df} \tag{II.27}$$

These energy-weighted Fourier moments are then used to define bulk mean wave angle and directional spread $\overline{\theta}$ and $\overline{\sigma_\theta}$ as (Kuik et al., 1988):

$$\overline{\theta}(f) = \frac{1}{2} \arctan\left(\frac{\overline{b_2}(f)}{\overline{a_2}(f)}\right) \tag{II.28}$$

$$\overline{\sigma_\theta^2} = \frac{1 - \overline{a_2}(f)\, \cos\left(2\overline{\theta}(f)\right) - \overline{b_2}(f)\, \sin\left(2\overline{\theta}(f)\right)}{2} \tag{II.29}$$

This diagnostic was used throughout the thesis to ensure that the correct directional spread was forced, especially for the problems described in Chapter III. Other types of more complex estimation, such as with EMEM or IMLM estimators, are also possible (e.g. Baker et al., 2023c).

II.4.3 Offshore extension of dye plume

In Chapter IV, we use the scalar indicator $x_{99\%}$ to estimate the seaward maximum extension of the dye plume. This represents the cross-shore position from which 99% of the tracer mass will be found on the way to the coast. It could be defined as:

$$0.99 = \frac{1}{M_T(t)} \int_{-h}^{\eta} \int_{0}^{L_y} \int_{-x_{99\%}(t)}^{0} C(x, y, z, t) dx dy dz \tag{II.30}$$

with $M_T(t) = \int_{-h}^{\eta}\int_{0}^{L_y}\int_{-Lx}^{0} C(x,y,z,t)dxdydz$ the total tracer mass at instant t and L_x,L_y the domain length in the cross-shore and longshore directions.

II.4.4 RGB analysis for dye concentration estimation

To infer dye concentration from video in the wave basin experiment by Baker et al. (2023c), we used a simple RGB analysis, allowing estimation of relative concentration. The method is described in more details in Chapter IV.

II.4.5 Characterization of turbulent cascade

Several diagnostics exist to evaluate the turbulent cascade of a given flow, providing valuable information such as injection scale or direction of the cascade (forward or inverse), as explained in Box I.12. Three are briefly summarized here.

II.4.5.1 Fourier decomposition

The spectral kinetic energy budget can be decomposed using Fourier transformation as (Marchesiello et al., 2011):

$$\begin{aligned} T(k) = & \underbrace{P(k)}_{\text{Pressure work}} + \underbrace{I(k)}_{\text{Conversion of PE to KE}} + \underbrace{A_H(k)}_{\text{Horizontal advection}} + \underbrace{A_V(k)}_{\text{Vertical advection}} \\ & + \underbrace{D_H(k)}_{\text{Lateral dissipation}} + \underbrace{D_V(k)}_{\text{Vertical dissipation}} \end{aligned} \tag{II.31}$$

with k the wavenumber. The spectral kinetic energy flux can then been expressed as:

$$\Pi_F(k) = \int_k^{k_{max}} (A_H + A_V)dk \tag{II.32}$$

For longshore uniform cases as in this thesis, it is generally convenient to consider only the advection term in v on a longshore array.

II.4.5.2 Coarse-graining method

The coarse-graining method is a method using spatial averaging to estimate kinetic energy flux (Aluie et al., 2018; Schubert et al., 2020). The velocity field $\mathbf{u} = (u, v)$ is low-pass filtered using

a convolution (typically a top-hat kernel), and the kinetic energy flux can be expressed as:

$$\Pi_{cg}(\mathbf{x}) = -\rho_0 \left[(\overline{u^2} - \overline{u}^2)\frac{\partial \overline{u}}{\partial x} + (\overline{uv} - \overline{u}\,\overline{v})(\frac{\partial \overline{u}}{\partial y} + \frac{\partial \overline{v}}{\partial x}) + (\overline{v^2} - \overline{v}^2)\frac{\partial \overline{v}}{\partial y} \right] \tag{II.33}$$

II.4.5.3 Structure functions

Structure functions of order p are statistical measures of the differences in velocity over spatial separations r that are defined as:

$$S_p(r) = \overline{[v'(y+r) - v'(y)]^p} \tag{II.34}$$

where $v' = v - \overline{v}$ is the eddy velocity field considered (here taken as alongshore velocities at a given x) and $\bar{\cdot}$ denotes a time average. Second-order structure function S_2 reflects the energy at different scales. We have $S_2 \propto r^{2/3}$ for direct and inverse cascade. Direction of the turbulent cascade is given by S_3: when $S_3 > 0$, the turbulence is consistent with a 2D inverse cascade, and with a 3D direct cascade when $S_3 < 0$. For an inverse cascade, $S_3 \propto 3/2r$ while $S_3 \propto -4/5r$ for direct cascade. For more details on structure functions for oceanic applications, the reader is referred to Baker et al. (2023b).

Chapter III

Correction of coherent interference in wave-resolving nearshore models and validation with experimental data

Les mathématiques ne sont pas une moindre immensité que la mer.

Proses philosophiques de 1860-65, Victor Hugo

Contents

III.1 Preamble

In the previous chapters, we explained the scientific background to this thesis and described its methodology. We can now turn to our objectives. The first challenge expressed in the introduction was:

- **How can we improve the realism of wave-resolving models?**

As a first answer, this Chapter is devoted to improving the wavemaker used in CROCO and other models. Specifically, an inherent problem with double-sum wavemakers, reported long ago (Jefferys, 1987; Miles & Funke, 1989), is presented and corrected. In wave-resolving models (2D or 3D), deterministic wavemakers are used to generate wave forcing at the offshore boundary or as a source function in the offshore region. Conventional wavemakers use double summation in frequency and direction, causing wave components of the same frequency but different directions to produce coherent interference. The result is spurious variations in the wave field as it approaches the beach, creating stationary rip currents of significant intensity.

In a study published in *Ocean Modelling* (Treillou et al., 2024), a solution to the coherent interference problem of double-sum wavemakers is proposed. It builds on previous work (Salatin et al., 2021; Pascal & Bryden, 2011) on single-sum wavemakers, with only one direction per frequency. For the first time, this solution is validated using experimental data in a directional wave basin (Baker et al., 2023c). The effect of coherent interference is clearly demonstrated and the correction, implemented in CROCO, is validated. The paper is reproduced below and additional material follows.

III.2 Article published in *Ocean modelling*

III.2.1 Introduction

The nearshore region, consisting of the surf zone (from shoreline to breaking point) and the inner shelf (up to approximately 20 meter depth), is a highly chaotic area, with various time and space scales interacting and coexisting with each other. Understanding the processes that govern transport and circulation in this region is of critical importance for many reasons: health issues associated with coastal pollutants (Boehm et al., 2005), safety of users exposed to drowning due to rip currents (Woodward et al., 2013), ecosystem issues associated with coastal retention or dispersal of plankton or larvae (Moulton et al., 2023; Shanks et al., 2017), and sediment transport and morphological changes (Marchesiello et al., 2022).

One of the most important processes for cross-shore exchange between the surf and shelf are rip currents. They are narrow offshore directed flow of time scale from $\mathcal{O}$(1 min) to much longer $\mathcal{O}$(1 hr) and cross-shore spatial scale $\mathcal{O}$(100 m). Rip currents are particularly important for cross-shore exchanges between the beach and the continental shelf, as they can extend seaward over a width 2 to 3 times that of the surfzone (Kumar & Feddersen, 2017c). Recent studies also underline the importance of rip currents in the shelf circulation of $\mathcal{O}$(1 km) (Wu et al., 2021). Rip currents are referred to as channeled (bathymetric) rip currents when driven by longshore variability in the bathymetry (Castelle, 2016), or transient rip currents (flash rips) when resulting from discontinuous breaking due to short crested waves (Peregrine, 1998; Clark et al., 2012; Johnson & Pattiaratchi, 2004). While channeled rip currents are relatively well understood (e.g., Marchesiello et al. 2015), flash rips are a more recent topic and are still incompletely assessed, even though they are thought to represent a large part of nearshore activity (Tang & Dalrymple, 1989).

The simulation of transient rip currents requires wave-resolving (or phase-resolving) models, which have the unambiguous ability to represent short-crested waves and associated vorticity injection into the surfzone. A necessary step in wave-resolving simulation is finding a way to force the wave field at the offshore boundary. There are three main options to do this: a wave generator at a source point inside the domain (Wei et al., 1999); a wave generator at a fixed offshore boundary point (Marchesiello et al., 2021); or a moving boundary simulating a pad (Higuera et al., 2015), but this technique is only used to generate long waves. CROCO,

the Coastal and Regional Ocean Community model used in the present study, focuses on the second method. More importantly here, regardless of the wave imposition technique, most wave-resolving models use double summation to represent a wave spectrum that distributes wave energy as a function of frequency and direction.

Double-sum wavemakers have been used extensively and helped improve our understanding of nearshore dynamics (Hally-Rosendahl et al., 2014; Suanda & Feddersen, 2015; Spydell et al., 2019). However, they suffer from a phase-locking or coherent interference phenomenon. This can be understood by considering two wave trains propagating towards the beach from different directions. These waves interfere, generating a longshore modulation of their amplitude (short-crested waves) which migrates along the beach at a speed increasing with their frequency difference (Fowler & Dalrymple, 1990). For waves of same frequency, the migration speed is zero, leaving a permanent pattern of short-crested waves (coherent interference) that always break at the same point on the beach, generating persistent rip currents in deterministic locations via more similar mechanisms to bathymetrically-driven rip currents. Coherent interference from intersecting ocean wave trains can be found in nature, e.g., resulting from reflection on a breakwater (Dalrymple, 1975; Smit & Janssen, 2013; Zhang et al., 2022). However, they tend to arise in models for nonphysical reasons, simply because of the deterministic nature of discretized wave generators. This can affect the model results in ways that are not necessarily noticed by modelers, as spurious rip currents are mixed among other rip current events.

This problem was reported long ago (Jefferys, 1987; Miles & Funke, 1989), noting the paradox of simulating a random sea state with a deterministic wavemaker. Early recommendations were to use stochastic implementations, but these models require a lot of computing time to be statistically reliable. Deterministic wavemakers therefore offer advantages, provided that wave coherence and associated stationary interference can be dealt with. A common solution is to increase the number of frequencies in the wavemaker spectrum, but this only reduces the probability of coherent interference, and is also computationally expensive. Building on previous work (Pascal & Bryden, 2011; Salatin et al., 2021), here we implement a single-sum wavemaker that is both computationally efficient and definitely devoid of coherent interference. To confirm that this is desirable in a numerical model, we validate the single-sum method for the first time with data from a directional wave basin experiment (Baker et al., 2023c). In addition, attention to energy conservation ensures that the wavemaker correction does not affect the integrity of the

physical solution, and that it accurately represents reality. We hope that our work will increase the modeling community's awareness of the coherent interference problem, and offer a simple and computationally efficient solution to resolve it.

III.2.2 Methods

III.2.2.1 The 3D wave-resolving model CROCO

CROCO is a non-hydrostatic, free-surface, terrain-following model developed around the regional oceanic modeling system (Shchepetkin & McWilliams, 2005; Debreu et al., 2012). Its capabilities include high-performance computation of high-order discretized equations and coupling with atmospheric, wave, biogeochemical, sediment and turbulence models. It has been applied to a variety of configurations, from regional and shelf circulations to very fine-scale processes, such as wave-induced nearshore circulation (Marchesiello et al., 2015, 2021, 2022). In its non-hydrostatic version, CROCO is able to resolve individual wave propagation, shoaling and breaker-induced circulation. Breaking waves are treated as bores with a shock-capturing advection scheme (WENO5), which transfers steep wave energy to the mean currents, while part of the breaking wave energy is transferred to subgrid-scale turbulence via a k-ω turbulence closure model. The latter corrects for an overmixing problem posed in the potential (irrotational) flow region of non-breaking waves (Marchesiello & Treillou, 2023), allowing stratification to be correctly included in our studies. CROCO is therefore well suited to the study of 3D nearshore dynamics and surf-shelf exchange in a rotating, stratified framework. Nonetheless, the wavemaker corrections proposed in the present study are relevant for all wave-resolving models, including the classical Boussinesq type.

III.2.2.2 Default double-sum wavemaker

The wavemaker implemented in CROCO (Marchesiello et al., 2021) forces a spectrum of 3D linear waves at the offshore boundary, much like SWASH (Zijlema et al., 2011), while Funwave (Wei et al., 1999) typically uses similar forcing but with an interior source function[1]. In all cases, the frequency and directional distribution of wave energy is discretized via a double summation (Feddersen et al., 2011). The free surface and velocities at the offshore boundary are then,

[1] FUNWAVE-TVD now has the option of a single-sum wavemaker following the study conducted by Salatin et al. (2021)

respectively, given by:

$$\eta_{bc}(y,t) = \Sigma_i^N a_i \Sigma_j^M d_j \cos(k_{y,i,j} y - \omega_i t - \phi_{i,j}) \tag{III.1}$$

$$u_{bc}(x,y,t) = \eta_{bc}(y,t)\omega_p \cos(\theta_m)\frac{\cosh(k_p(z+h))}{\sinh(k_p h)} \tag{III.2}$$

$$v_{bc}(x,y,t) = \eta_{bc}(y,t)\omega_p \sin(\theta_m)\frac{\cosh(k_p(z+h))}{\sinh(k_p h)} \tag{III.3}$$

where (x,y,z) are cross-shore, alongshore and vertical directions; a_i is the wave amplitude at each angular frequency ω_i from a given statistical distribution $S(\omega)$; d_j is the directional weight for wave angle θ_j from the given statistical distribution $D(\theta)$; $k_{y,i,j} = k_i \sin\theta_j$ is the alongshore wavenumber where k_i is the linear theory wavenumber: $\omega_i^2 = g\, k_i \tanh(k_i h)$ with h the water depth; θ_m is the mean wave angle; ω_p and k_p are peak frequency and wavenumber; $\phi_{i,j}$ is a uniformly distributed random phase; and N and M are respectively the number of frequencies and directions.

As described by Marchesiello et al. (2021), w_{bc} is here set to zero rather than the linear solution for w as only weak sensitivity to this choice was found. The depth-averaged (barotropic) velocities ($\overline{u}$,$\overline{v}$) are provided in the wavemaker because they are prognostic variables in our split-explicit model, advanced at the same time as the fast acoustic mode (see Marchesiello et al., 2021). The depth-averaged normal velocity $\overline{u}$ is supplemented at the boundary by an Eulerian anti-Stokes current, opposed to the Stokes drift and thus closing the mass balance. We do not directly impose the depth-averaged value of u_{bc} but the value of the incoming characteristic of the shallow water system as in Flather-type conditions (Marchesiello et al., 2001; Blayo & Debreu, 2005):

$$\overline{u} = \overline{u}_{bc} - \sqrt{\frac{g}{h}}(\eta - \eta_{bc}) \tag{III.4}$$

This allows infragravity waves generated inside the domain to propagate out as long waves, while ensuring a near conservation of mass and energy through the open boundary. Likewise, the baroclinic components (u_{bc},v_{bc},w_{bc}) are applied via an adaptive radiation condition which helps short waves and 3D flow perturbations to leave the domain with only a small effect on the

interior solution (Marchesiello et al., 2001).

In this study, the spectrum distributions is the product of a JONSWAP frequency spectrum $S(\omega)$ (Goda, 2000) and a Gaussian-type directional spectrum $D(\theta)$ (Feddersen et al., 2011): $S(\omega,\theta) = S(\omega) \times D(\theta)$. The JONSWAP spectrum is formulated as follows:

$$S(\omega) = H_s^2 \beta_J \omega_p^4 \omega^{-5} \exp[-1.25\omega^{-4}\omega_p^4]\gamma^r \tag{III.5}$$

H_s is the significant wave height, ω_p, the peak wave frequency, and γ^r, the peak enhancement factor, with:

$$r = \exp\left[-\frac{1}{2}\left(\frac{\omega-\omega_p}{\sigma_\omega \omega_p}\right)^2\right] \tag{III.6}$$

$$\sigma_\omega = \begin{cases} 0.07, & \text{if } \omega \leq \omega_p \\ 0.09, & \text{if } \omega > \omega_p \end{cases} \tag{III.7}$$

$$\beta_J = \frac{0.06238(1.094 - 0.01915\log\gamma)}{0.23 + 0.0336\gamma - 0.185(1.9+\gamma)^{-1}} \tag{III.8}$$

The directional spectrum around the mean direction θ_m, with directional spread σ_θ, is:

$$D(\theta) = \exp\left[-\left(\frac{\theta-\theta_m}{1.5\sigma_\theta}\right)^2\right] \tag{III.9}$$

with $\int_{\theta_{min}}^{\theta_{max}} D(\theta)d\theta = 1$ to ensure that the directional spread (σ_θ) around the mean wave angle does not affect wave energy.

III.2.2.3 Coherent interference principle

We illustrate here the principle behind coherent interference by reproducing the solution given by Fowler and Dalrymple (1990) for two wave trains propagating towards the beach with different wavenumbers and frequencies. For simplicity (and without modifying the general idea), we consider waves of same amplitude a propagating at an angle θ around the x axis normal to the coast (θ is the directional spread in this case and $\theta_m = 0$). The mean wavenumber k is along the x axis, while the difference between the wavenumbers $\Delta k = 2k\sin\theta \sim 2k\theta$ lies along the y longshore axis. Similarly, we consider that the mean frequency is ω and the frequency difference between the two wave trains is $\Delta\omega$. In this case, the wave interference solution for the free

surface η is :

$$\eta(x, y, t) = 2a \sin(kx - \omega t) \cos[0.5(\Delta k\, y - \Delta\omega\, t)] \tag{III.10}$$

The total surface elevation consists of a carrier wave (k,ω) modulated by a time-dependent envelope propagating along the coast at speed $\Delta\omega/\Delta k$. The envelope produces short crested waves of length $\lambda_c = 2\pi/\Delta k = \pi/k\theta$ — as first suggested by Longuet-Higgins 1956 and shown to apply to the more general case by comparison with experimental data (Baker et al., 2023c). Longshore envelope migration occurs when $\Delta\omega \neq 0$, i.e. the envelope is phase-shifted. In this case, waves have no persistent longshore variations (illustrated with H_s in Fig. III.1). However, if the wave trains share the same frequency ($\Delta\omega = 0$), the envelope phase is locked and the propagation speed is zero. In this case, H_s shows a pattern of nodes and antinodes along the beach (Fig. III.1), i.e. short-crested waves constantly travel towards the same location on the beach, thus creating stationary rip currents as they break.

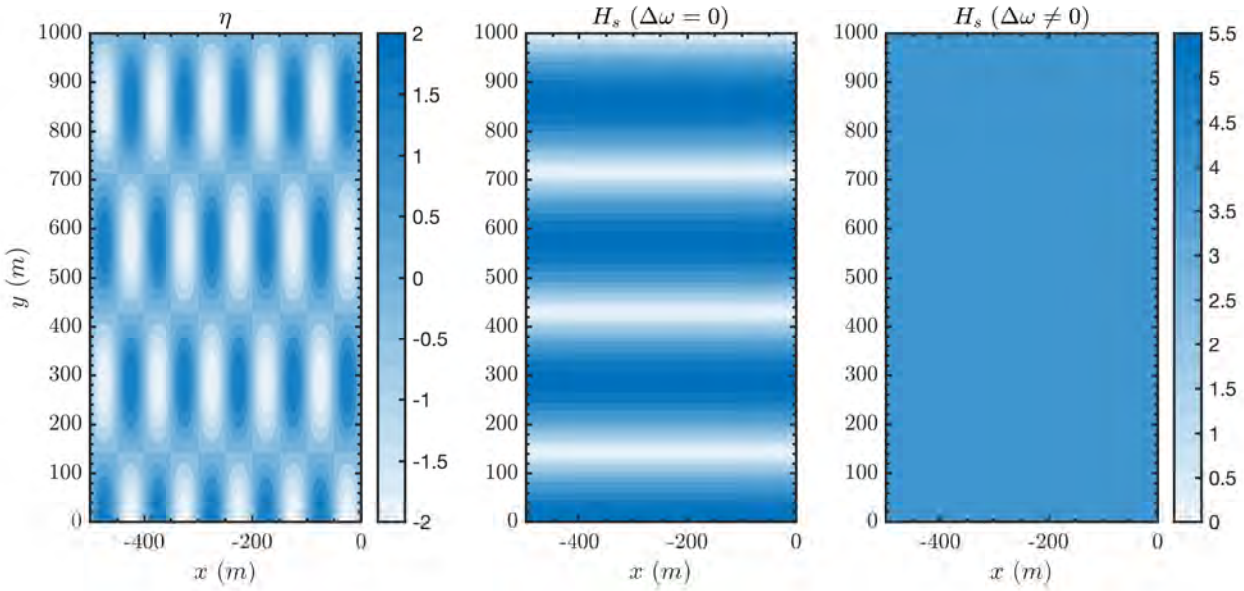

Figure III.1 Illustration of the coherent interference of two deep water wave trains propagating to the right at an angle of ±10 degrees to the x axis (amplitude 1 m, wavelength 100 m, period 10 s). The left panel shows a snapshot of surface elevation η featuring short-crested waves ∼286 m long, migrating along the y axis with a speed varying with the frequency difference $\Delta\omega$ between wave trains; the central panel shows H_s for $\Delta\omega = 0$, i.e. with no longshore migration. The right-hand panel shows the significant wave height H_s in the case where $\Delta\omega \neq 0$. In the first case, coherent interference produces a persistent H_s pattern that should create stationary rip currents as they break on the beach. In the second case, no pattern is produced and no persistent rip currents are expected.

This phenomenon is at the root of the coherent interference problem of discrete double-sum wavemakers. In the real ocean, with a continuous frequency spectrum of random waves, the

probability of phase-locking is minimal, over smooth topography at least, and generally only occurs in focal zones due to refraction, diffraction or reflection of monochromatic waves around obstacles such as breakwaters or headlands (Smit & Janssen, 2013). We will see that wave basin experiments also tend to show little coherent interference. We therefore consider the coherent interference generated by discretized double-sum wavemakers as spurious, and seek a definitive solution to avoid it by preventing the generated wave trains from sharing the same frequency. This is made possible by simple summation, presented below.

III.2.2.4 Corrected single-sum wavemaker

In order to avoid coherent waves, i.e., waves of different directions having same frequencies, a solution is presented by Salatin et al. (2021). Double-sum is converted into a single-sum wavemaker where each wave component has specific frequency and direction. Single summation was proposed before with variations in the distribution of wave components (Jefferys, 1987; Miles & Funke, 1989; Pascal & Bryden, 2011), and a useful schematic view was given in Pascal (2012). Based on this previous work, we rewrite the free-surface wave boundary condition :

$$\eta_{bc}(y,t) = \Sigma_i^{N\times M} a_i \cos(k_{y,i} y - \omega_i t - \phi_i) \tag{III.11}$$

where a_i is now the amplitude of the i-th wave component taken as:

$$a_i = \sqrt{\frac{H_s^2\, \overline{D(\theta_i)}\, S(\omega_i) d\omega}{8 \Sigma_i S(\omega_i) d\omega}} \tag{III.12}$$

which is the product of the wave amplitude $A = \sqrt{H_s^2/8}$, the square root of the normalized frequency spectrum $S(\omega)d\omega / \Sigma_i S(\omega_i) d\omega$ (with frequency resolution $d\omega$), and the square root of the normalized directional spectrum $\overline{D(\theta)}$:

$$\overline{D(\theta)} = \frac{D(\theta) \Sigma_i S(\omega_i) d\omega}{\Sigma_i^D (\theta_i) S(\omega_i) d\omega} \tag{III.13}$$

The wave angles around the mean direction are:

$$\theta_i = (-1)^i \left(-\frac{\pi}{2} + \frac{\pi}{2} \frac{i-1}{N-1} \right) + \theta_m, \tag{III.14}$$

ensuring that all wave angles are included between $-\frac{\pi}{2}$ and $\frac{\pi}{2}$.

III.2.2.5 Periodic boundary conditions

Most nearshore circulation studies use periodic alongshore boundary conditions, to allow longshore drift to develop and surfzone eddies to propagate freely. It is therefore essential that waves entering the domain satisfy these periodic conditions. Following the suggestion of Johnson and Pattiaratchi (2006), we impose that each i-th wave component satisfies the following equation:

$$k_{y,i} = k_i \sin\theta_i = \frac{2\pi p}{L_y} \tag{III.15}$$

where L_y is the domain longshore length and p an integer. This relationship guarantees that for each wave train component i (with given frequency and direction), there is an integer number of these waves projected in the longshore direction, as schematized in Fig. III.2. This is sufficient to ensure periodicity. Otherwise, shadow zones can form, where strong wave height gradients can develop, generate parasite rip currents near the boundaries and affect longshore drift.

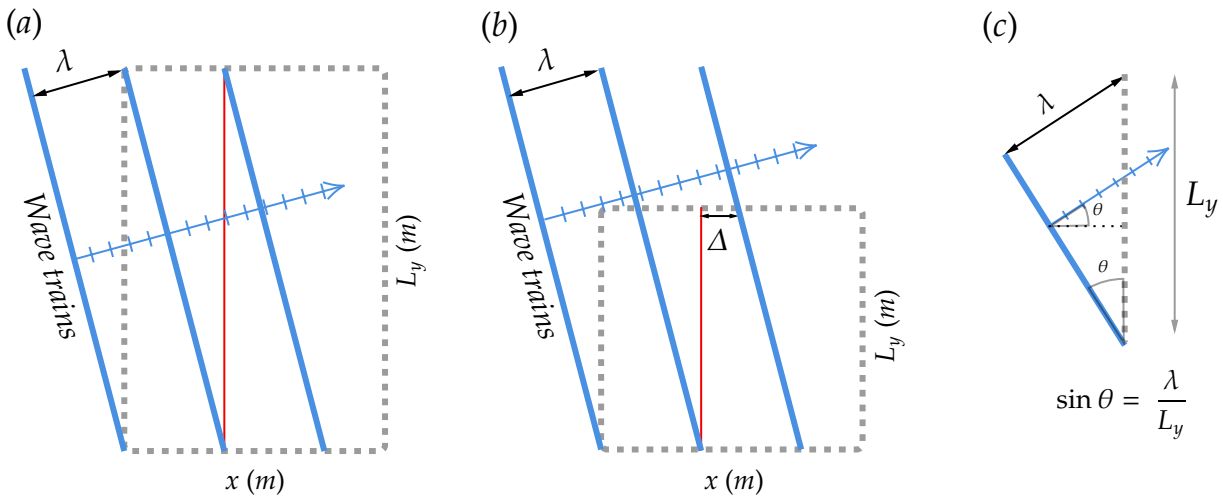

Figure III.2 Schematic view of the periodicity condition for obliquely incident long-crested waves over a finite domain. (a) the periodicity is respected by the right combination of domain length L_y and wavelength λ; (b) the domain size breaks periodicity by introducing a small gap Δ between wave crests at the northern and southern boundaries; (c) relationship linking wave direction to L_y and λ to ensure periodicity. Note that the scheme assumes only one periodic wavelength for simplicity but there can be an integer number p of smaller wavelength (the relation is then $\sin\theta = \frac{p\lambda}{L_y}$).

Periodization can be obtained by modifying the angle θ_i to satisfy Eq. III.15 :

$$\theta_i = \arcsin\left(\frac{2\pi p}{k_i L_y}\right) \tag{III.16}$$

In CROCO, the directional spectrum and associated unrestricted wave angles are first calculated. Then, all wave angles are corrected according to Eq. III.16, ensuring that the mean wave angle θ_m remains unchanged. The correction is made by selecting the integer p that produces the smallest change in θ_i (for the double-sum wavemaker, the correction is applied to all angles at each frequency). In practice, the differences between the original and corrected wave angles are relatively small and do not significantly impact the directional spectrum. All simulations presented in this article are therefore expected to respect boundary periodicity.

III.2.3 Validation with laboratory wave basin

III.2.3.1 Laboratory experiments

The data used to validate the new wavemaker comes from an experiment conducted in the Directional Wave Basin at the Oregon State University O.H. Hinsdale Wave Research Laboratory (Baker et al., 2023c). The goal of this experiment was to gain a better understanding of the processes involved in the generation of flash rips and surfzone eddies, by investigating the effect of directional spread on breaking crest length. For this purpose, a barred beach was recreated in the wave basin, respecting the surf similarity number (ratio of wave steepness to slope) of real scale beaches. A 29-board piston-type wavemaker could simulate a continuous distribution of multidirectional waves with JONSWAP frequency spectrum of width $\gamma = 3.3$. Several experiments were run for a range of different significant wave heights, peak periods and directional spreads. These experiments are of high interest to validate our wavemaker as the wave basin is large enough (48.8 m long, 26.5 m wide) to investigate longshore variation of the wave field. Each run lasted 45 minutes ($\sim$ 1350 wave periods), providing sufficiently long time series to study coherent wave interference. The free surface and velocities were measured with in situ sensors (pressure gauges, ADV[2]s, and resistance gauges). The in-situ sensors were deployed as longshore arrays: two offshore arrays, one on the inner shelf and two in the surfzone (Fig. III.3). The in-situ sensors had a frequency of 100 Hz. We refer the reader to Baker et al.

[2] Acoustic Doppler Velocimeter

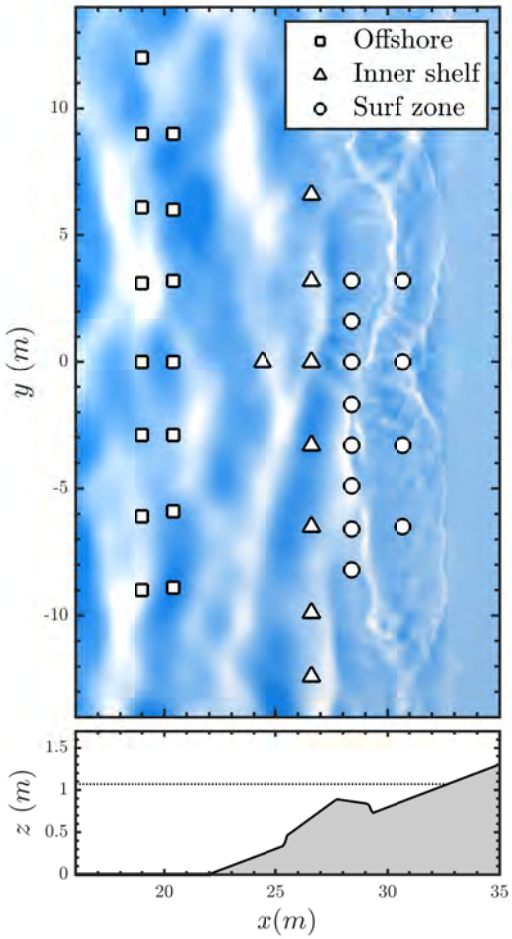

Figure III.3 (Top) Snapshot of simulated free surface elevation in the case G1d ($\sigma_\theta = 26.1°$) after 15 minutes. The stations where experimental data were collected are displayed. Squares represent offshore wire resistance gauges, triangles innershelf pressure gauges and circles surf zone pressure gauges. (Bottom) Cross-shore profile of the bathymetry (shaded) and still water level (dashed line, at 1.07 m).

(2023c) for more details about the experiment.

We focus on two experiments with low (G1a) and high (G1d) directional spread and otherwise similar bulk wave statistics (Table III.1). We use the wave conditions recorded onshore of the wavemaker rather than those theoretically imposed at the wavemaker, partly because directional errors affects the intended wave spectrum and do not, for example, allow G1a to be a truly unidirectional experiment (Baker et al., 2023c). We have verified that the two types of discretized wavemakers in the model give very similar results when directional spread is exactly zero (case

Table III.1 Significant wave height H_s, peak period T_p, mean wave angle θ_m and directional spread σ_θ for cases used in this study. H_s, T_p, θ_m and σ_θ were estimated at the offshore wave gauges and are used as wavemaker forcing conditions in the model.

Case	H_s (m)	T_p (s)	θ_m (°)	σ_θ (°)
G1a	0.28	2.1	-0.1	2.4
G1d	0.27	2.0	-3.3	26.1

G1a with σ_θ=0° gives H_s RMSE< 1mm), and that the differences in model results between the two wavemakers are due solely to directional spread.

Table III.2 Longshore standard deviation of 20-min time-averaged surface vertical vorticity (σ_{ω_z}), longshore velocity (v) and significant wave height (H_s) (see Fig. III.5) for the case G1d. RMSE between in-situ and simulations H_s for $t = 10 - 30$ min (see Fig. III.6). σ_{ω_z} and σ_v are averaged in the surfzone ($27 < x < 31$ m) while σ_{H_s} is averaged on the whole domain. The RMSE of H_s indicating the error between model and data over the whole domain is also reported.

	Single sum (50 freq.)	Double sum (50 freq.)	Double sum (300 freq.)
$\langle\sigma_{\omega_z}\rangle_{SZ}$ (s^{-1})	0.03	0.16	0.08
$\langle\sigma_v\rangle_{SZ}$ $(m.s^{-1})$	0.01	0.05	0.02
$\langle\sigma_{H_s}\rangle$ (m)	0.02	0.04	0.03
H_s RMSE (m)	0.010	0.047	0.020

Free surface model spectra ($S_{\eta\eta}$) are computed similarly to Baker et al. (2023c), using a Hanning window period of 256 s with an overlap period of 128 s and correcting for depth attenuation (frequency cutoff = 1.2 Hz) over a 20-minute time series (t = 10-30 minutes, with 10 min of spin-up). The significant wave height (H_s) is calculated as $4\sqrt{\int_{0.3}^{1.2} S_{\eta\eta}(f)df}$. Velocity spectra are computed using a Hanning window period of 256 s with an overlap period of 128 s over the same 20-minute time series. Reducing the time series by half did not significantly affect the results.

III.2.3.2 Model configuration

The alongshore-uniform bathymetry in the model is identical to the experiment (Fig. III.3), without smoothing. The position of the shoreline is time-dependent, owing to a wetting-drying scheme (Warner et al., 2013). The cross-shore and longshore domain lengths are respectively 20 m and 30 m. The horizontal resolution is $\Delta x = 0.1$ m and there are 10 vertical levels. The model time step is 0.003 s and total computed time is ∼30 min (∼900 wave periods were enough for significant results). The bottom stress is modeled as a quadratic friction using the law of the wall with roughness $z_{0,b} = 1 \times 10^{-5}$ m. Turbulent kinetic energy is solved via a $k - \omega$ turbulent closure model (Marchesiello & Treillou, 2023).

The wavemaker has a resolution of $N = 50$ frequencies and $M = 31$ directions, corresponding to default settings in FUNWAVE-TVD (Salatin et al., 2021). However, to be comparable

with studies using a larger number of frequencies, we have added an experiment with 300 frequencies for the double-sum wavemaker. This is 7% more expensive than the double-sum case with 50 frequencies, which is itself 20% more expensive than the single-sum wavemaker simulation (also with 50 frequencies). Unlike the laboratory experiment, the model's northern and southern boundaries are periodic, and the western (offshore) boundary is open to long waves. Wave-averaged and instantaneous fields are output every 12 s (corresponding to 6 peak periods) on the entire domain, while model results at specific grid points corresponding to the experimental stations are extracted at a frequency of $\sim$ 6 Hz.

III.2.3.3 Comparison of double and single sum wavemaker cases

Directional spreading produces short-crested waves, which can generate flash rips when they break in the surf zone. The G1d experiment, with its fairly large directional spread (σ_θ=26.1°), is particularly effective at generating surfzone eddies and flash rips, as illustrated by snapshots of vertical surface vorticity from the model solutions with double (50 freq.) or single-sum wavemakers (Fig. III.4). In both cases, flash rips and smaller-scale rib structures, referred to as mini-rips Marchesiello et al. (2021), can be observed in the surf zone. These rib structures with longshore scale of $\sim$1 m here and frequencies in the infragravity band are associated with 3D shear instability of the undertow.

From the snapshots alone, the difference between the two simulations could be accounted for by the stochastic nature of the eddy field rather than coherent interference, but the 20-min time-averaged fields are unambiguous (Fig. III.5 and Table III.2). No stationary vorticity pattern is present in the case of the single-sum wavemaker, as might be expected if random waves were breaking on uniform longshore bathymetry (Fig. III.5, left). However, in the case of the double-sum wavemaker, the time-averaged vorticity shows strong stationary rip currents, reminiscent of the patterns observed in the vorticity snapshot. In the case where 50 frequencies are used, the longshore standard deviation of time-averaged surfzone vorticity is 0.16 s^{-1} (see Table III.2), whereas the single-sum wavemaker gives a lower value by an order of magnitude of 0.03 s^{-1}. With 300 frequencies, the double-sum wavemaker is improved as it produces a lower longshore standard deviation of surfzone vorticity (0.08 s^{-1}), but it remains higher than that produced by the single-sum wavemaker, at a higher computational cost.

Stationary rip currents are also apparent on the longshore velocity field (Fig. III.5, middle).

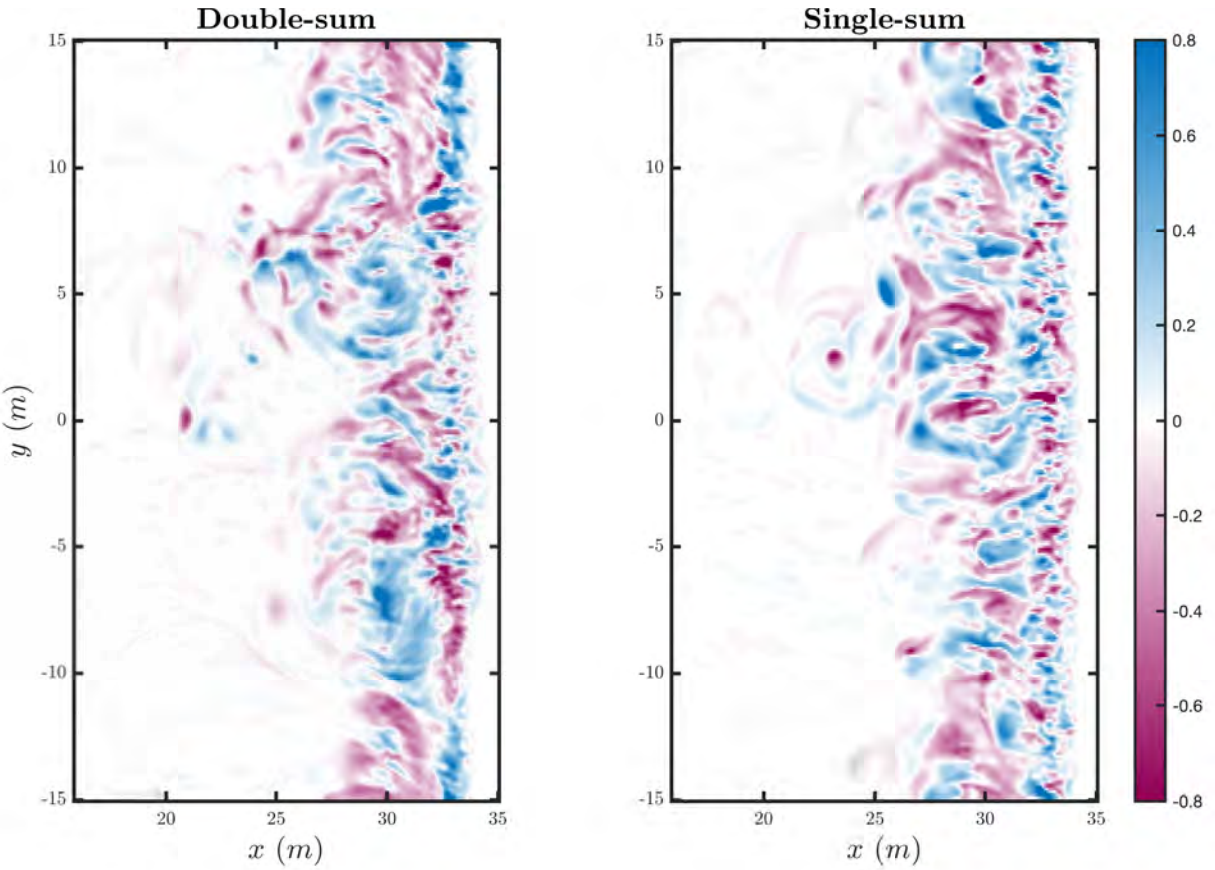

Figure III.4 Snapshot of instantaneous surface vertical vorticity ω_z (s^{-1}) for the double-sum (left, 50 freq.) and single-sum (right) wavemakers in the G1d experiment ($\sigma_\theta = 26.1°$).

With the double-sum wavemaker, the weak longshore drift expected from the mean wave angle ($\theta_m = -3.3°$) is hidden by a series of strong converging flows. These patterns are somewhat improved by the addition of wavemaker frequencies, but are much better corrected by the single-sum method, which produces a smooth mean longshore drift as expected. Note that the effect of double summation remains visible in case of weak directional spread (G1a, not shown[3]), with coherent wave-induced stationary rips that remain prominent.

Finally, we compare the significant wave height fields in Figure III.5 (right). Interestingly, the comparison between double and single wavemaker solutions has similar characteristics to the idealized case presented in Section III.2.2.3 of two wave trains with or without frequency difference. The pattern of wave height banding in the double-sum wavemaker simulations, and the absence of this banding in the single-sum wavemaker simulation, are reminiscent of the ideal patterns in Figure III.1. In both idealized and realistic cases, the coherent interference

[3] See Supporting information.

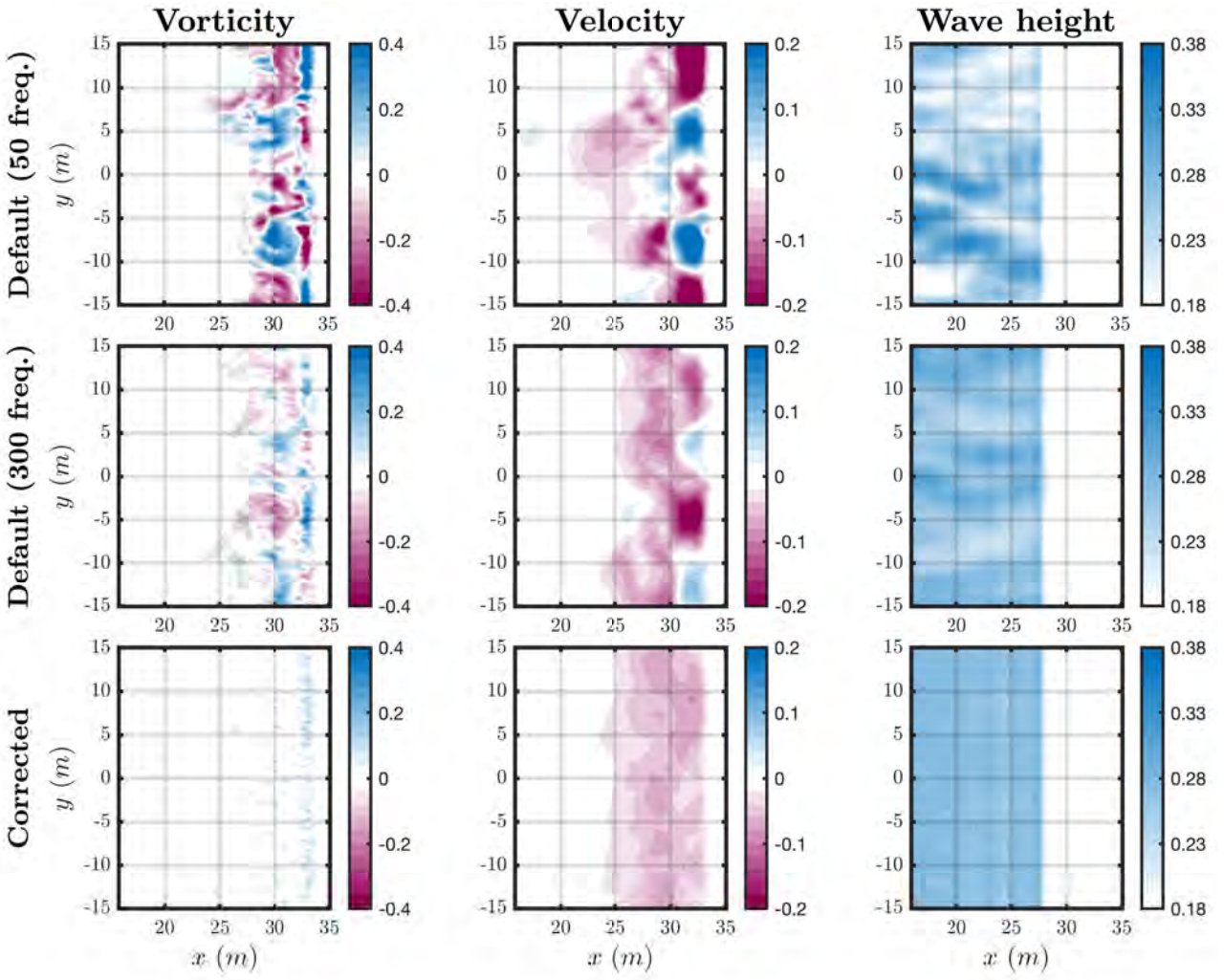

Figure III.5 Time-averaged ($t = 10 - 30$ min) surface vertical vorticity ω_z (s^{-1}, left), alongshore velocity v ($m.s^{-1}$, middle) and significant wave height H_s (m, right) for the double-sum (top: $N = 50$ freq., middle: $N = 300$ freq.) and single-sum (bottom: $N = 50$ freq.) wavemakers in the G1d case ($\sigma_\theta = 26.1°$).

associated with waves of different angles but same frequencies produces high and low H_s bands, which correlate perfectly with the persistent rip currents appearing in the vorticity and velocity fields. The single-sum wavemaker, by avoiding interference from waves of the same frequency, presents a homogeneous H_s field.

III.2.3.4 Comparison with data

A comparison between double and single wavemakers has already been carried out (Salatin et al., 2021), but no direct comparison has been made with data, and it is not clear how realistic is the idea of eliminating all coherent interference in models. In particular, we wondered whether the uncertainty inherent in the forcing frequencies of the basin experiment was sufficient to

preclude coherent interference. To answer this question, we present here a comparison between the model and the experimental data.

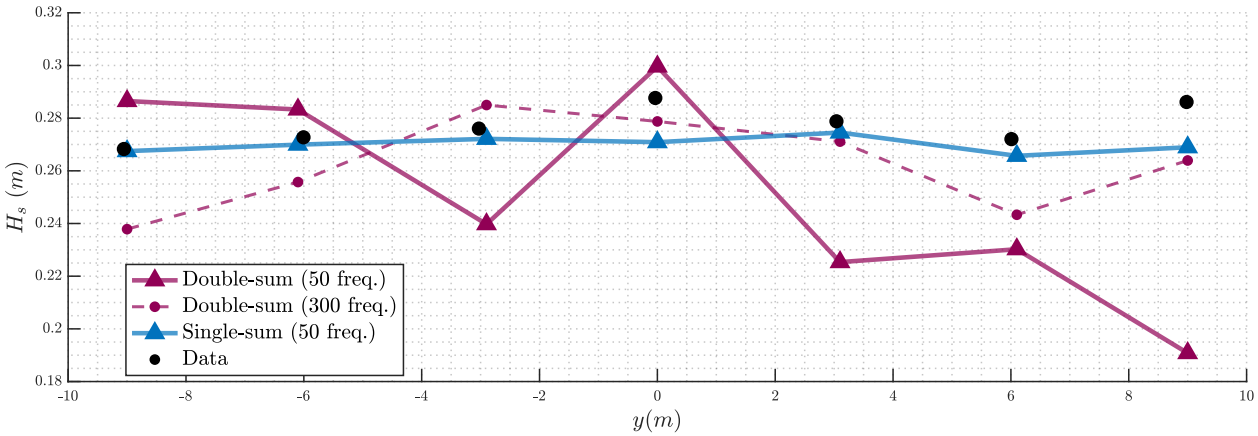

Figure III.6 Significant wave height H_s (m) for G1d ($\sigma_\theta = 26.1°$) at all offshore stations along the coast ($x = 19.0$ m, $-9 < y < 9$ m). The data (black circles) is from wave gauges and the model values from the double-sum (pink triangles for $N = 50$ freq. and pink dots for $N = 300$ freq.) and single-sum (blue triangles) wavemaker simulations computed at the same locations.

We showed in the last section that coherent interference patterns result in an alongshore-varying H_s field, that manifest as elongated cross-shore bands of highs and lows. We therefore first assess whether these signs of coherent interference are present in the data by examining H_s longshore variability. Figure III.6 shows H_s along the offshore gauges (at $x = 19$ m) in the G1d case, calculated from 20-minute time series. The experimental data show little longshore variability around the mean H_s value of 0.28 m, and present a good match with the single-sum wavemaker simulation. In contrast, the default double-sum wavemaker (with 50 frequencies) produces high longshore variability, with H_s as low as 0.19 m at some locations ($y = 9$ m), i.e. a third lower than the forcing value. The standard deviation of H_s reaches around 4 cm, compared with 2 cm for the single-sum wavemaker (in G1a, with low directional spread, the standard deviation is 0.8 cm and 0.04 cm for the double-sum and single-sum wavemakers, respectively). With 300 frequencies in G1d, the standard deviation reduces to 1.7 cm but coherent interference is still clearly present. The RMSE between the data and the single-sum wavemaker is around 1.0 cm, while it is around 4.7 cm for the 50-freq. double-sum wavemaker (with 2.0 cm with 300 freq.). It is important to note that, while laboratory experiments are prone to reflection and associated interference due to non-periodic boundaries, there is no evidence here of physical interference on the scale of that of the double-sum discretized wavemaker.

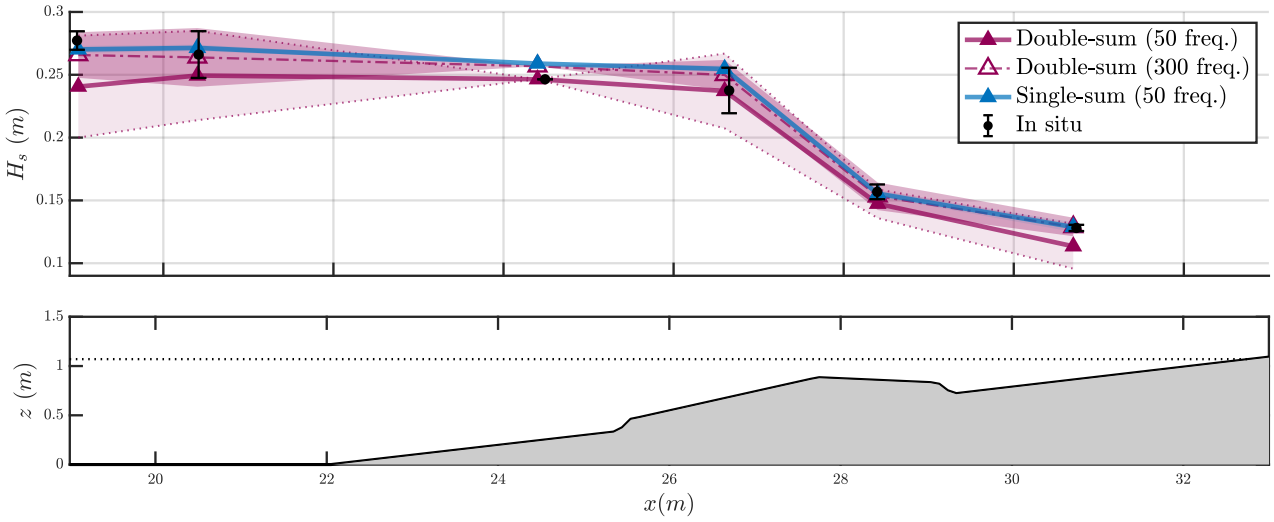

Figure III.7 (Top) Cross-shore profile of longshore and time-averaged significant wave height H_s (m) for G1d ($\sigma_\theta = 26.1°$). Comparison is made between experimental in-situ data (black dots) and the double-sum (pink solid line for $N = 50$ freq. and pink dashed line for $N = 300$ freq.) and single-sum (blue triangles) wavemaker simulations. The longshore standard deviation is shown as shaded areas for the model solutions, and as an error bar for the in-situ data. The longshore standard deviation for the double-sum (50 freq.) wavemaker simulation is enhanced with dashed fine pink line for readibility. (Bottom) Cross-shore bathymetry profile (shaded) and still water level (dashed line, at 1.07 meters).

The double-sum method not only affects longshore variability, but also the average wave energy in the domain. Figure III.7 presents a cross-shore profile of H_s averaged in the longshore direction from all sensors. Here also, the single-sum wavemaker shows an excellent match with the data over the whole profile. For the double-sum wavemaker, the coherent wave-induced H_s bands tend to cancel out when averaged alongshore, giving fairly similar cross-shore H_s profiles, but still leaving a negative bias of up to 2-3 cm (offshore stations), reduced by around half when the number of frequencies is increased to 300 (Fig. III.5).

The effect of wavemaker types on nearshore dynamics can also be assessed using power spectra (Fig. III.8 and III.9). Model and data free surface spectra $S_{\eta\eta}$ at points offshore ($x = 19$ m, $-9 < y < 9$ m) and in the outer surf zone ($x = 28.4$ m, $-8 < y < 3$ m) are shown in Figure III.8. The longshore mean and standard deviation of $S_{\eta\eta}$ are closer to the data for the single-sum wavemaker at almost all frequencies. Specifically, the spurious longshore variability for the double-sum wavemaker is far too high (the double-sum wavemaker here is with 300 freq., and the variability is even greater with 50 freq.), particularly in the low-frequency range, while the swell band is also affected, appearing noisy (Salatin et al., 2021).

The S_{uu} cross-shore velocity spectra on the innershelf (Fig. III.9) show similar differences to the free-surface spectra, with an even greater longshore standard deviation at low frequency

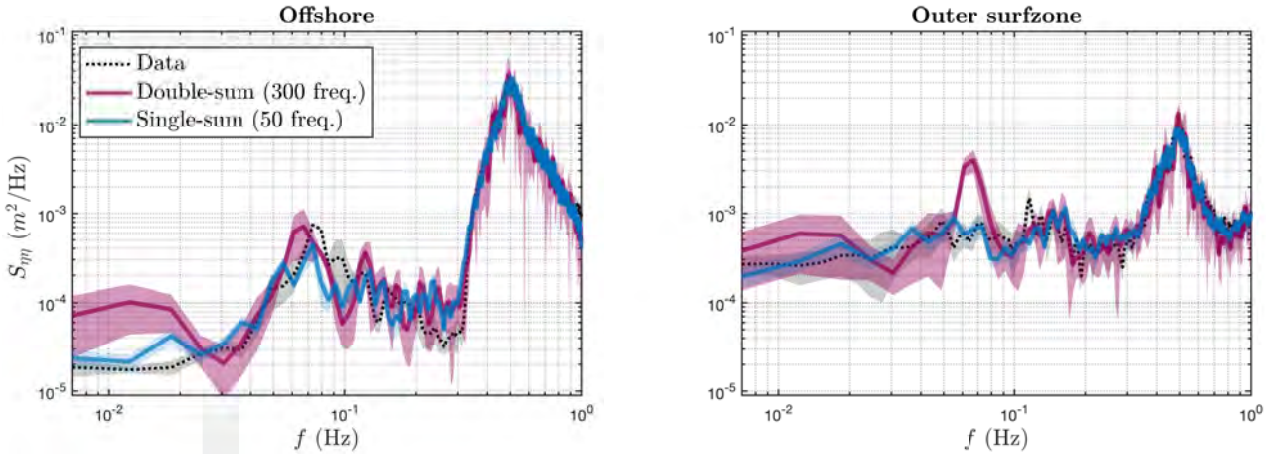

Figure III.8 Longshore-averaged power spectra of free surface ($S_{\eta\eta}$) as a function of frequency (f) for stations located offshore (left, $x = 19.0$ m, $-9 < y < 9$ m) and in the outer surfzone (right, $x = 28.4$ m, $-8 < y < 3$ m). Spectra from experimental data are shown as black dots, while those from simulations with the double-sum (300 freq.) and single-sum wavemakers are shown as pink and blue lines, respectively. The longshore standard deviations of the model and data spectra are represented by shaded areas.

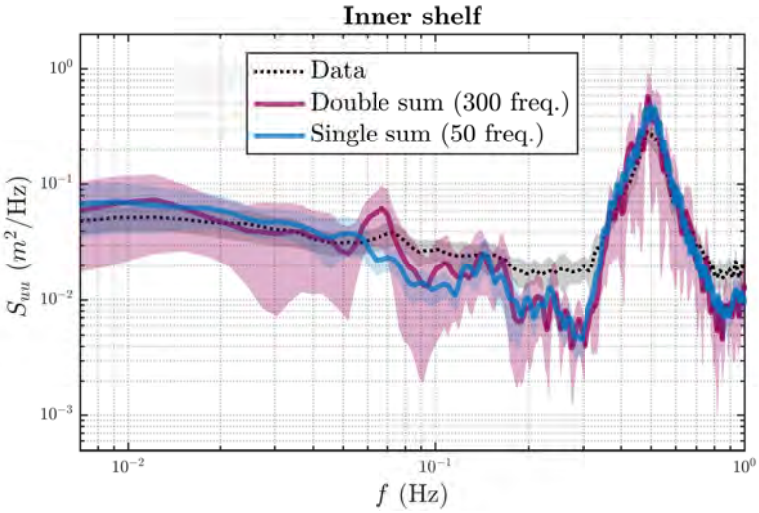

Figure III.9 Longshore-average power spectra of the cross-shore velocity (S_{uu}) as a function of frequency (f) for station located in the innershelf (left, $x = 26.6$ m, $-10 < y < 10$ m). The spectrum from experimental data is shown as black dots, while those from simulations with the double-sum (300 freq.) and single-sum wavemakers are shown as pink and blue lines, respectively. The longshore standard deviations of the model and data spectra are represented by shaded areas.

for the double-sum wavemaker. Both wavemakers show a good match with the data in the longshore mean, and the difference lies mainly in the standard deviation. Consequently, the surfzone eddies are affected by persistent spurious rip currents, but the effect tends to cancel out over the domain.

III.2.4 Conclusion

Over the past decade, studies has been carried out to find a suitable way of forcing a random sea state into wave-resolving models. Here, we build on the work of Salatin et al. (2021) and others

to define a wavemaker devoid of spurious coherent interference, apply it to the 3D wave-resolving model CROCO and validate it with experimental data. We show that a single-sum wavemaker that assigns only a pair direction and frequency values to each component of a wave spectrum definitively prevents coherent interference, in contrast to a conventional double-sum wavemaker that allows waves of different direction to share the same frequency. This method also saves a great deal of computing time — over 25% of the cost of the simulation, depending on the number of frequencies used in the first method to mitigate coherent interference. Another correction made to the wavemaker consists in periodizing each wave component by slightly modifying its direction. Similar correction is present in FUNWAVE-TVD (Salatin et al., 2021). The new wavemaker is then applied to a model setup of the laboratory wave basin experiment presented in Baker et al. (2023c).

In the double-sum wavemaker simulation, the generation of stationary rip currents from coherent interference is clearly visible in the mean vorticity field. The mean longshore drift also changes sign despite the longshore uniform bathymetry, and the significant wave height shows bands of high and low values oriented in the shore-normal direction (creating longshore pressure gradients). Increasing the number of frequencies in the classical double-sum wavemaker reduces the observed biases, but they remain significant and affect the production of transient rip and surf zone eddies, as can be seen in the velocity power spectra. The single-sum wavemaker has none of these characteristics, and consistently reproduces the experimental data with regard to the magnitude and variation of surface elevation and velocities, therefore, likely more realistically representing the transient rip current behaviors.

While the classical double-sum method cannot compete with the single-sum method in terms of accuracy and cost, we have more successfully tested (not shown) the double-sum method of Johnson and Pattiaratchi (2006), which added a time-dependent random phase shift to mitigate the phase-locking effect (similar to the effect of random errors in the forcing frequencies of the laboratory experiment). Yet even in this case, the computational cost remains prohibitive compared with the single-sum method (in addition, the added random phase shift modifies, albeit slightly, the dispersion relation; Johnson and Pattiaratchi 2006).

On the basis of a validation which, for the first time, uses experimental data, we conclude that a single-sum wavemaker gives the best results at low computational cost. We expect that our study will increase confidence in future wave-resolving simulations, and provide a necessary step

towards a more comprehensive investigation of rip currents, tracer dispersion or morphological evolution using this type of model.

III.3 Supporting material

Figures that were omitted from the article to maintain an acceptable length are added in this section.

In the basin experiment, zero directional propagation of waves generated by the wavemaker is difficult to achieve and it was therefore important to evaluate the effect of residual spread in experiment G1a ($\sigma_\theta = 2.4°$). In the simulation of this experiment, stationary rip currents are generated, although weaker than with larger spread, showing patterns of vorticity, velocity and wave height with significant amplitude compared to the single-sum simulation (Fig. III.10).

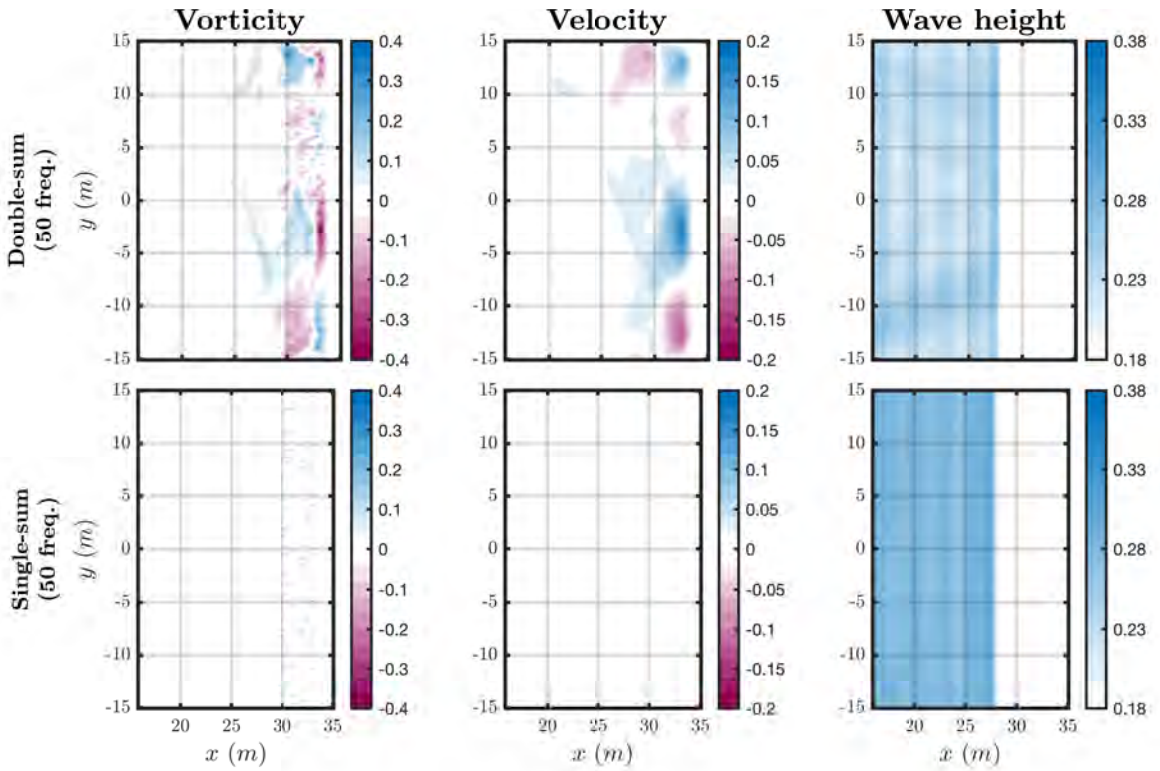

Figure III.10 Time-averaged ($t = 10 - 30$ min) surface vertical vorticity ω_z (s^{-1}, left), alongshore velocity v ($m.s^{-1}$, middle) and significant wave height H_s (m, right) for the double-sum (top: $N = 50$ freq.) and single-sum (bottom: $N = 50$ freq.) wavemakers in the G1a case ($\sigma_\theta = 2.4°$).

The modified double-sum method of Johnson and Pattiaratchi (2006) was also tested, which consisted in adding a time-dependent random phase into the double-sum function. The modified wavemaker is expressed as follows:

$$\eta_{bc}(y,t) = \Sigma_i^N a_i \Sigma_j^M d_j \cos(k_{y,i,j} y - \omega_i t - \phi_{i,j} - \alpha\phi_{i,j} t) \tag{III.17}$$

where α is a constant, arbitrarily set here to 0.2. This slight modification, similar in fact to laboratory experiments where the forced frequencies can never be exactly the same due to small stochastic errors, results in the effective elimination of coherent interference, as shown in Figure III.11 for the G1d case. This method is a good alternative to the single-sum wavemaker but is significantly more expensive, which justifies our choice.

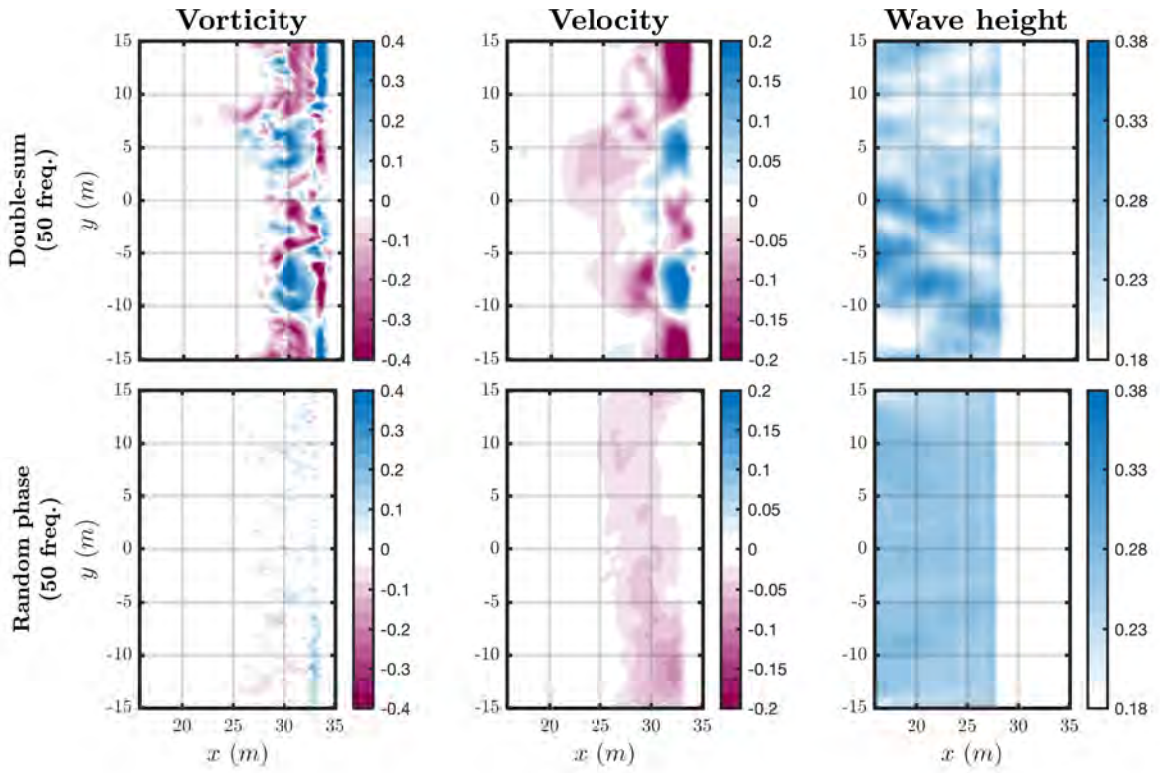

Figure III.11 Time-averaged ($t = 10 - 30$ min) surface vertical vorticity ω_z (s^{-1}, left), alongshore velocity v ($m.s^{-1}$, middle) and significant wave height H_s (m, right) for the default double-sum wavemaker (top) and the modified double-sum wavemaker with random phase (bottom), using $N = 50$ freq in the G1d case ($\sigma_\theta = 26.1°$).

III.4 Conclusion

III.4.1 Summary

This chapter addresses the issue of coherent interference in wave-resolving nearshore models, which has been a persistent problem affecting the representation of nearshore dynamics in experimental and numerical simulations since the late 1970s. We introduce a single-sum wavemaker formalism in the 3D wave-resolving model CROCO, which assigns only one pair of direction and frequency values to each component of the wave spectrum. This new approach prevents coherent interference, unlike the conventional double-sum wavemaker that allows waves of different directions to share the same frequency, leading to spurious persistent longshore variability.

The single-sum wavemaker is validated against experimental data collected in a wave basin experiment with longshore-uniform bathymetry and shows that it produces transient rips devoid of any coherent interference effects. Consequently, the model statistics closely match the experimental data, guaranteeing statistical integrity while reducing computational costs. These advances are essential for wave-resolving studies of nearshore dynamics, as they increase the accuracy with which transient eddies are generated. Another point of interest in this work is its contribution, following on from others (e.g., Salatin et al., 2021), to raising the scientific community's awareness of methodological issues. Lack of knowledge on the part of model users can bias their simulations and the results they produce.

We added in Appendix 2 the modified CROCO routines for the implementation of the new single-sum wavemaker.

Along with the correction of the turbulent closure described in Marchesiello and Treillou (2023) (see Appendix 1), this correction allowed us to answer the first objective of this thesis.

III.4.2 Author contributions

This work is based on a collaboration with my thesis supervisor, P. Marchesiello, and with Christine M. Baker, researcher in the USA. It began with the identification of a problem in my simulations, which I attributed to the design of our wavemaker. After implementing the proposed solution in CROCO, I came across an article about a recent wave basin experiment

conducted by C. Baker and used it to validate the correction and more generally the simulations carried out with CROCO as part of this thesis. I contacted her and had fruitful exchanges on experimental design and data. I carried out all the simulations and data processing and wrote the first version of the article. Meanwhile, C. Baker and P. Marchesiello contributed to improving the methodology, discussing the results and refining the article.

Chapter IV

Tracer dispersion by surfzone eddies: assessing the impact of undertow vertical shear

L'océan s'offrait, déshabité, calme au large,
effervescent sur les bords

Magie Noire, 1928, Paul Morand

Contents

IV.1 Preamble

We have increased confidence in the 3D wave-resolving model CROCO, thanks to the corrections presented in Chapter III and Appendix 1. We can now address our main scientific question concerning the impact of undertow vertical shear on tracer dispersion, formulated in the introduction as:

• **What is the impact of undertow vertical shear on tracer dispersion in the nearshore zone?**

In this Chapter, two experiments are used: the wave basin experiment by Baker et al. (2023c) and the large-scale field campaign IB09 (Hally-Rosendahl & Feddersen, 2016). In both experiments, dye was released and tracked using various measurements. A specific RGB analysis is implemented (as part of the thesis work) to assess the relative dye concentration observed during the wave basin experiment. Both experiments serve to validate CROCO for tracer dispersion and to evaluate the effect of 3D processes. Several semi-idealized simulations based on IB09 are carried out to isolate the impact of different processes. Consequently, laboratory and field experiments, supported by numerical simulations, provide a better understanding of tracer dispersion mechanisms.

This Chapter presents the results of this research, in the form of a preprint submitted to *Journal of Physical Oceanography* (Treillou et al., 2025).

IV.2 Article submitted to *Journal of Physical Oceanography*

IV.2.1 Introduction

The coastline, the dynamic interface between land and sea, is of critical importance for beach recreation, tourism and the health of coastal ecosystems and people. This area comprises the surf zone, which extends from the shoreline to the limit of depth-limited wave breaking, and the inner shelf, the region seaward of the surf zone, reaching depths of tens of meters, where surface and bottom layers overlap, modifying the theoretical Ekman transport (Estrade et al., 2008). Numerous materials, such as contaminants, larvae, sediments, and heat, transit through these zones, raising various health, environmental and ecological concerns. For example, water quality in the nearshore region is particularly vulnerable to anthropogenic influences, with coastal pollutants from terrestrial runoff often leading to beach closures due to degraded water quality (Boehm et al., 2002, 2005). The direct discharge of industrial and domestic waste on beaches in developing countries where wastewater treatment is inadequate is even more critical for the health of people and ecosystems, with consequences for key economic activities such as fishing (Middlebrooks et al., 1981). The coastal retention or dispersal of plankton and larvae also has direct ecosystem implications, affecting the distribution and health of marine populations (Shanks et al., 2017, 2010; Moulton et al., 2023). The safety of beach users associated with the risk of rip currents is another well-know problem (Castelle et al., 2018). Sediment transport is also a major issue, as it often determines the morphological evolution of the shoreline, affecting its structure and stability (Marchesiello et al., 2022). Given these challenges, understanding the dynamics that drive coastal transport and mixing is essential for effective coastal management and the preservation of the recreational and ecosystem services of coastal regions.

While longshore transport is predominantly driven by longshore drift, caused by the mean wave angle of incidence, key processes for cross-shore exchange between the surf zone and the inner shelf are related to rip currents associated with surf zone eddies. Rip currents are characterized as horizontal structures with time scales ranging from $\mathcal{O}(1\text{ min})$ to much longer $\mathcal{O}(1\text{ hr})$ and cross-shore spatial scales of $\mathcal{O}(100\text{ m})$. Rip currents are extremely important for cross-shore exchanges as they can extend seaward over a width 2 to 3 times that of the surf zone

(Kumar & Feddersen, 2017a) and can influence shelf circulation (Wu et al., 2021). There are two main types of rips: channeled (bathymetric) and transient (flash) rip currents. Channeled rip currents, which are the most extensively studied, are driven by longshore variations in bathymetry (Bowen, 1969; MacMahan et al., 2006; Marchesiello et al., 2015; Castelle, 2016). Flash rips, on the other hand, are purely wave-induced processes that can occur on uniform bathymetry along the coast. One of the earliest proposed mechanisms for flash rips was the horizontal shear instability of longshore currents (Bowen & Holman, 1989; Dodd et al., 1992; Allen et al., 1996; Uchiyama et al., 2010). However, over the last decade, the significance of this process has diminished as 3D models have questioned its importance (Newberger & Allen, 2007; Splinter & Slinn, 2003; Marchesiello et al., 2021) and studies found its magnitude significantly lower than that of the Peregrine process, representing the current consensus in the nearshore research community (Feddersen, 2014). The latter describes the generation of large surf zone eddies by short-crested waves (Peregrine, 1998; Clark et al., 2012). The differential breaking of short-crested waves in the surf zone leads to the formation of small eddies at the edges of the crest. These combine over time to form larger eddies through an inverse cascade mechanism consistent with 2D turbulence, which has recently been confirmed by observation (Elgar & Raubenheimer, 2020; Elgar et al., 2023; Baker et al., 2023b) and modeling (Marchesiello et al., 2021). The coastal boundary then constrains surf eddies to propagate offshore. The present study will focus on those processes occurring on uniform longshore bathymetry.

A number of field experiments have investigated the impact of flash rips on material dispersion within the surf zone and inner shelf using innovative methods such as Lagrangian drifters (Spydell et al., 2019; Spydell & Feddersen, 2009) and dye tracers (Inman et al., 1971; Clark et al., 2010; Hally-Rosendahl et al., 2014; Grimes et al., 2020a, 2021). In particular, Clark et al. (2010) estimated the surf zone cross-shore bulk diffusivity at $\kappa_{xx} = 0.5 - 2.5$ m^2.s^{-1} and examined three possible contributors:

- breaking-wave induced turbulent diffusion: $\kappa_{xx} \sim 0.05$ m^2.s^{-1} (Svendsen, 1987);
- undertow-driven shear dispersion : $\kappa_{xx} \sim 0.1$ m^2.s^{-1} (Pearson et al., 2009);
- dispersion due to surfzone eddies : $\kappa_{xx} \sim 1$ m^2.s^{-1} (Clark et al., 2010).

Shear dispersion is the process resulting from the vertical flow variation in the on-off shore direction (undertow profile), i.e. the process of opposing advection of surface landward (U_+)

and bottom seaward (U_-) velocities, which, combined with vertical turbulent diffusion κ_{zz}, can disperse an initial patch of tracers. Assuming a stepped velocity profile, Fischer (1978) proposed a simple theoretical relationship, validated with experimental data by Pearson et al. (2009):

$$\kappa_{xx}^{\text{ShearD}} = \frac{(U_+ - U_-)^2 h^2}{48 \kappa_{zz}} \tag{IV.1}$$

According to the literature (Clark et al., 2010, 2011; Geiman et al., 2011), the intensity of breaker-induced turbulence correlates weakly with the observed surf zone diffusivity, while shear dispersion explains little of its amplitude, leaving surf eddies as the dominant mechanism, even if good correlations only appear on the infragravity range of eddies.

To date, most studies of the effect of transient rip currents on tracer transport in coastal zones have been carried out using depth-averaged models of the Boussinesq type (e.g., Feddersen et al., 2011; Hally-Rosendahl & Feddersen, 2016). Therefore, the impact of vertical shear on tracer dispersion has never been fully examined beyond the shear dispersion process. Attempts have been made to estimate 3D transport mechanisms between the surf zone and the inner shelf by coupling a 2D wave-resolving Boussinesq model and a 3D wave-averaged circulation model (Kumar & Feddersen, 2017a,b), allowing a stratified inner shelf. However, the surf zone remains shear-free in these experiments, as the breaking force of the Boussinesq model is introduced into the circulation model as a depth-averaged body force. The recent availability to the community of cost-effective 3D free-surface, wave-resolving models, such as CROCO (Marchesiello et al., 2021; Marchesiello & Treillou, 2023; Treillou et al., 2024, www.croco-ocean.org), SWASH (Zijlema et al., 2011) or NHWAVE (Derakhti et al., 2016) allows us to fully address the impact of vertical shear on tracer dispersion driven by transient rip currents. CROCO has recently been enriched with a non-hydrostatic pseudo-compressible solver, allowing explicit resolution of surface waves and their energy transfer to the three-dimensional circulation. Early model results on flash rips (Marchesiello et al., 2021) have shown a significant impact of vertical shear on nearshore dynamics, notably by reducing the inverse cascade mechanism and generating a newly identified phenomenon of intermediate turbulence in the surf zone called mini-rips.

Mini-rips are rib-structured currents resulting from the vertical shear instability of wave-averaged cross-shore surfzone currents, composed of breaker-induced shoreward surface flow and seaward undertow, as illustrated in Figure IV.1a. More precisely, vertical shear instability

follows the linear instability mechanism demonstrated by Pierrehumbert and Widnall (1982): a primary Kelvin-Helmholtz instability forms large spanwise vortices (Fig. IV.1b), then spanwise perturbations trigger a secondary instability that causes streamwise vortices across the primary billows (Fig. IV.1c). 3D shear instability is a common feature of turbulence (e.g., Pierrehumbert & Widnall, 1982; Rogers & Moser, 1992), but has been largely ignored in the surf zone, apart from the "undertow instability" described by Li and Dalrymple (1998). Mini-rips are also reminiscent of the structures associated with breaking-wave turbulence (Watanabe et al., 2005; Lubin & Glockner, 2015), but their scales and generation mechanisms are different: mini-rips originate from wave-averaged shear flow, not from breaking rollers, which are not resolved in a free-surface model (they are parameterized instead); mini-rips have a time scale in the infragravity range, i.e., much longer than the peak period, and extend more widely in space across the surf zone. As will be shown, the larger mixing length scale of mini-rips can lead to much greater mixing in the surf zone than that produced by the turbulence of breaking waves.

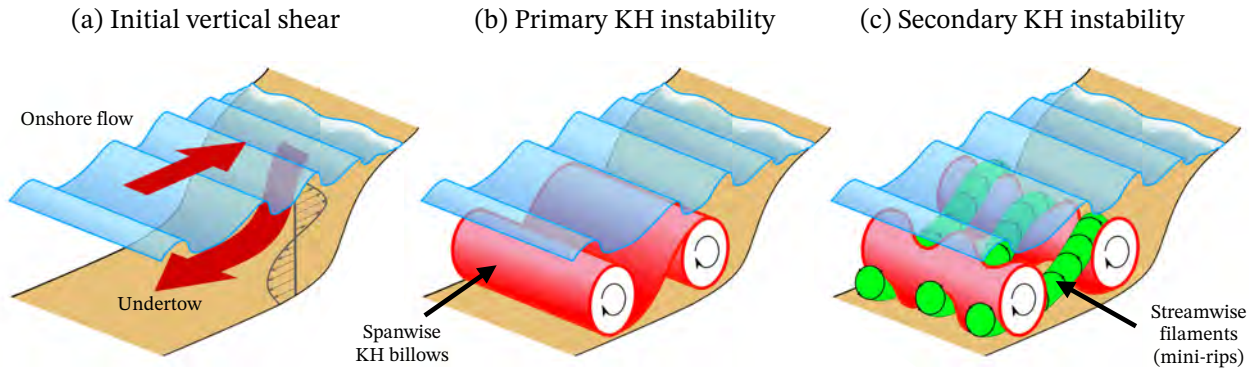

Figure IV.1 Schematic view of the processes leading to the creation of mini-rips in the surf zone by shear instability. (a) Initial conditions, with shoreward surface flow (breaking acceleration and Stokes drift) and seaward bottom return flow (undertow). (b) Primary instability arising from vertical shear, creating large spanwise billows (in red). (c) Secondary instability due to the tridimensionality of the flow, creating streamwise vortices (in green), called mini-rips.

Here, we propose to apply for the first time a 3D wave-resolving model to the study of nearshore pollutant dispersion, by simulating two complementary experiments, one in a wave basin and the other in the field. In both the basin experiment (Baker, 2023; Baker et al., 2023c) and the IB09 field experiment (Hally-Rosendahl et al., 2014, 2015; Hally-Rosendahl & Feddersen, 2016), dye was released and tracked, enabling an effective evaluation of the impact of vertical shear. CROCO with recent corrections for nearshore applications is presented in Section IV.2.2. A first validation in a controlled environment is provided with the wave basin experiment

conducted by Baker et al. (2023c) in Section IV.2.3, before applying CROCO to IB09 in Section IV.2.4. Semi-idealized cases from the IB09 configuration are presented in Section IV.2.5 to discriminate the relative importance of each dispersion process, including, briefly, innershelf contributions such as longshore wind, stratification and Coriolis force. The results are discussed and summarized in Section IV.2.6.

IV.2.2 Methods & Materials

IV.2.2.1 Non-hydrostatic free-surface model CROCO

CROCO is a free-surface, terrain-following model developed around the Regional Oceanic Modeling System (Shchepetkin & McWilliams, 2005; Debreu et al., 2012). It has been applied to a wide range of regional oceanic problems and, over the last decade, to nearshore problems such as channeled rip current circulation (Marchesiello et al., 2015) and morphodynamic evolution (Marchesiello et al., 2022; Shafiei et al., 2023). In its non-hydrostatic (non-Boussinesq) version, it resolves the full set of Navier-Stokes equations, including the momentum and continuity equations, free-surface kinematic relation and the transport equation of tracer C (heat, salt or any type of passive tracer):

$$\frac{\partial \rho u}{\partial t} = -\overrightarrow{\nabla}.\left(\rho \overrightarrow{\mathbf{v}} u\right) + \rho f v - \rho \tilde{f} w - \frac{\partial P}{\partial x} + \mathcal{F}_u + \mathcal{D}_u + \lambda \frac{\partial \overrightarrow{\nabla}.\overrightarrow{\mathbf{v}}}{\partial x} \tag{IV.2}$$

$$\frac{\partial \rho v}{\partial t} = -\overrightarrow{\nabla}.\left(\rho \overrightarrow{\mathbf{v}} v\right) - \rho f u - \frac{\partial P}{\partial y} + \mathcal{F}_v + \mathcal{D}_v + \lambda \frac{\partial \overrightarrow{\nabla}.\overrightarrow{\mathbf{v}}}{\partial y} \tag{IV.3}$$

$$\frac{\partial \rho w}{\partial t} = -\overrightarrow{\nabla}.\left(\rho \overrightarrow{\mathbf{v}} w\right) + \rho \tilde{f} u - \frac{\partial P}{\partial z} - \rho g + \mathcal{F}_w + \mathcal{D}_w + \lambda \frac{\partial (\overrightarrow{\nabla}.\overrightarrow{\mathbf{v}})}{\partial z} \tag{IV.4}$$

$$\frac{\partial \rho}{\partial t} = -\overrightarrow{\nabla}.(\rho \overrightarrow{\mathbf{v}}) \tag{IV.5}$$

$$\frac{\partial \eta}{\partial t} = w_f|_{z=\eta} - \overrightarrow{\mathbf{v}}|_{z=\eta}.\overrightarrow{\nabla}\eta \tag{IV.6}$$

$$\frac{\partial \rho C}{\partial t} = -\overrightarrow{\nabla}.(\rho \overrightarrow{\mathbf{v}} C) + \mathcal{F}_C + \mathcal{D}_C \tag{IV.7}$$

(u, v, w) are the (x, y, z) (cross-shore, alongshore and vertical) components of vector velocity $\overrightarrow{\mathbf{v}}$; η is the free surface; P the total pressure; ρ the density; $f(x, y)$ and $\tilde{f}(x, y)$ are the traditional and non-traditional Coriolis parameters, function of latitude; g is acceleration of gravity; $\mathcal{D}_u, \mathcal{D}_v, \mathcal{D}_C$

are eddy-diffusion terms requiring second-moment turbulence closure models; $\mathcal{F}_u, \mathcal{F}_v, \mathcal{F}_C$ are forcing terms; λ is the second (bulk) viscosity, associated with compressibility (used to damp acoustic waves).

CROCO is discretized on an Arakawa C-grid using finite difference methods and a split-explicit treatment of slow and fast modes (acoustic waves and shallow-water motions). The discretization in time is made using a third-order predictor-corrector scheme. Vertical flux terms which are not requiring specific accuracy are computed using an implicit time stepping to increase computational stability. Horizontal and vertical advection terms are discretized using the WENO5-Z improved version of the 5th-order weighted essentially non-oscillatory scheme (Borges et al., 2008). This scheme is accurate for hyperbolic problems containing both shocks and smooth structures, and particularly adapted for breaking waves (Tissier et al., 2012; Lubin & Chanson, 2017; Bonneton, 2023). The breaking arises naturally when waves are steepening, transferring energy to the mean currents via the advection scheme and to subgrid turbulence via the turbulence closure model. It is not necessary to use a *ad-hoc* criterion to estimate the onset of wave breaking, which gives this class of wave-resolving models an advantage over Boussinesq-type models (Smit et al., 2013, 2014; Marchesiello et al., 2021). More details about non-hydrostatic CROCO can be found in Marchesiello et al. (2021).

IV.2.2.2 Wavemaker

A spectrum of 3D linear waves is forced at the offshore boundary via an analytical wavemaker. Here the spectrum is based on a JONSWAP statistical distribution and has frequency and directional spreading. Free surface elevation η, cross-shore and alongshore velocities (u, v) are given by:

$$\eta_{bc}(y,t) = \Sigma_i^{N\times M} a_i \cos(k_{y,i} y - \omega_i t - \phi_i) \tag{IV.8}$$

$$u_{bc}(x,y,t) = \eta_{bc}(y,t)\omega_p \cos(\theta_m)\frac{\cosh(k_p(z+h))}{\sinh(k_p h)} \tag{IV.9}$$

$$v_{bc}(x,y,t) = \eta_{bc}(y,t)\omega_p \sin(\theta_m)\frac{\cosh(k_p(z+h))}{\sinh(k_p h)} \tag{IV.10}$$

where i represent indices of spectral distribution in frequency and direction, a_i the amplitude associated with frequency ω_i given by the JONSWAP statistical distribution, $k(y,i) = k_i \sin(\sigma_i)$ the alongshore wavenumber (k_i being the linear theory wavenumber given by $\omega_i^2 = g k_i \tanh(k_i h)$ with h the mean water depth), θ_i the wave angle, θ_m the mean wave direction and σ_θ the directional spread around the mean. ω_p and k_p are peak frequency and wavenumber, d_i is a normalized frequency-dependent directional distribution and ϕ_i an uniformly distributed random phase. This single-sum wavemaker is a recent correction to CROCO to alleviate the problem of coherent wave interference arising from double-summation methods (Treillou et al., 2024; Salatin et al., 2021). Double-sum wavemakers allow the presence of wave components of distinct directions but same frequencies to produce phase-locking or coherent interference leading to spurious variability along the coast in the form of stationary nodes and anti-nodes. This can lead to stationary rip currents, detrimental to the entire solution. Using a single-sum wavemaker (i.e. each wave component has distinct frequency and direction) resolves this issue. More details can be found in Treillou et al. (2024).

IV.2.2.3 Turbulence closure

In addition to managing breaking wave fronts using a shock-capturing numerical scheme (WENO5), wave-breaking turbulence is represented by a $k-\omega$ model that solves the closure equations for turbulent kinetic energy k and dissipation rate ω ($\propto \epsilon k^{-1}$), within a Generic Length Scale (GLS) method (Warner et al., 2005; Marchesiello & Treillou, 2023). In the absence of buoyancy forcing, the turbulence equations manifest a balance encompassing shear production, dissipation, transport, and diffusion:

$$\frac{\partial \rho k}{\partial t} = -\overrightarrow{\nabla} \cdot (\rho \overrightarrow{v} k) + D_k + \rho(P - \epsilon) \tag{IV.11}$$

$$\frac{\partial \rho \omega}{\partial t} = -\overrightarrow{\nabla} \cdot (\rho \overrightarrow{v} \omega) + D_\omega + \rho \frac{\omega}{k}(c_{\omega 1} P - c_{\omega 2} \epsilon) \tag{IV.12}$$

where D_k, D_ω are the diffusion terms, ϵ the turbulent kinetic dissipation and $c_{\omega 1}$, $c_{\omega 2}$ the stability functions. The eddy viscosity $\nu_t = c_\mu l k^{1/2}$ is derived from these equations with coefficient c_μ dependent on stability functions and mixing length $l \propto k^{3/2}\epsilon^{-1}$. A recent correction of the

turbulent closure was implemented in CROCO to address an overmixing issue in potential flow regions (non-breaking waves on the continental shelf) due to an intrinsic linear instability of two-equation closure systems (Marchesiello & Treillou, 2023; Larsen & Fuhrman, 2018). This correction maintains stratification in 3D wave-resolving simulations.

IV.2.2.4 Deep and shallow breaking

To assess the effect of vertical shear, it is useful to compare the results of the 3D model with those of an equivalent depth-averaged 2D model, in the same setting. To this end, we have developed a method for emulating depth-averaged behavior in CROCO, which has already been used in Marchesiello et al. (2021). We assume that the main distinction between 2D and 3D models lies in the breaker forcing mechanism. In 2D models, the momentum input from breaking waves is applied to the entire water column (deep breaking), whereas in a 3D paradigm, breaking acceleration is confined to the surface (shallow breaking). In other words, a 2D model assumes that breaking turbulence is strong enough throughout the water column to immediately vertically mix the mean current during breaking (in this case, the undertow is reduced to an anti-Stokes current).

A few studies have examined the effects of deep and shallow breaking in wave-averaged models (Splinter & Slinn, 2003; Uchiyama et al., 2010), concluding that the most realistic solutions are obtained with shallow breaking. These studies have imposed deep or shallow breaking by specifying the breaking force profile or the turbulent viscosity profile. In CROCO, the breaking acceleration profile emerges from that of the parameterized turbulent viscosity resulting from breaking waves (without any particular adjustment to the closure model). Consequently, it seems natural that to mimic deep breaking, we only need to increase the surfzone vertical viscosity by a certain factor, taken here as 30. This factor was chosen on the basis of a series of tests to ensure that increasing the viscosity of the surf zone can eliminate sufficient vertical shear (by vertical momentum mixing) without excessive dissipation of wave and current energy.

To validate the method, we present in Figure IV.2 the cross-shore velocity spectra at stations located on the inner shelf and outer surf zone of the wave basin experiment of Baker et al. (2023c). This figure compares the spectra of the CROCO pseudo-2D simulation with an equivalent simulation using FUNWAVE-TVD. The close correspondence between the two spectra is striking, and clearly validates our attempt at a pseudo-2D version of CROCO. It

should also be noted that this CROCO pseudo-2D configuration is analogous in principle to that of Kumar and Feddersen (2017a), where a wave-averaged 3D circulation model (ROMS from the COAWST system) is forced by a depth-uniform body force (∼ deep breaking) issued by funwaveC (a reimplementation of the FUNWAVE model).

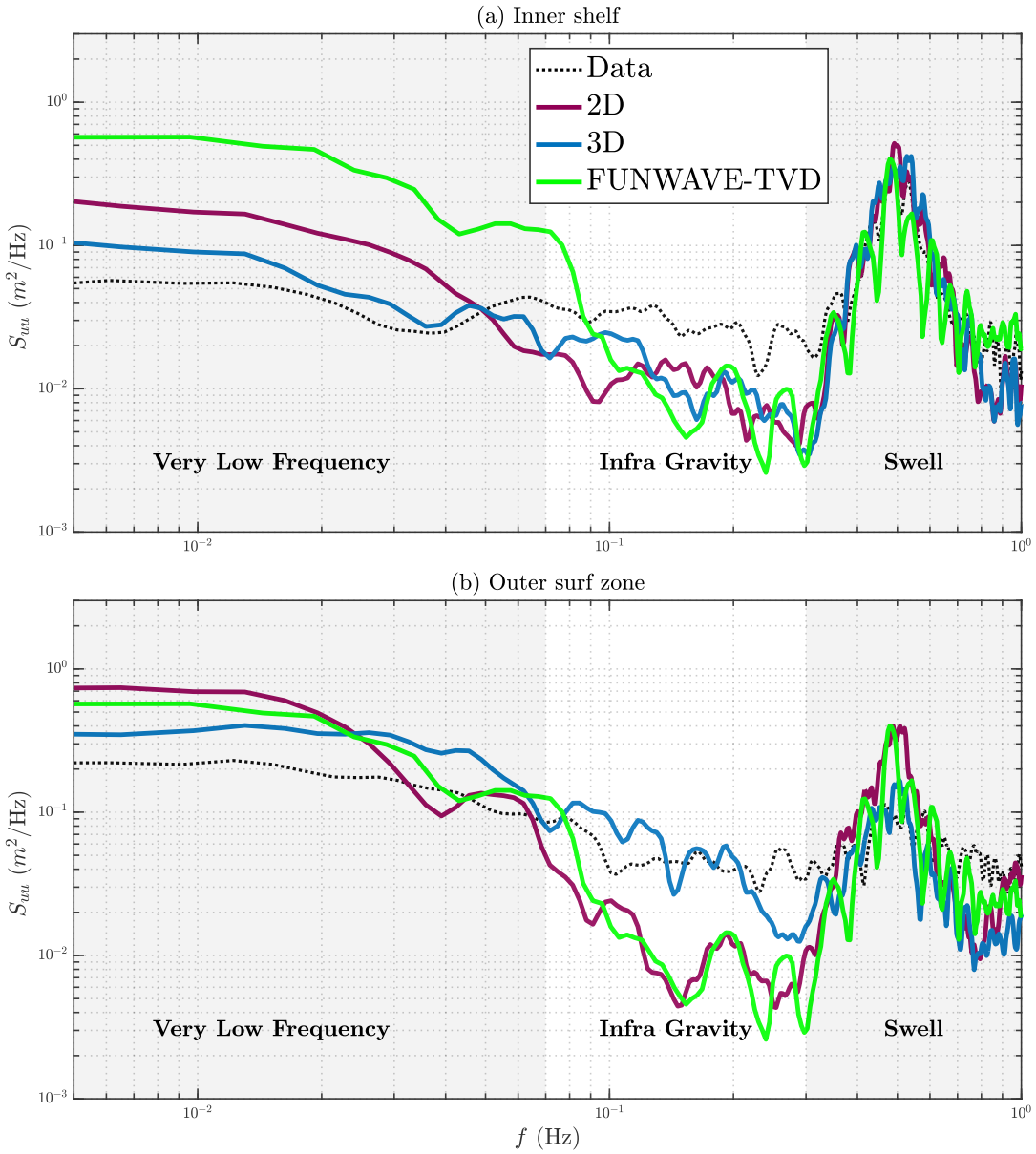

Figure IV.2 Cross-shore velocity spectra in the inner shelf ($x = 26$ m, $y = 0$ m) and the outer surf zone ($x = 28.4$ m, $y = 0$ m) for the wave basin experiment (black dots), and for simulations with CROCO 2D (red line), CROCO 3D (blue line), and FUNWAVE-TVD (green line). Frequency ranges are shown in gray.

IV.2.2.5 Diffusivity estimation by the method of moments

In the present study, dispersion is estimated using a simple Fickian diffusion model with constant cross-shore diffusivity κ_{xx}, in line with previous studies using Lagrangian drifters or continuous dye release (e.g., Spydell et al., 2019; Clark et al., 2010, 2011). κ_{xx} is calculated only for semi-idealized simulations, which are carried out without longshore drift (zero mean wave direction) or longshore wind stress, so that the tracer concentration can be averaged in the alongshore direction. We also consider only depth-averaged concentrations for fair comparison with 2D models. Assuming constant cross-shore diffusion ($\partial^2/\partial y^2 \ll \partial^2/\partial x^2$), Fick's second law of diffusion can be stated as follows:

$$\frac{\partial \overline{C}(x,t)}{\partial t} = \kappa_{xx} \frac{\partial}{\partial x}\left(\frac{\partial \overline{C}(x,t)}{\partial x}\right) + Q_0(x,t) \tag{IV.13}$$

with $\overline{C}$ the longshore averaged concentration, κ_{xx} the cross-shore diffusivity and Q_0 the tracer source at a given location (for example $Q_0(x,t) = Q_0\delta(x - x_0)$). Considering a semi-infinite domain with a no-flux condition $\frac{\partial \overline{C}}{\partial x}\,|_{x=0} = 0$, the solutions of Equation IV.13, calculated with the method of images (Clark et al., 2010), are in the form of a shoreline-attached half-Gaussian:

$$\overline{C}(x,t) = \frac{Q_0}{2\sqrt{\pi \kappa_{xx} t}}\left(e^{-\frac{(x-x_0)^2}{4\kappa_{xx}t}} + e^{-\frac{(x+x_0)^2}{4\kappa_{xx}t}}\right) \tag{IV.14}$$

where κ_{xx} can be derived from the variance σ^2, i.e. the second central moment (hence the "standard method of moments"), by:

$$\kappa_{xx} = \frac{1}{2}\frac{d\sigma^2}{dt} \tag{IV.15}$$

σ^2 evaluates the cross-shore width of tracer plume and in this case is defined by:

$$\sigma^2(t) = \frac{\int_{-L_x}^{0}(x-\mu)^2 \overline{C}(x,t)dx}{\int_{-L_x}^{0}\overline{C}(x,t)dx} \tag{IV.16}$$

where L_x is the offshore limit of the calculation. The offshore limit can be taken as the width of the surf zone ($L_x = W_{SZ}$, when the focus is on the surf zone, or as $L_x = W_x$, the cross-shore length of the domain, when the focus is on the whole domain). The center of mass μ of the

tracer is defined as:

$$\mu(t) = \frac{\int_{-L_x}^{0} x\overline{C}(x,t)dx}{\int_{-L_x}^{0} \overline{C}(x,t)dx} \tag{IV.17}$$

Since our focus is on absolute dispersion, i.e. on all processes that lead to the dispersion of the original tracer patch, μ is fixed at 0 (or at the cross-shore position of the shoreline). Accounting for time-dependent μ is useful when considering relative dispersion, with particular emphasis on small-scale processes diffusing around the center of mass (which can meander). Bulk diffusivity is then estimated by fitting the following equation with classic linear regression methods:

$$\sigma^2 = 2\kappa_{xx}t + \beta \tag{IV.18}$$

We also use the method of a saturation ratio developed by Clark et al. (2010) based on non-dimensional analysis, to constrain the estimation within the Fickian assumption. $\mathcal{R}$ is defined as the ratio between actual σ^2 and the domain saturated variance (i.e., with constant concentration):

$$\mathcal{R} = \sigma^2(t) / \left[\frac{\int_{-L_x}^{0} x^2 dx}{\int_{-L_x}^{0} dx}\right] \tag{IV.19}$$

Only $\sigma^2(t)$ satisfying $\mathcal{R} < 0.55$ are used to derive κ_{xx}. Finally, errors on σ^2, ϵ_{σ^2}, are computed by propagating the longshore standard error of $\overline{C}$, as:

$$\epsilon_{\sigma^2}^2(t) = \left(\frac{\mathrm{SE}_{\overline{C}} \cdot \int_{-L_x}^{0} x^2 dx}{\int_{-L_x}^{0} \overline{C}(x,t)dx}\right)^2 + \left(\frac{\sigma^2(t) \cdot \mathrm{SE}_{\overline{C}} \cdot L_x}{\int_{-L_x}^{0} \overline{C}(x,t)dx}\right)^2 \tag{IV.20}$$

The error on κ_{xx} is then estimated from the fit slope error, assuming residual variance is equal to $\epsilon_{\sigma^2}^2$, similarly to Clark et al. (2010). The κ_{xx} standard error is then defined as:

$$\mathrm{SE}_{\kappa_{xx}} = \frac{1}{2}\sqrt{\frac{\epsilon_{\sigma^2}^2}{\Sigma_i^N (t_i - \bar{t})^2}} \tag{IV.21}$$

with t_i the *ith*-component of the time series used to compute κ_{xx} and $\bar{t}$ the mean of the time series.

IV.2.3 Validation in a wave basin experiment

IV.2.3.1 Wave basin experiment

Before applying CROCO to a field experiment, we validate the model using a more controlled experiment conducted in the Directional Wave Basin at the Oregon State University O.H. Hinsdale Wave Research Laboratory (Baker et al., 2023c,a). In a relatively large 3D wave tank (48.8 m long, 26.5 m wide), a 29-paddle piston-type wavemaker produced short-crested waves with the aim of studying flash rips, focusing on the impact of directional spread on breaking crest length. Several trials were conducted, with varying significant wave heights (from 0.21 to 0.28 m), peak periods (from 1.5 to 3 s) and directional spreads (from 2 to 40 degrees). Measuring equipment included in situ sensors, 3D Lidar and optical imagery, with acoustic Doppler velocimeters longshore arrays in the inner shelf and the surf zone. These data have already been used to validate CROCO's new single-sum wavemaker with very satisfactory results (Treillou et al., 2024). In addition, dye release was monitored in this experiment in two trials using a JONSWAP spectrum ($H_s = 0.3$ m, $T_p = 2$ s, $\theta = 0°$, $\sigma_\theta = 40°$ and γ=3.3). In the first trial, the dye was manually injected near the shoreline in the form of a longitudinal band (at around $x = 31$ m) after 45 minutes of spin-up and lasted for around 2 minutes (60 peak periods), as the basin quickly filled up. The second trial was carried out in the same way after the dye from the first one had been properly mixed. Dye spreading was evaluated using three cameras mounted to a beam on the building ceiling (Point Grey GS3-PGE-91S6C-C Grasshopper3, 9.1 MP, Sony ICX814 Color, Resolution: 3376 × 2704) with resolution ranging from 0.05-2 cm. For more details about the experiment, the reader is referred to Baker et al. (2023c).

IV.2.3.2 Dye concentration evaluation with RGB analysis

To extract information from dye release videos and estimate diffusivity, we developed a framework based on the work of Clark et al. (2014) and more recently Johansen et al. (2022). Using the radiance spectrum of hyperspectral cameras, Clark et al. (2014) showed that a ratio $\mathcal{R}_v$ between the mean radiance in the emission and excitation bands of Rhodamine WT can be used to infer the dye concentration, since this ratio has an almost linear relationship with measured dye concentrations:

$$C_{\text{video}} = \alpha \mathcal{R}_v + \beta \tag{IV.22}$$

C_{video} is the video estimation of dye concentration and α, β are two constants fitted with measured concentration. Johansen et al. (2022) have built on this work to refine an index capable of reconstructing dye concentration. They compare different indices in coastal waters to assess the best way to estimate dye concentration, based on the RGB part of the spectrum. They conclude that an index based on the interaction term between the Red:Blue and Red:Green ratios is the most effective, with a coefficient of determination $R^2 = 0.96$. These results are useful to us, as we only have access to an RGB image. We therefore use the same index $\mathcal{R}_v = \frac{R}{B} \times \frac{R}{G}$ to provide a video estimate of the dye concentration C_{video}. There is no need to calibrate the estimated absolute dye concentration, as diffusivity, which is our objective, is based solely on relative concentration. We simply need to calibrate the constant β so that $C_{\text{video}} = 0$ in the dye-free images. Here, $\beta \sim -1$ ppb, which leads to the relationship :

$$C_{video} = \frac{R}{B} \times \frac{R}{G} - 1 \tag{IV.23}$$

Each image is then cropped along the boundaries to avoid wall effects, and the estimated concentration is extracted. The resulting 2D arrays of C_{video} are averaged in the longshore direction and smoothed before diffusivity is calculated with a fixed value of $\mu = 32$ m (position of the waterline). This method is a robust approach for analyzing dye dispersion in coastal environments based solely on visual data. However, RGB analysis cannot compete with more refined imaging techniques, involving for example multispectral cameras (Clark et al., 2014), and only allows for bulk analysis.

IV.2.3.3 Model configuration

A CROCO configuration is defined for comparison with the dye release experiment. The uniform bathymetry along the coast in the model is identical to that in the experiment, with a steep bar. The robustness of the numerical methods makes it possible to manage the steep slope without the need for smoothing. Alongshore boundaries are periodic, allowing the tracer to move freely in and out of the boundaries. The shoreline is time-dependent as we use a wetting-drying scheme (Warner et al., 2013) with critical depth of 1 cm. The offshore boundary is open to long-waves (Marchesiello et al., 2001). The cross-shore and alongshore domain lengths are respectively 20 and 30 m. The time step is set at 3 ms and the horizontal spatial resolution is 10 cm with 10

terrain-following levels in the vertical. An initial spin-up period of about 1500 s is used for dynamical fields ($\sim$ 750 peak periods). The dye is then introduced in the form of a longshore uniform strip 1 m thick for 10 seconds (corresponding approximately to the duration of the release in the experiment). Wave-averaged fields are stored every 6 s (corresponding to 3 peak periods), while high-frequency fields are stored at $\sim$ 6 Hz at specific locations corresponding to ADV stations.

IV.2.3.4 Hydrodynamic validation

Validation of the significant wave height was carried out in Treillou et al. (2024) – with the aim of correcting the wavemaker – and showed that CROCO is capable of reproducing the main features present in the experiment. Here we repeat this validation procedure with the same test ($H_s = 0.27$ m, $T_p = 2.1$ s, $\theta = -3.3°$, $\sigma_\theta = 26.1°$ and $\gamma = 3.3$), adding the examination of CROCO pseudo-2D and FUNWAVE-TVD simulations and focusing on cross-shore velocity spectra. As shown in Figure IV.2, the results of the 3D simulation agree well with the data, whereas there are more significant differences with the two 2D simulations, which are similar to each other.

More specifically, at the station located on the inner shelf (Fig. IV.2a), all simulations match the data in the swell frequency range. In the infragravity (IG) range, all simulations tend to underestimate energy compared with the data, and this result does not appear to be affected by 3D effects. Interesting differences are observed in the very low frequency (VLF) range, where the 2D models (FUNWAVE-TVD and CROCO-2D) show the energy to be an order of magnitude higher than the data. The 3D simulation manages to correct this difference and is much closer to the data. This is consistent with the results of (Marchesiello et al., 2021), which attribute the reduction in energy in the 3D case to a reduction in the 2D inverse cascade through vortex stretching by the vertical shear flow (see also McWilliams et al. 2018 for the process of fragmentation by 3D currents in the nearshore zone). This effect appears to be greater in the case of FUNWAVE-TVD, suggesting that the 3D dynamics preserved on the inner shelf in the pseudo-2D version of CROCO may have a detrimental effect on 2D dynamics.

The results are different in the outer surf zone (Fig. IV.2b). Here again, the models tend to reproduce the swell range faithfully (although the 2D models seem to overestimate the peak frequency at $f = 0.5$ Hz). In the VLF region, the differences between the models do not appear

significant, although the 3D model remains the closest to the data. Here, the interesting result lies in the IG range, where a clear improvement is brought about by the 3D simulation. The CROCO-2D and FUNWAVE-TVD simulations are very close to each other, and significantly underestimate the IG energy by an order of magnitude. As in (Marchesiello et al., 2021), we attribute this difference to the presence of mini-rips in the 3D simulation, giving a strong signature in the IG range, and which are totally absent in the 2D simulations. These results in a controlled environment give us great confidence that our model can correctly reproduce the dynamics of the inner shelf and surf zone. They also give us confidence in our attempt to mimic Boussinesq-type models with CROCO-2D, given the generally close correspondence with FUNWAVE-TVD. In fact, CROCO-2D tends to underestimate the excess energy provided by depth-averaged nearshore dynamics. Consequently, the differences observed in the following between 2D and 3D simulations can be considered as a conservative evaluation. Finally, our results on 2D velocity spectra with FUNWAVE-TVD are very similar to those recently obtained elsewhere for the same basin experiment (Nuss et al., 2025).

IV.2.3.5 Model-data comparison of dye dispersion

The results on hydrodynamics have a significant impact on tracer transport, as illustrated in Figure IV.3. In this figure, we can see the estimated dye concentration deduced from the video compared with the surface tracer concentration of the 3D simulation 70 s after the initial release. Note that here, the video estimate is calibrated to match the magnitude of the tracer concentration in the model at the time of release. Video concentration produces visually satisfying results, with little visible noise and physically meaningful patterns that are qualitatively similar to that of the model (an exact match cannot be expected due to the chaotic nature of the dynamics involved). Remarkably, almost the entire surf zone is filled by the tracer in the experiment and the simulation after 70 seconds of dye release. We will see in following sections that this is likely the result of mini-rips (with cross-shore length of about the surf zone width), which provides a very efficient mixing process within the surf zone. In both the video and the simulation, the tracer extends somewhat outside the surf zone (located at $x_b = 27.5$ m) and begins to spread over the inner shelf.

Visual inspection is confirmed by a more quantitative analysis of the time evolution of tracer variance calculated in the surf zone and presented in Figure IV.4. Experiment and simulation

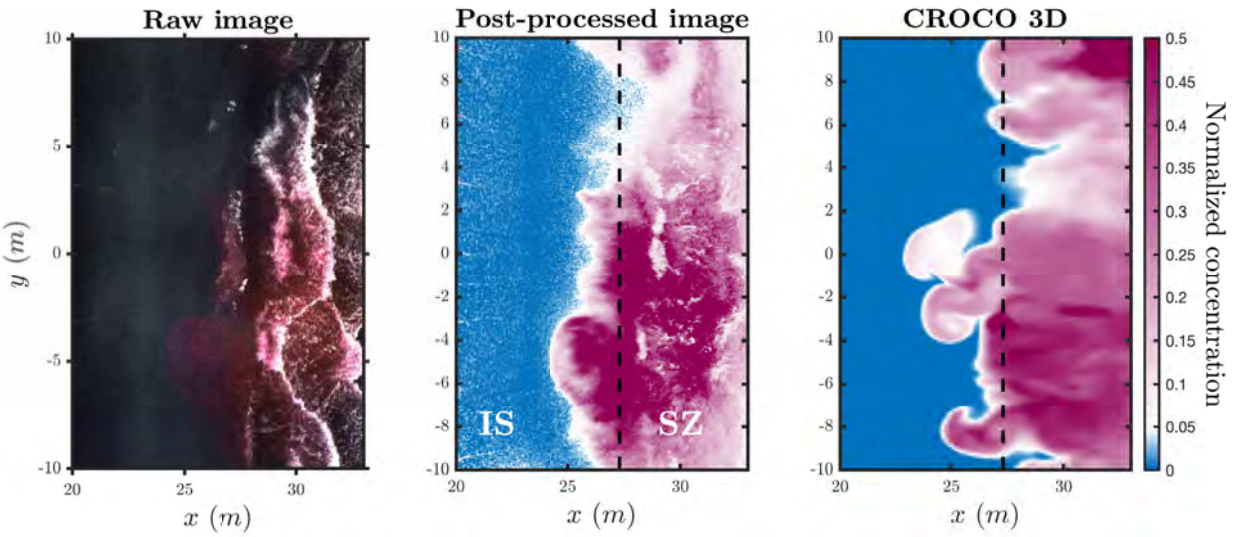

Figure IV.3 Instantaneous snapshots of dye release in the basin experiment after 70 s: raw video image with plume appearing in red over the white foam (left), post-processed dye concentration (middle) and 3D simulation of surface dye concentration (right). The dashed black line indicates the separation between inner shelf (IS) and surf zone (SZ).

present a very good match. In the first 30 seconds we observe the same ballistic regime with quadratic growth $\sigma^2 \sim t^2$, while at larger time scales we observe a typical Brownian diffusion regime with linear growth $\sigma^2 \sim t$. The surf zone bulk diffusivity is $\kappa_{xx} = 0.043 \pm 0.03$ m^2.s^{-1} ($r^2 = 0.92$) for the video and $\kappa_{xx} = 0.039 \pm 0.02$ m^2.s^{-1} ($r^2 = 0.87$) for the simulation. These results are satisfying, again considering the chaotic nature of processes at play, but also the impact of the limited size of the basin. In the future, an ensemble approach to experiments will be necessary to obtain statistically significant results. Nevertheless, the correct simulation of tracer patterns and their time evolution is very encouraging for the model.

IV.2.4 Natural beach: IB09 Model data comparisons

IV.2.4.1 IB09 field campaign

Field observations were collected during the IB09 field campaign conducted at Imperial Beach, California (32.6°N, 117.1°W) on October 13, 2009 (Hally-Rosendahl et al., 2014; Hally-Rosendahl & Feddersen, 2016). This large-scale dye release experiment was carried out on an approximately longshore-uniform beach, and therefore unfavorable to bathymetric rip currents. The experiment spanned approximately six hours, during which the swell came from the south with an oblique incidence angle $\theta \sim 10°$, peak period $T_p = 13$ s and significant wave height $H_s \approx 0.7$ m, creating

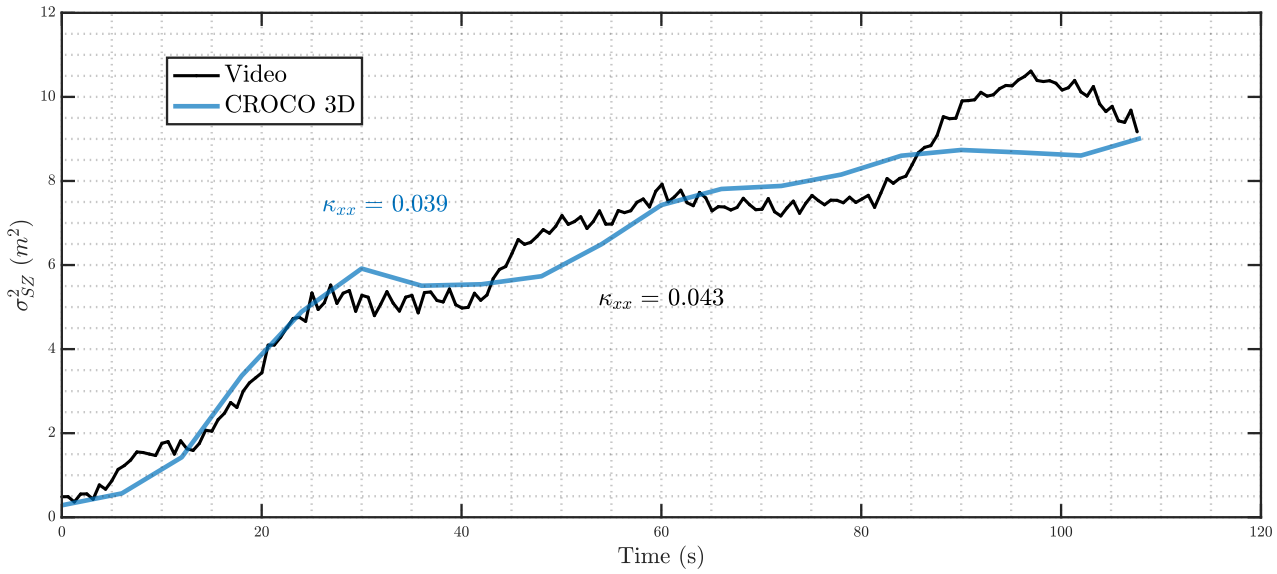

Figure IV.4 Tracer variance σ^2 as a function of time for video dye estimation (black line) and CROCO simulation (blue line), from calculation restricted to the surf zone.

strong northward longshore current. The winds were also from the south at 4-7 m.s^{-1}. The incident wave field can be considered constant and the tidal range relatively low throughout the experiment (less than 0.7 m). Fluorescent Rhodamine WT dye was continuously released at 2.4 mL.s^{-1} near the shoreline from 10:39 to 17:07 h.

Observations were collected using different instruments. A cross-shore array of six fixed near-bed captors was used at $y = 248$ m with ADVs (Acoustic Doppler Velocimeters), thermistors and fluorometers to measure dye concentration (f1-f6, onshore to offshore). Four thermistors and fluoremeters were deployed alongshore (SA1-SA4). Dye concentration was also observed using jetski cross-shore transects and inner shelf alongshore boat transects. To complete the analysis, a small plane with a multispectral camera system captured images of the dye plume to monitor surface concentration. Surfzone concentration was poorly resolved due to white foam from breaking waves. For more details on the experiment, the reader is referred to Hally-Rosendahl et al. (2015); Hally-Rosendahl and Feddersen (2016).

IV.2.4.2 Model configuration

CROCO was configured for this experiment on par with a configuration of funwaveC by Hally-Rosendahl and Feddersen (2016). The size of the computational domain is 400 m and 1430 m in the cross-shore and alongshore directions respectively. In the cross-shore direction, $x = 0$

m represents the position of the shoreline and x decreases seaward. The longshore coordinate y is zero at the dye release point, 60 m from the model's southern boundary, and increases to the north. The bathymetry used in the present study is an average of surveys conducted on October 9 and 19, which showed similar features. The shoreline is straight and faces west (269.6°). The model is forced by a southerly longshore-uniform wind stress of 0.85 N.m^{-2} and a JONSWAP wave spectrum characterized by $H_s = 0.68$ m, peak period $T_p = 13$ s and peak enhancement factor $\gamma = 3.3$. The mean wave angle and directional spread, essential for generating short-crested waves and flash rips, were calibrated using observed data (see next section). Specifically, the mean wave angle was adjusted with observations of longshore mean currents based on the bathymetry measured at the sensor array location, which differed slightly from the averaged bathymetry (see Figure 2 in Hally-Rosendahl & Feddersen, 2016). Optimal results were obtained with a mean wave angle $\theta = 13°$ and $\sigma_\theta = 10°$.

The northern and southern boundaries are periodic for dynamic fields (the longshore domain length is set according to mean wave angle; see Treillou et al. 2024), but the tracer is treated differently with radiative boundary conditions (Marchesiello et al., 2001) to avoid dye re-entry from the southern boundary. The tracer is released at $(x, y) = (-10, 0)$ m, setting the maximum longshore tracer extension to 1370 m, approximately 600 m shorter than Hally-Rosendahl and Feddersen (2016). The time step is set to 20 ms with 10 fast time steps to resolve the fast dynamics — the pseudo-acoustic velocity is set at 100 m.s^{-1} to reduce the stability constraint, with no effect on calculation accuracy. The spatial resolution is 1 m in the horizontal with 10 vertical levels. The temperature stratification is given by $\partial T/\partial z = 0.06$ °C.m^{-1} ($N^2 = 10^{-4}$ s^{-1}), which represents a gentle stratification in Southern California (Hally-Rosendahl et al., 2014). A summary of the simulation parameters is presented in Table IV.1.

Table IV.1 CROCO and funwaveC (Hally-Rosendahl & Feddersen, 2016) simulation parameters for the IB09 experiment: breaking type, wind stress, mean wave angle, directional spread and background diffusion.

Simulation	Breaking	Wind stress (N.m^{-2})	θ (°)	σ_θ (°)	κ_0 (m^2.s^{-2})
CROCO-3D	shallow (3D)	0.85	13	10	0
funwaveC (HR16)	deep (2D)	0.85	–	–	0.075

IV.2.4.3 Wave height and currents

To validate the model using data from Hally-Rosendahl and Feddersen (2016), a simulation is run with bathymetry measured at the cross-shore array of frames f1-f6 (see Figure 2 from Hally-Rosendahl & Feddersen, 2016). With a mean wave angle of 13° and offshore significant wave height of 0.68 m, the H_s profile across the domain is well reproduced by the model (Fig. IV.5), in both 2D and 3D simulations, with RMSE of 0.019 m and 0.025 m, respectively. The maximum wave height is obtained at $x = -72$ m in the model, similar to observation, although the low resolution of the data array does not allow a very accurate comparison.

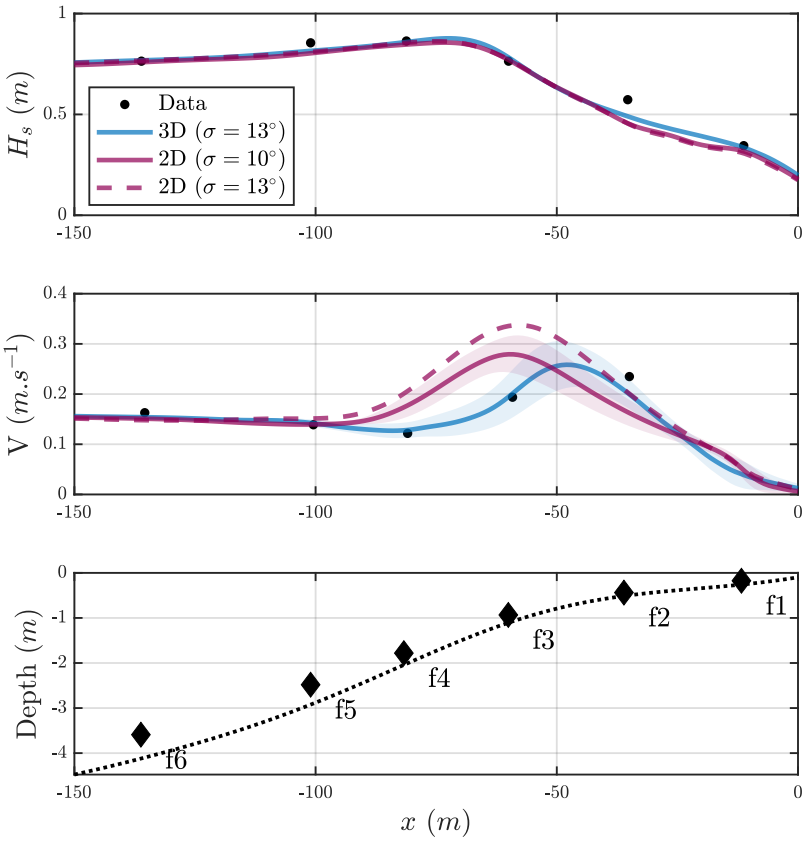

Figure IV.5 Observed (dots) and modeled time-averaged significant wave height (top) and longshore velocity (middle) for CROCO 3D (blue), CROCO 2D with $\sigma = 10°$ (pink) and CROCO 2D with $\sigma = 13°$ (dashed pink). The bathymetry and velocity sensors measured on the same transect are shown in the bottom panel.

Before comparing the cross-shore profiles of alongshore velocity, it is useful to examine the modeled cross-shore currents. Figure IV.6 shows vertical cross-shore velocity sections across the surf zone, highlighting the effect of deep and shallow breaking. In the case of shallow breaking (3D), the shear flow in the surf zone is strong, consisting of a shoreward surface flow of ~ 0.05 m.s^{-1} and undertow of $\sim$ -0.2 m.s^{-1}. In the deep breaking case (2D), there is no vertical shear,

no surface onshore flow and the undertow is reduced to an anti-Stokes mean flow. The shear flow in the shallow breaking case depends essentially on the momentum mixing produced by the turbulent viscosity calculated by the k-ω closure model. No data are available to validate this shear in IB09, but we refer the reader to Marchesiello et al. (2021) and Marchesiello and Treillou (2023) for relevant comparison with the full-scale LIP experiment. The latter shows the robustness of the k-ω model in reproducing the observed surfzone shear flow through different choices of grid resolution.

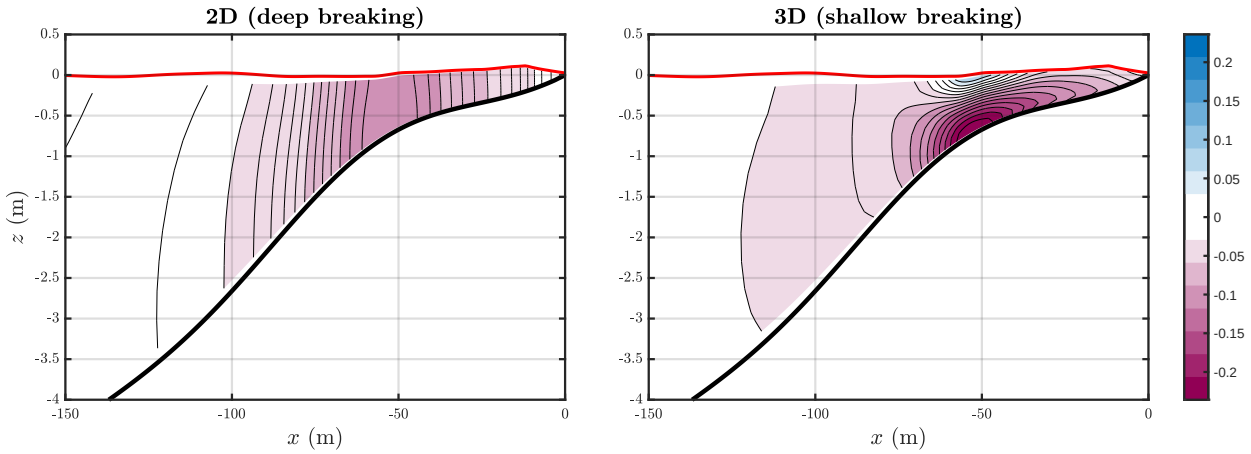

Figure IV.6 Vertical section of time-averaged cross-shore velocities for CROCO 2D (deep breaking case; left) and CROCO 3D (shallow breaking case; right) on the IB09 simulation.

The cross-shore profile of longshore currents in the 3D case (blue line in Fig. IV.5) matches the data well, with a similar maximum amplitude of around 0.26 m.s^{-1} and RMSE of 0.017 m.s^{-1}. Consistent with (Marchesiello et al., 2021), the velocity profile of the deep breaking case with $\theta = 13°$ (dashed pink line) is more symmetrical, centered further offshore around the outer surf zone and with a larger maximum amplitude of 0.34 m. s^{-1} (RMSE = 0.076 m.s^{-1}). In the deep breaking case, a cross-shore advection process is missing, which would shift the longshore drift towards shallower water, where dissipation is greater. The effect of this process is generally emulated in Boussinesq models with a roller-type parameterization (Svendsen, 1984; Schäffer et al., 1993). Reducing the wave angle to $\theta = 10°$ (solid pink line) reduces the amplitude bias of the longshore drift (maxima of 0.28 m.s^{-1}, RMSE = 0.056 m.s^{-1}), but the position bias remains. For this reason, we reserve the use of pseudo-2D simulations for a semi-idealized case with no longshore drift (Sec. IV.2.5).

IV.2.4.4 Dye transport alongshore

In what follows, we use the longshore mean bathymetry (see Figure 1 of Hally-Rosendahl & Feddersen, 2016), which is more representative of the whole domain, instead of the bathymetry along the cross-shore measurement array (f1-f6). To ensure that the dye is transported along the coast at the observed speed, we perform the same analysis as Hally-Rosendahl and Feddersen (2016), i.e. following the leading edge of the plume downstream. The leading edge of the observed dye plume $y_{p_o}(t)$ is defined as the furthest downstream location where the observed concentration exceeds 3 ppb within a 40 m distance of x_b. The model location y_m is defined in the same way. We are concentrating here on the first 10^4 seconds, after which the dye extends outside the boundaries of the model domain. As shown in Figure IV.7, the CROCO simulation of dye extension along the coast is in good agreement with observations, confirming that the transport velocities of the model, due to wind and wave forcing, are adequate. The leading edge of the plume increases almost linearly, confirming the existence of almost constant forcing in the surf zone and inner shelf (wind stress) during the first four hours of the experiment. However, in the following sequence (see Fig. 6 of Hally-Rosendahl & Feddersen, 2016), transport increased. We will therefore limit our analysis to the first 4.5 hours of the experiment. Figure IV.8 shows an example of a surface concentration map of the modeled tracer, together with a surface concentration map derived from observations at 4.5 hours. Note the good agreement between model and data for the tracer, although only statistical agreement is possible as the model wave forcing is out of phase with the observations.

IV.2.4.5 Cross-shore dye extension

As we are focusing on the impact of vertical shear on cross-shore exchange, we now propose to evaluate the cross-shore profiles of dye concentration. Jetski observation in IB09 measured dye concentration up to 350 m offshore, revealing the full dynamics of tracer dispersion in the surf zone and inner shelf. In comparison, previous observational studies (Clark et al., 2010, 2011) presented cross-shore profiles reaching no further than 160 m offshore. It should be noted that the dye was well mixed vertically in the surf zone ($x > -80$ m), but was observed to be intensified at the surface on the inner shelf. Therefore, in order to fairly compare their depth-averaged funwaveC model solution with the surface dye concentration observed by jetski,

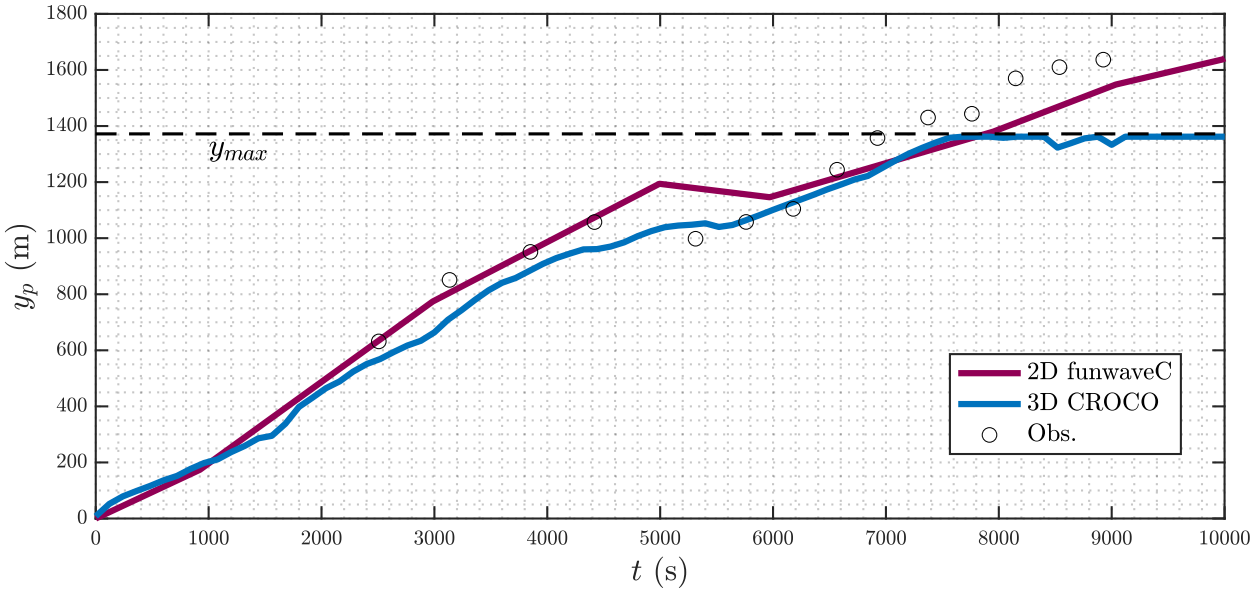

Figure IV.7 Observed (circles) and modeled longshore position y_p of the leading edge of the dye plume as a function of time in 2D (pink line) and 3D (blue line) simulations. The methodology is derived from Hally-Rosendahl and Feddersen (2016). The horizontal gray dashed line represents the downstream boundary of the model domain.

Hally-Rosendahl and Feddersen (2016) assumed the following relationship:

$$D_{obs}(x) = \left(\frac{h_{dye}}{h}\right) D^s_{obs}(x) \tag{IV.24}$$

where D^s_{obs} is the observed surface dye concentration, D_{obs} the estimated depth-averaged dye concentration and $h_{dye} = \min(h(x), 2.7 \text{ m})$ the depth to which the dye is detected. In the present study, we also hope to improve the accuracy of our comparison by applying the same relationship to surface dye concentration of the 3D simulation. We thus compare the estimated depth-mean dye concentration in all cases (observation, 2D and 3D models). The resulting cross-shore profile is also time-averaged over the observed period (see shaded area in Fig. 7 of Hally-Rosendahl & Feddersen, 2016), which spans around 4.5 hours.

The transect at $y = 1069$ m (position shown in Fig. IV.8) is presented in Figure IV.9. This transect is of particular interest in our study as it encompasses many rip events that occurred from the release point to the transect in 4.5 hours. It is therefore less sensitive than near-field measurements to dye release conditions and to the chaotic occurrence of individual events, making it statistically more significant (it should be stressed again that our JONSWAP reconstruction of wave forcing is not in phase with observations and is only relevant from a

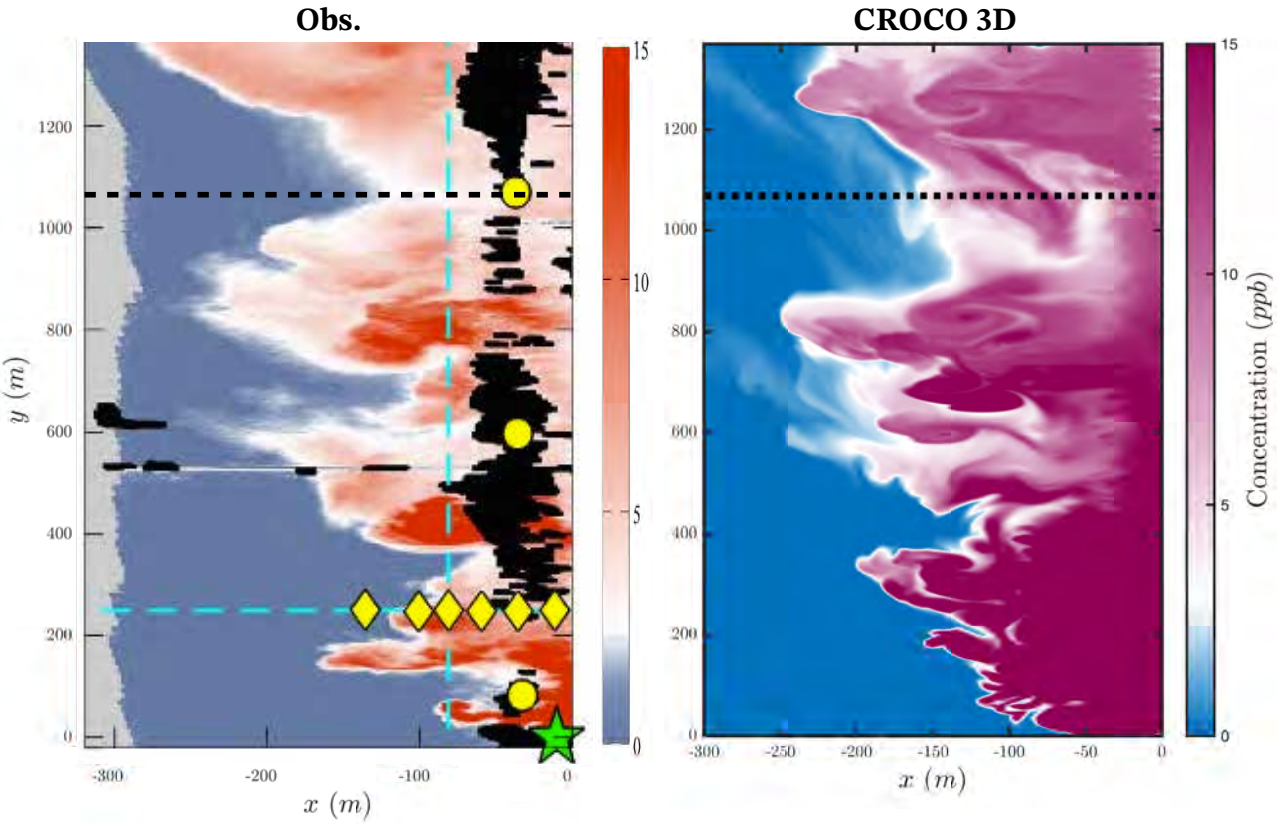

Figure IV.8 Snapshot of surface tracer concentration 4:53 h after release for the IB09 observations (left, modified from Hally-Rosendahl and Feddersen (2016)) and 4:29 h for the 3D CROCO simulation (right). In the observations, the vertical cyan dashed line separates the inner shelf from the surf zone, and the horizontal cyan line separates the near-field from the far-field tracer region. The green star represents the tracer release position, while the yellow diamonds and circles represent the positions of tracer measurement. The horizontal dashed black line represents the 1069 m transect shown in Fig. IV.9.

statistical point of view). To confirm statistical reliability, we ran a series of simulations, slightly modifying the dye release conditions (position, flux) and the wave forcing phase. The 1069 m cross-shore profile showed little variance, unlike the transects closer to the source ($y < 248$ m).

Figure IV.9 shows major differences between funwaveC (2D) and CROCO (3D) simulations. The 3D model is strikingly close to observation (RMSE = 0.42 ppb) and, in particular, closely matches the exponential-type decay found on the inner shelf. The depth-averaged funwaveC simulation, on the other hand, deviates more significantly from the data (RMSE = 1.18 ppb), showing a lower concentration in the surf zone but higher on the inner shelf where a linear decay extends further offshore (at $x = -200$ m, the dye concentration is twice as high as the data or the 3D model calculation). In both simulations, the tracer is well mixed in the surf zone, even extending slightly outside (approximately 1.5 x_b), but then, the decay is much sharper in 3D model as in the observation. These first results, validated with field data, will serve as a basis

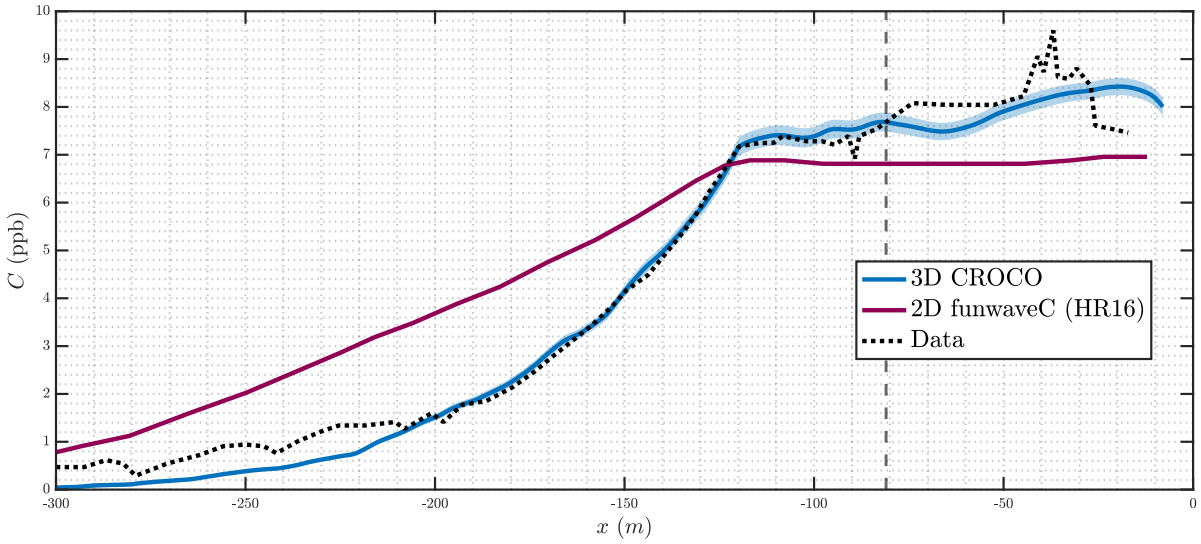

Figure IV.9 Cross-shore profile of time-averaged dye concentration at station SA4 of experiment IB09, 1069 meters downstream of the dye release. Observations are represented by a dashed black line, the funwaveC simulation of Hally-Rosendahl and Feddersen (2016) by a pink line and the CROCO simulation by a blue line. The blue shaded area represents the standard error of CROCO simulation ($\sigma/\sqrt{\mathcal{N}}$ with $\mathcal{N}$ the number of points in the series). The gray dashed vertical line indicates the surfzone edge.

to understand in the following analyses the role of 3D processes, in particular of the vertical shear, on tracer dispersion.

IV.2.5 Analysis and sensitivity

IV.2.5.1 A framework for separating processes

The previous comparison with the IB09 experiment suggests that three-dimensional processes have a significant effect on tracer dispersion, and we now need to understand what these processes are and quantify them in terms of diffusivity. We will also carry out sensitivity tests on the impact of various factors in the 3D simulations. To achieve this, the IB09 configuration presented in Section IV.2.4 needs to be simplified. Waves are taken normal to the coast, and longshore wind stress is removed, so that there is no mean longshore current and the tracer can only move offshore on average. Consequently, the tracer must now be injected as a longshore uniform, continuous source between $x = -10$ and $x = 0$ m (location similar to IB09). These changes allow us to calculate mean statistics on both time and longshore direction, focusing on cross-shore dispersion. The grid size is 1 m and the domain size is reduced in the longshore direction to $L_y = 500$ m. Finally, we remove the thermal stratification in the reference simulation, but its

addition will be tested later, along with that of wind and Coriolis force.

Each simulation is designed to highlight a particular process (Table IV.2). With shore-normal waves, the only wave-driven processes considered are : flash rips, mini-rips and shear dispersion.

The presence of flash rips depends on the directional spread of the waves. Here, we generate short-crested waves with a directional spread of 10°. In pseudo-2D CROCO simulations with deep breaking, flash rips represent the only resolved dynamical process. With shallow breaking, mini-rips are naturally generated by the vertical shear flow as long as an initial perturbation is present. We can avoid flash rips by forcing long-crested waves (no directional spread), but, in this case, a small perturbation must be added to the bathymetry (or, alternatively, to the initial velocity fields) to trigger the initial shear instability required for mini-rips. Finally, the shear dispersion process (defined in the introduction) is also present in all shallow breaking simulations, since only vertical flow variations and vertical mixing are required. When no bathymetric perturbation is added and long-crested waves are used as forcing, shear dispersion is the only process allowed in the model.

We also investigate the role of *ad-hoc* background diffusivity, as this parameterization is always present in Boussinesq-type model simulations (Geiman et al., 2011). For our deep breaking tests, where flash rips represent the only resolved process affecting tracer dispersion, the background diffusivity is set at a value similar to the diffusivity estimated from 3D simulations, when flash rips are precluded ($\kappa_0^a \sim 0.3$ m^2.s^{-1}; see below). Another 2D simulation test is performed with a lower diffusivity value of $\kappa_0^b = 0.075$ m^2.s^{-1}, in line with funwaveC in Hally-Rosendahl and Feddersen (2016).

In addition, we will briefly test innershelf processes that are often ignored in nearshore studies, but which may have an impact on cross-shore dispersion. They are associated with wind stress, thermal stratification and Coriolis force. We describe these processes here as "innershelf" because their impact in the surf zone is rightly assumed to be negligible or of secondary importance. For the tests, we use the longshore wind stress value of IB09 conditions, i.e. $\tau_w = 0.85$ N.m^{-2}. Thermal stratification is also set from IB09 as $\partial T/\partial z = 0.06$ °C.m^{-1} ($N^2 = 10^{-4}$ s^{-1}), which represents mild stratification in Southern California (Hally-Rosendahl et al., 2014). The Coriolis parameter is $f = 10^{-4}$ s^{-1}, typical of mid-latitudes. We do not consider here the possibility of cross-shore winds, assuming that coastal winds outside storms tend to line up with the coast, due to land drag, coastal ranges or the Coriolis force (Renault et al., 2016). Although this is a

Table IV.2 List of CROCO simulations for the semi-idealized IB09 configuration, allowing comparison between wave-driven processes.

Simulation	Breaking	Shear dispersion	Mini-rips	Flash rips	κ_0
3D-ShearD	shallow (3D)	✓			
3D-MiniR	shallow	✓	✓		
3D-FlashR (reference)	shallow	✓	✓	✓	
2D-κ_0^a	deep (2D)				0.3 $m^2.s^{-2}$
2D-κ_0^a-FlashR	deep			✓	0.3 $m^2.s^{-2}$
2D-κ_0^b-FlashR	deep			✓	0.075 $m^2.s^{-2}$
2D-FlashR	deep			✓	

rather crude assumption, we consider that a complete study of the effect of wind is beyond the scope of the present study.

Table IV.3 List of CROCO simulations for semi-idealized IB09 configuration, allowing comparison between inner shelf forcing processes: longshore wind (W), thermal stratification (S) and Coriolis force (C).

Simulation	Alongshore wind	Stratification	Coriolis
3D Reference			
3D Wind	$\tau_w = 8.5 \times 10^{-5}$ $m^2.s^{-2}$		
3D Stratification		$N^2 = 10^{-4}$ s^{-1}	
3D Coriolis			$f = 10^{-4}$ s^{-1}

Finally, we ran a small set of 5 simulations with the 3D reference configuration, varying the random wave phase used in the wavemaker (the only non-deterministic parameter in the configuration). The ensemble average will provide a measure of the standard error in our analysis.

IV.2.5.2 Wave-driven processes

Figure IV.10 shows snapshots of depth-averaged tracer concentration 7000 s after the start of release for each test case (Tab. IV.2). In 3D-ShearD, shear dispersion alone produces a uniform spread of the tracer up to 100 m from the coast, due to advection by the undertow. At

$x < -100$ m, vertical shear is greatly reduced (see Fig. IV.6) and shear dispersion no longer operates. The visual extension of the tracer is quantitatively confirmed by the evolution of $x_{99\%}$ shown in Figure IV.11, which defines the offshore boundary where 99% of the tracer mass is concentrated. When vertical shear instability is triggered by small perturbations, mini-rips are generated in addition to shear dispersion (3D-MiniR) presenting numerous finger-like (or rib-like) structures with a longshore length scale of about 5 m. As with shear dispersion, the mini-rips depend on vertical shear and only extend about 30 m beyond the surf zone, due to rip advection (see Figure IV.11). On the other hand, the tracer appears to be better mixed in the surf zone than with shear dispersion alone. The inclusion of short-crested waves in the simulation (3D-FlashR) produces surf eddies and flash rips that result in large plumes extending far offshore to $x < -300$ m, i.e. approximately three times the width of the surf zone (80 m), in line with previous studies (Kumar & Feddersen, 2017c). This is more of a stirring process and, due to the large recirculation cells that carry tracer-free water to shore, tracer concentration is not evenly distributed in the surf zone, although the imprint of mini-rips remains visible (see for example at $y = 50$ m).

These 3D cases are now compared with 2D simulations (Fig. IV.10, bottom). When flash rips are excluded (long-crested waves) and background diffusion is the only active process (case 2D-κ_0), the tracer extends slowly offshore, but this time without limitation (Fig. IV.11), unlike in the case of shear dispersion or mini-rips, since κ_0 is imposed over the whole domain. When short-crested waves are included (2D-FlashR and 2D-κ_0-FlashR), background diffusivity seems to affect dispersion. When $\kappa_0 = 0$ m^2.s^{-1}, rips and eddies produce sharp and narrow filaments, indicating a classic stirring process of 2D turbulence. Much of the tracer remains constrained near the shoreline, where the concentration is higher than in any other simulation. This is particularly clear in the recirculation regions (around $y = 1500$ m for example), where advection can deplete the tracer almost to the shoreline, while in the 3D simulation diffusion remains active within the surfzone. When κ_0 is activated, the filaments appear more diffuse and the tracer patterns are more comparable to the 3D case, although the filaments now appear to extend further offshore. The effect of background diffusivity has been reported in previous studies (e.g. Fig. 19 of Geiman et al. 2011) as helping the simulation to appear more realistic.

The fate of tracer concentration is determined by velocity fields and is reflected, in particular, in vorticity patterns, as shown in Figure IV.12. The rib structure of mini-rips is striking in the

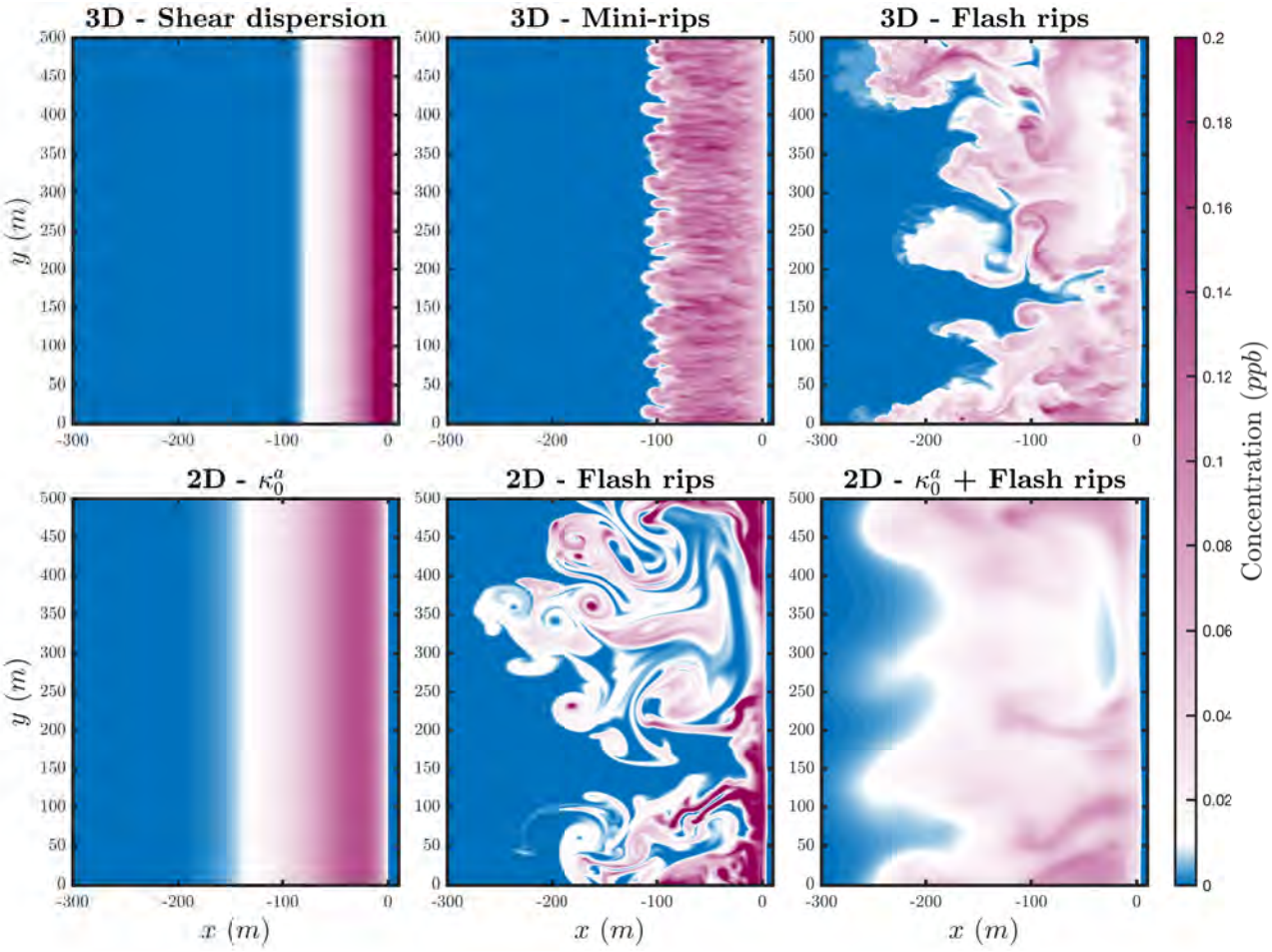

Figure IV.10 Snapshots of depth-integrated tracer concentration (normalized by mean depth) for different simulations 6000 s after the start of release. 3D simulations are shown in the top panels: shear dispersion only (left); shear dispersion and mini-rips (middle); and shear dispersion, mini-rips and flash rips (right). 2D simulations are shown in the bottom panels: background diffusion only (left); flash rips only (middle); and flash rips with background diffusion (right).

3D-MiniR simulation, with a longshore scale ($\sim$ 5 m) and a time scale ($\sim$ 100 s) determined by the intensity of the shear flow (Marchesiello et al., 2021). This pattern remains visible in the 3D-FlashR case, cross-hatching the surf zone, while the large-scale filaments have a fragmented appearance (Sous et al., 2005), suggesting a forward cascade of energy (Uchiyama et al., 2017; McWilliams et al., 2018). In the 2D case, the large-scale flash rips are present but the small-scale vorticity pattern looks quite different, with no rib structure and more coherent surf eddies, as previously reported (Marchesiello et al., 2021).

Analysis of criterion Q from Figure IV.13, where $Q = -\frac{1}{2}\frac{\partial u_i}{\partial x_j}\frac{\partial u_j}{\partial x_i}$ in Einstein notation, can help us better understand how mini-rips work. It allows us to isolate and observe the various stages of 3D instability. In the first stage, just a few seconds after the first waves hit the shore, primary

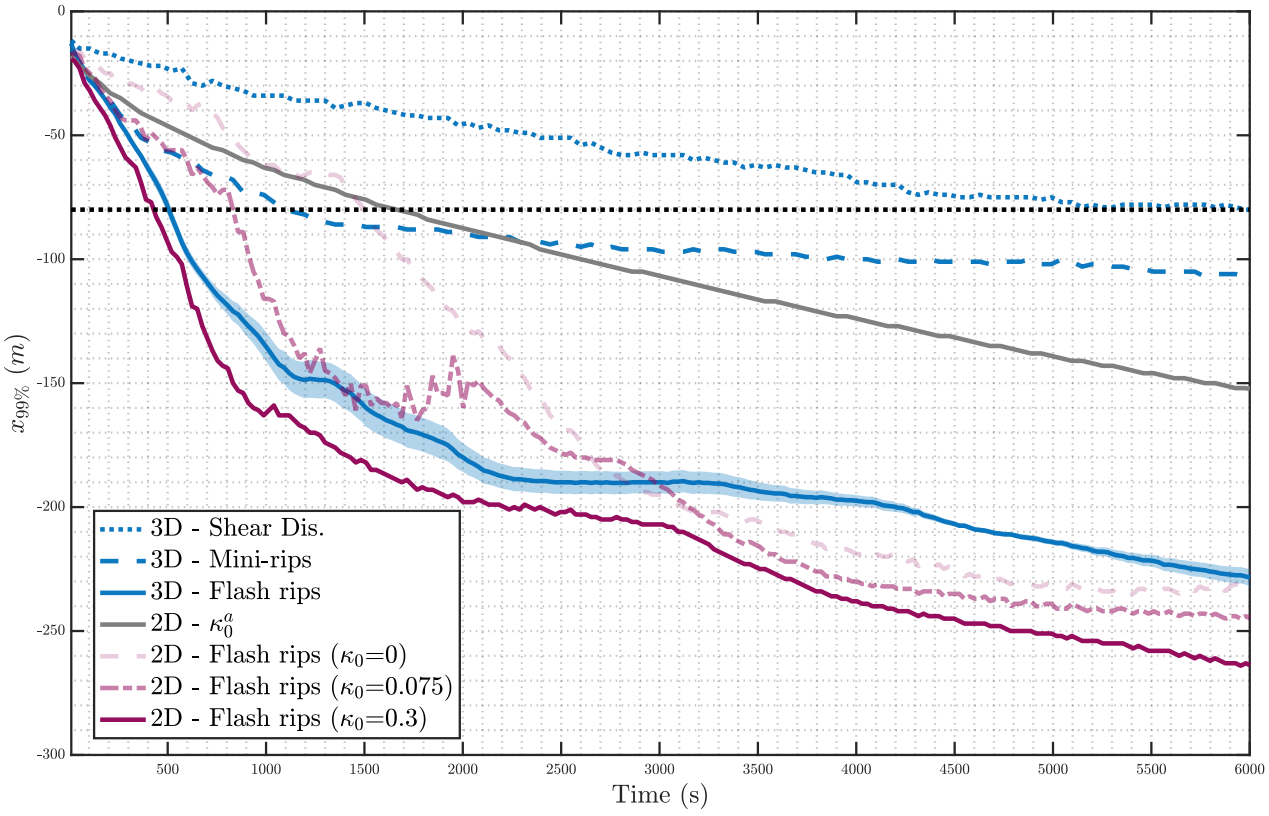

Figure IV.11 Time evolution of the seaward tracer extension, defined as the offshore limit bounding 99% of the tracer mass, for the idealized IB09 simulations described in Table IV.2. The shaded area represents the standard error of ensemble simulations of 3D-FlashR ($\sigma/\sqrt{\mathcal{N}}$ with $\mathcal{N}$ the number of simulations performed). The horizontal black dashed line denotes the surfzone edge.

Kelvin-Helmholtz instabilities develop under the effect of vertical shear, giving rise to large spanwise billows (Fig. IV.13a, red). These billows already begin a three-dimensional evolution, as longshore disturbances trigger secondary shear instabilities that develop into streamwise whirls (Fig. IV.13b, green). In the final stage, these whirls, which we call mini-rips, extend across the width of the surf zone and play an active part in mixing.

According to linear stability theory of mixing layers (Pierrehumbert & Widnall, 1982; Metcalfe et al., 1987), the spanwise wavelength of the primary instability is 14δ, δ being the mixing layer width. We estimate δ at ~ 0.35 m from visual inspection of the mean shear (Fig. IV.6), which gives a wavelength of about 5 m. Mini-rips resulting from the secondary instability have a similar wavelength (2/3 in Pierrehumbert & Widnall, 1982). This theoretical wavelength is consistent with the visual estimate in figures IV.12 and IV.13, as well as with the wavenumber spectrum of the 3D_MiniR simulation (not shown). The theoretical frequency of the most

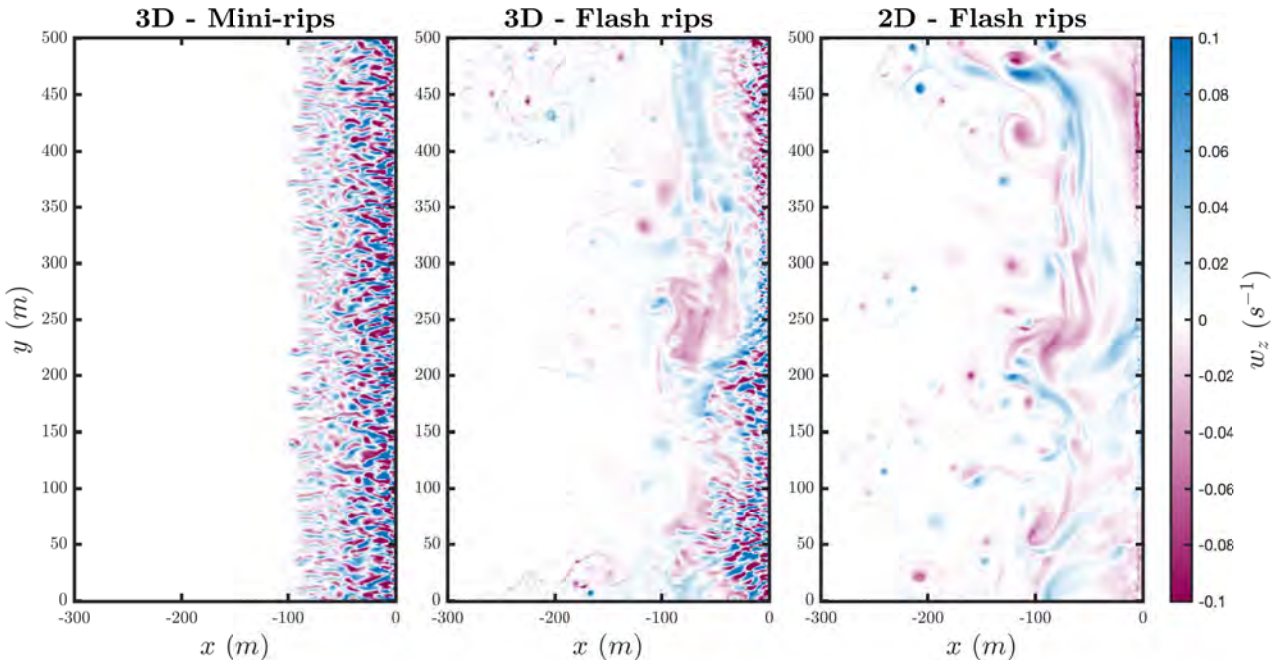

Figure IV.12 Snapshots of surface vertical vorticity for 3 cases with shore-normal forcing (idealized IB09): 3D simulation of mini-rips with long-crested wave forcing (left); reference 3D simulation (center); and pseudo-2D simulation (right).

unstable waves is 0.015 $\frac{U}{\delta} \sim 0.009$ Hz ($T \sim 110$ s), with U=0.2 m/s , the undertow velocity, which is in the infragravity range. Mini-rips can also develop localized pairing, as suggested by the diamond pattern in Figure IV.13, which is evidence of subharmonic resonance, another instability associated with shear layers (Craik, 1971; Pierrehumbert & Widnall, 1982; Metcalfe et al., 1987). This description recalls the schematic presentation of mini-rips proposed earlier (Fig. IV.1), based on their first depiction by Marchesiello et al. (2021).

Before turning to the quantification of tracer dispersion, the differences between the simulations presented can be synthesized using cross-shore profiles of eddy kinetic energy (EKE; Fig. IV.14). Here, EKE is depth-integrated (and normalized by mean h) in order to compare 2D and 3D simulations. The simulation where background diffusivity is the only acting process does not produce EKE and is not shown. The ensemble members of the reference case is used to estimate standard error for comparison with other cases. In the case of total (unfiltered) EKE (Fig. IV.14, top), shear dispersion is the least energetic process (0.003 $m^2.s^{-2}$ in the surf zone) because the energy results solely from the variability of wave forcing, and not from any instability process. Mini-rips exhibit more energy, with a peak near the shoreline about 4 times that of shear dispersion, but the EKE is also confined to the surf zone. With flash rips, 2D

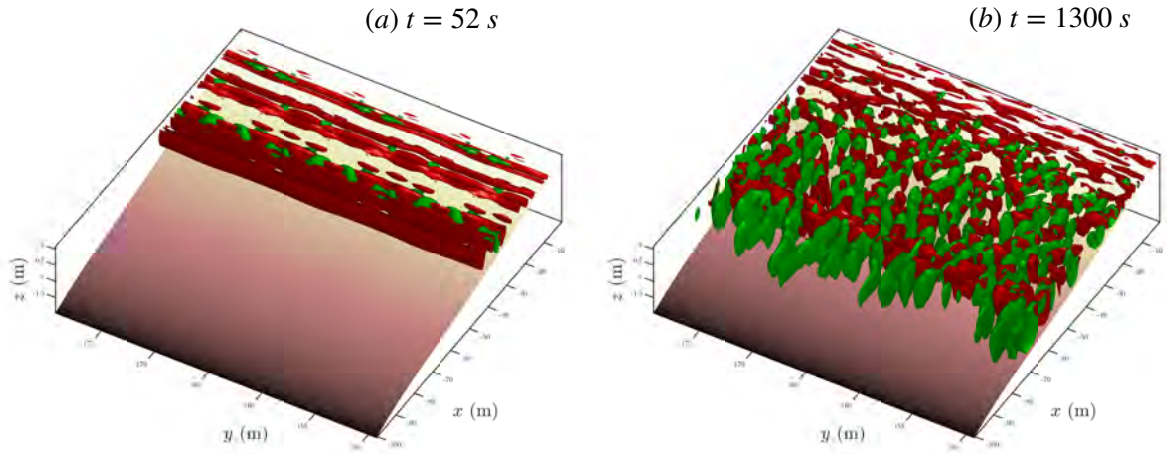

Figure IV.13 Q field defined by $Q = -\frac{1}{2}\frac{\partial u_i}{\partial x_j}\frac{\partial u_j}{\partial x_i}$, showing coherent structures of roll and rib vortices typical of 3D shear instability at (a) $t = 52$ s and (b) $t = 1300$ s. Cross-shore and alongshore Q terms are split: spanwise rolls (along wave crests) are identified by $Q_y = -\frac{\partial u}{\partial z}\frac{\partial w}{\partial y} - \frac{1}{2}\frac{\partial u}{\partial x}^2$ in red; and streamwise ribs (across wave crests) are identified by $Q_x = -\frac{\partial v}{\partial z}\frac{\partial w}{\partial y} - \frac{1}{2}\frac{\partial v}{\partial y}^2$ in green. The fields are normalized. Only the positive isosurface values of 0.05 are plotted.

and 3D simulations have total EKE of similar magnitude in the surf zone. The 3D case gives a slightly higher energy in the inner surf zone, due to the additional presence of mini-rips and onshore advection, but the main difference appears on the inner shelf, where the EKE is much higher in the 2D case (by a factor of 2 at $x = -150$ m). The contrast becomes even more striking when we examine the VLF part of EKE (calculated from low-passed filtered currents at $f < 0.003$ Hz; Fig. IV.14, bottom). While little residual energy remains in the cases of shear dispersion and mini-rips, plenty of VLF energy remains when flash rips are included, but with a clearer difference between the 2D and 3D cases (by a factor of 3 or more). The difference is essentially present over the inner shelf, where a reduction of KE inverse cascade in 3D simulations can be linked to vortex stretching, which limits the size and lifetime of vortices, and therefore their seaward extension (Marchesiello et al., 2021).

We now estimate bulk diffusivity in semi-idealized simulations. We separate our calculations between the diffusivity of the surf zone (κ_{xx}^{SZ}, with $L_x = 80$ m) and that of the whole domain (κ_{xx}, with $L_x = 350$ m). The results on bulk diffusivity are presented in Table IV.4, while tracer variance evolution is shown in Figure IV.15. To validate the method for estimating κ_{xx}, we rely on the simulation in which the background diffusivity $\kappa_0 = 0.3$ m^2.s^{-1} is the only source of mixing. κ_{xx} in this case takes the value of κ_0, as expected, giving us confidence on the method.

In the case of shear dispersion (3D-ShearD), κ_{xx} is approximately 0.05 m^2.s^{-1}. For compari-

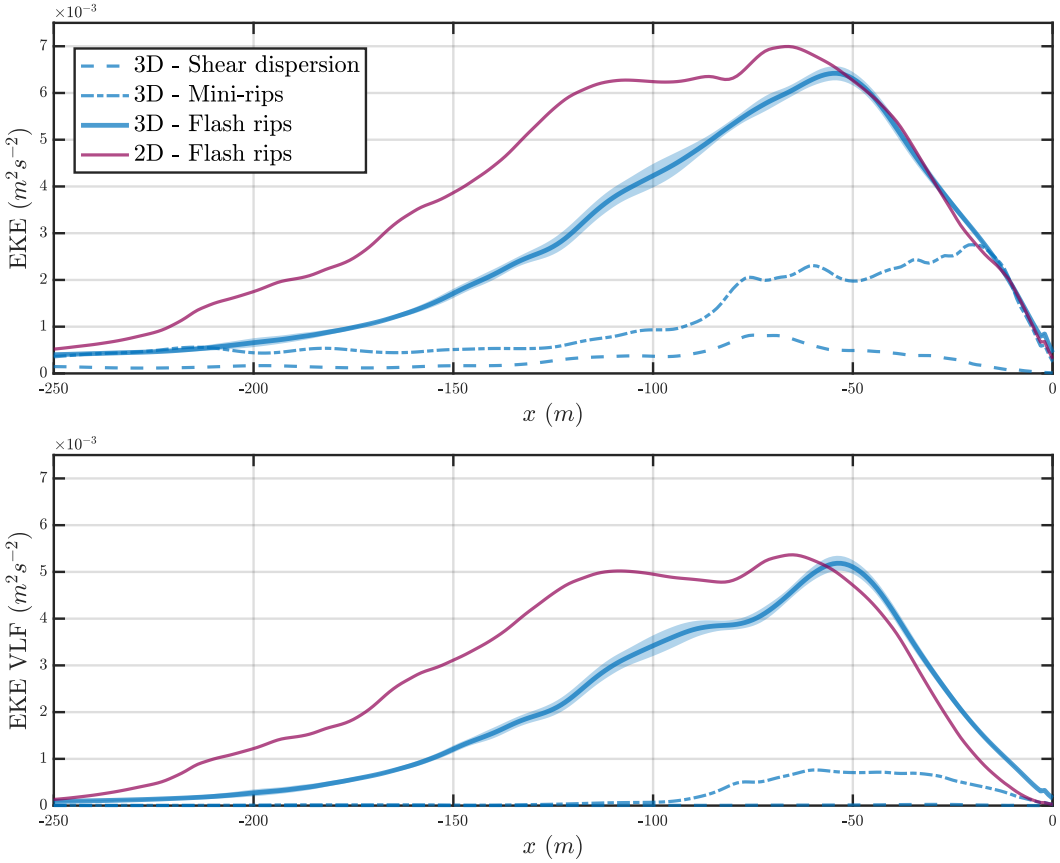

Figure IV.14 Cross-shore profile of depth-integrated (normalized by mean depth), time-averaged and longshore-averaged EKE for 4 different cases: 3D reference simulation (3D-FlashR; dark blue line); 3D simulation with shear dispersion only, generated by long-crested waves without any perturbation (3D-ShearD; light dashed blue line); same as 3D-ShearD but with small perturbations added, leading to mini-rips (3D-MiniR; light blue line); and pseudo-2D simulation (2D-FlashR; purple line). The top panel presents the total EKE of wave-averaged currents, while the bottom panel shows the EKE of VLF currents (low-pass filtered at $f < 0.003$ Hz). The shaded blue area shows the standard deviation from ensemble simulations of the reference case.

son, we consider the theoretical relationship for $\kappa_{xx}^{\text{ShearD}}$ in Eq. IV.1. Using the velocity profile in Figure IV.6, we have $U_- \sim -0.2$ m.s^{-1} and $U_+ \sim 0.1$ m.s^{-1}, then $\kappa_{zz} = 0.04$ m^2.s^{-1} and $h = 1$ m gives $\kappa_{xx}^{\text{ShearD}} \sim 0.047$ m^2.s^{-1}, which is very close to the estimate. Of all the mechanisms considered, shear dispersion has the least impact on tracer dispersion, as already suggested by Clark et al. (2010). In the presence of mini-rips (3D-MiniR), $\kappa_{xx} \sim 0.37$ m^2.s^{-1}, i.e., the diffusivity increases considerably to around 7 times that of shear dispersion alone. Note that κ_{xx} for mini-rips and shear dispersion is calculated with $L_x = 120$ m to remain in the linear growth regime, which is assumed in the estimation method. With $L_x = 350$ m, κ_{xx} would be deceptively low in these cases due to saturation. As an illustration, we see in Figure IV.15 that for $t < 5000$ s, the diffusivity of mini-rips is greater than $\kappa_0 = 0.3$ m^2.s^{-1} (gray line) but decreases significantly thereafter, as the tracer has filled the surf zone (see also tracer extension

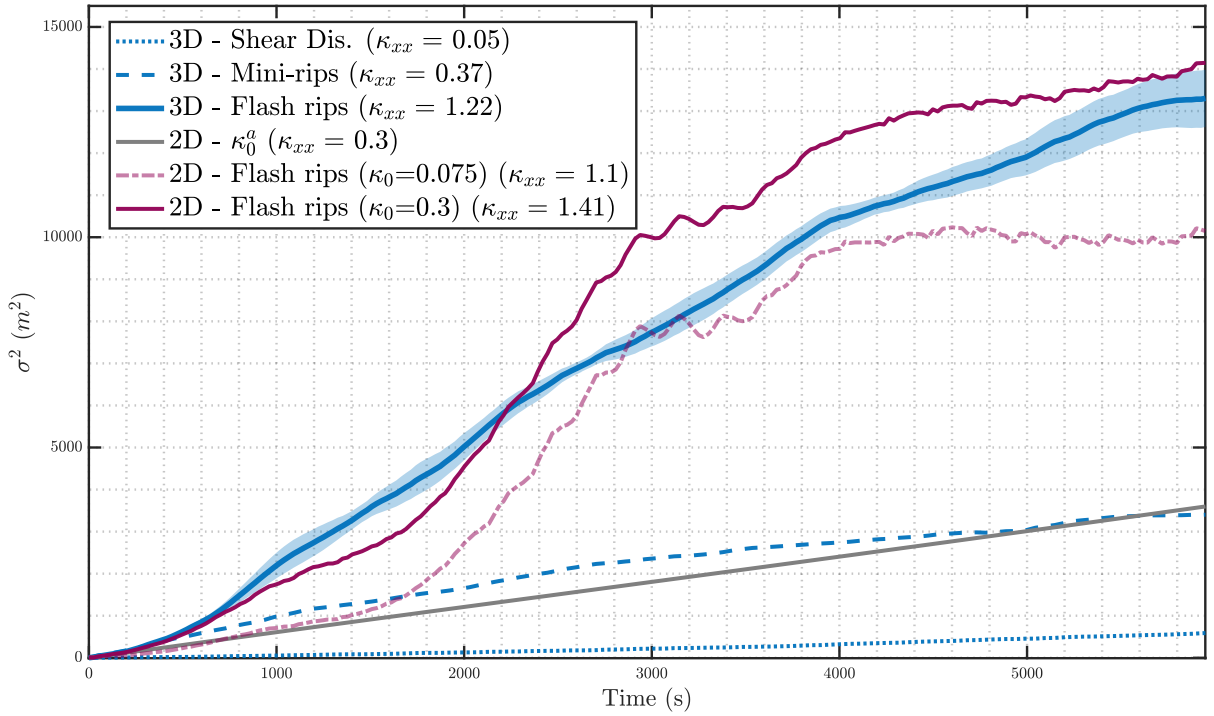

Figure IV.15 Cross-shore variance σ^2 of tracer concentration as a function of time for the idealized IB09 simulations described in Table IV.2. The shaded area represents the standard error of the ensemble simulations of 3D-FlashR ($\sigma/\sqrt{\mathcal{N}}$ with $\mathcal{N}$ the number of simulations performed).

in Fig. IV.11).

In the case of short-crested waves and flash rips, diffusivity reaches unprecedented levels. The 3D simulation gives $\kappa_{xx} \sim 1.22$ m^2.s^{-1}, which is consistent with previous results, after a ballistic regime lasting around 500 s. In 2D simulations, the diffusivity can reach more than 1.4 m^2.s^{-1}, depending on the use of background diffusivity. As shown in Figure 20 of Geiman et al. (2011), low background diffusivity introduces a delay in tracer diffusion from the point of origin. Our results confirm this. Without background diffusivity (not shown), it takes 6,000 s for the 2D simulation to reach the dispersion level of the 3D simulation, even though the wave forcing is the same. This is consistent with the idea that flash rips are an effective stirring mechanism, generating filaments of increasing gradients in the concentration field, but depend on other processes (molecular diffusion where turbulent processes are lacking) to arrest the filamentation and transition from a stirring to a mixing phase (Eckart, 1948). When $\kappa_0^b = 0.075$ m^2.s^{-1}, the initial stirring phase is shorter, but it takes $\kappa_0^a = 0.3$ m^2.s^{-1} to reach a dispersion level equivalent to that of mini-rips in the first 1000 s. In this 2D case, the variance σ_{2D}^2 reaches much higher values than in the 3D case. Our results suggest that background diffusivity is

necessary in depth-averaged models because they lack a significant mixing process in the surf zone, such as mini-rips, complementing the stirring by larger scales (flash rips). In this case, the overestimation of VLF by depth-averaged models results in a greater seaward extension of the tracer plume (Fig. IV.11).

Focusing on the surf zone (Tab. IV.4), we find that shear dispersion has a diffusivity κ_{xx}^{SZ} close to κ_{xx} (≈ 0.05 m^2.s^{-1}) as this process is limited to the surf zone. In 3D-miniR, κ_{xx} is a little higher than κ_{xx}^{SZ} as the mini-rips extend slightly further offshore than the surf zone. It is particularly interesting to note that κ_{xx}^{SZ} is similar for the 3D-FlashR and 3D-MiniR cases, meaning that mini-rips, and not flash rips, represent the dominant process in the surf zone. This is somewhat confirmed by the 2D cases, where κ_{xx}^{SZ} is very small (≈ 0.06 m^2.s^{-1}) when no background diffusion is added. Background diffusion therefore plays the role of mini-rips in the surf zone.

Table IV.4 Estimated cross-shore diffusivity for all semi-idealized simulations in the surf zone ($L_x = 80$ m) and in the entire domain. Tracer concentration is depth-averaged to ensure fair comparison between 2D and 3D cases. Standard errors (from linear regression) are displayed along with correlation coefficient r^2.

Simulation	Surf zone κ_{xx}^{SZ}	Total κ_{xx}
3D-ShearD	**0.05** $\pm$ 0.00 ($r^2 = 0.98$)	**0.05** $\pm$ 0.00 ($r^2 = 0.97$)
3D-MiniR	**0.44** $\pm$ 0.01 ($r^2 = 0.99$)	**0.37** $\pm$ 0.01 ($r^2 = 0.99$)
3D-FlashR	**0.49** $\pm$ 0.03 ($r^2 = 0.98$)	**1.22** $\pm$ 0.02 ($r^2 = 0.99$)
2D-κ_0^a	**0.27** $\pm$ 0.00 ($r^2 = 0.99$)	**0.30** $\pm$ 0.00 ($r^2 = 1.0$)
2D-FlashR	**0.06** $\pm$ 0.00 ($r^2 = 0.65$)	**0.91** $\pm$ 0.03 ($r^2 = 0.88$)
2D-κ_0^b-FlashR	**0.15** $\pm$ 0.01 ($r^2 = 0.82$)	**1.10** $\pm$ 0.02 ($r^2 = 0.91$)
2D-κ_0^a-FlashR	**0.34** $\pm$ 0.02 ($r^2 = 0.97$)	**1.41** $\pm$ 0.02 ($r^2 = 0.94$)

The residence time of contaminants in the surf zone is a useful indicator for beach public policy. To provide a rapid assessment of this indicator, we calculated the ratio of surfzone tracer mass to the total domain tracer mass, which indicates how much tracer remains in the surf zone. The evolution of this ratio is then fitted with an exponential function of time: $C(t) = C_0 e^{-\lambda t}$ (e.g., Das et al. 2000). We find that the e-folding residence time, $\frac{1}{\lambda}$, is approximately 2600 s. Inman et al. (1971) proposed a dimensional relationship for the diffusion time scale in the surf zone: $T_f = \frac{W^2}{4\kappa_{xx}}$, where W is the half-width of the surf zone and κ_{xx} the surfzone diffusivity.

Assuming that surfzone residence time is not related to surfzone mixing but to dispersion from it, we propose a modified relationship, where W m is taken as half the maximum tracer extent ($\sim$ 230 m for 3D-FlashR), and $\kappa_{xx} = 1.22$ m^{2}s^{-1} is the bulk diffusivity over the whole plume extension. This gives a time scale of 2710 s, consistent with the e-folding residence time.

IV.2.5.3 Sensitivity to innershelf forcing

We propose here to test the sensitivity of our tracer dispersion estimates to the processes that primarily affect the inner shelf: Coriolis force, thermal stratification and longshore wind stress. This is a preliminary approach, and we reserve a more explicit sensitivity study for the future. Nevertheless, by testing each of these forcing factors, we aim to provide at least a range of their effects on innershelf dynamics and associated tracer dispersion. Importantly, surfzone dynamics in our simulations are unchanged by the addition of these innershelf forcing (see surfzone diffusivity in Table IV.5).

The most significant impact on tracer dispersion is observed with longshore winds, which substantially increase cross-shore tracer variance σ^2 (Fig. IV.16), resulting in estimated diffusivity about 10% higher than in other cases (Tab. IV.5). Longshore wind stress enhances turbulent mixing on the inner shelf, leading to faster dispersion than in the reference simulation and achieving maximum extension nearly 2000 seconds earlier. Note that the difference seems more striking on the evolution of σ^2 in Figure IV.16, but there is saturation and the final tracer width is similar to that of the reference case.

The Coriolis force does not appear to have a significant impact on tracer dispersion, with σ^2 and bulk diffusivity similar to the reference case, although the final tracer extension is somewhat smaller. A similar lack of statistical validity on the depth-averaged diffusivity is presented in the case of stratification. However, stratification has a large impact on the vertical structure of tracer concentration on the inner shelf, clearly visible in Figure IV.17 after nearly 2 hours of simulation. Stratification tends to produce a strong vertical gradient, with surface-intensified concentration extending 50 m further offshore. This is consistent with recent results from observation and modeling of bathymetric rip currents (Moulton et al., 2021) and from modeling of transient rip currents (Grimes et al., 2020b), which show increased spreading of a near-surface buoyant layer in diurnal conditions (warmer surf zone). In our case, tracer confinement at the surface is due to a reduction of vertical turbulent mixing by the buoyancy effect of stratification

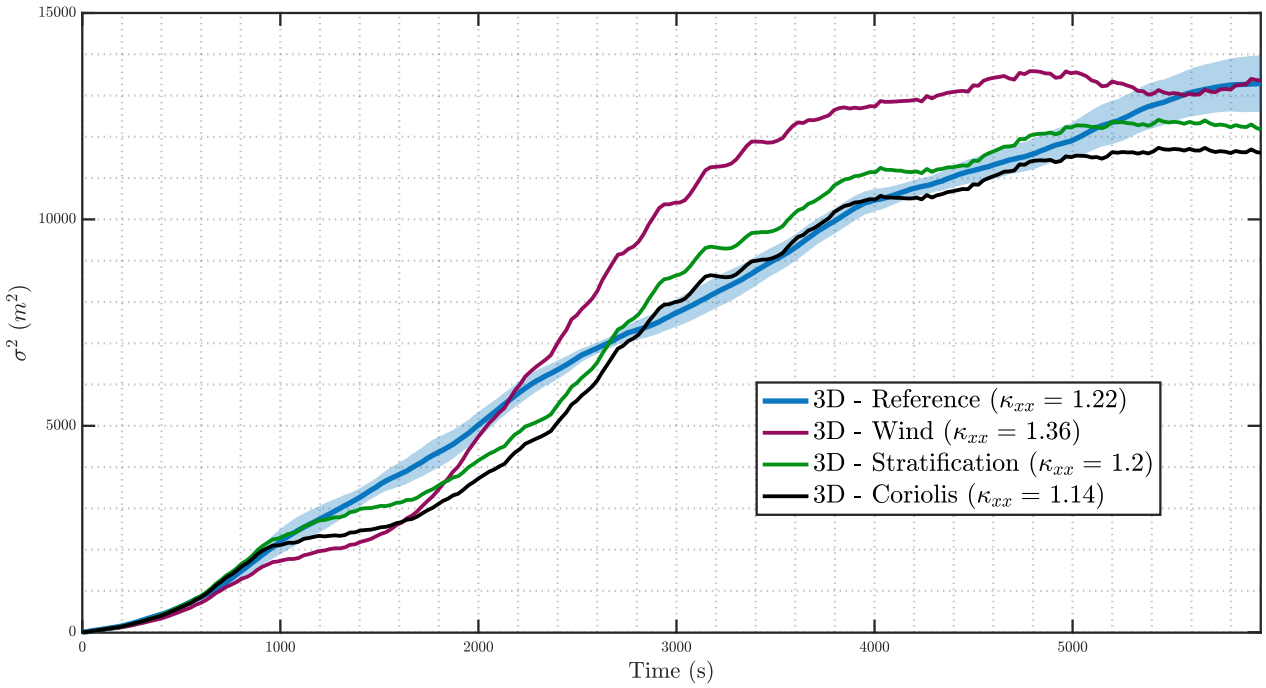

Figure IV.16 Cross-shore variance σ^2 as a function of time for idealized IB09 simulations with the addition of the innershelf processes described in Table IV.3.

(in the $k-\omega$ model). Although these results are preliminary and lack further parametric study, they demonstrate CROCO's ability to handle the effects of surfzone and shelf processes within the same framework (in the case of stratification, the correction of turbulence closure for non-breaking waves was decisive). Further efforts are needed to fully understand how transient rip currents interact with shelf dynamics.

Table IV.5 Estimated bulk diffusivity for semi-idealized simulations with added inner shelf processes.

Simulation	Surf zone κ_{xx}^{SZ}	Total κ_{xx}
3D Reference	**0.49** $\pm$ 0.03 ($r^2 = 0.98$)	**1.22** $\pm$ 0.02 ($r^2 = 0.99$)
3D Stratification	**0.37** $\pm$ 0.03 ($r^2 = 0.94$)	**1.2** $\pm$ 0.02 ($r^2 = 0.96$)
3D Coriolis	**0.42** $\pm$ 0.03 ($r^2 = 0.98$)	**1.15** $\pm$ 0.02 ($r^2 = 0.95$)
3D Wind	**0.39** $\pm$ 0.02 ($r^2 = 0.89$)	**1.36** $\pm$ 0.03 ($r^2 = 0.9$)

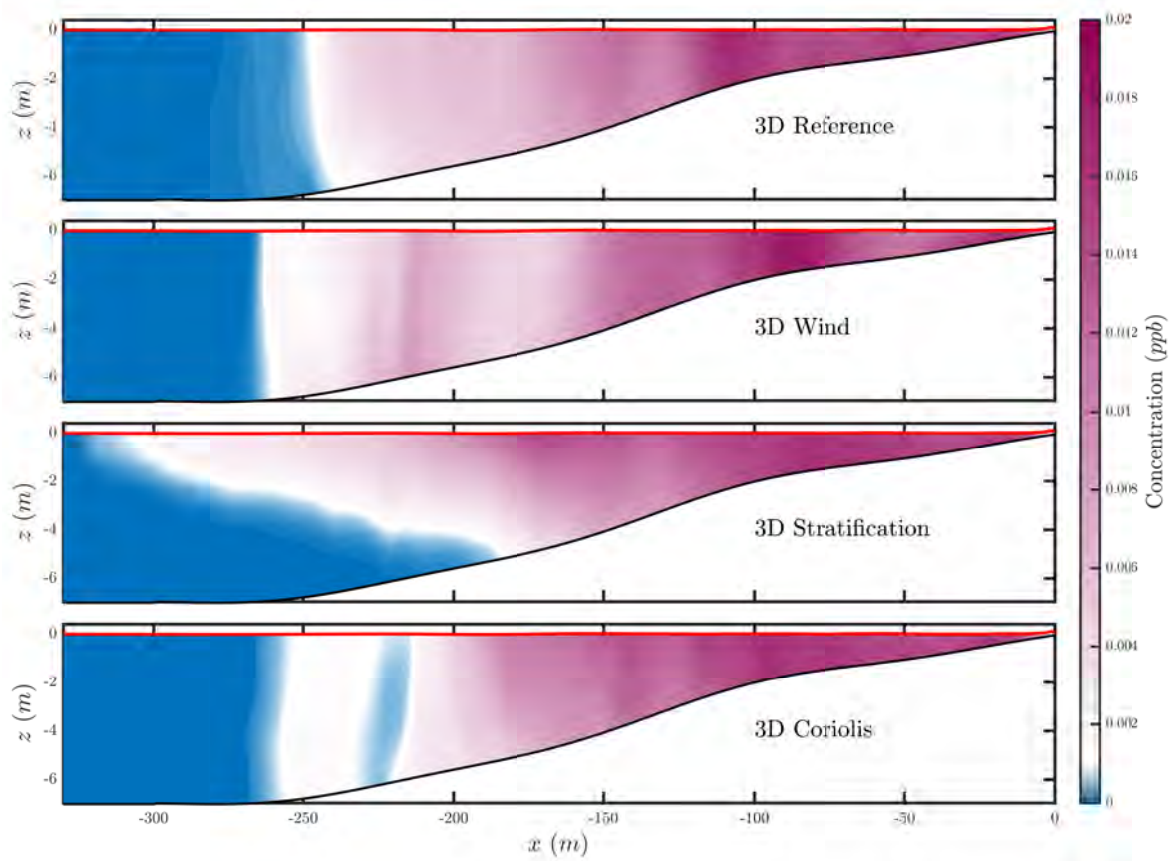

Figure IV.17 Cross-shore sections (longshore averaged) of tracer concentration (ppb) at $t = 6000$ s for the reference simulation 3D_FlashR (top); with added longshore winds (second from top); with stratification (third from top); and with Coriolis force (bottom).

IV.2.6 Discussion and conclusion

The majority of studies examining tracer dispersion by transient rip currents in coastal areas have employed depth-averaged models, assuming uniform vertical velocity profile in the surf zone and thus neglecting the potential influence of vertical shear. Recent research has challenged this hypothesis, pointing to the important role played in nearshore dynamics by the vertical shear associated with surface-intensified breaking acceleration, balanced by seaward undertow. Advances in numerical modeling have introduced the use of three-dimensional free-surface wave-resolving models, such as CROCO. These cost-effective models enable innovative research into issues such as the role of vertical shear in flash rips. In particular, work by Marchesiello et al. (2021) has demonstrated a reduction in the inverse kinetic energy cascade in 3D dynamics and revealed a previously undocumented phenomenon known as mini-rips. The aim of the present study was to assess the impact of these results on tracer dispersion.

Two experiments allowed us to validate the model for tracer dispersion. The first experiment

in a directional wave basin (Baker et al., 2023c), was used to validate the hydrodynamics of the model as well as to give a qualitative assessment of tracer dispersion, leveraging the advantages of a highly controlled environment. The wave basin case was also used to test the model's ability to mimic the behavior of depth-averaged models. This confirmed our hypothesis that the main dynamical distinction between 2D and 3D models is the vertical profile of currents in the surf zone, and that an appropriate methodology for imitating a 2D model (our pseudo-2D model) is to increase the turbulent viscosity in this zone. Comparison of our pseudo-2D model with the widely-used FUNWAVE-TVD Boussinesq model gave considerable confidence in this approach. Subsequently, the model was used to simulate a short-term dye release during the experiment. Although based solely on RGB videos, the observed dye dispersion could be evaluated and compared very favorably with the predictions of our 3D model — conversely, the 2D simulation had obvious difficulties in representing the observed surfzone mixing, a result we then assessed in quantitative terms with semi-idealized experiments. The comparison with the wave basin experiment was mainly qualitative, and further laboratory experiments will be useful in the future, focusing on dye tracking under different wave conditions.

The second experiment of interest (IB09) is a large-scale dye release at Imperial Beach, California, which has given the community the means to study tracer dispersion due to flash rips on an unprecedented scale. Previous field studies had been limited in terms of time and cross-shore extension, and therefore confined to the surf zone. After calibration and validation of the model's hydrodynamics on IB09, a comparison of CROCO results on dye dispersion with those of the Boussinesq funwaveC model and with observations revealed the importance of vertical shear on tracer dispersion. The results on cross-shore dye extension are unambiguous and demonstrate the impact that a reduction in the inverse cascade by vertical shear can have on tracer dispersion. The overestimation of tracer spread over the inner shelf by depth-averaged models can therefore be corrected in a full 3D approach. In this case, reproducing the observations, the tracer is well mixed over an extended region from the surf zone (by around 50%), then decreases exponentially over the inner shelf.

IB09 was a starting point for studying the impact of each wave-driven process on stirring and mixing, using a more idealized configuration that excludes any mean longshore transport (i.e. no wind and zero wave angle). With semi-idealized simulations, we can easily separate the processes and provide an estimate of bulk diffusivity using the standard method of moments.

In particular, we quantify the discrepancy between 2D and 3D simulations and show that the diffusivity due to flash rips is about 20% higher in 2D simulations, consistent with simulations of IB09. In the absence of flash rips, mini-rips represent the primary process, occurring mainly in the surf zone, with a slight extension beyond. Their diffusivity about 0.4 $\mathrm{m.s^{-1}}$, which is an order of magnitude higher than the estimated breaker-induced diffusivity (~ 0.04 $\mathrm{m.s^{-1}}$ here). This result is particularly relevant to coastal beaches that do not experience strong rip current activity (long-crested waves and nearly longshore-uniform bathymetry, such as encountered in West Africa; Floc'h et al. 2018). The estimated diffusivity due to mini-rips provides in this case a reasonable measure of surf zone mixing. On the other hand, we found shear dispersion (another process missing in 2D models) to be significantly less prevalent than mini-rips as a mixing process.

At this point, it is worth recalling the problem posed to modelers by the need for background diffusion in depth-averaged models. There is clearly a missing process that has long been noted and generally attributed to breaker-induced turbulence or shear dispersion, even though close inspection has revealed that these processes are too weak (Clark et al., 2010). Interestingly, our results on the role of mini-rips in surfzone mixing can reconcile apparent contradictions in Clark et al. 2010, where vertical shear and eddies in the infragravity range are both linked to the observed surfzone mixing. In absence of mini-rips (or without background diffusion), we show that there is a delay in the mixing of filaments produced by flash rips. Close to shore, which acts like a wall condition, the energy and mixing length of flash rips can also be considerably reduced, limiting the entrainment of tracer released in this zone. On the contrary, mini-rips are very effective (more so than breaker-induced turbulence and shear dispersion), making it unnecessary to use an ad hoc background diffusivity. It would be interesting in the future of 2D models to develop an appropriate parameterization of mini-rips, with mixing limited to the surf zone, or slightly beyond.

As IB09 has incorporated both longshore wind stress and thermal stratification, our idealized simulations are useful for separating their effect, in addition to that of the Coriolis force. These innershelf forcing factors are generally neglected and have only recently been addressed, since shelf-surf interactions have received some attention (Kumar & Feddersen, 2017a; Grimes et al., 2020b; Wang et al., 2021; Moulton et al., 2021). For stratification at least, 3D models are required, and the effect of stratification on flash rips can only be fully represented in wave-

resolving 3D models, provided the turbulence closure is corrected for the spurious effects of non-breaking waves (Marchesiello & Treillou, 2023). Our results seem to agree with those of Grimes et al. (2020b) and Moulton et al. (2021), showing that buoyant plumes can contribute to extending tracers further offshore in a surface layer. The Coriolis force, like stratification, seems to affect the VLF energy but does not alter the tracer dispersion significantly in our simulations. Longshore winds have a larger effect and tend to increase tracer dispersion through additional innershelf mixing. A full parametric study of longshore and cross-shore wind stress remains to be done.

Another series of tests were conducted to assess the sensitivity of the simulations to numerical methods and model parameters. In all experiments, we observed a significant impact of the critical depth of the wetting-drying scheme. The critical water depth that determines when a cell should be considered dry (in this case, the flow of water out of this cell is prevented) is set in our simulations to $D_{\rm crit} = 0.05$ m, but we found this choice to be sensitive. A higher critical depth ($D_{textcrit} = 0.2$ m) leads to a drastic reduction in kinetic energy near the shoreline ($x > -10$ m), with implications for mini-rips and flash-rips too, and consequently for tracer dispersion. Next, the convergence of the model solution with the grid resolution was also verified. We compared the reference configuration (3D-FlashR) with different horizontal resolutions of $\Delta x = 0.5$, 1 and 2 m. With $\Delta x = 2$ m, there is notable degradation of the results on dynamics and, consequently, tracer dispersion. Considering the effective resolution of $5 - 10\Delta x$ given for CROCO (Soufflet et al., 2016), we expect some key processes to be under-resolved with this mesh size, e.g., the breaker-induced transfer of momentum at the wave front; and mini-rips, which have longshore scales of about 5 m. On the other hand, a 50 cm mesh provided better resolution of the dynamics, with finer structures and more energy in the mini-rips, but this had no significant impact on our estimate of tracer dispersion. Yet, interestingly enough, as resolution increases, bulk diffusivity decreases slightly. We may attribute this to a more efficient limitation of the inverse cascade by 3D dynamics. As for vertical resolution of the shear flow, we assumed that 10 vertical levels were sufficient, based on the study by (Marchesiello et al., 2021), and this was not re-evaluated here.

Sensitivity to wave energy forcing was tested by doubling the significant wave height H_s in the reference case. In this case, κ_{xx} is double that of the reference simulation. The relationship between κ_{xx} and H_s is unknown for mixing dominated by surf eddies. Like (Clark et al., 2010),

we can use a mixing length scale: $\kappa_{xx}^{\text{rip}} \propto U_{\text{rip}} L_{\text{rip}}$, where U_{rip} and L_{rip} are the velocity and length scales of flash rips or mini-rips. A specific sensitivity study would then be required to deduce an empirical relationship.

Finally, to ensure a fair comparison between Boussinesq and non-hydrostatic models, it is also necessary to take into account their computational cost. A simple calibration exercise was carried out between FUNWAVE-TVD and CROCO, with a setup as close as possible in both models. CROCO is run with its most expensive set of numerical methods, including the WENO5 advection scheme for all variables, the highest precision NBQ solver (all terms solved at each fast time step), and 10 vertical levels. We obtained for CROCO a computational cost 7 times higher than FUNWAVE-TVD on a single processor, but only 1.7 times higher on 140 processors. As a result, the number of vertical levels (10 here) is more than offset by CROCO's efficiency, particularly with regard to parallelization. Boussinesq-type models have the disadvantage of requiring global calculations to solve the dispersive terms of the equations. Global calculations are both costly to perform and difficult to parallelize, whereas CROCO's pseudo-compressive approach allows exclusively local calculations (Auclair et al., 2018). Some attempts are made to optimize Boussinesq models as well, and a similar form of pseudo-compressibility is currently being investigated for 2D models in the hope of improving their efficiency (Richard, 2021). Other attempts have been made to deal with numerical methods, as in BOSZ (Roeber et al., 2010). Meanwhile, 3D wave-resolving models such as CROCO appear as very attractive alternatives in terms of cost versus accuracy.

In conclusion, our results demonstrate the impact of vertical shear on nearshore dispersion through two mechanisms: the reduction of the inverse cascade, which leads to a decrease in tracer stirring by surf eddies and flash rips, and the presence of shear-driven mini-rips, a novel and efficient mixing process in the surf zone. We believe that this work will contribute to a more comprehensive understanding of the processes governing nearshore dispersion, and provide information that can inform the development of more accurate simplified models. Future studies should focus on the parameterization of these processes, their generalization to other beach types and their sensitivity to forcing parameters.

IV.3 Supporting material: Benchmarking CROCO and FUNWAVE-TVD

IV.3.1 Configuration

In order to make a robust and fair comparison between the CROCO 3D wave-resolving model and FUNWAVE-TVD Boussinesq model, we carried out a series of simulations and evaluated the computational cost of these models.

The bathymetry is that of a planar beach with a slope of 0.05, typical of dissipative beaches. A JONSWAP spectrum is used for wave forcing, with $H_s = 0.75$ m, $T_p = 10$ s, and $\gamma = 3.3$. The waves are shore-normal with a directional spread of $\sigma_\theta = 10°$. The domain size is 400 m by 200 m in the longshore and cross-shore direction, respectively, and the horizontal resolution is $\Delta x = 1$ m. The timestep in CROCO is 0.02 s, with 10 fast timesteps and a pseudo-acoustic velocity of 100 m $\cdot$ s^{-1}. In FUNWAVE-TVD, the timestep is approximately 0.05 s (with a CFL condition set to 0.5, as FUNWAVE-TVD uses adaptative timestep). Both simulations are run for 1800 s. The critical depth for the wetting-drying scheme is set to 5 cm, identical in both models.

Outputs in both models are recorded at a frequency of 1/20 Hz (every two peak periods) with average and instantaneous fields (grid variables; u, v, η, u_{bar}, v_{bar}). In CROCO, u and v are 4D arrays, while in FUNWAVE-TVD all variables are 3D arrays. Both simulations are run with 1, 36, 70 and 140 CPU[1] cores, and results are averaged over 4 runs.

IV.3.2 Dynamics

The computational efficiency of a model is usually evaluated in terms of computational cost versus accuracy. To guarantee a fair comparison between models, we therefore need to ensure that they solve at least similar dynamics. To that end, we examine the longshore and time averaged cross-shore profiles of depth-integrated eddy kinetic energy (normalized par mean depth), as shown in Figure IV.18. The profiles correspond to a period after a spin-up of 1000 s. EKE is similar in both simulations, with peaks of the same magnitude, but as expected (Section IV.2.5.2), FUNWAVE-TVD shows an excess on the inner shelf.

[1] Central Processing Unit

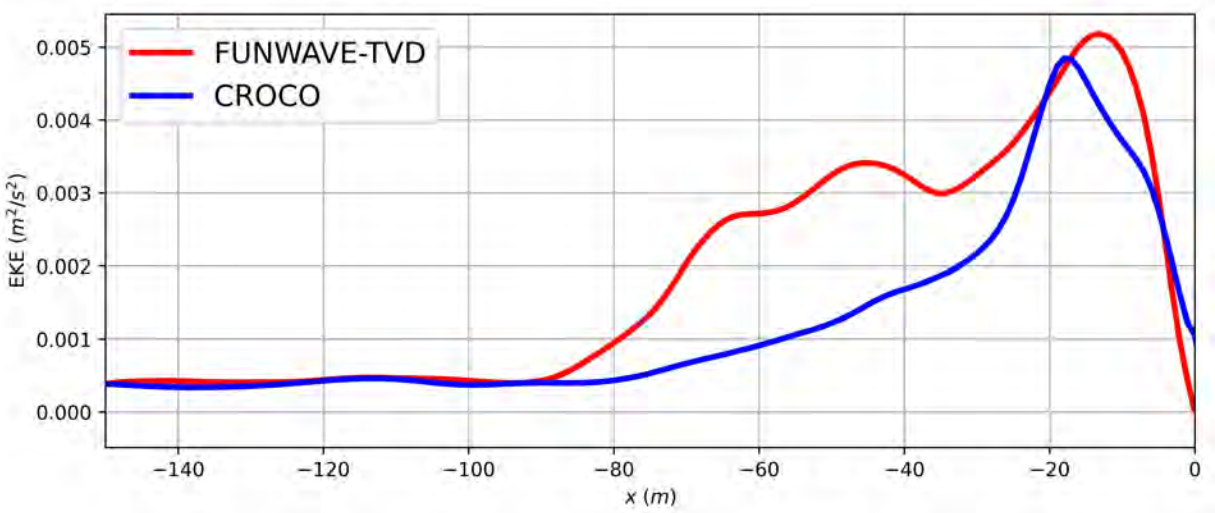

Figure IV.18 Cross-shore profile of depth-integrated (normalized by mean depth), time-averaged and longshore-averaged EKE for CROCO (blue line) and FUNWAVE-TVD (red line) on a planar beach.

IV.3.3 Computational cost

We now proceed to compare the model computational costs. For this, we measure the real elapsed time (i.e., the actual time from the start to the end of the simulation). All times are compiled in Table IV.6.

Table IV.6 Total real elapsed time required to run 30-min simulations with CROCO and FUNWAVE-TVD for an increasing number of processors. Times are ensemble averaged.

# of CPU cores	1 proc.	36 proc.	70 proc.	140 proc.
CROCO	158 640 s	8340 s	4300 s	2020 s
FUNWAVE-TVD	23 552 s	1920 s	1664 s	1203 s

The differences between CROCO and FUNWAVE-TVD are well summarized by a graphic display in Figure IV.19, where we show the evolution of the ratio between CROCO and FUNWAVE-TVD for different numbers of processors. In particular, on a single processor, CROCO is almost 7 times more expensive than FUNWAVE-TVD. Although this difference may seem important, it is in fact smaller than expected, since CROCO operates on 10 vertical levels. More importantly, the figure shows CROCO's good scalability on multiprocessors, since the difference between the two models decreases sharply with the number of processors to be only 1.7 slower on 140 processors. This reduction can be attributed to the global calculations required in Boussinesq-type models to solve the dispersive terms of the equations.

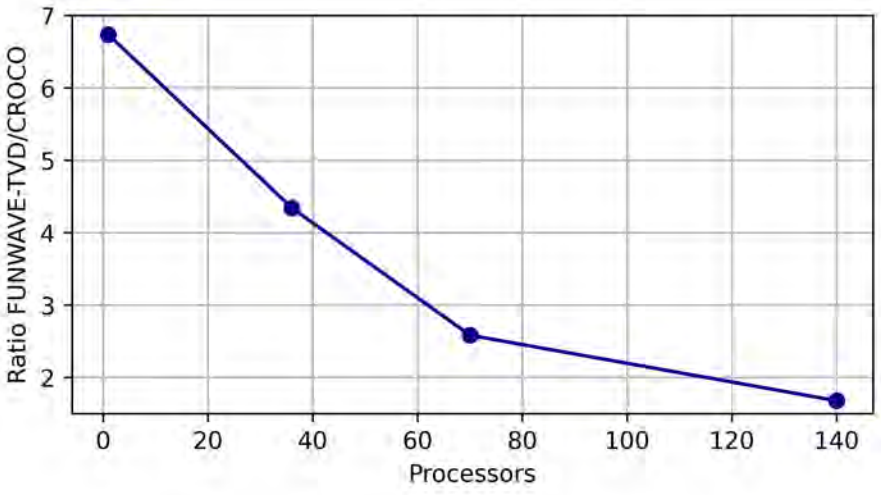

Figure IV.19 Ratio of real elapsed time between CROCO and FUNWAVE-TVD with increasing number of processors.

It is important to note that the version of FUNWAVE-TVD used[2] does not include the NetCDF[3] module, which is expected to improve computing efficiency during file writing. To mitigate this bias, the exported files were reduced in size. Additionally, it is important to acknowledge that the amount of data produced by both models is different, with approximately 1.4 GB of data for CROCO and 0.87 GB for FUNWAVE-TVD.

Attention should also be paid to the size of the domain. While the domains are identical in this study, they may vary depending on the application. CROCO's wave forcing is applied at the offshore boundary, whereas FUNWAVE-TVD uses an interior source function, which would require an extended offshore domain to accommodate sponge layers.

[2] This version is available at github.com/fengyanshi/FUNWAVE-TVD.
[3] See www.unidata.ucar.edu/software/netcdf/.

IV.4 Conclusion

IV.4.1 Summary

Using the 3D wave-resolving model CROCO, we were able to assess, for the first time, the impact of undertow vertical shear on tracer dispersion. The wave-basin experiment of Baker et al. (2023c) allowed us to validate the full 3D CROCO and its pseudo-2D version designed to mimic Boussinesq models. Thanks to RGB analysis, we were also able to compare surfzone mixing in CROCO and in the dye release trials of the laboratory experiment. Once validated, CROCO was applied to the large-scale IB09 field experiment, with remarkably accurate results: the observed quasi-exponential decay of tracer concentration over the innershelf was closely matched by CROCO, whereas the 2D model overestimated tracer dispersion on the inner shelf.

Based on this experiment, several semi-idealized test cases were conducted to assess the impact of each process on cross-shore diffusivity. The results confirmed that transient rip currents represent the most significant process connecting the surf zone with the inner shelf, with $\kappa_{xx} \sim 1.5$ m^{2}s^{-1}. However, the undertow vertical shear significantly reduces the upscale flux of eddy energy produced by short-crested waves, and therefore the bulk diffusivity. In the surf zone, mini-rips – 3D small infragravity eddies originating from the vertical shear instability of the undertow – were identified as the most efficient mixing process with $\kappa_{xx} \sim 0.4$ m^{2}s^{-1}, justifying the use of background diffusivity in Boussinesq models. Innershelf processes, such as stratification, winds, and Coriolis force, were also tested in this new 3D framework. Onshore winds increased diffusivity, the Coriolis force had little impact, and thermal stratification led to a strong surface intensification of tracer concentration.

This work answers the second open question of this thesis, revealing a significant impact of undertow vertical shear. It suggests that surfzone mixing is dominated by mini-rips, originating from shear instability, but that flash rips are required to extend the mixing seaward over the inner shelf. However, the energy of flash rips is inhibited by the same shear flow, which affects their dispersal effect. These results explain why Boussinesq models tend to overestimate shelf-surf exchanges, while underestimating surfzone mixing, unless some background diffusivity is added.

IV.4.2 Author contribution

This work is based on a collaboration between my PhD advisor P. Marchesiello, C.M. Baker, J. McWilliams, F. Dumas and myself. The study was first conceptualized by P. Marchesiello. I performed the simulations, the processing of the data, the analysis and the original writing of the draft. C.M. Baker processed the data of the laboratory dye release. We all contributed to improving the methodology, discussing the results and improving the article.

Conclusions and Perspectives

— Conclusions —

The nearshore zone, a highly dynamic and ever-changing environment, is under constant pressure from both human activities and natural forces. As a critical interface for continuous exchanges, it plays a key role in the transport of various tracers, whether they move from land to ocean or vice versa. As outlined in the introduction of this thesis, these tracers are varied and numerous, representing major environmental challenges such as coastal pollution by pathogens, microplastics and heavy metals; ecosystem services and biodiversity (through the transport of plankton and larvae); and sediment transport. Understanding the mechanisms driving the dispersion of these tracers is therefore essential and has been the subject of extensive research over the past several decades. This thesis builds on these efforts, aiming to deepen our understanding of the processes important to ever-growing coastal populations.

The scope of this study is limited to longshore-uniform sandy beaches, with a focus on transient rip currents rather than bathymetric rip currents, and on neutrally buoyant tracers (such as pathogens). **The originality of this thesis lies in the evaluation of the impact of vertical shear of the undertow on tracer dispersion**, a phenomenon that has been largely overlooked in traditional approaches based on 2D (Boussinesq) models. We can now conclude on how this thesis has addressed its primary objectives.

- **How can we improve the realism of wave-resolving models?**

In the initial phase of this work, it was necessary to focus on methodological aspects to improve the realism of wave-resolving simulations in CROCO. Several corrections were made to the model (as detailed in Chapter II), but the two main contributions were made to the wavemaker and to the turbulence closure model.

The work on the **wavemaker correction**, described in Chapter III and published in *Ocean Modelling* (Treillou et al., 2024), stems from a problem encountered during early attempts to simulate the IB09 experiment. Although the longshore drift was correctly represented, persistent flow structures were superimposed, particularly near the boundaries. After investigation, it appeared that the problem was linked to both the wavemaker formalism and the periodic

boundary conditions. The classical wavemaker is based on a double summation, where each wave component has a given frequency and direction. When two or more components differ in direction but share the same frequency, coherent interference develops, creating longshore variability in wave height. This in turn leads to differential wave breaking at the beach and to stationary rip currents. While this phenomenon can occur in the real world (e.g., the *focused rip currents* described in Chapter I), in this case it was caused by an undesirable feature of the model forcing. To remedy this, a single-sum wavemaker was implemented (Salatin et al., 2021), where each wave component has a unique frequency and direction, thus completely eliminating the source of coherent interference. Additionally, a correction for periodic boundaries was proposed, in the form of a minimal adjustment of wave directions so that each angle satisfies periodicity, so that the domain length in y is a multiple of the wavelength of each wave component. This correction is essential to eliminate the H_s shadows that can develop near lateral boundaries, creating spurious rip currents. These corrections, and the nearshore application of CROCO as a whole, were validated using a wave basin experiment (Baker et al., 2023c). It clearly illustrated the coherence interference generated by the original double-sum wavemaker, and demonstrated CROCO's ability to accurately reproduce flash rip dynamics, complementing validations carried out in channel experiments by Marchesiello et al. (2021).

The work on the **correction of turbulence closure**, published as second author in *Ocean Modelling* (Marchesiello & Treillou, 2023) and available in Appendix 1, marks another major improvement for 3D wave-resolving models. Two-equation turbulence closure models (such as $k-\omega$ or $k-\epsilon$) present a well-known issue: overproduction of turbulence in regions where the flow is irrotational, typically on the inner shelf where waves do not break. This excess turbulent energy causes too much vertical mixing, destroying stratification on the shelf. Based on the theoretical work of Mayer and Madsen (2000) and Larsen and Fuhrman (2018), this instability was controlled by limiting turbulence production in areas where the vorticity is significantly lower than the strain rate. This correction is crucial, as it enables the study of stratification and its effect on surf eddies (or internal waves, for example), within a single wave-resolving model.

In conclusion, the two corrections presented here are essential for a complete and reliable study of tracer transport mechanisms in coastal environments.

• What is the impact of undertow vertical shear on tracer dispersion in the nearshore zone?

Once the necessary improvements were implemented and validated, the central issue of this thesis could be addressed: the impact of vertical shear induced by the undertow, which is the focus of Chapter IV. In this chapter, two complementary experiments are used: a wave basin experiment and a field campaign involving a dye release. The dye, measured through various techniques (video, fluorometers), is used to estimate diffusivity.

The first experiment, carried out in a wave basin (Baker et al., 2023c), tests the model in a controlled environment and validates the method used to produce the pseudo-2D version of CROCO. By increasing turbulent viscosity by a factor of $\mathcal{O}(30)$ in the surf zone, vertical shear is eliminated, and the model behaves like a 2D model. This is demonstrated through comparison of velocity spectra with the Boussinesq model FUNWAVE-TVD. The two key biases of 2D models, as described by Marchesiello et al. (2021), are observed: an underestimation of energy in the infragravity (IG) band and an overestimation of energy in the very low frequency (VLF) band. The VLF overestimation bias in the CROCO pseudo-2D is actually lower than in FUNWAVE-TVD, probably due to the preserved vertical profiles on the inner shelf. We therefore conclude that the assessment of 2D bias with CROCO is conservative, meaning that the bias is worse in real 2D models. Next, surfzone mixing in CROCO (3D) is compared with the observation of dye released during the basin experiment (using a RGB analysis method implemented specifically for this thesis). The results are highly satisfactory and confirm the model's ability to accurately replicate dispersion dynamics. However, this experiment does not provide sufficient statistics to rigorously analyze dispersion outside the surf zone.

The second experiment, IB09 (Hally-Rosendahl et al., 2014), was based on a large-scale dye release on Imperial Beach, California. With substantial resources (jetski transects, aerial tracking, and fluorometers), the dye's evolution was tracked over several kilometers along the longshore uniform beach, providing robust and varied statistics, making this experiment an ideal candidate for studying exchanges between the inner shelf and the surf zone. After validating the wave forcing conditions, the results from CROCO were compared with a cross-section of concentrations measured 1 km downstream from the dye source. The difference between funwaveC (2D) and CROCO (3D) is striking: while the 2D model overestimates concentration on the shelf by a factor of 2, following a linear decay, CROCO realistically reproduces a quasi-exponential decay. This result is important because it offers new insights into the overestimation of cross-shore exchanges in 2D models. While an impact of tides was suspected in previous

studies, our results provide clear evidence of the role of undertow vertical shear. Our conclusion is that **vertical shear, through its influence on the inverse kinetic energy cascade, significantly reduces the energy of surfzone eddies and the associated exchange towards the inner shelf**.

To confirm this, a series of semi-idealized tests were conducted based on the IB09 configuration, omitting wind and longshore drift effects to focus solely on cross-shore exchange and better distinguish the different processes. This approach allowed for the estimation of bulk diffusivity specific to each process. Our results for IB09 conditions are summarized here:

- shear dispersion $\kappa_{xx} \sim 0.05$ m^2.s^{-1};
- mini-rips $\kappa_{xx} \sim 0.4$ m^2.s^{-1};
- flash rips $\kappa_{xx} \sim 1.2$ m^2.s^{-1};

These results show that **mini-rips form the dominant mixing process on a beach devoid of rip currents**, surpassing shear dispersion. Additionally, surfzone mixing is an important element of dispersion to the inner shelf when larger-scale surf eddies are present. In 2D simulations, tracer dispersion depend significantly on a background diffusivity, κ_0, which is chosen arbitrarily but appears to represent the effect of mini-rips: the value of κ_0 that enables the 2D model to reproduce the dispersion in 3D simulations is similar to the diffusivity associated with mini-rips. For example, Grimes et al. (2020b) and Kumar and Feddersen (2017b) use $\kappa_0 = 0.2$ m.s^{-1} in the surf zone (and a lower value offshore). This leads to the hypothesis that **mini-rips represent the missing process, allowing a fast transition from stirring to mixing in the nearshore zone**. These observations align with previous studies, particularly those of Clark et al. (2010), which found that surfzone diffusivity was best explained by infragravity rotational velocities, which is totally consistent with the description of mini-rips. Nevertheless, if mini-rips are the dominant surfzone mixing process, even when large surf eddies are present (more conducive to stirring of filaments), they rely on surf eddies to extend mixing to the inner shelf.

Finally, specific tests allowed for the examination of **the interaction of flash rips with shelf processes, involving: the Coriolis force, longshore winds, and thermal stratification** (enabled in CROCO by the correction of Marchesiello & Treillou, 2023). While the Coriolis force seems to have a minimal impact, stratification induces a marked vertical tracer profile on the

inner shelf, due to a limitation of vertical mixing, similar to results obtained for bathymetric rip currents (Moulton et al., 2021) or transient rips (Grimes et al., 2020b). Longshore winds, on the other hand, generate additional mixing on the inner shelf, facilitating faster tracer dispersion out to sea. Although these results are preliminary and require further parametric study, they highlight the potential of 3D wave-resolving models like CROCO to more fully include the full range of nearshore dynamics.

The results of this thesis provide a more nuanced understanding of nearshore dispersion processes, suggesting possible feedback on Boussinesq and simplified models through parametrization. Parameterization would also be useful for 3D models used at coarser resolutions (when $\Delta x > 1$ m, mini-rips are clearly under-resolved).

— Perspectives —

While this thesis has improved our understanding of coastal dispersion mechanisms, many questions remain open or have arisen as a result of this work. Below is a non-exhaustive list of questions that have emerged from this thesis or could be explored in future research.

- **How can our results be generalized to other coastlines?**

This thesis, like many other studies, has focused on uniform sandy beaches, leaving a wide variety of coastlines unaddressed. While this approximation is well-suited to the beaches of southern California (where a high number of studies are conducted) or other dissipative systems characterized by exposed open coast, many coastlines exhibit different characteristics, such as more varied bathymetry with channelled rip currents. There is a continuum of bathymetry types (uniform or variable, dissipative or reflective, with or without sandbars, etc.) that would be worth further exploration to generalize our results. Other types of coastlines, such as rocky shores or coral reefs, also deserve better representation in studies of this kind. Additionally, it would be interesting to assess the impact of man-made infrastructures.

- **What is the impact of adjacent processes?**

It would also be valuable to deepen our understanding of the influence of other physical processes on the dynamics explored in this thesis. For example, the presence of estuaries, which introduce freshwater inputs, or tidal forces, could significantly affect nearshore dynamics.

Tides can alter the beach configuration, modifying the interaction between bathymetry and incident waves (Bondehagen et al., 2024). The processes related to the inner shelf, which were discussed quite briefly in this thesis, also warrant closer examination. While the Coriolis force appeared to have a negligible effect in the given simplified configuration, we may wonder if this remains true for all types of conditions. Could much stronger rip currents, such as those generated during storms, be sensitive to Coriolis effects? The impact of stratification and its amplitude in wave-resolving models still needs deeper exploration, while the effect of winds deserves a full parametric study, considering both wind magnitude and direction (cross-shore or longshore), with special reference to whether winds align with longshore drift. Additionally, other phenomena like wave streaming would deserve specific attention, as it is suggested to strongly impact the nearshore circulation in presence of stratification (Wang et al., 2020). 3D wave-resolving models would be excellent candidates for simulating more explicitly this poorly explored phenomenon.

- **How would other types of tracer behave?**

This thesis is based on the assumption of a neutrally buoyant tracer diluting in water. While this assumption is valid for dissolved passive tracers, such as chemical compounds or pathogens, it presents limitations for other types of tracers. For example, sediments, whose settling velocity varies depending on their characteristics, hydrocarbons that tend to remain at the surface, or microplastics, whose behavior depends on their specific properties (see for example Forsberg et al., 2020; Kim & Kim, 2024). A better understanding of plastic dispersion in coastal zones would be particularly useful for regional models, as rip currents can remobilize plastics offshore (van Sebille et al., 2020). Additionally, the impact of flash rips on cross-shore sediment exchanges remains virtually unexplored (but see recent studies by Park et al., 2020; Kim, 2021). Biological tracers, such as larvae, can exhibit specific behavior, like autonomous motion, which can help their coastal retention or dispersion (Moulton et al., 2023). For contaminants, sources and sinks, including bacterial mortality, could be incorporated into the dispersion model. CROCO already has capabilities in sediment dynamics, biogeochemical cycles or Lagrangian transport. We could use them in the future or extend their capabilities to deal with relevant tracers in the coastal zone.

- **Can we refine our understanding of the turbulent cascade in the nearshore**

zone?

The present study used the model results of Marchesiello et al. (2021) on the turbulent cascade in the nearshore zone. A global view of the sources, transfers and sinks of kinetic energy was proposed, in which transient rip currents (flash rips and mini-rips) could find their place. This conceptual model has been proposed in a rather idealized framework, and to go further, it would be interesting to explore how the turbulent cascade would be affected by the environmental conditions, such as bathymetry or wave spectrum. A recent study pointed out the difficulty of observing an inverse cascade when the directional spread $\sigma_\theta < 10°$ (Baker et al., 2023b). The inverse cascade may also be affected by a highly random wave field with an excessively large σ_θ (Kellay & Goldburg, 2002). It would also be useful to look in more detail at the dynamics associated with wave breaking, particularly the injection of vorticity caused by short-crested waves and the eddy merging process that leads to upscale energy fluxes. There is still much to be explored in this relatively young field of study to better understand the dynamics.

- **How to parameterize flash rips and mini-rips?**

Parameterization would benefit from a comprehensive parametric study on both flash rips and mini-rips. For flash rips, existing parameterizations, such as the exchange velocity proposed by Suanda and Feddersen (2015), could be revisited and refined using 3D wave-resolving models. On the other hand, the dispersion induced by mini-rips has been described here for the first time and within a limited parametric framework. Although their generation process appears very robust, their effect in other environments remains an open question. Would they be more effective on reflective beaches? For example, Brown et al. (2019) observed that when dye was released on a steep beach, the tracer dispersed rapidly and uniformly a little beyond the surf zone. They did not clearly identify the mechanism responsible, but our results strongly suggest the action of mini-rips. Another question is how do mini-rips react to variations in wave forcing? This question is directly related to the sensitivity of the undertow and associated vertical shear, which is has no clear behavior (Faria et al., 2000). The undertow profile responds to the surface mass flux during breaking but also to the turbulent viscosity, both of which are sensitive to wave height in ways that are difficult to predict — Svendsen and Putrevu (1994) proposes the relation $0.06\,h\,\sqrt{gh}$, which gives an order of magnitude but hardly explains the

wave height sensitivity, according to Faria et al. (2000). The undertow would also be affected by nonlinear advection. Finally, for a given vertical shear, the growth rate of 3D shear instability, producing mini-rips, would depend on the turbulent viscosity and bottom friction. A final question arises: how would mini-rips behave with different bathymetry? Would irregularities affect, for example, the most unstable scales or the pairing mechanism inherent to secondary instability? All these questions and others deserve to be further investigated, through numerical modeling or laboratory experiments.

- **What are the modeling challenges?**

Finally, as with any study based on numerical modeling, constant attention must be paid to the techniques used. For nearshore modeling, wave breaking appears to be quite well represented in free-surface Navier-Stokes models. Unlike Boussinesq-type models derived from ideal and irrotational flow equations (Kazolea & Ricchiuto, 2018), there is no explicit criterion for wave breaking, which is instead handled by a shock-capturing advection scheme to produce rollers, analogous to a bore or hydraulic front, and by turbulence closure to model breaking-wave turbulence. While this provides greater flexibility compared to criterion-based models, it is essential to understand how numerical schemes impact the representation of wave breaking. For example, while the WENO5 advection scheme proved particularly effective, the results were somewhat sensitive to interpolation choices for advection velocities. Perhaps more importantly, the implicit Euler Backward scheme used to handle acoustic waves in the vertical direction has been shown to produce significant errors with large time steps at relatively coarser resolution (> 2 m). Alternatives to this scheme or the implementation of safeguards to avoid crossing the validity limits would be desirable. The number of vertical levels may also be important (Smit et al., 2013), although 10 levels were probably sufficient for the purposes of this thesis.

Further study, as well as a benchmark comparison of several wave-resolving models, that would include cost estimates, would be useful to the scientific community. Our attempted comparison in Chapter IV provided very encouraging results on the computational efficiency of CROCO compared with Boussinesq models, despite the addition of the vertical dimension in a full Navier-Stokes framework. The exclusively local computations enabled by a pseudo-compressible approach proved beneficial for (massively) parallel computing, showing good scalability. A GPU[4]

[4] Graphics Processing Unit

version of the model is now available, which will certainly take the computational capacity of the code to a new level, meaning that several days or months of wave-resolving simulations in the nearshore zone will be available.

Conclusions et Perspectives

— Conclusions —

Le littoral, environnement très dynamique et en perpétuelle évolution, est soumis à une pression constante de la part des activités humaines et des forces naturelles. Interface critique d'échanges continus, il joue un rôle clé dans le transport de divers traceurs, qui se déplacent de la terre vers l'océan ou inversement. Comme souligné dans l'introduction de cette thèse, ces traceurs sont variés et nombreux, représentant des enjeux environnementaux majeurs tels que la pollution côtière par les pathogènes, les microplastiques et les métaux lourds ; les services écosystémiques et la biodiversité (via le transport de plancton et de larves) ; et le transport sédimentaire. La compréhension des mécanismes de dispersion de ces traceurs est donc essentielle et a fait l'objet de recherches approfondies au cours des dernières décennies. Cette thèse s'appuie sur ces efforts et vise à approfondir notre compréhension de processus importants pour les populations côtières qui ne cessent de croître.

Le cadre de cette étude est limité aux plages sableuses quasi-uniformes sur leur longueur, et se concentre sur les courants d'arrachement transitoires plutôt que sur les courants d'arrachement bathymétriques, ainsi que sur les traceurs à flottabilité neutre (tels que les pathogènes). **L'originalité de cette thèse réside dans l'évaluation de l'impact du cisaillement vertical du courant de fond sur la dispersion des traceurs**, un phénomène qui a été largement négligé dans les approches traditionnelles basées sur des modèles 2D (Boussinesq). Nous pouvons maintenant conclure sur la façon dont cette thèse a répondu à ses objectifs principaux.

- **Comment améliorer le réalisme des modèles à vagues résolues ?**

Dans un premier temps, il a été nécessaire de se concentrer sur des aspects méthodologiques afin d'améliorer le réalisme des simulations à vagues résolues de CROCO. Plusieurs corrections ont été apportées au modèle (décrites dans le Chapitre II), mais les deux principales contributions concernent le générateur de vagues et le modèle de fermeture turbulente.

Les travaux sur **la correction du générateur de vagues**, décrits dans le Chapitre III et publiés dans *Ocean Modelling* (Treillou et al., 2024), découlent d'un problème rencontré lors

des premières tentatives de simulation de l'expérience IB09. Bien que la dérive littorale ait été correctement représentée, des fluctuations persistantes étaient observées, en particulier près des frontières. Après recherche, il s'est avéré que le problème était lié à la fois au formalisme du générateur de vagues et aux conditions limites périodiques. Le générateur de vagues classique est basé sur une double sommation, où chaque composante de vague a une fréquence et une direction données. Lorsque deux ou plusieurs composantes diffèrent en direction mais partagent la même fréquence, une interférence cohérente se développe, créant une variabilité *longshore* de la hauteur significative. Ce phénomène entraîne à son tour un déferlement différencié des vagues sur la plage et des courants d'arrachement stationnaires. Si ce phénomène peut se produire dans le monde réel (par exemple, les *focused rips* décrits dans le Chapitre I), il est dans notre cas causé par une caractéristique indésirable du forçage du modèle. Pour y remédier, un générateur de vagues à somme unique a été mis en oeuvre (Salatin et al., 2021), où chaque composante d'onde a une fréquence et une direction uniques, éliminant ainsi complètement la source d'interférence cohérente. En outre, une correction pour les limites périodiques a été proposée : elle consiste à ajuster les directions des vagues afin que chaque angle respecte la condition de périodicité, c'est-à-dire que la longueur du domaine en y soit un multiple de la longueur d'onde associée à chaque composant. Cette correction est cruciale, car sans elle, des zones à faible H_s apparaissent près des frontières latérales, générant des courants d'arrachement non désirés, semblables aux *boundary rip currents* mentionnés dans le Chapitre I. Ces corrections, et l'application littorale de CROCO dans son ensemble, ont été validées à l'aide d'une expérience de bassin à vagues (Baker et al., 2023c). Cette expérience a clairement illustré l'interférence cohérente créée par le générateur de vagues à double sommation et a démontré la capacité de CROCO à reproduire avec précision la dynamique des *flash rips*, complétant les validations effectuées dans les expériences en canal par Marchesiello et al. (2021).

Le travail sur la **correction de la fermeture turbulente**, publié en tant que deuxième auteur dans *Ocean Modelling* (Marchesiello & Treillou, 2023) et disponible en Annexe 1, marque une autre amélioration majeure pour les modèles de résolution des vagues en 3D. Les modèles de fermeture turbulente à deux équations (tels que $k-\omega$ ou $k-\epsilon$) présentent un problème bien connu : la surproduction de turbulence dans les régions où l'écoulement est irrotationnel, typiquement sur le plateau interne où les vagues ne se brisent pas. Cet excès d'énergie turbulente provoque un mélange vertical trop important, détruisant la stratification sur le plateau. Sur la

base des travaux théoriques de Mayer and Madsen (2000) et Larsen and Fuhrman (2018), cette instabilité a été contrôlée en limitant la production de turbulence dans les zones où la vorticité est significativement plus faible que le taux de déformation. Cette correction est cruciale, car elle permet d'étudier la stratification et son effet sur les tourbillons de déferlement (ou les ondes internes, par exemple), au sein d'un même modèle à vagues résolues.

En conclusion, les deux corrections présentées ici sont indispensables pour garantir une étude fiable et approfondie des mécanismes de transport des traceurs dans les environnements côtiers.

- **Quel est l'impact du cisaillement vertical du courant de retour sur la dispersion des traceurs en zone littorale ?**

Une fois les améliorations nécessaires mises en œuvre et validées, la question centrale de cette thèse a pu être abordée : l'impact du cisaillement vertical induit par le courant de retour, qui fait l'objet du Chapitre IV. Dans ce chapitre, deux expériences complémentaires sont utilisées : une expérience en bassin à vagues et une campagne sur le terrain impliquant le rejet d'un colorant. Le colorant, mesuré par diverses techniques (vidéo, fluoromètres), est utilisé pour estimer la diffusivité.

La première expérience, réalisée dans un bassin à vagues (Baker et al., 2023c), teste le modèle dans un environnement contrôlé et valide la méthode utilisée pour la version pseudo-2D de CROCO. En augmentant la viscosité turbulente d'un facteur de $\mathcal{O}(30)$ dans la zone de déferlement, le cisaillement vertical est éliminé et le modèle se comporte comme un modèle 2D. Ceci est démontré par la comparaison des spectres de vitesse avec le modèle de Boussinesq FUNWAVE-TVD. Les deux principaux biais des modèles 2D, décrits par Marchesiello et al. (2021), sont observés : une sous-estimation de l'énergie dans la bande d'infragravité (IG) et une surestimation de l'énergie dans la bande de très basse fréquence (VLF). Le biais de surestimation des VLF dans la version pseudo-2D CROCO est en fait plus faible que dans FUNWAVE-TVD, probablement en raison des profils verticaux préservés sur le plateau interne. Nous concluons donc que l'évaluation du biais 2D avec CROCO est conservatrice, ce qui signifie que le biais est plus fort dans les modèles 2D réels. Ensuite, le mélange de la zone de déferlement avec CROCO (3D) est comparé à l'observation du colorant libéré lors de l'expérience en bassin (en utilisant une méthode d'analyse RGB mise en œuvre spécifiquement pour cette thèse). Les résultats sont très satisfaisants et confirment la capacité du modèle à reproduire avec précision la dynamique

de dispersion. Cependant, cette expérience ne fournit pas suffisamment de statistiques pour analyser rigoureusement la dispersion en dehors de la zone de déferlement.

La seconde expérience, IB09 (Hally-Rosendahl et al., 2014), était basée sur un rejet de colorant à grande échelle sur la plage *longshore uniform* d'Imperial Beach, en Californie. Avec des moyens importants (transects de jetskis, suivi aérien et fluoromètres), l'évolution du colorant a été suivie sur plusieurs kilomètres le long de la plage, fournissant des statistiques robustes et variées, faisant de cette expérience un candidat idéal pour l'étude des échanges entre le plateau interne et la zone de déferlement. Après avoir validé les conditions de forçage des vagues, les résultats de CROCO ont été comparés à une coupe transversale des concentrations mesurées à 1 km en aval de la source de colorant. La différence entre funwaveC (2D) et CROCO (3D) est frappante : alors que le modèle 2D surestime d'un facteur 2 la concentration sur le plateau, suivant une décroissance linéaire, CROCO reproduit de manière réaliste une décroissance quasi-exponentielle. Ce résultat est important car il offre de nouvelles perspectives sur la surestimation des échanges *cross-shore* dans les modèles 2D. Alors que l'impact des marées a été suspecté dans des études précédentes, nos résultats fournissent des preuves claires du rôle du cisaillement vertical du courant de fond. Notre conclusion est que **le cisaillement vertical, par son influence sur la cascade inverse d'énergie cinétique, réduit de manière significative l'énergie des tourbillons de la zone de déferlement et l'échange associé vers le plateau interne**.

Pour le confirmer, une série de tests semi-idéalisés a été réalisée sur la base de la configuration IB09, en omettant les effets du vent et de la dérive littorale pour se concentrer uniquement sur les échanges *cross-shore* et mieux distinguer les différents processus. Cette approche a permis d'estimer la diffusivité spécifique à chaque processus. Nos résultats pour les conditions IB09 sont résumés ici :

- dispersion de cisaillement $\kappa_{xx} \sim 0.05$ m^2.s^{-1};
- mini-rips $\kappa_{xx} \sim 0.4$ m^2.s^{-1};
- *flash rips* $\kappa_{xx} \sim 1.2$ m^2.s^{-1};

Ces résultats montrent que les **mini-rips constituent le processus de mélange dominant sur une plage dépourvue de courants d'arrachement**, surpassant la dispersion par cisaillement. En outre, le mélange dans la zone de déferlement est important pour la dispersion vers le plateau interne lorsque des tourbillons de grande échelle sont présents. Dans les simulations

2D, la dispersion du traceur dépend de manière significative d'une diffusivité de fond, κ_0, qui est choisie arbitrairement mais qui semble représenter l'effet des mini-rips : la valeur de κ_0 qui permet au modèle 2D de reproduire la dispersion des simulations 3D est similaire à la diffusivité associée aux mini-rips. Par exemple, Grimes et al. (2020b) et Kumar and Feddersen (2017b) utilisent $\kappa_0 = 0.2$ m.s^{-1} dans la zone de déferlement (et une valeur plus faible au large). Cela conduit à l'hypothèse que **les mini-rips représentent le processus manquant, permettant une transition rapide du *stirring*[5] au mélange dans la zone littorale**. Ces observations s'alignent sur les études précédentes, en particulier celles de Clark et al. (2010), qui a trouvé que la diffusivité de la zone de déferlement était mieux expliquée par les vitesses de rotation infragravitaires, ce qui est cohérent avec la description des mini-rips. Néanmoins, si les mini-rips sont le processus de mélange dominant de la zone de déferlement même en présence de grands tourbillons (plus propices à l'étirement des filaments), ils dépendent des tourbillons de la zone de déferlement pour étendre le mélange au plateau interne.

Enfin, des tests spécifiques ont permis d'examiner **l'interaction des *flash rips* avec les processus du plateau, impliquant : la force de Coriolis, les vents *longshore*, et la stratification thermique** (permis dans CROCO par la correction de Marchesiello & Treillou, 2023). Alors que la force de Coriolis semble avoir un impact minime, la stratification induit un profil vertical marqué du traceur sur le plateau interne, en raison d'une limitation du mélange vertical, similaire aux résultats obtenus pour les courants d'arrachement bathymétriques (Moulton et al., 2021) ou les courants d'arrachement transitoires (Grimes et al., 2020b). Les vents *longshore*, quant à eux, génèrent un mélange supplémentaire sur le plateau interne, facilitant une dispersion plus rapide du traceur vers le large. Bien que ces résultats soient préliminaires et nécessitent une étude paramétrique plus approfondie, ils mettent en évidence le potentiel des modèles 3D à vagues résolues comme CROCO pour évaluer plus complètement la gamme complète des dynamiques littorales.

Les résultats de cette thèse fournissent une compréhension plus nuancée des processus de dispersion littorale, suggérant une rétroaction possible sur les modèles de Boussinesq et les modèles simplifiés par le biais de la paramétrisation. La paramétrisation serait également utile pour les modèles 3D utilisés à des résolutions plus fines (lorsque $\Delta x > 1$ m, les mini-rips sont clairement sous-résolus).

[5] Le *stirring* fait référence au brassage du fluide par advection, formant de forts gradients (Eckart, 1948).

— Perspectives —

Bien que cette thèse ait amélioré notre compréhension des mécanismes de dispersion côtière, de nombreuses questions restent ouvertes ou ont été soulevées à la suite de ce travail. Voici une liste non exhaustive de questions qui ont émergé de cette thèse et qui pourraient être explorées dans de futures recherches.

- **Comment généraliser ces résultats à d'autres littoraux ?**

Cette thèse, comme beaucoup d'autres études, s'est concentrée sur les plages sableuses uniformes, laissant de côté une grande variété de littoraux. Bien que cette approximation soit bien adaptée aux plages du sud de la Californie (où un grand nombre d'études ont été menées) ou à d'autres systèmes dissipatifs caractérisés par une côte ouverte exposée, de nombreux littoraux présentent des caractéristiques différentes, telles qu'une bathymétrie plus variée avec des courants d'arrachement bathymétriques. Il existe un continuum de types de bathymétrie (uniforme ou variable, dissipative ou réfléchissante, avec ou sans barres sableuses, etc). D'autres types de côtes, comme les côtes rocheuses ou les récifs coralliens, mériteraient également d'être mieux représentés dans des études de ce type. En outre, il serait intéressant d'évaluer l'impact des infrastructures construites par l'homme.

- **Quel impact de processus adjacents ?**

Il serait également utile d'approfondir notre compréhension de l'influence d'autres processus physiques sur la dynamique étudiée dans cette thèse. Par exemple, la présence d'estuaires, qui introduisent des apports d'eau douce, ou les forces de marée, pourraient affecter de manière significative la dynamique du littoral. Les marées peuvent altérer la configuration de la plage, modifiant l'interaction entre la bathymétrie et les vagues incidentes (Bondehagen et al., 2024). Les processus liés au plateau interne, qui ont été abordés assez brièvement dans cette thèse, méritent également un examen plus approfondi. Si la force de Coriolis semble avoir un effet négligeable dans la configuration simplifiée donnée, on peut se demander si cela reste vrai pour tous les types de conditions. Des courants d'arrachement beaucoup plus forts, tels que ceux générés lors de tempêtes, pourraient-ils être sensibles aux effets de Coriolis ? L'impact de la stratification et de son amplitude dans les modèles de résolution des vagues doit encore être approfondi, tandis que l'effet des vents mérite une étude paramétrique complète, prenant en

compte à la fois la magnitude et la direction du vent (*cross-shore* ou *longshore*), avec une référence particulière à l'alignement ou non des vents sur la dérive littorale. En outre, d'autres phénomènes tels que le *wave streaming* mériteraient une attention particulière, car il est suggéré qu'ils ont un impact important sur la circulation littorale en présence de stratification (Wang et al., 2020). Les modèles 3D à vagues résolues seraient d'excellents candidats pour simuler plus explicitement ce phénomène peu exploré.

- **Quels résultats pour d'autres types de traceurs ?**

Cette thèse est basée sur l'hypothèse d'un traceur à flottabilité neutre se diluant dans l'eau. Si cette hypothèse est valable pour les traceurs passifs dissous, tels que les composés chimiques ou les pathogènes, elle présente des limites pour d'autres types de traceurs. Par exemple, les sédiments, dont la vitesse de sédimentation varie en fonction de leurs caractéristiques, les hydrocarbures qui ont tendance à rester en surface, ou les microplastiques, dont le comportement dépend de leurs propriétés spécifiques (voir par exemple Forsberg et al., 2020; Kim & Kim, 2024). Une meilleure compréhension de la dispersion des plastiques dans les zones côtières serait particulièrement utile pour les modèles régionaux, car les courants d'arrachement peuvent remobiliser les plastiques au large (van Sebille et al., 2020). En outre, l'impact des *flash rips* sur les échanges de sédiments *cross-shore* reste peu inexploré (voir les études récentes de Park et al., 2020; Kim, 2021). Les traceurs biologiques, tels que les larves, peuvent présenter un comportement spécifique, comme un mouvement autonome, qui peut favoriser leur rétention ou leur dispersion sur les côtes (Moulton et al., 2023). Pour les contaminants, les sources et les puits, y compris la mortalité bactérienne, pourraient être incorporés dans le modèle de dispersion. CROCO dispose déjà de capacités en matière de dynamique sédimentaire, de cycles biogéochimiques ou de transport lagrangien. Nous pourrions les utiliser à l'avenir ou étendre leurs capacités pour traiter les traceurs pertinents dans la zone côtière.

- **Pouvons-nous affiner notre compréhension de la cascade turbulente dans la zone littorale ?**

La présente étude a utilisé les résultats de Marchesiello et al. (2021) sur la cascade turbulente dans la zone littorale. Une vision globale des sources, des transferts et des puits d'énergie cinétique a été proposée, dans laquelle les courants d'arrachement transitoires (*flash rips* et

mini-rips) pourraient trouver leur place. Ce modèle conceptuel a été proposé dans un cadre plutôt idéalisé, et pour aller plus loin, il serait intéressant d'explorer comment la cascade turbulente serait affectée par les conditions environnementales, telles que la bathymétrie ou le spectre des vagues. Une étude récente a souligné la difficulté d'observer une cascade inverse lorsque la dispersion directionnelle $\sigma_\theta < 10°$ (Baker et al., 2023b). La cascade inverse pourrait aussi être affectée par un champ de vagues très aléatoire (Kellay & Goldburg, 2002) avec un σ_θ excessivement grand. Il serait également utile d'examiner plus en détail la dynamique associée au déferlement des vagues, en particulier l'injection de vorticité causée par les vagues à crête courte et le processus de fusion des tourbillons qui conduit à des flux d'énergie à grande échelle. Il reste encore beaucoup à faire dans ce domaine d'étude relativement jeune pour mieux comprendre la dynamique.

- **Quelle paramétrisation des *flash rips* et des mini-rips ?**

Le paramétrisation évoquée plus haut bénéficierait d'une étude paramétrique complète à la fois sur les *flash rips* et les mini-rips. Pour les *flash rips*, les paramétrisations existantes, tels que la vitesse d'échange proposée par Suanda and Feddersen (2015), pourraient être revus et affinés à l'aide de modèles 3D à vagues résolues. D'autre part, la dispersion induite par les mini-rips a été décrite ici pour la première fois et dans un cadre paramétrique limité. Bien que leur processus de génération semble très robuste, leur effet dans d'autres environnements reste une question ouverte. Seraient-ils plus efficaces sur les plages réfléchissantes ? Par exemple, Brown et al. (2019) a observé que lorsque le colorant était libéré sur une plage à forte pente, le traceur se dispersait rapidement et uniformément un peu au-delà de la zone de déferlement. Ils n'ont pas clairement identifié le mécanisme responsable, mais nos résultats suggèrent fortement l'action des mini-rips. Une autre question est de savoir comment les mini-rips réagissent aux variations du forçage des vagues. Cette question est directement liée à la sensibilité du courant de retour et du cisaillement vertical associé, dont le comportement n'est pas clair (Faria et al., 2000). Le profil du courant de retour répond au flux de masse de surface pendant le déferlement mais aussi à la viscosité turbulente, tous deux sensibles à la hauteur de vague d'une manière difficile à prévoir — Svendsen and Putrevu (1994) propose la relation $0.06\,h\sqrt{gh}$, qui donne un ordre de grandeur mais explique difficilement la sensibilité à la hauteur de la vague, selon Faria et al. (2000). Le courant de retour serait également affecté par l'advection non linéaire.

Enfin, pour un cisaillement vertical donné, le taux de croissance de l'instabilité de cisaillement 3D, produisant des mini-rips, dépendrait de la viscosité turbulente et de la friction du fond. Une dernière question se pose : comment les mini-rips se comporteraient-ils en fonction de la bathymétrie ? Les irrégularités affecteraient-elles, par exemple, les échelles les plus instables ou le mécanisme d'appariement inhérent à l'instabilité secondaire ? Toutes ces questions et d'autres encore méritent d'être approfondies, par le biais de la modélisation numérique ou d'expériences en laboratoire.

- **Quels défis de modélisation ?**

Enfin, comme pour toute étude basée sur la modélisation numérique, une attention constante doit être portée aux techniques utilisées. Pour la modélisation du littoral, le déferlement des vagues semble assez bien représenté dans les modèles Navier-Stokes à surface libre. Contrairement aux modèles de type Boussinesq dérivés d'équations d'écoulement idéal et irrotationnel (Kazolea & Ricchiuto, 2018), il n'y a pas de critère explicite pour le déferlement des vagues, qui est plutôt traité par un schéma d'advection à capture des chocs pour produire des rouleaux, analogues à un bore ou à un front hydraulique, et par la fermeture turbulente pour modéliser la turbulence de la vague déferlante. Bien que cela offre une plus grande flexibilité par rapport aux modèles basés sur des critères, il est essentiel de comprendre comment les schémas numériques influencent la représentation du déferlement des vagues. Par exemple, alors que le schéma d'advection WENO5 s'est avéré particulièrement efficace, les résultats ont été quelque peu sensibles aux choix d'interpolation pour les vitesses d'advection. Peut-être plus important encore, le schéma implicite d'Euler Backward utilisé pour traiter les ondes acoustiques dans la direction verticale s'est avéré produire des erreurs significatives avec de grands pas de temps à une résolution relativement plus grossière (> 2 m). Il serait souhaitable de trouver des alternatives à ce schéma ou de mettre en œuvre des gardes-fous pour éviter de franchir les limites de validité. Le nombre de niveaux verticaux peut également être important (Smit et al., 2013), bien que 10 niveaux soient probablement suffisants pour les besoins de cette thèse.

Une étude plus approfondie, ainsi qu'un benchmark de plusieurs modèles à vagues résolues qui inclurait des estimations de coûts, seraient utiles à la communauté scientifique. Notre tentative de comparaison dans le Chapitre IV a fourni des résultats très encourageants sur l'efficacité de calcul de CROCO par rapport aux modèles Boussinesq, malgré l'ajout de la dimension verticale

dans un cadre Navier-Stokes complet. Les calculs exclusivement locaux permis par une approche pseudo-compressible se sont avérés bénéfiques pour le calcul (massivement) parallèle, montrant une bonne scalabilité. Une version GPU du modèle est maintenant disponible, ce qui portera certainement la capacité de calcul du code à un niveau supérieur, ce qui signifie que plusieurs jours ou mois de simulations à vagues résolues dans la zone littorale seront disponibles.

Appendix A

Correction of GLS turbulence closure for wave-resolving models with stratification

* * *

A.1 Summary

The paper *Correction of GLS turbulence closure for wave-resolving models with stratification* addresses the issue of excessive vertical mixing in potential flow regions of wave-resolving models due to the linear instability of two-equation closure systems. Building on the works of Mayer and Madsen (2000) and Larsen and Fuhrman (2018), we extend this correction to the Generic Length Scale (GLS) turbulence closure approach and test it on a stratified nearshore problem. We propose a modification to the turbulence equations that limits overmixing in non-breaking wave regions, thus preserving stratification on the inner shelf under favorable heat and wind conditions.

The study demonstrates the necessity of these corrections for accurate 3D wave-resolving studies of surf-shelf exchanges, which are critical for understanding the dynamics of pollutants, biological matter, and sediments in coastal zones. We provide detailed numerical experiments, including an ideal test case and validation against flume experiments, showing the effectiveness of the proposed correction in maintaining realistic stratification without compromising the model performance in the surf zone.

This development in the CROCO model (and in other 3D models soon) opens up a new page in the study of transient rip currents. Until now, the study of the combined effects of stratified shelf and transient rips within the same framework was not possible. The COAWST framework for example (Kumar & Feddersen, 2017b,a), allows to couple a 3D circulation model with a 2D wave-resolving model for the surf zone, but breaking force issued from the 2D model is taken

as a depth-uniform body force. Therefore, CROCO with the presented correction is a great modeling tool to investigate scientific questions about vertical structure of rip currents.

A.2 Author contribution

This work is a collaboration with my PhD advisor P. Marchesiello. The conceptualization of the study has been imagined by P. Marchesiello, who implemented the correction, performed the simulations, and wrote the original draft. I helped to validate the correction with simulations. We all contributed to improving the methodology, discussing the results and improving the article.

Ocean Modelling 184 (2023) 102212

Contents lists available at ScienceDirect

Ocean Modelling

journal homepage: www.elsevier.com/locate/ocemod

Short communication

Correction of GLS turbulence closure for wave-resolving models with stratification

Patrick Marchesiello *, Simon Treillou

IRD/LEGOS, University of Toulouse, France

ARTICLE INFO

Keywords:
Nearshore
Wave-resolving model
Wave-induced mixing
Turbulence closure

ABSTRACT

We build on the work of Mayer and Madsen (2000) and Larsen and Fuhrman (2018) to correct for overmixing in wave potential flow regions due to the linear instability of two-equation closure systems. We extend it to the Generic Length Scale (GLS) turbulent closure approach, while testing it for the first time on a stratified nearshore problem. The modified turbulence equations affect only the nonbreaking wave potential flow region where the vorticity is less than 10% of the strain rate and thus can preserve stratification on the innershelf under favorable heat and wind forcing conditions. This work is a necessary step before engaging in full 3D wave-resolving studies of surf–shelf exchange.

1. Introduction

Several 3D wave-resolving, free-surface and terrain-following models based on the Reynolds-Averaged Navier–Stokes (RANS) equations have emerged for the nearshore zone, e.g., SWASH (Zijlema et al., 2011), NHWAVE (Derakhti et al., 2016) and CROCO (Marchesiello et al., 2021). In these models, the explicit overturning of the free surface is excluded and the breaking wave is modeled with a single-valued free surface which behaves as a dissipating bore. Despite the absence of explicit overturning (replaced by parameterized turbulence), these models can be accurate as well as computationally efficient in the study of waves and wave-driven mean and transient circulation. They can thus be applied to the entire 3D nearshore zone, including the innershelf area and be coupled with biogeochemical or sediment transport models to explicitly simulate the effects of realistic short-crested and asymmetric waves (Marchesiello et al., 2021, 2022). But stratification or Earth rotation has not been included in these earlier works, even though they may be important on the shelf and in the exchange mechanisms with the surfzone.

In previous studies (Marchesiello et al., 2021, 2022), the Coastal and Regional Ocean COmmunity model (CROCO) was used with the $k-\omega$ or $k-\epsilon$ two-equation turbulence closure models as part of a Generic Length Scale (GLS) method (Warner et al., 2005). The $k-\omega$ model generally performed best in the surfzone without modification of the standard model parameters from Wilcox (1988). This is a conclusion shared by several modeling studies since Mayer and Madsen (2000), possibly due to a more accurate near-wall treatment by $k-\omega$ models (Devolder et al., 2018), which is needed in the wall-bounded turbulent shear flows of the surfzone (Trowbridge and Elgar, 2001). However, both models suffer from overmixing in areas of potential (irrotational) flow, typically in regions outside the surfzone where waves are not breaking. This problem has long been identified (Lin and Liu, 1998; Mayer and Madsen, 2000; Bradford, 2011; Brown et al., 2016; Devolder et al., 2018; Larsen and Fuhrman, 2018) and understood as a kind of paradox where vorticity, rather than strain rate, should be the source of turbulence, even though the role of strain rate is theoretically justified by the Reynolds averaging process (Kato and Launder, 1993). The generation of turbulence in unexpected regions may thus appear to challenge the validity of Boussinesq eddy viscosity hypothesis on the local relationship between mean and turbulent quantities (Schmitt, 2007), which led to the introduction of a realizability constraint based on physical assumptions (Durbin, 2009).

Recently, however, Larsen and Fuhrman (2018), building on earlier analysis of Mayer and Madsen (2000) that went rather unnoticed, have better identified the causes of excessive vertical mixing in areas of potential flow, revealing a linear instability of the two-equation closure system. It is the interaction between the two turbulent prognostic variables in the system that can exponentially amplify the generation of turbulent energy in unexpected regions. The resulting overmixing can affect the amplitude of waves propagating to the nearshore zone and degrade the prediction of the wave breaking point (Lin and Liu, 1998; Bradford, 2000; Mayer and Madsen, 2000). We found in the present study that, perhaps more importantly, overmixing can also affect the maintenance of stratification on the innershelf. The last point is generally overlooked because 3D wave-resolving models have been primarily focused on the surfzone without considering exchanges with the innershelf, in contrast to recently emerging wave-averaged model studies (Kumar and Feddersen, 2017; Wang et al., 2021), which do not suffer from the overmixing problem. With advances in non-hydrostatic

* Corresponding author.
E-mail address: patrick.marchesiello@ird.fr (P. Marchesiello).

https://doi.org/10.1016/j.ocemod.2023.102212
Received 28 February 2023; Received in revised form 11 May 2023; Accepted 12 May 2023
Available online 18 May 2023

models and computational resources, the study of surf–shelf exchange — describing the fate of pollutants, biological matter, and sediments in the nearshore zone (e.g., Brown et al. 2015) — can now also be accessed by representing phase-resolved waves and stratification. However, to proceed in this direction, the problem of excessive mixing in nonbreaking waves must first be corrected.

Note that in wave-averaged models, a certain amount of nonbreaking wave-induced mixing is actually introduced by semi-empirical formulas (Qiao et al., 2004; Ghantous and Babanin, 2014). It is much smaller than that caused by wave breaking but it reaches deeper and can affect the sea surface temperature of ocean general circulation models (Babanin, 2023). The wave-induced turbulence involved in these parameterizations assumes various processes, such as interaction with pre-existing turbulence. Here, the generation of intense innershelf turbulent mixing appears to be more of an artifact of the turbulent models under conditions of nearly potential flow. To address this specific issue, we build on the works of Mayer and Madsen (2000) and Larsen and Fuhrman (2018) and extend it to a more generic approach within GLS, while testing for the first time the effect that a stabilized turbulence model has on innershelf stratification in an idealized nearshore configuration.

2. Modification of the turbulence closure model

CROCO is a nonhydrostatic, free-surface and terrain-following model, developed around the Regional Oceanic Modeling System (Shchepetkin and McWilliams, 2005; Debreu et al., 2012). Its capabilities include high-performance computation of high-order-accurate discretized equations, and coupling with atmosphere, waves, biogeochemistry, sediment and turbulence models. It has been applied to a variety of configurations, from regional and shelf circulations to very fine-scale processes, such as wave-induced nearshore circulation (Marchesiello et al., 2015, 2021, 2022). It thus appears naturally suited for addressing surf–shelf exchange processes in a 3D, rotating and stratified framework. However, innershelf stratification cannot be preserved if the turbulence closure equations produce excessive mixing, as is often the case for RANS wave-resolving models (Larsen and Fuhrman, 2018).

2.1. Turbulence closure

The treatment of breaking waves in CROCO involves both a shock-capturing advection scheme (WENO5) and a second-order turbulence closure system — a $k-\epsilon$ or $k-\omega$ model solving the equations for turbulent kinetic energy k and dissipation ϵ or dissipation rate $\omega \propto \epsilon k^{-1}$ — as part of a Generic Length Scale (GLS) method (Warner et al., 2005). In the absence of buoyancy forcing, the turbulence equations express a balance between transport, diffusion, shear production and dissipation:

$$\frac{\partial \rho k}{\partial t} = -\vec{\nabla}.(\rho \vec{\mathbf{v}}\, k) + D_k + \rho(P-\epsilon) \tag{1}$$

$$\frac{\partial \rho \epsilon}{\partial t} = -\vec{\nabla}.(\rho \vec{\mathbf{v}}\, \epsilon) + D_\epsilon + \rho \frac{\epsilon}{k}(c_{\epsilon 1} P - c_{\epsilon 2}\epsilon) \tag{2}$$

$$\text{or} \quad \frac{\partial \rho \omega}{\partial t} = -\vec{\nabla}.(\rho \vec{\mathbf{v}}\, \omega) + D_\omega + \rho \frac{\omega}{k}(c_{\omega 1} P - c_{\omega 2}\epsilon) \tag{3}$$

The eddy viscosity $\nu_t = c_\mu\, l\, k^{\frac{1}{2}}$ is derived from these equations, with coefficient c_μ dependent on stability functions, and mixing length $l \propto k^{\frac{3}{2}} \epsilon^{-1}$. According to the Boussinesq eddy viscosity hypothesis, the shear production term for k is $P = 2\nu_t S^2$, with $S^2 = S_{ij} S_{ij}$ and $S_{ij} = \frac{1}{2}(\frac{\partial u_i}{\partial x_j} + \frac{\partial u_j}{\partial x_i})$ (using Einstein notation), which is the mean 3D strain rate tensor.[1] All turbulence model parameters are given in Warner et al. (2005), based on Burchard et al. (1998) for $k-\epsilon$ and Wilcox (1988) for $k-\omega$. The turbulence models perform very well in the surfzone, compared with flume experiments (Marchesiello et al., 2021, 2022). However, as in previous studies, they tend to produce excessive mixing in potential flow regions, i.e., on the innershelf.

[1] The use of a 3D strain rate tensor differs from the GLS approach presented in Warner et al. (2005), where energy production is only due to vertical shear of horizontal flows.

2.2. Correction in potential flow regions

In many studies of breaking waves (see the literature reviews by Devolder et al., 2018; Larsen and Fuhrman, 2018), the predicted turbulence levels from two-equation closures are much higher than what has actually been measured. While many attempts were made for limiting mixing in supposed low-turbulence regions, Larsen and Fuhrman (2018) more specifically identify the causes of overmixing in areas of potential (irrotational) flow, typical of nonbreaking waves. The problem is common to the entire class of 2-equation closure models ($k-\omega$, $k-\epsilon$, and variants) because it is related to an unconditional linear instability of the equation system under low vorticity conditions.

For the $k-\omega$ model, a linearized homogeneous system suitable for the potential flow region beneath surface waves (where a fixed strain rate S and negligible advection and diffusion can be assumed) is :

$$\frac{\partial k}{\partial t} = P - \epsilon \tag{4}$$

$$\frac{\partial \omega}{\partial t} = \frac{\omega}{k}(c_{\omega 1} P - c_{\omega 2}\epsilon) \tag{5}$$

Noting that the specific dissipation rate ω is related to the energy dissipation ϵ by $\epsilon = c_\mu\, k\, \omega$ and that the eddy viscosity $\nu_t = \frac{k}{\omega}$, we can rewrite the system of equations in terms of only the variables k and ω:

$$\frac{\partial k}{\partial t} = 2\frac{k}{\omega} S^2 - c_\mu\, k\, \omega \tag{6}$$

$$\frac{\partial \omega}{\partial t} = 2c_{\omega 1} S^2 - c_{\omega 2}\, c_\mu\, \omega^2 \tag{7}$$

Considering as Larsen and Fuhrman (2018) that ω tends asymptotically to ω_∞ as $\partial\omega/\partial t$ tends to 0 and replacing ω by ω_∞ in the k equation gives an exponential growth $k \sim e^{\sigma_\infty t}$ with σ_∞ a fraction of S always positive, i.e., the model is unconditionally unstable.

The instability of this system thus corresponds to an exponential increase in the turbulent energy k, particularly in areas of potential flow where dissipation is never strong enough to control it. Larsen and Fuhrman (2018) propose to curb the excessive energy production where the strain rate S is much greater than the vorticity Ω (defined by $\Omega^2 = \Omega_{ij}\Omega_{ij}$ with $\Omega_{ij} = \frac{1}{2}(\frac{\partial u_i}{\partial x_j} - \frac{\partial u_j}{\partial x_i})$, the rotation rate tensor) and demonstrate that this correction stabilizes the solution of the linear system as σ_∞ becomes negative. The limitation is written as a majoration of ω in the viscosity $\nu_t = \frac{k}{\omega^*}$ used in the production term $P = 2\nu_t S^2$, with the following function:

$$\omega^* = \max\left(1\,,\ \lambda \frac{c_{\omega 2}}{c_{\omega 1}} \frac{S^2}{\Omega^2}\right) \omega \tag{8}$$

where λ is a limitation parameter (taken as 0.05 in Larsen and Fuhrman 2018). A similar condition is given for the $k-\epsilon$ model ($\nu_t = c_\mu \frac{k^2}{\epsilon^*}$), where:

$$\epsilon^* = \max\left(1\,,\ \lambda \frac{c_{\epsilon 2}}{c_{\epsilon 1}} \frac{S^2}{\Omega^2}\right) \epsilon \tag{9}$$

This correction is reminiscent of the one proposed for the stagnation point anomaly by Kato and Launder (1993), in a different study context, where the turbulent energy production $P = 2\nu_t S^2$ is replaced by $P = 2\nu_t S\Omega$. It also resembles that of Mayer and Madsen (2000) who take $P = 2\nu_t \Omega^2$, thus making production vanish in pure straining flow. According to Larsen and Fuhrman (2018), these attempts significantly reduce the growth of instability in the potential flow region, but do not resolve its formal unconditionality. In addition, in our numerical experiments, the use of vorticity to replace all or part of the strain rate in the production term P tends to under-represent the production of turbulent energy in the surfzone, which is undesirable. We thus concur with Mayer and Madsen (2000) and Durbin (2009) that altering the

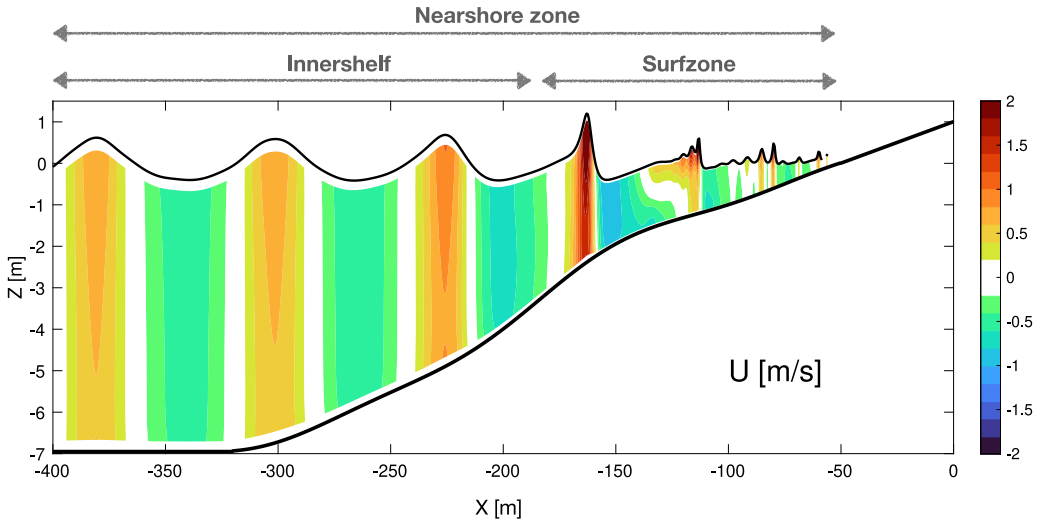

Fig. 1. Snapshot of CROCO wave height and cross-shore velocity u propagating across an idealized nearshore configuration. The simulation is done at 50 cm resolution and with the $k-\omega$ turbulence closure model.

strain rate tensor in P is not a satisfactory solution and we choose instead to majorate ϵ (when computing ν_t) to control the instability of the turbulence equation system. The latter solution may appear merely as an alternative to limiting the mixing length l as in Bradford (2011) or the coefficient c_μ as in realizable models (Shih et al., 1995), but a limitation based on the ratio S/Ω makes it a more effective constraint on the instability (Fuhrman and Li, 2020).

2.3. Implementation in GLS

For the implementation in the CROCO GLS code, we impose the Larsen and Fuhrman (2018) limitation on the variable ϵ whatever the choice of closure, since the turbulent dissipation ϵ is computed in all types of two-equation models handled by GLS. Starting from the $k-\omega$ model, we use the relation between ϵ and ω ($\epsilon = c_\mu k\omega$) to assume a limitation of the form:

$$\epsilon^* = \max\left(1\,,\,\lambda\frac{c_{\omega 2}}{c_{\omega 1}}\frac{S^2}{\Omega^2}\right)\epsilon \tag{10}$$

This expression is similar to Eq. (9) for the $k-\epsilon$, apart from the factor $c_{\omega 2}/c_{\omega 2}$ replacing $c_{\epsilon 2}/c_{\epsilon 1}$. However, the fraction c_2/c_1 does not vary much with the choice of closure model (Warner et al., 2005) and is 1.2–1.5. Considering the uncertainty in choosing λ, we can propose a generic limitation:

$$\epsilon^* = \max\left(1\,,\,\lambda\frac{S^2}{\Omega^2}\right)\epsilon \tag{11}$$

In our numerical experiments (next section), this formulation controlled the growth of instability on the innershelf with $\lambda \sim 0.1$. In this case, the correction is triggered as soon as the vorticity is less than about 10% of the strain rate. We also note that increasing the power law of the correction function stiffens the intensity of the correction below the 10% threshold and further decreases the mixing on the innershelf. Therefore, in the following, we will test the modified formulation:

$$\epsilon^* = \max\left(1\,,\,\lambda\frac{S^4}{\Omega^4}\right)\epsilon \tag{12}$$

with a baseline λ value of 0.01.

3. Numerical experiments

3.1. Ideal test case

The idealized model configuration is representative of a nearly planar beach representative of southern California (Kumar and Feddersen, 2017) or elsewhere with a smooth sandbar that triggers wave breaking, and a cross-shore circulation (Fig. 1). Details of the numerical implementation of CROCO for wave-resolving simulations is given in Marchesiello et al. (2021, 2022), only the configuration is presented here. For simplicity, we use a 2D (x–z) channel with no alongshore dimension. Depths range from 7 m offshore to 1 m above mean sea level at the coast and a gentle sandbar is present about 100 m from shore. The shoreline position is allowed to vary with swash oscillation, based on a wetting-drying scheme (Warner et al., 2013). Initially, the water is at rest and the stratification is given by a temperature profile $T(z) = 8 + 10e^{z/50}$ (Fig. 2), roughly representing the mid-latitude summer situation.

A monochromatic wave is generated at the offshore boundary with 0.5 m wave amplitude and 10 s period. A non-slip condition is imposed on the boundaries of the channel sidewalls. The horizontal grid spacing is 0.5 m, the vertical grid has 10 vertical levels refined at the surface and bottom and the model time step is 0.025 s. For bed shear stress, the logarithmic law of the wall is used with a roughness length of 1 mm.

The comparison of velocity u, temperature T and eddy viscosity ν_t at 30 min after the start of the simulation is presented in Fig. 2. It can be seen that without limitation, the eddy viscosity produced by the $k-\omega$ model increases to values well above $0.01\,\mathrm{m^2/s}$ and the high viscosity signal propagates from the surfzone to the shelf and gradually invade the entire model area (Fig. 3). With the corrected closure system, the viscosity does not develop outside the surfzone, i.e., in the potential flow region where waves do not break. In this case, the viscosity in the surfzone has the expected structure and magnitude ($\nu_t = 0.01$–$0.05\,\mathrm{m^2/s}$; Battjes 1975). It is important to note that in the breaker zone, the viscosity — and related velocity profile — is similar in both the standard and corrected cases, showing that the limitation does not seem to affect the assumed turbulent zone much (which is desirable), but this will be verified against laboratory data in the next section.

The effect of vertical mixing on stratification is dramatic (Fig. 2). At viscosity values of about $0.01\,\mathrm{m^2/s}$ and above, mixing can break up the stratification in a matter of minutes ($\tau_{mix} = l^2/\nu_t$ with l limited by bottom depth). With the original $k-\omega$ model, such high viscosity values reach the entire domain within half an hour and stratification breakdown follows everywhere. On the contrary, stratification is maintained on the innershelf outside the surfzone with the corrected turbulence model. In this case, the result becomes similar to those presented by wave-averaged models (lacking a process to generate a nonbreaking wave eddy viscosity; Kumar and Feddersen 2017) and to nearshore observations (Sinnett and Feddersen, 2019), where spring–summer stratification is preserved outside the surfzone as long as winds are sufficiently light.

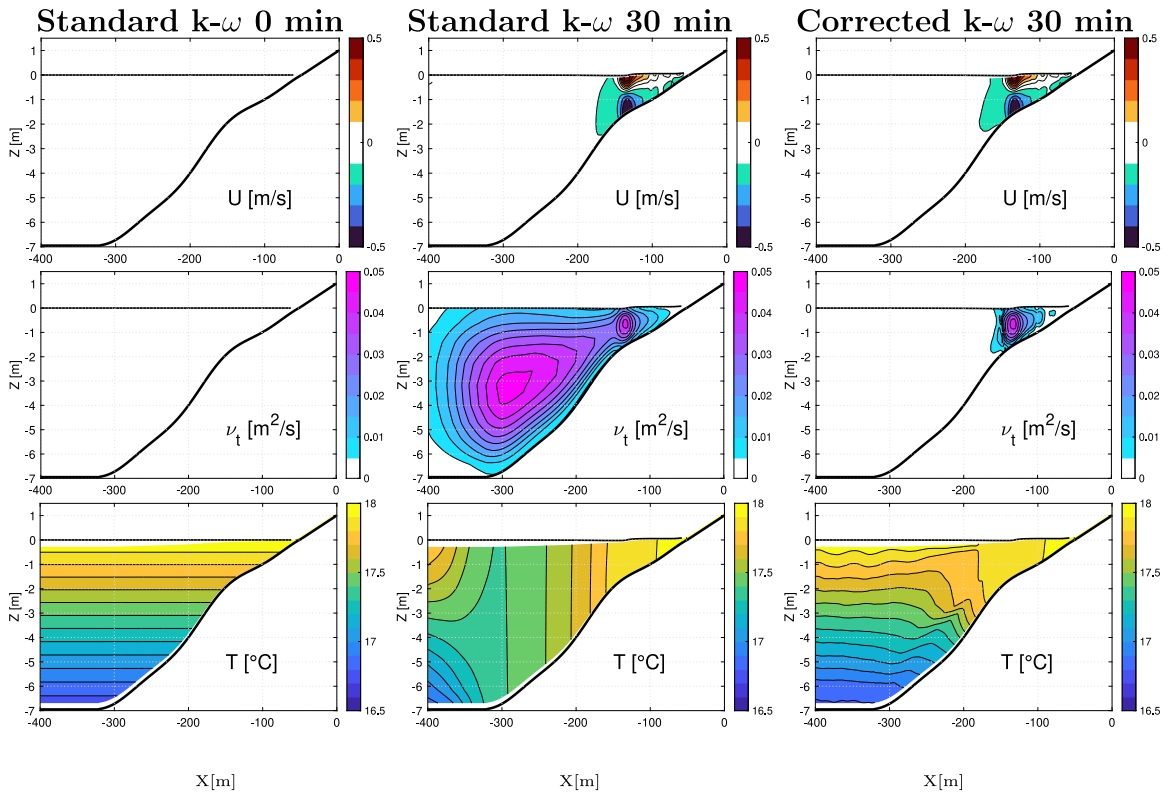

Fig. 2. Wave-mean velocity u, temperature T and eddy viscosity ν_t at initial time (left) and 30 min into the simulation (center and right panels). Center: solution of the standard $k-\omega$ closure model; right: solution of the corrected closure model.

Next, we checked that the corrections made on the turbulent dissipation ϵ are working not only for the $k-\omega$ model but also for the $k-\epsilon$ and the generic model of Umlauf et al. (2003) which is referred to as *gen* model in Warner et al. (2005). Fig. 4 shows the result of the three models. It confirms the report of Marchesiello et al. (2021) that the $k-\epsilon$ model produces less turbulent energy than the $k-\omega$ model, with as a consequence an over-prediction of velocity shear and undertow magnitude. The *gen* model gives intermediate results. Most importantly here, the correction has worked in all cases and no exponential growth of turbulent energy and viscosity has occurred outside of the surfzone. Our correction of turbulent dissipation thus appears appropriate for a GLS approach.

3.2. Surfzone verification with LIP experiment

Validation of surfzone currents by comparison with flume experiments are provided in Marchesiello et al. (2021, 2022). To make sure that the change of mixing due to the GLS corrections does not affect the surfzone excessively, we present here again some comparison with the full-scale LIP experiment of Roelvink and Reniers (1995). Following Durbin (2009), we assume that since eddy viscosity models are intended for prediction of mean flow, mean flow data are a good basis for calibration.

In the LIP1B experiment, a JONSWAP wave spectrum with significant wave height $H_s = 1.4$ m and period $T_p = 5$ is generated that produces wave breaking at various position around a sandbar. The horizontal grid resolution is 25 cm with 20 vertical levels refined near the bottom. For more details on the LIP experiment and model configuration, the reader is referred to the previous reports cited above.

Fig. 5 shows a comparison of the model cross-shore currents with data, and the match appears very good throughout the complex morphology of the beach. The waves break everywhere depending on their height but the breaking is more intense on the sandbar, where the undertow has a strong shear and maximum intensity of about 30 cm/s. The mean absolute error of all experiments (Fig. 5, bottom panel) is 3–4 cm/s (RMSE = 2–3 cm), close to the measurement error of 2 cm/s. As discussed in Marchesiello et al. (2021), these results show the validity of a RANS approach for estimating breaking-induced turbulence (via parameterization) and calculating lower frequency circulation explicitly.

The experiments with correction of the $k-\omega$ model do not modify much the results, but differences appear between the case with strong limitation ($\lambda = 0.1$) and moderate limitation ($\lambda = 0.01$). In the former, the mean error with measurements is 4.9 cm while the latter is 3.7 cm, close to 3.6 cm for the standard case. The error in the strong limitation case is most significant in the offshore region of the sandbar where only the largest waves in the spectrum break, implying intense but transient turbulent energy. However, the error reduces again at the most offshore location where turbulent energy is supposedly weakening. The moderate limitation case performs well and even reduces the error, relative to the standard model, at a few inshore locations as well as at the most offshore location. The λ value of 0.01 confirms to be a good choice for an optimal correction level. By further decreasing λ, the instability reappears.

The genericity of the λ value is unclear. We have increased the power law of the limiting function (Section 2.3) in order to make the correction more robust and less sensitive to the limiting value. The fact that the correction works for different GLS model types seems to confirm this idea. We believe that the method is robust, at least for the problem of waves propagating in the nearshore zone. We also verified that adding wind stress to the model (in the idealized nearshore configuration of Section 3.1) allows mixing of the stratified innershelf as expected, i.e. the correction does not prevent the generation of mixing outside the surfzone if the forcing conditions are favorable.

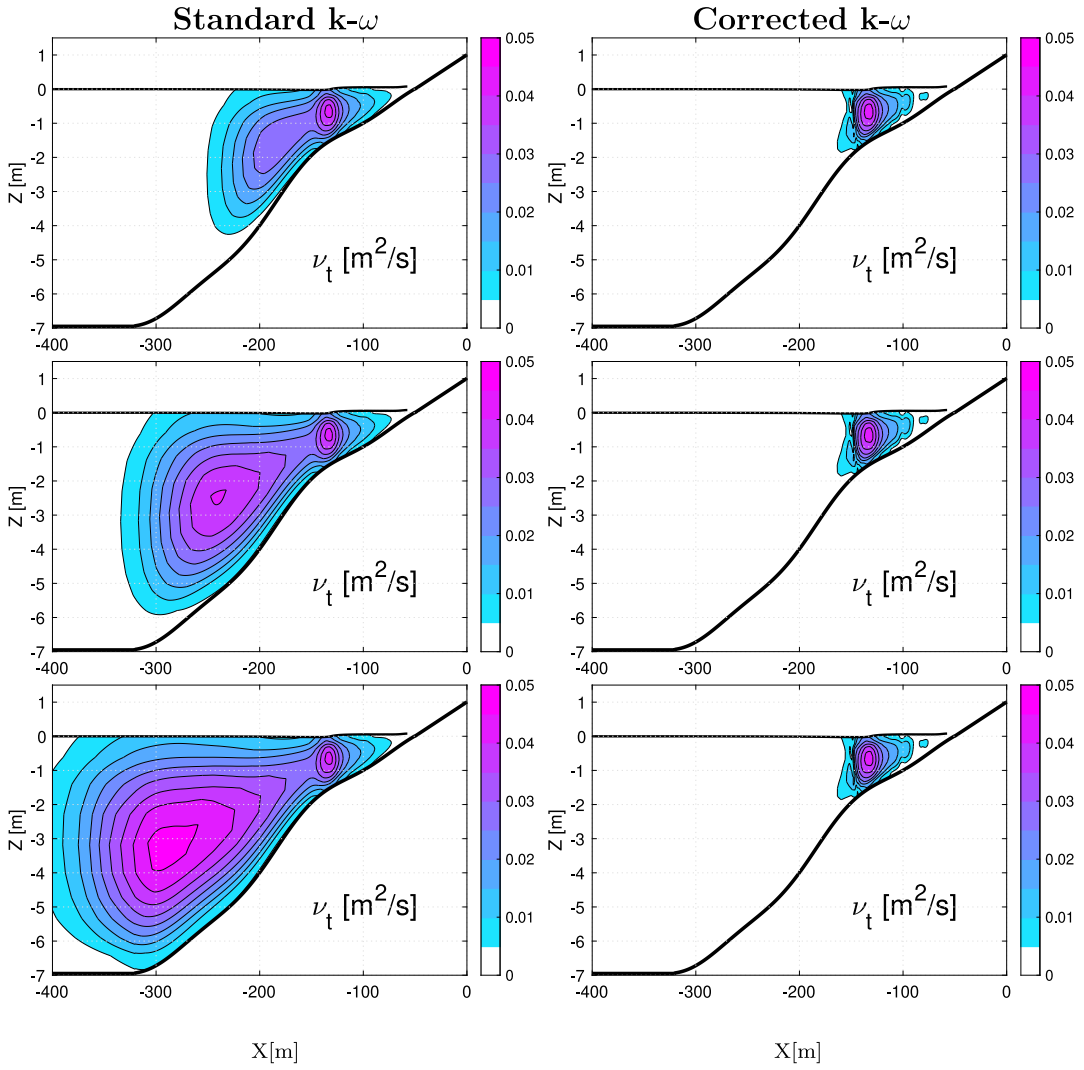

Fig. 3. Evolution of eddy viscosity ν_t 10, 20 and 30 min after the start of the simulation. Left: solution resulting from the standard $k-\omega$ closure model; right: solution from the corrected closure model.

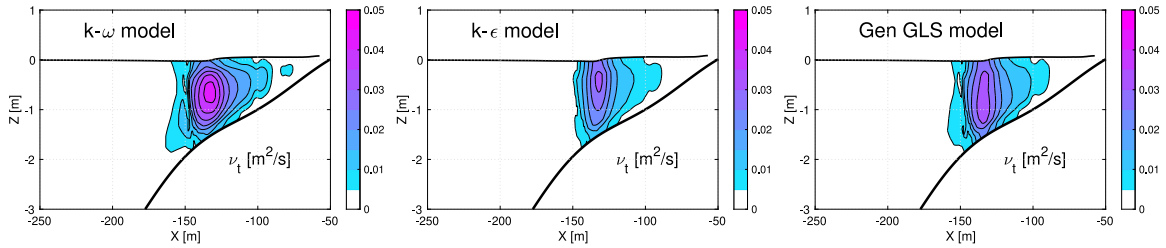

Fig. 4. Eddy viscosity ν_t 30 min into the simulation from three different version of the GLS closure model: $k-\omega$, $k-\epsilon$ and gen.

4. Conclusion

In this paper, we build on the work of Mayer and Madsen (2000) and Larsen and Fuhrman (2018) to correct for overmixing in potential flow regions due to the linear instability of two-equation closure systems. We extend it to a more generic GLS approach, while testing for the first time the corrected closure model on a stratified nearshore problem. The corrected GLS formulation changes little in the surfzone where high vorticity and turbulence are expected, while successfully addressing the problem of overmixing in regions where the waves are not breaking, allowing the model to maintain stratification on the shelf provided the vorticity is less than 10% of the strain rate. This work is a necessary step before engaging in full wave-resolving 3D studies of surf–shelf exchange that involve transient rip currents, stratification and also Earth rotation. This will be possible due to advances in non-hydrostatic free-surface models, which are emerging as a cost-effective

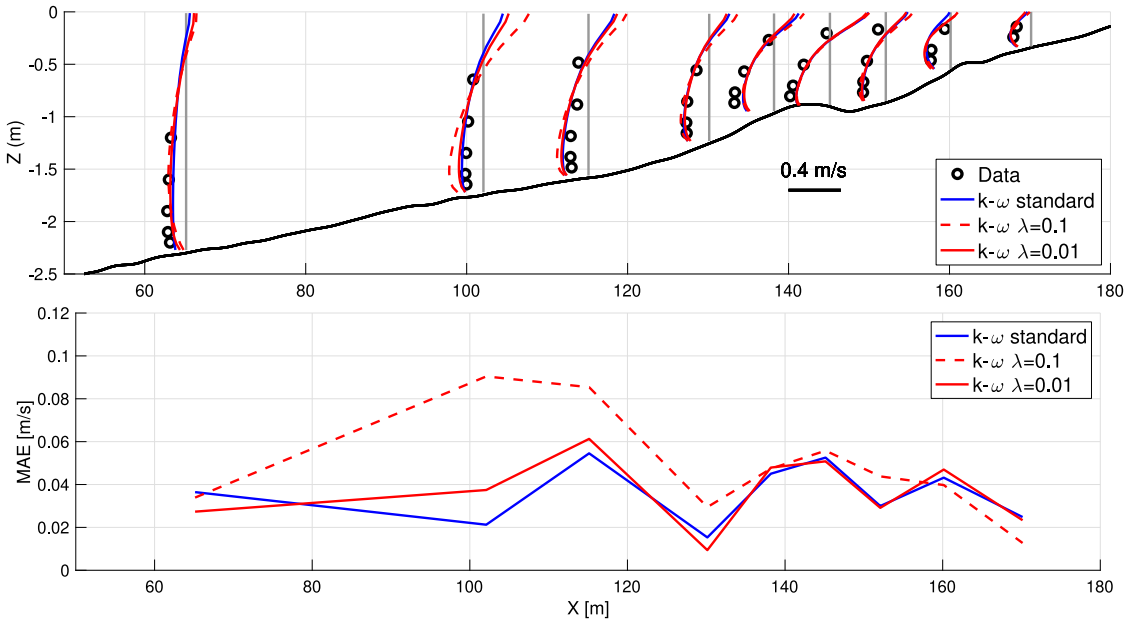

Fig. 5. Model simulation of the large-scale LIP11-1B Flume experiment. (Top) Comparison of simulated and measured current profiles u and sensitivity to the $k-\omega$ turbulence model correction ($\lambda = 0.1$ and 0.01); (Bottom) Mean Absolute Error of u relative to measurements for all experiments.

and accurate alternative to models that fully resolve the wave breaking process (Marchesiello et al., 2021).

CRediT authorship contribution statement

Patrick Marchesiello: Conceptualization, Methodology, Software, Validation, Writing – original draft. **Simon Treillou:** Methodology, Software, Validation, Writing – review & editing.

Declaration of competing interest

The authors declare the following financial interests/personal relationships which may be considered as potential competing interests: MARCHESIELLO Patrick reports financial support was provided by French Navy Hydrographic and Oceanographic Service. MARCHESIELLO Patrick reports a relationship with French National Research Institute for Sustainable Development that includes: employment.

Data availability

Data will be made available on request.

Acknowledgment

This research has received support from a consortium of French research agencies, as part of CROCO's development project (Insu GdR n°2014 named CROCO) and from the French Naval Hydrographic and Oceanographic Service (SHOM grant 20CP05). We thank Dano Roelvink for sharing the LIP data. Apart from these, all data were acquired by the authors and the CROCO source code is freely available at www.croco-ocean.org. Both laboratory and modeling data are available upon request.

References

Babanin, A.V., 2023. Ocean waves in large-scale air-sea weather and climate systems. J. Geophys. Res.: Oceans 128 (3), e2023JC019633.
Battjes, J., 1975. Modeling of turbulence in the surfzone. In: A.S.C.E., New York, N. (Eds.), Symposium on Modeling Techniques, Vol. II. pp. 1050–1061.
Bradford, S., 2000. Numerical simulation of surf zone dynamics. J. Waterw. Port Coast. Ocean Eng. 126, 1–13.
Bradford, S., 2011. Nonhydrostatic model for surf zone simulation. J. Waterw. Port Coast. Ocean Eng. 137, 163–174.
Brown, S., Greaves, D.M., Magar, V., Conley, D.C., 2016. Evaluation of turbulence closure models under spilling and plunging breakers in the surf zone. Coast. Eng. 114, 177–193.
Brown, J.A., MacMahan, J.H., Reniers, A.J.H.M., Thornton, E.B., 2015. Field observations of surf zone–Inner shelf exchange on a rip-channeled beach. J. Phys. Oceanogr. 45 (9), 2339–2355.
Burchard, H., Petersen, O., Rippeth, T.P., 1998. Comparing the performance of the mellor-yamada and the $k-\epsilon$ two-equation turbulence models. J. Geophys. Res.: Oceans 103 (C5), 10543–10554.
Debreu, L., Marchesiello, P., Penven, P., Cambon, G., 2012. Two-way nesting in split-explicit ocean models: Algorithms, implementation and validation. Ocean Model. 49–50, 1–21.
Derakhti, M., Kirby, J.T., Shi, F., Ma, G., 2016. NHWAVE: Consistent boundary conditions and turbulence modeling. Ocean Model. 106, 121–130.
Devolder, B., Troch, P., Rauwoens, P., 2018. Performance of a buoyancy-modified $k-\omega$ and $k-\omega$ sst turbulence model for simulating wave breaking under regular waves using OpenFOAM. Coast. Eng. 138, 49–65.
Durbin, P.A., 2009. Limiters and wall treatments in applied turbulence modeling. Fluid Dyn. Res. 41 (1), 012203.
Fuhrman, D.R., Li, Y., 2020. Instability of the realizable k–ϵ turbulence model beneath surface waves. Phys. Fluids 32 (11), 115108.
Ghantous, M., Babanin, A.V., 2014. One-dimensional modelling of upper ocean mixing by turbulence due to wave orbital motion. Nonlinear Processes Geophys. 21 (1), 325–338.
Kato, M., Launder, B., 1993. The modelling of turbulent flow around stationary and vibrating square cylinders. pp. 1–6.
Kumar, N., Feddersen, F., 2017. The effect of Stokes drift and transient rip currents on the inner shelf. Part I: No stratification. J. Phys. Oceanogr. 47 (1), 227–241.
Larsen, B.E., Fuhrman, D.R., 2018. On the over-production of turbulence beneath surface waves in Reynolds-averaged Navier–Stokes models. J. Fluid Mech. 853, 419–460.
Lin, P., Liu, P.L.-F., 1998. A numerical study of breaking waves in the surf zone. J. Fluid Mech. 359, 239–264.
Marchesiello, P., Auclair, F., Debreu, L., McWilliams, J., Almar, R., Benshila, R., Dumas, F., 2021. Tridimensional nonhydrostatic transient rip currents in a wave-resolving model. Ocean Model. 163, 101816.
Marchesiello, P., Benshila, R., Almar, R., Uchiyama, Y., McWilliams, J.C., Shchepetkin, A., 2015. On tridimensional rip current modeling. Ocean Model. 96, 36–48, Waves and coastal, regional and global processes.
Marchesiello, P., Chauchat, J., Shafiei, H., Almar, R., Benshila, R., Dumas, F., Debreu, L., 2022. 3D wave-resolving simulation of sandbar migration. Ocean Model. 180, 102127.
Mayer, S., Madsen, P.A., 2000. Simulation of breaking waves in the surf zone using a Navier-Stokes solver. In: Coastal Engineering 2000. pp. 928–941.
Qiao, F., Yuan, Y., Yang, Y., Zheng, Q., Xia, C., Ma, J., 2004. Wave-induced mixing in the upper ocean: Distribution and application to a global ocean circulation model. Geophys. Res. Lett. 31 (11).

Roelvink, J.A., Reniers, 1995. IP 11D Delta Flume Experiments : A Dataset for Profile Model Validation. WL / Delft Hydraulics.
Schmitt, F.G., 2007. About Boussinesq's turbulent viscosity hypothesis: historical remarks and a direct evaluation of its validity. C. R. Méc. 335 (9), 617–627, Joseph Boussinesq, a Scientist of bygone days and present times.
Shchepetkin, A.F., McWilliams, J.C., 2005. The regional oceanic modeling system (ROMS): A split-explicit, free-surface, topography-following-coordinate oceanic model. Ocean Model. 9 (4), 347–404.
Shih, T.H., Liou, W.W., Shabbir, A., Yang, Z., Zhu, J., 1995. A new k-ϵ eddy viscosity model for high reynolds number turbulent flows. Comput. & Fluids 24 (3), 227–238.
Sinnett, G., Feddersen, F., 2019. The nearshore heat budget: Effects of stratification and surfzone dynamics. J. Geophys. Res.: Oceans 124 (11), 8219–8240.
Trowbridge, J., Elgar, S., 2001. Turbulence measurements in the surf zone. J. Phys. Oceanogr. 31 (8).
Umlauf, L., Burchard, H., Hutter, K., 2003. Extending the k- ω turbulence model towards oceanic applications. Ocean Model. 5, 195–218.
Wang, P., McWilliams, J.C., Uchiyama, Y., 2021. A nearshore oceanic front induced by wave streaming. J. Phys. Oceanogr. 51 (6), 1967–1984.
Warner, J.C., Defne, Z., Haas, K., Arango, H.G., 2013. A wetting and drying scheme for ROMS. Comput. Geosci. 58, 54–61.
Warner, J., Sherwood, C., Arango, H., Signell, R., 2005. Performance of four turbulence closure methods implemented using a generic length scale method. Ocean Model. 8, 81–113.
Wilcox, D.C., 1988. Reassessment of the scale-determining equation for advanced turbulence models. AIAA J. 26 (11), 1299–1310.
Zijlema, M., Stelling, G., Smit, P., 2011. SWASH: An operational public domain code for simulating wave fields and rapidly varied flows in coastal waters. Coast. Eng. 58 (10), 992–1012.

Appendix B

Single-sum wavemaker Fortran routines

* * *

Below are the modified sections of the routines `wave_maker.h` and `forces.h` that implement a single-sum wavemaker. The complete files will be made available soon in the main branch of CROCO.

B.1 `wave_maker.h`

```
        wp=13.0             ! period
        wa=0.24             ! amplitude (Hs/sqrt(8))
        wd=0.0              ! incidence angle (deg)
        wds=10.0            ! directional spread (deg)
                            !  -> crest length = wl/(2*sin(wds))
        gamma=3.3           ! JONSWAP peakedness parameter
# if defined WAVE_MAKER_DSPREAD && defined NS_PERIODIC
!   correct wave directions for periodicity
!   if periodic boundaries
#  define WAVE_MAKER_DSPREAD_PER
# endif

!
!  Build wave spectrum
!
        if (FIRST_TIME_STEP) then

          fmin=0.2*wf   ! frequency spread
          fmax=3.0*wf
```

```
            df=(fmax-fmin)/Nfrq
            cff2=0.
            do iw=1,Nfrq
              wf_bry(iw)=fmin+float(iw)*df
              khd=h(IB0,0)*wf_bry(iw)**2/g
              kh=sqrt( khd*khd+khd/(1.+khd*(K1+khd*(K2+khd*(K3+khd*(K4+
     &                                          khd*(K5+K6*khd)))))) )
              wk_bry(iw)=kh/h(IB0,0)
            enddo
# ifdef WAVE_MAKER_JONSWAP
            sumspec=0.0
            do iw=1,Nfrq
              sigma=0.5*( 0.09*(1.+sign(1.,wf_bry(iw)-wf))+
     &                    0.07*(1.-sign(1.,wf_bry(iw)-wf)) )
              cff0=exp(-0.5*((wf_bry(iw)-wf)/(sigma*wf))**2)
              beta=(0.06238 * (1.094 - 0.01915 * log(gamma)))
     &  / (0.23 + 0.0336 * gamma - 0.185 * (1.9 + gamma) ** -1)
              cff1=beta*(wf**4)/(wf_bry(iw)**5)
     &                  *exp(-1.25*(wf/wf_bry(iw))**4)*gamma**cff0
              cff2=16.*cff1*df  ! integral must be 1
              wa_bry(iw)=cff2
              sumspec=sumspec+cff2
            enddo

# ifdef WAVE_MAKER_DSPREAD
!
! Single-sum wave-maker description in Treillou et al. (2024)
!
            displacetheta=minloc(abs(wf_bry-wf))
            cff2=MOD(displacetheta(1),Ndir)
            cff4=0.0
```

```
            do jw=1,Nfrq
              wd_bry(jw)=MOD(jw-cff2,float(Ndir))
              if (wd_bry(jw).le.0.0) wd_bry(jw)=wd_bry(jw)+Ndir
              wd_bry(jw)=(-1.0)**real(jw)*(-pi*0.5 +
     &            pi*(floor(real(wd_bry(jw))/2.0 -
     &            0.5))/(real(Ndir)-1.0))
              wd_bry(jw)=wd_bry(jw)+wd
              if (wd_bry(jw).ge.0.5*pi) wd_bry(jw)=0.5*pi
              if (wd_bry(jw).le.-0.5*pi) wd_bry(jw)=-0.5*pi
              cff3=exp(-((wd_bry(jw)-wd)/max(1.5*wds,1.e-12))**2)
              wa_bry_d(jw)=cff3
              cff4=cff4+wa_bry_d(jw)*wa_bry(jw)
            enddo

!         Normalisation
            cff1=sumspec/DOT_PRODUCT(wa_bry_d,wa_bry)
            do jw=1,Nfrq
              wa_bry_d(jw)=sqrt(wa_bry_d(jw)*cff1)
              wa_bry(jw)=wa*sqrt(wa_bry(jw)/sumspec)
            enddo

#  ifdef WAVE_MAKER_DSPREAD_PER
!
! Forcing periodicitiy on all wave components such that
! k_i*sin(theta_i)=p*(2*pi/Ly) with p an integer
!
            cff3=2*pi/el      ! domain wavenumber
            diff=0.0
            do jw=1,Nfrq
              cff1=wd_bry(jw)      ! angle before correction
              cff6=cff1
```

```
            cff2=wk_bry(jw)      ! associated wavenumber
            mindiff=abs((cff2 * sin(cff1))
     &         / cff3 -  nint((cff2 * sin(cff1)) / cff3))
            if (cff3.lt.cff2) then
              iw=1
              do while ((iw<10000) .AND. (mindiff.gt.1e-6))
                cff4 = (cff2 * sin(cff1 + 1.e-4))/cff3
                cff5 = (cff2 * sin(cff1 - 1.e-4))/cff3
                if (abs(cff4-nint(cff4)).lt.mindiff) then
                  mindiff = abs(cff4-nint(cff4))
                  cff1 = cff1 + 1e-4
                else if (abs(cff5-nint(cff5)).lt.mindiff) then
                  mindiff = abs(cff5-nint(cff5))
                  cff1 = cff1 - 1.e-4
                endif
                iw=iw+1
              enddo
              wd_bry(jw)=cff1
            endif
            diff = diff + abs((cff6 - wd_bry(jw))/cff6)
          enddo
          diff = (diff/Nfrq)*100.
          write (*,*) "WAVEMAKER: Wave directions have been modified",
     &      " of an average of ",diff,"%"
#   endif /* WAVE_MAKER_DSPREAD_PER  */

           call RANDOM_NUMBER(wpha_bry)  ! random phase
           do iw=1,Nfrq
             wpha_bry(iw)=(wpha_bry(iw))*2.*pi
             wkx_bry(iw)=wk_bry(iw)*cos(wd_bry(iw))
             wky_bry(iw)=wk_bry(iw)*sin(wd_bry(iw))
```

```
          enddo
# endif /* WAVE_MAKER_DSPREAD */
```

B.2 forces.h

```
#ifdef WAVE_MAKER
      integer Nfrq, Ndir
      parameter (Nfrq=1550, Ndir=31)
      real wf_bry(Nfrq), wk_bry(Nfrq), wa_bry(Nfrq)
      real wd_bry(Nfrq), wa_bry_d(Nfrq)
      real sumspec, cff6, diff, mindiff, beta
      common /wave_maker/ wf_bry, wk_bry, wa_bry
      common /wave_maker/ wd_bry, wa_bry_d
      common /sumspec/ sumspec
# ifdef WAVE_MAKER_DSPREAD
      integer displacetheta(1)
      real wpha_bry(Nfrq)
      real wkx_bry(Nfrq)
      real wky_bry(Nfrq)
      common /wave_maker_k/ wkx_bry, wky_bry
# else
      real wpha_bry(Nfrq)
# endif
      common /wave_maker_pha/ wpha_bry
#endif
```

Acronyms

ADV	Acoustic Doppler Velocimeter	83
BOSZ	Boussinesq Ocean and Surf Zone (model)	53
CEW	Current Effect on Waves	50
CFL	Courant-Friedrich-Levy (condition)	61
COAWST	Coupled Ocean-Atmosphere-Wave-Sediment Transport (model)	51
CPU	Central Processing Unit	142
CROCO	Coastal and Regional Ocean COmmunity (model)	58
ENSO	El Niño Southern Oscillation	16
FUNWAVE	FUlly Nonlinear Boussinesq WAVE (model)	65
GLS	Generic Length Scale (turbulence closure)	62
GPU	Graphics Processing Unit	154
IG	Infra-Gravity	25
JONSWAP	JOint North Sea WAve Project	20
KPP	K-Profile Parametrization (turbulence closure)	62
LES	Large-Eddy Simulation	54
NHWAVE	Non-Hydrostatic WAVE (model)	53
NSWE	Nonlinear Shallow Water equations	66
RANS	Reynolds-Averaged Navier-Stokes equations	53
ROMS	Regional Ocean Modeling System (model)	58
SPH	Smooth-Particle Hydrodynamics	54
SWAN	Simulating WAves Nearshore (model)	51
SWASH	Simulating WAves till Shore (model)	53
TVD	Total Variation Diminishing	66
VF	Vortex Force	50
VLF	Very Low Frequency	25
WEC	Wave Effect on Currents	50
WENO5	Weighted Essentially Non-Oscillatory scheme at 5^{th} order (scheme)	62
WW3	Wave Watch III (model)	51

Index

Bibliography

Adams, NG., MacFadyen, A., Hickey, BM., & Trainer, VL. (2006). The nearshore advection of a toxigenic Pseudo-nitzschia bloom and subsequent domoic acid contamination of intertidal bivalves. *African Journal of Marine Science 28*(2), 271–276. https://doi.org/10.2989/18142320609504161

Alexakis, A., & Biferale, L. (2018). Cascades and transitions in turbulent flows. *Physics Reports 767–769*, 1–101. https://doi.org/10.1016/j.physrep.2018.08.001

Allen, J. S., Newberger, P. A., & Holman, R. A. (1996). Nonlinear shear instabilities of alongshore currents on plane beaches. *Journal of Fluid Mechanics 310*, 181–213. https://doi.org/10.1017/S0022112096001772

Almar, R., Boucharel, J., Graffin, M., Abessolo, G. O., Thoumyre, G., Papa, F., Ranasinghe, R., Montano, J., Bergsma, E. W. J., Baba, M. W., & Jin, F. F. (2023). Influence of El Niño on the variability of global shoreline position. *Nature Communications 14*(1), 3133. https://doi.org/10.1038/s41467-023-38742-9

Aluie, H., Hecht, M., & Vallis, G. K. (2018). Mapping the Energy Cascade in the North Atlantic Ocean: The Coarse-Graining Approach. *Journal of Physical Oceanography 48*(2), 225–244. https://doi.org/10.1175/JPO-D-17-0100.1

Auclair, F., Bordois, L., Dossmann, Y., Duhaut, T., Paci, A., Ulses, C., & Nguyen, C. (2018). A non-hydrostatic non-Boussinesq algorithm for free-surface ocean modelling. *Ocean Modelling 132*, 12–29. https://doi.org/10.1016/j.ocemod.2018.07.011

Baker, C., Moulton, M., & Nuss, E. (2023a). *Experimental Investigation of Short-Crested Wave Breaking in a Laboratory Directional Wave Basin*. DesignSafe-CI. https://doi.org/10.17603/ds2-qgd5-jk92

Baker, C. M. (2023). *Surfzone Vorticity Dynamics in a Directional Wave Basin*. [Doctoral dissertation, University of Washington, Seattle, WA, USA]. http://hdl.handle.net/1773/49872

Baker, C. M., Moulton, M., Chickadel, C. C., Nuss, E. S., Palmsten, M. L., & Brodie, K. L. (2023b). Two-dimensional inverse energy cascade in a laboratory surf zone for varying wave directional spread. *Physics of Fluids 35*(12), 125140. https://doi.org/10.1063/5.0169895

Baker, C. M., Moulton, M., Palmsten, M. L., Brodie, K., Nuss, E., & Chickadel, C. C. (2023c). Remotely sensed short-crested breaking waves in a laboratory directional wave basin. *Coastal Engineering 183*, 104327. https://doi.org/10.1016/j.coastaleng.2023.104327

Baker, C. M., Moulton, M., Raubenheimer, B., Elgar, S., & Kumar, N. (2021). Modeled Three-Dimensional Currents and Eddies on an Alongshore-Variable Barred Beach. *Journal of Geophysical Research: Oceans 126*(7), e2020JC016899. https://doi.org/10.1029/2020JC016899

Blayo, E., & Debreu, L. (2005). Revisiting open boundary conditions from the point of view of characteristic variables. *Ocean Modelling 9*(3), 231–252. https://doi.org/10.1016/j.ocemod.2004.07.001

Boehm, A. B., Grant, S. B., Kim, J. H., Mowbray, S. L., McGee, C. D., Clark, C. D., Foley, D. M., & Wellman, D. E. (2002). Decadal and Shorter Period Variability of Surf Zone Water Quality at Huntington Beach, California. *Environmental Science & Technology 36*(18), 3885–3892. https://doi.org/10.1021/es020524u

Boehm, A. B., Keymer, D. P., & Shellenbarger, G. G. (2005). An analytical model of enterococci inactivation, grazing, and transport in the surf zone of a marine beach. *Water Research 39*(15), 3565–3578. https://doi.org/10.1016/j.watres.2005.06.026

Bondehagen, A., Roeber, V., Kalisch, H., Buckley, M. P., Streßer, M., Cysewski, M., Horstmann, J., Bjørnestad, M., Ige, O. E., Frøysa, H. G., & Carrasco-Alvarez, R. (2024). Wave-driven current and vortex patterns at an open beach: Insights from phase-resolving numerical computations and Lagrangian measurements. *Coastal Engineering 193*, 104591. https://doi.org/10.1016/j.coastaleng.2024.104591

Bonnet-Ben Dhia, A. S., Bristeau, M. O., Godlewski, E., Impériale, S., Mangeney, A., & Sainte-Marie, J. (2021). Pseudo-compressibility, Dispersive Model and Acoustic Waves in Shallow Water Flows. In M. L. Muñoz-Ruiz, C. Parés & G. Russo (Eds.), *Recent Advances in Numerical Methods for Hyperbolic PDE Systems* (pp. 209–250). Cham. https://doi.org/10.1007/978-3-030-72850-2_10

Bonneton, P. (2023). Energy and dissipation spectra of waves propagating in the inner surf zone. *Journal of Fluid Mechanics 977*, A48. https://doi.org/10.1017/jfm.2023.878

Bonneton, P., Barthelemy, E., Chazel, F., Cienfuegos, R., Lannes, D., Marche, F., & Tissier, M. (2011). Recent advances in Serre–Green Naghdi modelling for wave transformation, breaking and runup processes. *European Journal of Mechanics - B/Fluids 30*(6), 589–597. https://doi.org/10.1016/j.euromechflu.2011.02.005

Borges, R., Carmona, M., Costa, B., & Don, W. S. (2008). An improved weighted essentially non-oscillatory scheme for hyperbolic conservation laws. *Journal of Computational Physics 227*(6), 3191–3211. https://doi.org/10.1016/j.jcp.2007.11.038

Bowen, A. J. (1969). Rip currents: 1. Theoretical investigations. *Journal of Geophysical Research (1896-1977) 74*(23), 5467–5478. https://doi.org/10.1029/JC074i023p05467

Bowen, A. J., & Holman, R. A. (1989). Shear instabilities of the mean longshore current: 1. Theory. *Journal of Geophysical Research: Oceans 94*(C12), 18023–18030. https://doi.org/10.1029/JC094iC12p18023

Brocchini, M. (2013). A reasoned overview on Boussinesq-type models: The interplay between physics, mathematics and numerics. *Proceedings. Mathematical, Physical, and Engineering Sciences / The Royal Society 469*(2160), 20130496. https://doi.org/10.1098/rspa.2013.0496

Brown, J., MacMahan, J., Reniers, A., & Thornton, E. (2009). Surf zone diffusivity on a rip-channeled beach. *Journal of Geophysical Research: Oceans 114*(C11). https://doi.org/10.1029/2008JC005158

Brown, J. A., MacMahan, J. H., Reniers, A. J. H. M., & Thornton, E. B. (2015). Field Observations of Surf Zone–Inner Shelf Exchange on a Rip-Channeled Beach. *Journal of Physical Oceanography 45*(9), 2339–2355. https://doi.org/10.1175/JPO-D-14-0118.1

Brown, J. A., MacMahan, J. H., Reniers, A. J. H. M., Thornton, E. B., Shanks, A. L., Morgan, S. G., & Gallagher, E. L. (2019). Observations of mixing and transport on a steep beach. *Continental Shelf Research 178*, 1–14. https://doi.org/10.1016/j.csr.2019.03.009

Castelle, B. (2016). Rip current types, circulation and hazard. *Earth-Science Reviews 163*, 1–21. https://doi.org/10.1016/j.earscirev.2016.09.008

Castelle, B., Almar, R., Dorel, M., Lefebvre, J. P., Senechal, N., Anthony, E. J., Laibi, R., Chuchla, R., & du Penhoat, Y. (2014). Rip currents and circulation on a high-energy low-tide-terraced beach (Grand Popo, Benin, West Africa). *Journal of Coastal Research 70*(sp1), 633–638. https://doi.org/10.2112/SI70-107.1

Castelle, B., Brander, R., Tellier, E., Simonnet, B., Scott, T., McCarroll, J., Campagne, J. M., Cavailhes, T., & Lechevrel, P. (2018). Surf zone hazards and injuries on beaches in SW France. *Natural Hazards 93*(3), 1317–1335. https://doi.org/10.1007/s11069-018-3354-4

Center For International Earth Science Information Network-CIESIN-Columbia University. (2012). *National Aggregates of Geospatial Data Collection: Population, Landscape, And Climate Estimates, Version 3 (PLACE III)*. [object Object]. https://doi.org/10.7927/H4F769GP

Clark, D. B., Elgar, S., & Raubenheimer, B. (2012). Vorticity generation by short-crested wave breaking. *Geophysical Research Letters 39*(24). https://doi.org/10.1029/2012GL054034

Clark, D. B., Feddersen, F., & Guza, R. T. (2010). Cross-shore surfzone tracer dispersion in an alongshore current. *Journal of Geophysical Research: Oceans 115*(C10). https://doi.org/10.1029/2009JC005683

Clark, D. B., Feddersen, F., & Guza, R. T. (2011). Modeling surf zone tracer plumes: 2. Transport and dispersion. *Journal of Geophysical Research: Oceans 116*(C11). https://doi.org/10.1029/2011JC007211

Clark, D. B., Lenain, L., Feddersen, F., Boss, E., & Guza, R. T. (2014). Aerial Imaging of Fluorescent Dye in the Near Shore. *Journal of Atmospheric and Oceanic Technology 31*(6), 1410–1421. https://doi.org/10.1175/JTECH-D-13-00230.1

Clarke, L. B., Ackerman, D., & Largier, J. (2007). Dye dispersion in the surf zone: Measurements and simple models. *Continental Shelf Research 27*(5), 650–669. https://doi.org/10.1016/j.csr.2006.10.010

Contardo, S., Hoeke, R., Branson, P., Hernaman, V., & Pitman, T. (2020). *Hydrodynamic modelling for nearshore predictions*. CSIRO Australia. https://research.csiro.au/bluelink/wp-content/uploads/sites/352/2020/09/Hydrodynamic_Modelling_for_nearshore_predictions_V1_CSIRO_REPORT_2020.pdf

Cornell, S., Brander, R., Roberts, A., Koon, W., Peden, A., & Lawes, J. (2023). 'I actually thought that I was going to die': Lessons on the rip current hazard from survivor experiences. *Health promotion journal of Australia : official journal of Australian Association of Health Promotion Professionals 35*. https://doi.org/10.1002/hpja.785

Craik, A. D. D. (1971). Non-linear resonant instability in boundary layers. *Journal of Fluid Mechanics 50*(2), 393–413. https://doi.org/10.1017/S0022112071002635

Croitoru, L., Miranda Montero, J. J., & Sarraf, M. (2019). *The Cost of Coastal Zone Degradation in West Africa : Benin, Cote d'Ivoire, Senegal, and Togo 1*. Washington, D.C. : World Bank Group.

Dada, O., Almar, R., Morand, P., & Menard, F. (2021). "Towards West African coastal social-ecosystems sustainability: Interdisciplinary approaches". *Ocean & Coastal Management 211*, 105746. https://doi.org/10.1016/j.ocecoaman.2021.105746

Dada, O. A., Almar, R., Morand, P., Bergsma, E. W., Angnuureng, D. B., & Minderhoud, P. S. (2023). Future socioeconomic development along the west african coast forms a larger hazard than sea level rise. *Communications Earth & Environment 4*(1), 150. https://doi.org/10.1038/s43247-023-00807-4

Dalrymple, R. A. (1975). A mechanism for rip current generation on an open coast. *Journal of Geophysical Research (1896-1977) 80*(24), 3485–3487. https://doi.org/10.1029/JC080i024p03485

Das, P., Marchesiello, P., & Middleton, J. H. (2000). Numerical modelling of tide-induced residual circulation in Sydney harbour. *Marine and Freshwater Research 51*, 97–112. https://doi.org/10.1071/MF97177

De-la-Torre, G. E., Dioses-Salinas, D. C., Castro, J. M., Antay, R., Fernández, N. Y., Espinoza-Morriberón, D., & Saldaña-Serrano, M. (2020). Abundance and distribution of microplastics on sandy beaches of Lima, Peru. *Marine Pollution Bulletin 151*, 110877. https://doi.org/10.1016/j.marpolbul.2019.110877

Debreu, L., Marchesiello, P., Penven, P., & Cambon, G. (2012). Two-way nesting in split-explicit ocean models: Algorithms, implementation and validation. *Ocean Modelling 49–50*, 1–21. https://doi.org/10.1016/j.ocemod.2012.03.003

Derakhti, M., Kirby, J. T., Shi, F., & Ma, G. (2016). NHWAVE: Consistent boundary conditions and turbulence modeling. *Ocean Modelling 106*, 121–130. https://doi.org/10.1016/j.ocemod.2016.09.002

Dione, C. T., Diagne, I., Ndiaye, M., Diebakate, C., Ndiaye, B., & Diop, A. (2018). Contamination Métallique D'une Espèce De Poisson (Brama Brama) De La Côte Dakaroise. *European Scientific Journal, ESJ 14*(12), 374–374. https://doi.org/10.19044/esj.2018.v14n12p374

Dodd, N., Oltman-Shay, J., & Thornton, E. B. (1992). Shear Instabilities in the Longshore Current: A Comparison of Observation and Theory. *Journal of Physical Oceanography 22*(1), 62–82. https://doi.org/10.1175/1520-0485(1992)022⟨0062:SIITLC⟩2.0.CO;2

Duval, E. (2022). *Vers Le Couplage de Modèles de Circulation Océanique Hydrostatique et Non Hydrostatique*. [Doctoral dissertation, Université Grenoble Alpes].

Earle, S. (2019). *Physical Geology - 2nd Edition*. BCcampus.

Eckart, C. (1948). An analysis of the stirring and mixing processes in incompressible fluids. *Journal of Marine Research 7*(3).

Einstein, A. (1905). INVESTIGATIONS ON THE THEORY OF THE BROWNIAN MOVEMENT. *Annalen der Physik 17*.

Elgar, S., Dooley, C., Gorrell, L., & Raubenheimer, B. (2023). Observations of two-dimensional turbulence in the surfzone. *Physics of Fluids 35*(8), 085142. https://doi.org/10.1063/5.0159170

Elgar, S., & Raubenheimer, B. (2020). Field Evidence of Inverse Energy Cascades in the Surfzone. *Journal of Physical Oceanography 50*(8), 2315–2321. https://doi.org/10.1175/JPO-D-19-0327.1

Elko, N., Feddersen, F., Foster, D., Hapke, C., McNinch, J., Mulligan, R., Özkan-Haller, H., Plant, N., & Raubenheimer, B. (2015). The future of nearshore processes research. *Shore and Beach 83*, 13–38.

Estrade, P., Marchesiello, P., Colin de Verdiere, A., Roy, C., Colin de Verdiere, A., & Roy, C. (2008). Cross-shelf structure of coastal upwelling : A two - dimensional extension of Ekman's theory and a mechanism for inner shelf upwelling shut down. *Journal of Marine Research 66*(5), 589–616. https://doi.org/10.1357/002224008787536790

Faria, A. F. G., Thornton, E. B., Lippmann, T. C., & Stanton, T. P. (2000). Undertow over a barred beach. *Journal of Geophysical Research: Oceans 105*(C7), 16999–17010. https://doi.org/10.1029/2000JC900084

Feddersen, F. (2007). Breaking wave induced cross-shore tracer dispersion in the surf zone: Model results and scalings. *Journal of Geophysical Research: Oceans 112*(C9). https://doi.org/10.1029/2006JC004006

Feddersen, F. (2014). The Generation of Surfzone Eddies in a Strong Alongshore Current. *Journal of Physical Oceanography 44*(2), 600–617. https://doi.org/10.1175/JPO-D-13-051.1

Feddersen, F., Clark, D. B., & Guza, R. T. (2011). Modeling surf zone tracer plumes: 1. Waves, mean currents, and low-frequency eddies. *Journal of Geophysical Research: Oceans 116*(C11). https://doi.org/10.1029/2011JC007210

Fischer, H. B. (1978). On the tensor form of the bulk dispersion coefficient in a bounded skewed shear flow. *Journal of Geophysical Research: Oceans 83*(C5), 2373–2375. https://doi.org/https://doi.org/10.1029/JC083iC05p02373

Fischer, S., & Thatje, S. (2008). Temperature-induced oviposition in the brachyuran crab *Cancer setosus* along a latitudinal cline: Aquaria experiments and analysis of field-data. *Journal of Experimental Marine Biology and Ecology 357*(2), 157–164. https://doi.org/10.1016/j.jembe.2008.01.007

Floc'h, F., Mabiala, G. R., Almar, R., Castelle, B., Hall, N., Penhoat, Y. D., Scott, T., & Delacourt, C. (2018). Flash Rip Statistics from Video Images. *Journal of Coastal Research 81*(sp1), 100–106. https://doi.org/10.2112/SI81-013.1

Forsberg, P. L., Sous, D., Stocchino, A., & Chemin, R. (2020). Behaviour of plastic litter in nearshore waters: First insights from wind and wave laboratory experiments. *Marine Pollution Bulletin 153*, 111023. https://doi.org/10.1016/j.marpolbul.2020.111023

Fowler, R. E., & Dalrymple, R. A. (1990). Wave Group Forced Nearshore Circulation. In *Coastal Engineering* (pp. 729–742). American Society of Civil Engineers. https://doi.org/10.1061/9780872627765.058

Geiman, J. D., Kirby, J. T., Reniers, A. J. H. M., & MacMahan, J. H. (2011). Effects of wave averaging on estimates of fluid mixing in the surf zone. *Journal of Geophysical Research: Oceans 116*(C4). https://doi.org/10.1029/2010JC006678

Gobbi, M. F., Kirby, J. T., & Kennedy, A. B. (2001). On the consistency of boussinesq models and their ability to predict vertical vorticity fields. In *Coastal Engineering 2000* (pp. 1321–1334). American Society of Civil Engineers. https://doi.org/10.1061/40549(276)102

Gobbi, M. F., Kirby, J. T., & Wei, G. (2000). A fully nonlinear Boussinesq model for surface waves. Part 2. Extension to O(kh)4. *Journal of Fluid Mechanics 405*, 181–210. https://doi.org/10.1017/S0022112099007247

Goda, Y. (2000). *Random Seas and Design of Maritime Structures* (2nd ed., vol. 15). WORLD SCIENTIFIC. https://doi.org/10.1142/3587

Graffin, M., Taherkhani, M., Leung, M., Vitousek, S., Kaminsky, G., & Ruggiero, P. (2023). Monitoring interdecadal coastal change along dissipative beaches via satellite imagery at regional scale. *Cambridge Prisms: Coastal Futures 1*, e42. https://doi.org/10.1017/cft.2023.30

Grimes, D. J., Feddersen, F., & Giddings, S. N. (2021). Long-Distance/Time Surf-Zone Tracer Evolution Affected by Inner-Shelf Tracer Retention and Recirculation. *Journal of Geophysical Research: Oceans 126*(12), e2021JC017661. https://doi.org/10.1029/2021JC017661

Grimes, D. J., Feddersen, F., Giddings, S. N., & Pawlak, G. (2020a). Cross-Shore Deformation of a Surfzone-Released Dye Plume by an Internal Tide on the Inner Shelf. *Journal of Physical Oceanography 50*(1), 35–54. https://doi.org/10.1175/JPO-D-19-0046.1

Grimes, D. J., Feddersen, F., & Kumar, N. (2020b). Tracer Exchange Across the Stratified Inner-Shelf Driven by Transient Rip-Currents and Diurnal Surface Heat Fluxes. *Geophysical Research Letters 47*(10), e2019GL086501. https://doi.org/10.1029/2019GL086501

Guza, R., & Feddersen, F. (2011). *Lagrangian Tracer Transport and Dispersion in Shallow Tidal Inlets & River Mouths 1.* Scripps Institution of Oceanography.

Hally-Rosendahl, K., & Feddersen, F. (2016). Modeling surfzone to inner-shelf tracer exchange: MODELING SURFZONE/INNER-SHELF EXCHANGE. *Journal of Geophysical Research: Oceans 121*(6), 4007–4025. https://doi.org/10.1002/2015JC011530

Hally-Rosendahl, K., Feddersen, F., Clark, D. B., & Guza, R. T. (2015). Surfzone to inner-shelf exchange estimated from dye tracer balances. *Journal of Geophysical Research: Oceans 120*(9), 6289–6308. https://doi.org/10.1002/2015JC010844

Hally-Rosendahl, K., Feddersen, F., & Guza, R. T. (2014). Cross-shore tracer exchange between the surfzone and inner-shelf. *Journal of Geophysical Research: Oceans 119*(7), 4367–4388. https://doi.org/10.1002/2013JC009722

Harris, T. F., Jordaan, J. M., Mcmurray, W. R., Verwey, C. J., & Anderson, F. P. (1963). MIXING IN THE SURF ZONE. *Air and Water Pollution 7*, 649–667.

Hasselmann, K., Barnett, T. P., Bouws, E., Carlson, H., Cartwright, D. E., Enke, K., Ewing, J. A., Gienapp, A., Hasselmann, D. E., Kruseman, P., Meerburg, A., Müller, P., Olbers, D. J., Richter, K., Sell, W., & Walden, H. (1973). Measurements of wind-wave growth and swell decay during the joint North Sea wave project (JONSWAP). *Ergänzungsheft zur Deutschen Hydrographischen Zeitschrift, Reihe A Nr. 12*.

Henderson, S. M., Arnold, J., Özkan-Haller, H. T., & Solovitz, S. A. (2017). Depth Dependence of Nearshore Currents and Eddies. *Journal of Geophysical Research: Oceans 122*(11), 9004–9031. https://doi.org/10.1002/2016JC012349

Herbers, T. H. C., Elgar, S., & Guza, R. T. (1999). Directional spreading of waves in the nearshore. *Journal of Geophysical Research: Oceans 104*(C4), 7683–7693. https://doi.org/10.1029/1998JC900092

Higuera, P., Losada, I. J., & Lara, J. L. (2015). Three-dimensional numerical wave generation with moving boundaries. *Coastal Engineering 101*, 35–47. https://doi.org/10.1016/j.coastaleng.2015.04.003

Hilt, M., Roblou, L., Nguyen, C., Marchesiello, P., Lemarié, F., Jullien, S., Dumas, F., Debreu, L., Capet, X., Bordois, L., Benshila, R., & Auclair, F. (2020). Numerical modeling of hydraulic control, solitary waves and primary instabilities in the Strait of Gibraltar. *Ocean Modelling 155*, 101642. https://doi.org/10.1016/j.ocemod.2020.101642

Holmedal, L. E., & Myrhaug, D. (2009). Wave-induced steady streaming, mass transport and net sediment transport in rough turbulent ocean bottom boundary layers. *Continental Shelf Research 29*(7), 911–926. https://doi.org/10.1016/j.csr.2009.01.012

Hunt, J., Wray, A., & Moin, P. (1988). Eddies, streams, and convergence zones in turbulent flows. In *Proceedings of the Summer Program 1988*.

Inman, D. L., Tait, R. J., & Nordstrom, C. E. (1971). Mixing in the surf zone. *Journal of Geophysical Research (1896-1977) 76*(15), 3493–3514. https://doi.org/10.1029/JC076i015p03493

Jambeck, J. R., Geyer, R., Wilcox, C., Siegler, T. R., Perryman, M., Andrady, A., Narayan, R., & Law, K. L. (2015). Plastic waste inputs from land into the ocean. *Science 347*(6223), 768–771. https://doi.org/10.1126/science.1260352

Jefferys, E. R. (1987). Directional seas should be ergodic. *Applied Ocean Research 9*(4), 186–191. https://doi.org/10.1016/0141-1187(87)90001-0

Johansen, K., Dunne, A. F., Tu, Y. H., Almashharawi, S., Jones, B. H., & McCabe, M. F. (2022). Dye tracing and concentration mapping in coastal waters using unmanned aerial vehicles. *Scientific Reports 12*(1), 1141. https://doi.org/10.1038/s41598-022-05189-9

Johnson, D., & Pattiaratchi, C. (2004). Transient rip currents and nearshore circulation on a swell-dominated beach. *Journal of Geophysical Research: Oceans 109*(C2). https://doi.org/10.1029/2003JC001798

Johnson, D., & Pattiaratchi, C. (2006). Boussinesq modelling of transient rip currents. *Coastal Engineering 53*(5), 419–439. https://doi.org/10.1016/j.coastaleng.2005.11.005

Kazolea, M., & Ricchiuto, M. (2018). On wave breaking for Boussinesq-type models. *Ocean Modelling 123*, 16–39. https://doi.org/10.1016/j.ocemod.2018.01.003

Kellay, H., & Goldburg, W. I. (2002). Two-dimensional turbulence: A review of some recent experiments. *Reports on Progress in Physics 65*(5), 845. https://doi.org/10.1088/0034-4885/65/5/204

Kennedy, A. B., Kirby, J. T., Chen, Q., & Dalrymple, R. A. (2001). Boussinesq-type equations with improved nonlinear performance. *Wave Motion 33*(3), 225–243. https://doi.org/10.1016/S0165-2125(00)00071-8

Ki, S. J., Hwang, J. H., Kang, J. H., & Kim, J. H. (2009). An analytical model for non-conservative pollutants mixing in the surf zone. *Water Science and Technology 59*(11), 2117–2124. https://doi.org/10.2166/wst.2009.231

Kim, D. H. (2021). Flash rip current driven suspended sediment flushing amplification in depth-integrated modeling framework. *Advances in Water Resources 155*, 103997. https://doi.org/10.1016/j.advwatres.2021.103997

Kim, S., & Kim, D. H. (2024). Short-term buoyant microplastic transport patterns driven by wave evolution, breaking, and orbital motion in coast. *Marine Pollution Bulletin 201*, 116248. https://doi.org/10.1016/j.marpolbul.2024.116248

Kirby, J. T. (2016). Boussinesq Models and Their Application to Coastal Processes across a Wide Range of Scales. *Journal of Waterway, Port, Coastal, and Ocean Engineering 142*(6), 03116005. https://doi.org/10.1061/(ASCE)WW.1943-5460.0000350

Kirby, J. T. (2017). Recent advances in nearshore wave, circulation, and sediment transport modeling. *Journal of Marine Research 75*(3), 263–300. https://doi.org/10.1357/002224017821836824

Kirby, J. T., & Derakhti, M. (2019). Short-crested wave breaking. *European Journal of Mechanics - B/Fluids 73*, 100–111. https://doi.org/10.1016/j.euromechflu.2017.11.001

Klotz, A. N., Almar, R., Quenet, Y., Bergsma, E. W. J., Youssefi, D., Artigues, S., Rascle, N., Sy, B. A., & Ndour, A. (2024). Nearshore satellite-derived bathymetry from a single-pass satellite video: Improvements from adaptive correlation window size and modulation transfer function. *Remote Sensing of Environment 315*, 114411. https://doi.org/10.1016/j.rse.2024.114411

Kolmogorov, A. N. (1941). The Local Structure of Turbulence in Incompressible Viscous Fluid for Very Large Reynolds Numbers. *Proceedings: Mathematical and Physical Sciences 434*(1890,), 9–13.

Kraichnan, R. H. (1967). Inertial Ranges in Two-Dimensional Turbulence. *The Physics of Fluids 10*(7), 1417. https://doi.org/10.1063/1.1762301

Kranenburg, W. M., Ribberink, J. S., Uittenbogaard, R. E., & Hulscher, S. J. M. H. (2012). Net currents in the wave bottom boundary layer: On waveshape streaming and progressive wave streaming. *Journal of Geophysical Research: Earth Surface 117*(F3). https://doi.org/10.1029/2011JF002070

Kuik, A. J., van Vledder, G. P., & Holthuijsen, L. H. (1988). A Method for the Routine Analysis of Pitch-and-Roll Buoy Wave Data. *Journal of Physical Oceanography 18*(7), 1020–1034. https://doi.org/10.1175/1520-0485(1988)018⟨1020:AMFTRA⟩2.0.CO;2

Kumar, N., & Feddersen, F. (2017a). The Effect of Stokes Drift and Transient Rip Currents on the Inner Shelf. Part I: No Stratification. *Journal of Physical Oceanography 47*(1), 227–241. https://doi.org/10.1175/JPO-D-16-0076.1

Kumar, N., & Feddersen, F. (2017b). The Effect of Stokes Drift and Transient Rip Currents on the Inner Shelf. Part II: With Stratification. *Journal of Physical Oceanography 47*(1), 243–260. https://doi.org/10.1175/JPO-D-16-0077.1

Kumar, N., & Feddersen, F. (2017c). A new offshore transport mechanism for shoreline-released tracer induced by transient rip currents and stratification. *Geophysical Research Letters 44*(6), 2843–2851. https://doi.org/10.1002/2017GL072611

Kumar, N., Voulgaris, G., Warner, J. C., & Olabarrieta, M. (2012). Implementation of the vortex force formalism in the coupled ocean-atmosphere-wave-sediment transport (COAWST) modeling system for inner shelf and surf zone applications. *Ocean Modelling 47*, 65–95. https://doi.org/10.1016/j.ocemod.2012.01.003

Lane, E. M., Restrepo, J. M., & McWilliams, J. C. (2007). Wave–Current Interaction: A Comparison of Radiation-Stress and Vortex-Force Representations. *Journal of Physical Oceanography 37*(5), 1122–1141. https://doi.org/10.1175/JPO3043.1

Larsen, B. E., & Fuhrman, D. R. (2018). On the over-production of turbulence beneath surface waves in Reynolds-averaged Navier–Stokes models. *Journal of Fluid Mechanics 853*, 419–460. https://doi.org/10.1017/jfm.2018.577

Lentz, S. J., & Fewings, M. R. (2012). The Wind- and Wave-Driven Inner-Shelf Circulation. *Annual Review of Marine Science 4*(1), 317–343. https://doi.org/10.1146/annurev-marine-120709-142745

Leslie, H. M., Breck, E. N., Chan, F., Lubchenco, J., & Menge, B. A. (2005). Barnacle reproductive hotspots linked to nearshore ocean conditions. *Proceedings of the National Academy of Sciences 102*(30), 10534–10539. https://doi.org/10.1073/pnas.0503874102

Li, L., & Dalrymple, R. A. (1998). Instabilities of the undertow. *Journal of Fluid Mechanics 369*, 175–190. https://doi.org/10.1017/S0022112098001694

Lippmann, T. C., & Bowen, A. J. (2016). The Vertical Structure of Low-Frequency Motions in the Nearshore. Part II: Theory. *Journal of Physical Oceanography 46*(12), 3713–3727. https://doi.org/10.1175/JPO-D-16-0015.1

Lippmann, T. C., Herbers, T. H. C., & Thornton, E. B. (1999). Gravity and Shear Wave Contributions to Nearshore Infragravity Motions. *Journal of Physical Oceanography 29*(2), 231–239. https://doi.org/10.1175/1520-0485(1999)029⟨0231:GASWCT⟩2.0.CO;2

Liu, Y., & Wu, C. H. (2022). Drowning incidents and conditions due to hidden flash rips in Lake Michigan. *Science of The Total Environment 827*, 154314. https://doi.org/10.1016/j.scitotenv.2022.154314

Longuet-Higgins, M. S. (1956). The refraction of sea waves in shallow water. *Journal of Fluid Mechanics 1*(2), 163–176. https://doi.org/10.1017/S0022112056000111

Longuet-Higgins, M. S., & Stewart, R. W. (1962). Radiation stress and mass transport in gravity waves, with application to 'surf beats'. *Journal of Fluid Mechanics 13*(4), 481–504. https://doi.org/10.1017/S0022112062000877

Longuet-Higgins, M. S., & Stewart, R. W. (1964). Radiation stresses in water waves; a physical discussion, with applications. *Deep Sea Research and Oceanographic Abstracts 11*(4), 529–562. https://doi.org/10.1016/0011-7471(64)90001-4

Longuet-Higgins, M. S., & Stoneley, R. (1953). Mass transport in water waves. *Philosophical Transactions of the Royal Society of London. Series A, Mathematical and Physical Sciences 245*(903), 535–581. https://doi.org/10.1098/rsta.1953.0006

Lubin, P., & Chanson, H. (2017). Are breaking waves, bores, surges and jumps the same flow? *Environmental Fluid Mechanics 17*(1), 47–77. https://doi.org/10.1007/s10652-016-9475-y

Lubin, P., & Glockner, S. (2015). Numerical simulations of three-dimensional plunging breaking waves: Generation and evolution of aerated vortex filaments. *Journal of Fluid Mechanics 767*, 364–393. https://doi.org/10.1017/jfm.2015.62

Luijendijk, A., Hagenaars, G., Ranasinghe, R., Baart, F., Donchyts, G., & Aarninkhof, S. (2018). The State of the World's Beaches. *Scientific Reports 8*(1), 6641. https://doi.org/10.1038/s41598-018-24630-6

Lynett, P., & Liu, P. L. F. (2004). A two-layer approach to wave modelling. *Proceedings of the Royal Society of London. Series A: Mathematical, Physical and Engineering Sciences 460*(2049), 2637–2669. https://doi.org/10.1098/rspa.2004.1305

Ma, G., Shi, F., & Kirby, J. T. (2012). Shock-capturing non-hydrostatic model for fully dispersive surface wave processes. *Ocean Modelling 43–44*, 22–35. https://doi.org/10.1016/j.ocemod.2011.12.002

MacMahan, J. H., Reniers, A. J. H. M., & Thornton, E. B. (2010). Vertical surf zone velocity fluctuations with 0(10) min period. *Journal of Geophysical Research: Oceans 115*(C6). https://doi.org/10.1029/2009JC005383

MacMahan, J. H., Thornton, E. B., & Reniers, A. J. H. M. (2006). Rip current review. *Coastal Engineering 53*(2), 191–208. https://doi.org/10.1016/j.coastaleng.2005.10.009

Marchesiello, P., Auclair, F., Debreu, L., McWilliams, J., Almar, R., Benshila, R., & Dumas, F. (2021). Tridimensional nonhydrostatic transient rip currents in a wave-resolving model. *Ocean Modelling 163*, 101816. https://doi.org/10.1016/j.ocemod.2021.101816

Marchesiello, P., Benshila, R., Almar, R., Uchiyama, Y., McWilliams, J. C., & Shchepetkin, A. (2015). On tridimensional rip current modeling. *Ocean Modelling 96*, 36–48. https://doi.org/10.1016/j.ocemod.2015.07.003

Marchesiello, P., Capet, X., Menkes, C., & Kennan, S. C. (2011). Submesoscale dynamics in tropical instability waves. *Ocean Modelling 39*(1), 31–46. https://doi.org/10.1016/j.ocemod.2011.04.011

Marchesiello, P., Chauchat, J., Shafiei, H., Almar, R., Benshila, R., Dumas, F., & Debreu, L. (2022). 3D wave-resolving simulation of sandbar migration. *Ocean Modelling 180*, 102127. https://doi.org/10.1016/j.ocemod.2022.102127

Marchesiello, P., McWilliams, J. C., & Shchepetkin, A. (2001). Open boundary conditions for long-term integration of regional oceanic models. *Ocean Modelling 3*(1), 1–20. https://doi.org/10.1016/S1463-5003(00)00013-5

Marchesiello, P., McWilliams, J. C., & Shchepetkin, A. (2003). Equilibrium Structure and Dynamics of the California Current System. *Journal of Physical Oceanography 33*(4), 753–783. https://doi.org/10.1175/1520-0485(2003)33⟨753:ESADOT⟩2.0.CO;2

Marchesiello, P., Nguyen, N. M., Gratiot, N., Loisel, H., Anthony, E. J., Dinh, C. S., Nguyen, T., Almar, R., & Kestenare, E. (2019). Erosion of the coastal mekong delta: Assessing natural against man induced processes. *Continental Shelf Research 181*, 72–89. https://doi.org/https://doi.org/10.1016/j.csr.2019.05.004

Marchesiello, P., & Treillou, S. (2023). Correction of GLS turbulence closure for wave-resolving models with stratification. *Ocean Modelling 184*, 102212. https://doi.org/10.1016/j.ocemod.2023.102212

Mayer, S., & Madsen, P. A. (2000). Simulation of Breaking Waves in the Surf Zone using a Navier-Stokes Solver. *Coastal Engineering 1*, 928–941. https://doi.org/10.1061/40549(276)72

McLachlan, A., & Hesp, P. (1984). Faunal response to morphology and water circulation of a sandy beach with cusps. *Mar. Ecol. Prog. Ser. 19*. https://doi.org/10.3354/meps019133

McWilliams, J., Restrepo, J., & Lane, E. (2004). An asymptotic theory for interaction of waves and currents in coastal waters. *Journal of Fluid Mechanics 511*, 135–178. https://doi.org/10.1017/S0022112004009358

McWilliams, J. C., Akan, C., & Uchiyama, Y. (2018). Robustness of nearshore vortices. *Journal of Fluid Mechanics 850*, R2. https://doi.org/10.1017/jfm.2018.510

Metcalfe, R. W., Orszag, S. A., Brachet, M. E., Menon, S., & Riley, J. J. (1987). Secondary instability of a temporally growing mixing layer. *Journal of Fluid Mechanics 184*, 207–243. https://doi.org/10.1017/S0022112087002866

Miche, M. (1944). Mouvements ondulatoires de la mer en profondeur constante ou décroissante. *Ann. Ponts et Chaussée 114*.

Middlebrooks, E., Armenante, P., & Carmichael, J. (1981). Industrial pollution discharges from the west african region. *Environment International 5*(3), 177–191.

Miles, J. W. (1957). On the generation of surface waves by shear flows. *Journal of Fluid Mechanics 3*(2), 185–204. https://doi.org/10.1017/S0022112057000567

Miles, M. D., & Funke, E. R. (1989). A Comparison of Methods for Synthesis of Directional Seas. *Journal of Offshore Mechanics and Arctic Engineering 111*(1), 43–48. https://doi.org/10.1115/1.3257137

Morgan, S. G., Shanks, A. L., MacMahan, J. H., Reniers, A. J., & Feddersen, F. (2018). Planktonic Subsidies to Surf-Zone and Intertidal Communities. *Annual Review of Marine Science 10*(1), 345–369. https://doi.org/10.1146/annurev-marine-010816-060514

Motte, E. (2017). *Iconographie et Géomorphologie : l'usage de représentations artistiques des rivages comme outil de connaissance de l'évolution du littoral.* [Doctoral dissertation, Université Rennes 2].

Moulton, M., Chickadel, C. C., & Thomson, J. (2021). Warm and Cool Nearshore Plumes Connecting the Surf Zone to the Inner Shelf. *Geophysical Research Letters 48*(10), e2020GL091675. https://doi.org/10.1029/2020GL091675

Moulton, M., Suanda, S. H., Garwood, J. C., Kumar, N., Fewings, M. R., & Pringle, J. M. (2023). Exchange of Plankton, Pollutants, and Particles Across the Nearshore Region. *Annual Review of Marine Science 15*(1), 167–202. https://doi.org/10.1146/annurev-marine-032122-115057

Munk, W. (1950). Origin and generation of waves. *Proceedings of the International Conference on Coastal Engineering; Vol 1, No 1 (1950): Proceedings of First Conference on Coastal Engineering, Long Beach, California, October, 1950. 1.* https://doi.org/10.9753/icce.v1.1

Munk, W. H. (1944). *Proposed uniform procedure for observing waves and interpreting instrument records Wave Project Rep. 26.* Scripps Institution of Oceanography.

Munk, W. H., Miller, G. R., Snodgrass, F. E., Barber, N. F., & Deacon, G. E. R. (1963). Directional recording of swell from distant storms. *Philosophical Transactions of the Royal Society of London. Series A, Mathematical and Physical Sciences 255*(1062), 505–584. https://doi.org/10.1098/rsta.1963.0011

Newberger, P. A., & Allen, J. S. (2007). Forcing a three-dimensional, hydrostatic, primitive-equation model for application in the surf zone: 2. Application to DUCK94. *Journal of Geophysical Research: Oceans 112*(C8). https://doi.org/10.1029/2006JC003474

Nuss, E. S., Moulton, M., Suanda, S. H., & Baker, C. M. (2025). Modeled Surf-Zone Eddies on a Laboratory Scale Barred Beach With Varying Wave Conditions. *Journal of Geophysical Research: Oceans 130*(1), e2023JC020549. https://doi.org/10.1029/2023JC020549

Nwogu, O. (1993). Alternative Form of Boussinesq Equations for Nearshore Wave Propagation. *Journal of Waterway, Port, Coastal, and Ocean Engineering 119*(6), 618–638. https://doi.org/10.1061/(ASCE)0733-950X(1993)119:6(618)

O'Dea, A., Kumar, N., & Haller, M. C. (2021). Simulations of the Surf Zone Eddy Field and Cross-Shore Exchange on a Nonidealized Bathymetry. *Journal of Geophysical Research: Oceans 126*(5), e2020JC016619. https://doi.org/10.1029/2020JC016619

Ono, K., Knutsen, H., Olsen, E. M., Ruus, A., Hjermann, D. Ø., & Chr. Stenseth, N. (2019). Possible adverse impact of contaminants on Atlantic cod population dynamics in coastal ecosystems. *Proceedings of the Royal Society B: Biological Sciences 286*(1908), 20191167. https://doi.org/10.1098/rspb.2019.1167

Özkan-Haller, H. (2008). Three-dimensional currents in the outer nearshore zone. In *AGU Fall Meeting Abstracts*.

Özkan-Haller, H. T., & Kirby, J. T. (1999). Nonlinear evolution of shear instabilities of the longshore current: A comparison of observations and computations. *Journal of Geophysical Research: Oceans 104*(C11), 25953–25984. https://doi.org/10.1029/1999JC900104

Özkan-Haller, H. T., & Li, Y. (2003). Effects of wave-current interaction on shear instabilities of longshore currents. *Journal of Geophysical Research: Oceans 108*(C5). https://doi.org/10.1029/2001JC001287

Park, S., Kim, D. H., & Yoo, H. (2020). Morphodynamic Modelling of Flash Rip Current Driven Coastal Sediment Transport. *Journal of Coastal Research 95*(SI), 1229–1234. https://doi.org/10.2112/SI95-238.1

Pascal, R. (2012). *Quantification of the Influence of Directional Sea State Parameters over the Performances of Wave Energy Converters*. [Doctoral dissertation, The University of Edinburgh].

Pascal, R., & Bryden, I. (2011). Directional spectrum methods for deterministic waves. *Ocean Engineering 38*(13), 1382–1396. https://doi.org/10.1016/j.oceaneng.2011.05.021

Pearson, J. M., Guymer, I., West, J. R., & Coates, L. E. (2009). Solute Mixing in the Surf Zone. *Journal of Waterway, Port, Coastal, and Ocean Engineering 135*(4), 127–134. https://doi.org/10.1061/(ASCE)0733-950X(2009)135:4(127)

Peregrine, D. (1998). Surf Zone Currents. *Theoretical and Computational Fluid Dynamics 10*(1), 295–309. https://doi.org/10.1007/s001620050065

Peregrine, D. H. (1967). Long waves on a beach. *Journal of Fluid Mechanics 27*(4), 815–827. https://doi.org/10.1017/S0022112067002605

Phillips, O. M. (1957). On the generation of waves by turbulent wind. *Journal of Fluid Mechanics 2*(5), 417–445. https://doi.org/10.1017/S0022112057000233

Pierrehumbert, R. T., & Widnall, S. E. (1982). The two- and three-dimensional instabilities of a spatially periodic shear layer. *Journal of Fluid Mechanics 114*, 59–82. https://doi.org/10.1017/S0022112082000044

Pierson, W. J., & Moskowitz, L. (1964). A proposed spectral form for fully developed wind seas based on the similarity theory of S. A. Kitaigorodskii. *Journal of Geophysical Research (1896-1977) 69*(24), 5181–5190. https://doi.org/10.1029/JZ069i024p05181

Pineda, J. (1999). Circulation and larval distribution in internal tidal bore warm fronts. *Limnology and Oceanography 44*(6), 1400–1414. https://doi.org/10.4319/lo.1999.44.6.1400

Pope, S. B. (2000). *Turbulent Flows*. Cambridge University Press. https://doi.org/10.1017/CBO9780511840531

Raubenheimer, B., Guza, R. T., & Elgar, S. (1996). Wave transformation across the inner surf zone. *Journal of Geophysical Research: Oceans 101*(C11), 25589–25597. https://doi.org/10.1029/96JC02433

Renault, L., Hall, A., & McWilliams, J. (2016). Orographic shaping of us west coast wind profiles during the upwelling season. *Climate Dynamics 46*, 273–289. https://doi.org/10.1007/s00382-015-2583-4

Richard, G. L. (2021). An extension of the boussinesq-type models to weakly compressible flows. *European Journal of Mechanics - B/Fluids 89*, 217–240. https://doi.org/10.1016/j.euromechflu.2021.05.011

Richardson, L. F. (1922). *Weather Prediction by Numerical Process*. Cambridge, The University press.

Rippy, M. A., Franks, P. J. S., Feddersen, F., Guza, R. T., & Moore, D. F. (2013a). Physical dynamics controlling variability in nearshore fecal pollution: Fecal indicator bacteria as passive particles. *Marine Pollution Bulletin 66*(1), 151–157. https://doi.org/10.1016/j.marpolbul.2012.09.030

Rippy, M. A., Franks, P. J. S., Feddersen, F., Guza, R. T., & Warrick, J. A. (2013b). Beach Nourishment Impacts on Bacteriological Water Quality and Phytoplankton Bloom Dynamics. *Environmental Science & Technology 47*(12), 6146–6154. https://doi.org/10.1021/es400572k

Roberts, P., & Webster, D. (2002). Turbulent diffusion. *Environmental Fluid Mechanics: Theories and Applications 7-47*.

Roeber, V., Cheung, K. F., & Kobayashi, M. H. (2010). Shock-capturing Boussinesq-type model for nearshore wave processes. *Coastal Engineering 57*(4), 407–423. https://doi.org/10.1016/j.coastaleng.2009.11.007

Roelvink, J. A., & Banning, G. K. F. M. V. (1995). Design and development of DELFT3D and application to coastal morphodynamics. *Oceanographic Literature Review 11*(42), 925.

Rogers, M. M., & Moser, R. D. (1992). The three-dimensional evolution of a plane mixing layer: The Kelvin–Helmholtz rollup. *Journal of Fluid Mechanics 243*, 183–226. https://doi.org/10.1017/S0022112092002696

Salatin, R., Chen, Q., Bak, A. S., Shi, F., & Brandt, S. R. (2021). Effects of Wave Coherence on Longshore Variability of Nearshore Wave Processes. *Journal of Geophysical Research: Oceans 126*(11), e2021JC017641. https://doi.org/10.1029/2021JC017641

Saleem, F., Schellhorn, H. E., Simhon, A., & Edge, T. A. (2023). Same-day Enterococcus qPCR results of recreational water quality at two Toronto beaches provide added public health protection and reduced beach days lost. *Canadian Journal of Public Health 114*(4), 676–687. https://doi.org/10.17269/s41997-023-00763-8

Schäffer, H. A., Madsen, P. A., & Deigaard, R. (1993). A Boussinesq model for waves breaking in shallow water. *Coastal Engineering 20*(3), 185–202. https://doi.org/10.1016/0378-3839(93)90001-O

Schramek, T. A., Colin, P. L., Merrifield, M. A., & Terrill, E. J. (2018). Depth-Dependent Thermal Stress Around Corals in the Tropical Pacific Ocean. *Geophysical Research Letters 45*(18), 9739–9747. https://doi.org/10.1029/2018GL078782

Schubert, R., Gula, J., Greatbatch, R. J., Baschek, B., & Biastoch, A. (2020). The Submesoscale Kinetic Energy Cascade: Mesoscale Absorption of Submesoscale Mixed Layer Eddies and Frontal Downscale Fluxes. *Journal of Physical Oceanography 50*(9), 2573–2589. https://doi.org/10.1175/JPO-D-19-0311.1

van Sebille, E., Aliani, S., Law, K. L., Maximenko, N., Alsina, J. M., Bagaev, A., Bergmann, M., Chapron, B., Chubarenko, I., Cózar, A., Delandmeter, P., Egger, M., Fox-Kemper, B., Garaba, S. P., Goddijn-Murphy, L., Hardesty, B. D., Hoffman, M. J., Isobe, A., Jongedijk, C. E., Kaandorp, M. L. A., Khatmullina, L., Koelmans, A. A., Kukulka, T., Laufkötter, C., Lebreton, L., Lobelle, D., Maes, C., Martinez-Vicente, V., Maqueda, M. A. M., Poulain-Zarcos, M., Rodríguez, E., Ryan, P. G., Shanks, A. L., Shim, W. J., Suaria, G., Thiel, M., van den Bremer, T. S., & Wichmann, D. (2020). The physical oceanography of the transport of floating marine debris. *Environmental Research Letters 15*(2), 023003. https://doi.org/10.1088/1748-9326/ab6d7d

Shafiei, H., Chauchat, J., Bonamy, C., & Marchesiello, P. (2023). Adaptation of the SANTOSS transport formula for 3D nearshore models: Application to cross-shore sandbar migration. *Ocean Modelling 181*, 102138. https://doi.org/10.1016/j.ocemod.2022.102138

Shanks, A. L. (1995). Mechanisms of Cross-Shelf Dispersal of Larval Invertebrates and Fish. In *Ecology of Marine Invertebrate Larvae*. CRC Press.

Shanks, A. L., Morgan, S. G., MacMahan, J., Reniers, A. J., Jarvis, M., Brown, J., Fujimura, A., Ziccarelli, L., & Griesemer, C. (2018). Persistent Differences in Horizontal Gradients in Phytoplankton Concentration Maintained by Surf Zone Hydrodynamics. *Estuaries and Coasts 41*(1), 158–176. https://doi.org/10.1007/s12237-017-0278-2

Shanks, A. L., Morgan, S. G., MacMahan, J., & Reniers, A. J. H. M. (2010). Surf zone physical and morphological regime as determinants of temporal and spatial variation in larval recruitment. *Journal of Experimental Marine Biology and Ecology 392*(1), 140–150. https://doi.org/10.1016/j.jembe.2010.04.018

Shanks, A. L., Morgan, S. G., MacMahan, J., & Reniers, A. J. H. M. (2017). Alongshore variation in barnacle populations is determined by surf zone hydrodynamics. *Ecological Monographs 87*(3), 508–532. https://doi.org/10.1002/ecm.1265

Shanks, A. L., Morgan, S. G., MacMahan, J., Reniers, A. J. H. M., Kudela, R., Jarvis, M., Brown, J., Fujimura, A., Ziccarelli, L., & Griesemer, C. (2016). Variation in the abundance of *Pseudo-nitzschia* and domoic acid with surf zone type. *Harmful Algae 55*, 172–178. https://doi.org/10.1016/j.hal.2016.03.004

Shchepetkin, A. F., & McWilliams, J. C. (2005). The regional oceanic modeling system (ROMS): A split-explicit, free-surface, topography-following-coordinate oceanic model. *Ocean Modelling 9*(4), 347–404. https://doi.org/10.1016/j.ocemod.2004.08.002

Shi, F., Kirby, J. T., Harris, J. C., Geiman, J. D., & Grilli, S. T. (2012). A high-order adaptive time-stepping TVD solver for Boussinesq modeling of breaking waves and coastal inundation. *Ocean Modelling 43–44*, 36–51. https://doi.org/10.1016/j.ocemod.2011.12.004

Silva-Cavalcanti, J. S., Costa, M. F., & Pereira, P. S. (2018). Rip currents signaling and users behaviour at an overcrowded urban beach. *Ocean & Coastal Management 155*, 90–97. https://doi.org/10.1016/j.ocecoaman.2018.01.031

Sinnett, G., & Feddersen, F. (2014). The surf zone heat budget: The effect of wave heating. *Geophysical Research Letters 41*(20), 7217–7226. https://doi.org/10.1002/2014GL061398

Sinnett, G., & Feddersen, F. (2018). The Competing Effects of Breaking Waves on Surfzone Heat Fluxes: Albedo Versus Wave Heating. *Journal of Geophysical Research: Oceans 123*(10), 7172–7184. https://doi.org/10.1029/2018JC014284

Sinnett, G., Feddersen, F., Lucas, A. J., Pawlak, G., & Terrill, E. (2018). Observations of Nonlinear Internal Wave Run-Up to the Surfzone. *Journal of Physical Oceanography 48*(3), 531–554. https://doi.org/10.1175/JPO-D-17-0210.1

Smit, P., Janssen, T., Holthuijsen, L., & Smith, J. (2014). Non-hydrostatic modeling of surf zone wave dynamics. *Coastal Engineering 83*, 36–48. https://doi.org/10.1016/j.coastaleng.2013.09.005

Smit, P., Zijlema, M., & Stelling, G. (2013). Depth-induced wave breaking in a non-hydrostatic, near-shore wave model. *Coastal Engineering 76*, 1–16. https://doi.org/10.1016/j.coastaleng.2013.01.008

Smit, P. B., & Janssen, T. T. (2013). The evolution of inhomogeneous wave statistics through a variable medium. *Journal of Physical Oceanography 43*(8), 1741 – 1758. https://doi.org/10.1175/JPO-D-13-046.1

Soufflet, Y., Marchesiello, P., Lemarié, F., Jouanno, J., Capet, X., Debreu, L., & Benshila, R. (2016). On effective resolution in ocean models. *Ocean Modelling 98*, 36–50. https://doi.org/10.1016/j.ocemod.2015.12.004

Sous, D., Bonneton, N., & Sommeria, J. (2005). Transition from deep to shallow water layer: Formation of vortex dipoles. *European Journal of Mechanics - B/Fluids 24*(1), 19–32. https://doi.org/10.1016/j.euromechflu.2004.06.002

Splinter, K., & Slinn, D. (2003). Three-dimensional modeling of alongshore current dynamics. In *Canadian Coastal Conference, Kingston, Ontario.*

Spydell, M., & Feddersen, F. (2009). Lagrangian Drifter Dispersion in the Surf Zone: Directionally Spread, Normally Incident Waves. *Journal of Physical Oceanography 39*(4), 809–830. https://doi.org/10.1175/2008JPO3892.1

Spydell, M., Feddersen, F., Guza, R. T., & Schmidt, W. E. (2007). Observing Surf-Zone Dispersion with Drifters. *Journal of Physical Oceanography 37*(12), 2920–2939. https://doi.org/10.1175/2007JPO3580.1

Spydell, M. S. (2016). The suppression of surfzone cross-shore mixing by alongshore currents. *Geophysical Research Letters 43*(18), 9781–9790. https://doi.org/10.1002/2016GL070626

Spydell, M. S., & Feddersen, F. (2012a). The effect of a non-zero Lagrangian time scale on bounded shear dispersion. *Journal of Fluid Mechanics 691*, 69–94. https://doi.org/10.1017/jfm.2011.443

Spydell, M. S., & Feddersen, F. (2012b). A Lagrangian stochastic model of surf zone drifter dispersion. *Journal of Geophysical Research: Oceans 117*(C3). https://doi.org/10.1029/2011JC007701

Spydell, M. S., Feddersen, F., & Guza, R. T. (2009). Observations of drifter dispersion in the surfzone: The effect of sheared alongshore currents. *Journal of Geophysical Research: Oceans 114*(C7). https://doi.org/10.1029/2009JC005328

Spydell, M. S., Feddersen, F., & Suanda, S. (2019). Inhomogeneous turbulent dispersion across the nearshore induced by surfzone eddies. *Journal of Physical Oceanography 49*(4), 1015 – 1034. https://doi.org/10.1175/JPO-D-18-0102.1

Stewart, R. H. (2008). *Introduction to Physical Oceanography.* Robert H. Stewart.

Stokes, G. (1847). On the theory of oscillatory waves. *Transactions of the Cambridge Philosophical Society 8*, 441.

Suanda, S. H., & Feddersen, F. (2015). A self-similar scaling for cross-shelf exchange driven by transient rip currents: SCALING TRANSIENT RIP CURRENT EXCHANGE. *Geophysical Research Letters 42*(13), 5427–5434. https://doi.org/10.1002/2015GL063944

Svendsen, I. A. (1984). Wave heights and set-up in a surf zone. *Coastal Engineering 8*(4), 303–329. https://doi.org/10.1016/0378-3839(84)90028-0

Svendsen, I. A. (1987). Analysis of surf zone turbulence. *Journal of Geophysical Research: Oceans 92*(C5), 5115–5124. https://doi.org/10.1029/JC092iC05p05115

Svendsen, I. A. (2005). *Introduction to Nearshore Hydrodynamics* (Vol. 24). WORLD SCIENTIFIC. https://doi.org/10.1142/5740

Svendsen, I. A., & Putrevu, U. (1994). Nearshore mixing and dispersion. *Proceedings: Mathematical and Physical Sciences 445*(1925), 561–576. http://www.jstor.org/stable/52519

Tang, E. C. S., & Dalrymple, R. A. (1989). Rip Currents and Wave Groups. In R. J. Seymour (Ed.), *Nearshore Sediment Transport* (pp. 205–230). Springer US. https://doi.org/10.1007/978-1-4899-2531-2_22

Taveneau, A., Almar, R., Bergsma, E. W. J., Sy, B. A., Ndour, A., Sadio, M., & Garlan, T. (2021). Observing and Predicting Coastal Erosion at the Langue de Barbarie Sand Spit around Saint Louis (Senegal, West Africa) through Satellite-Derived Digital Elevation Model and Shoreline. *Remote Sensing 13*(13), 2454. https://doi.org/10.3390/rs13132454

Taylor, G. I. (1921). DIFFUSION BY CONTINUOUS MOVEMENTS. *Proceedings of the London Mathematical Society 20*.

Tissier, M., Bonneton, P., Marche, F., Chazel, F., & Lannes, D. (2012). A new approach to handle wave breaking in fully non-linear Boussinesq models. *Coastal Engineering 67*, 54–66. https://doi.org/10.1016/j.coastaleng.2012.04.004

Tonelli, M., & Petti, M. (2009). Hybrid finite volume – finite difference scheme for 2DH improved Boussinesq equations. *Coastal Engineering 56*(5), 609–620. https://doi.org/10.1016/j.coastaleng.2009.01.001

Treillou, S., & Marchesiello, P. (2022). Impact of 3D non-hydrostatic dynamics on tracer transport in the nearshore region. In *XVIIèmes Journées Nationales Génie Côtier Génie Civil, Chatou* (pp. 191–200). https://doi.org/10.5150/jngcgc.2022.021

Treillou, S., & Marchesiello, P. (2024). Effets du cisaillement vertical sur le transport en zone littorale à l'aide d'un modèle 3D à vagues résolues. In *XVIIIèmes Journées Nationales Génie Côtier Génie Civil, Anglet* (pp. 205–214). https://doi.org/DOI:10.5150/jngcgc.2024.022

Treillou, S., Marchesiello, P., Baker, C., McWilliams, J., & Dumas, F. (2025). Tracer dispersion by surfzone eddies: assessing the impact of undertow vertical shear. *Journal of Physical Oceanography*.

Treillou, S., Marchesiello, P., & Baker, C. M. (2024). Correction of coherent interference in wave-resolving nearshore models and validation with experimental data. *Ocean Modelling 189*, 102369. https://doi.org/10.1016/j.ocemod.2024.102369

Trowbridge, J., & Madsen, O. S. (1984). Turbulent wave boundary layers: 1. Model formulation and first-order solution. *Journal of Geophysical Research: Oceans 89*(C5), 7989–7997. https://doi.org/10.1029/JC089iC05p07989

Uchiyama, Y., McWilliams, J. C., & Akan, C. (2017). Three-dimensional transient rip currents: Bathymetric excitation of low-frequency intrinsic variability. *Journal of Geophysical Research: Oceans 122*(7), 5826–5849. https://doi.org/10.1002/2017JC013005

Uchiyama, Y., McWilliams, J. C., & Restrepo, J. M. (2009). Wave-current interaction in nearshore shear instability analyzed with a vortex force formalism. *Journal of Geophysical Research: Oceans 114*(C6). https://doi.org/10.1029/2008JC005135

Uchiyama, Y., McWilliams, J. C., & Shchepetkin, A. F. (2010). Wave–current interaction in an oceanic circulation model with a vortex-force formalism: Application to the surf zone. *Ocean Modelling 34*(1), 16–35. https://doi.org/10.1016/j.ocemod.2010.04.002

van Heijst, G. J. F. (2014). Shallow flows: 2D or not 2D? *Environmental Fluid Mechanics 14*(5), 945–956. https://doi.org/10.1007/s10652-013-9305-4

Villermaux, E. (2019). Mixing Versus Stirring. *Annual Review of Fluid Mechanics 51*(Volume 51, 2019), 245–273. https://doi.org/10.1146/annurev-fluid-010518-040306

Wang, P., McWilliams, J. C., & Uchiyama, Y. (2021). A Nearshore Oceanic Front Induced by Wave Streaming. *Journal of Physical Oceanography 51*(6), 1967–1984. https://doi.org/10.1175/JPO-D-21-0004.1

Wang, P., McWilliams, J. C., Uchiyama, Y., Chekroun, M. D., & Yi, D. L. (2020). Effects of Wave Streaming and Wave Variations on Nearshore Wave-Driven Circulation. *Journal of Physical Oceanography 50*(10), 3025–3041. https://doi.org/10.1175/JPO-D-19-0304.1

Warner, J. C., Defne, Z., Haas, K., & Arango, H. G. (2013). A wetting and drying scheme for ROMS. *Computers & Geosciences 58*, 54–61. https://doi.org/10.1016/j.cageo.2013.05.004

Warner, J. C., Sherwood, C. R., Arango, H. G., & Signell, R. P. (2005). Performance of four turbulence closure models implemented using a generic length scale method. *Ocean Modelling 8*(1), 81–113. https://doi.org/10.1016/j.ocemod.2003.12.003

Watanabe, Y., Saeki, H., & Hosking, R. J. (2005). Three-dimensional vortex structures under breaking waves. *Journal of Fluid Mechanics 545*, 291–328. https://doi.org/10.1017/S0022112005006774

Wei, G., & Kirby, J. T. (1995). Time-dependent numerical code for extended boussinesq equations. *Journal of Waterway, Port, Coastal, and Ocean Engineering 121*(5), 251–261. https://doi.org/10.1061/(ASCE)0733-950X(1995)121:5(251)

Wei, G., Kirby, J. T., Grilli, S. T., & Subramanya, R. (1995). A fully nonlinear Boussinesq model for surface waves. Part 1. Highly nonlinear unsteady waves. *Journal of Fluid Mechanics 294*, 71–92. https://doi.org/10.1017/S0022112095002813

Wei, G., Kirby, J. T., & Sinha, A. (1999). Generation of waves in Boussinesq models using a source function method. *Coastal Engineering 36*(4), 271–299. https://doi.org/10.1016/S0378-3839(99)00009-5

Weir, B., Uchiyama, Y., Lane, E. M., Restrepo, J. M., & McWilliams, J. C. (2011). A vortex force analysis of the interaction of rip currents and surface gravity waves. *Journal of Geophysical Research: Oceans 116*(C5). https://doi.org/10.1029/2010JC006232

Weiss, L. (2021). *Evaluation Des Apports Fluviaux de Microplastiques et Modélisation de Leur Dispersion En Mer Méditerranée*. [Doctoral dissertation, Perpignan].

Wilcox, D. C. (2008). Formulation of the k-w Turbulence Model Revisited. *AIAA Journal 46*(11), 2823–2838. https://doi.org/10.2514/1.36541

Woodson, C. B. (2018). The Fate and Impact of Internal Waves in Nearshore Ecosystems. *Annual Review of Marine Science 10*(Volume 10, 2018), 421–441. https://doi.org/10.1146/annurev-marine-121916-063619

Woodward, E., Beaumont, E., Russell, P., Wooler, A., & Macleod, R. (2013). Analysis of Rip Current Incidents and Victim Demographics in the UK. *Journal of Coastal Research 65*(sp1), 850 – 855. https://doi.org/10.2112/SI65-144.1

Wright, L. D., & Short, A. D. (1984). Morphodynamic variability of surf zones and beaches: A synthesis. *Marine Geology 56*(1), 93–118. https://doi.org/10.1016/0025-3227(84)90008-2

Wu, X., Feddersen, F., & Giddings, S. N. (2021). Diagnosing Surfzone Impacts on Inner-Shelf Flow Spatial Variability Using Realistic Model Experiments with and without Surface Gravity Waves. *Journal of Physical Oceanography 51*(8), 2505–2515. https://doi.org/10.1175/JPO-D-20-0324.1

Yuan, Y., Shi, F., Kirby, J. T., & Yu, F. (2020). FUNWAVE-GPU: Multiple-GPU Acceleration of a Boussinesq-Type Wave Model. *Journal of Advances in Modeling Earth Systems 12*(5), e2019MS001957. https://doi.org/10.1029/2019MS001957

Zhang, Y., Shi, F., Kirby, J. T., & Feng, X. (2022). Phase-Resolved Modeling of Wave Interference and Its Effects on Nearshore Circulation in a Large Ebb Shoal-Beach System. *Journal of Geophysical Research: Oceans 127*(10), e2022JC018623. https://doi.org/10.1029/2022JC018623

Zheng, P., Li, M., van der A, D. A., van der Zanden, J., Wolf, J., Chen, X., & Wang, C. (2017). A 3D unstructured grid nearshore hydrodynamic model based on the vortex force formalism. *Ocean Modelling 116*, 48–69. https://doi.org/10.1016/j.ocemod.2017.06.003

Zijlema, M., Stelling, G., & Smit, P. (2011). SWASH: An operational public domain code for simulating wave fields and rapidly varied flows in coastal waters. *Coastal Engineering 58*(10), 992–1012. https://doi.org/10.1016/j.coastaleng.2011.05.015

Zijlema, M., & Stelling, G. S. (2008). Efficient computation of surf zone waves using the nonlinear shallow water equations with non-hydrostatic pressure. *Coastal Engineering 55*(10), 780–790. https://doi.org/10.1016/j.coastaleng.2008.02.020

Titre : Effets des tourbillons de la zone de déferlement et du cisaillement vertical du courant de retour sur la dispersion des traceurs : approche de modélisation 3D à vagues résolues

Mots clés : Zone de déferlement, Plateau interne, Dispersion de traceur, Cisaillement vertical, Modèle à vagues résolues, Courant d'arrachement

Résumé : La zone côtière, englobant à la fois la zone de déferlement et le plateau interne, est une région extrêmement dynamique, où coexistent et interagissent des tourbillons et des courants d'arrachement à différentes échelles. Cette interface critique entre la terre et la mer joue un rôle essentiel dans le transport de divers éléments, tels que sédiments, contaminants (métaux lourds, microplastiques, pathogènes), et traceurs biologiques comme le plancton et les larves. Ces traceurs sont liés à des enjeux côtiers majeurs, comme l'érosion des plages, la pollution littorale et la préservation des écosystèmes. Sur des plages sableuses quasi uniformes le long du littoral, les principaux mécanismes de transport sont les courants d'arrachement transitoires, induits par des vagues multidirectionnelles. Bien que de nombreuses études aient exploré le transport de traceurs passifs dans ces conditions, la plupart reposent sur des modèles à vagues résolues bidimensionnels (Boussinesq), qui ne prennent pas en compte le cisaillement vertical, causé par les courants de surface dirigés vers la côte (dus au déferlement) et le courant de retour vers le large près du fond. Cette lacune conduit à sous-estimer le mélange dans la zone de déferlement et à le surestimer sur le plateau interne. Récemment, des modèles 3D à vagues résolues comme CROCO ont permis des études plus approfondies. L'objectif de cette thèse est d'améliorer ces modèles et d'évaluer l'impact du cisaillement vertical du courant d'arrachement sur la dispersion des traceurs. La première étape a consisté à corriger un problème d'interférence cohérente dans le générateur de vagues de CROCO, suivi de la validation de sa capacité à reproduire les dynamiques transitoires côtières à l'aide d'expériences en bassin à vagues. Une fois le modèle validé, l'influence du cisaillement vertical a été examinée à travers deux expériences de rejet de traceurs, l'une en bassin à vagues et l'autre lors d'une grande campagne de terrain à Imperial Beach, Californie. Les comparaisons des simulations avec et sans cisaillement vertical ont révélé deux résultats majeurs : une réduction de la dispersion vers le large due à l'affaiblissement de la cascade inverse de l'énergie cinétique 2D, et une augmentation du mélange dans la zone de déferlement via un nouveau processus 3D, impliquant les "mini-rips", des courants transitoires d'échelle intermédiaire récemment découverts. Ce travail, qui permet de mieux comprendre les mécanismes de transport dans les zones côtières, offre des perspectives pour améliorer la paramétrisation de modèles simplifiés.

Title: Surfzone eddies and undertow vertical shear effects on tracer dispersion: a 3D wave-resolving model approach

Key words: Surf zone, Inner shelf, Tracer dispersion, Undertow vertical shear, Wave-resolving model, Rip current

Abstract: The nearshore zone, encompassing the surf zone and the inner shelf, is a highly dynamic region where surfzone eddies and rip currents of varying scales coexist and interact. This critical interface between land and sea determines the transport of various elements, including sediments, contaminants (such as heavy metals, microplastics, and pathogens), as well as biological tracers like plankton and larvae. These tracers are central to addressing key coastal challenges, such as beach erosion, coastal pollution, and ecosystemic services. On longshore-uniform sandy beaches, one of the primary transport mechanisms is transient rip currents, driven by wave directional spread. While numerous studies have investigated passive tracer transport under these conditions, most have relied on depth-averaged wave-resolving models (Boussinesq models). Although these models offer valuable insights, they fail to capture the effect of vertical shear resulting from shoreward surface flow induced by breaking waves and seaward undertow. They typically underestimate mixing within the surf zone and overestimate offshore dispersion. Recently, 3D wave-resolving models such as CROCO have provided researchers with the tools to conduct more comprehensive studies. The objective of this thesis is to contribute to the ongoing improvement of these models and to assess the impact of undertow vertical shear on tracer dispersion. The first step was to correct a coherent interference problem in the CROCO wavemaker, then to validate its ability to resolve transient nearshore dynamics using a recent wave basin experiment. After confirming the robustness of the model, the influence of vertical shear was examined through two dye release experiments, one in a wave basin and the other during a large-scale field experiment at Imperial Beach, California. Comparisons of simulations with and without undertow vertical shear revealed two key findings: a reduction in offshore dispersion due to a weakening in the 2D inverse kinetic energy cascade, and enhanced mixing within the surf zone through a newly identified 3D process associated with "mini-rips", a type of intermediate-scale transient current recently discovered. This research, which provides a more accurate representation of transport mechanisms in the nearshore zone, offers valuable feedback for improving parameterizations in coarser models.